Controlling morphology of metal-organic frameworks and porous carbon materials: metal oxides as primary architecture-directing agents

Jongkook Hwang,[1] Aleksander Ejsmont,[2] Ralph Freund,[3] Joanna Goscianska,[2,*] Bernhard V. K. J. Schmidt,[4,*] and Stefan Wuttke[5,6,*]

[1]Inorganic Chemistry and Catalysis, Utrecht University, Universiteitsweg 99, 3584 CG, Utrecht, Netherlands

[2]Adam Mickiewicz University in Poznań, Faculty of Chemistry, Uniwersytetu Poznańskiego 8, 61-614 Poznań, Poland

[3]Chair of Solid State and Materials Chemistry, Institute of Physics, University of Augsburg, Universitätsstraße 1, 86159 Augsburg, Germany

[4]School of Chemistry, Joseph Black Building, University of Glasgow, G128QQ, UK

[5]BCMaterials, Basque Center for Materials, UPV/EHU Science Park, 48940 Leioa, Spain

[6]Ikerbasque, Basque Foundation for Science, 48013, Bilbao, Spain

*Correspondence to: joanna.goscianska@amu.edu.pl; Bernhard.Schmidt@glasgow.ac.uk; stefan.wuttke@bcmaterials.net

Abstract

Owing to their vast ratio of surface area to mass and volume, metal-organic frameworks and porous carbons revolutionized many applications that rely on chemical and physical interactions at surfaces. However, a major challenge today is to shape these porous materials to translate their enhanced performance from the laboratory into macroscopic real-world applications. In this review, we give a comprehensive overview of how the precise morphology control of metal oxides can be transferred to metal-organic framework and porous carbon materials. As such, tailored material structures can be designed in 0D, 1D, 2D, and 3D with considerable implications for applications like energy storage, catalysis or nanomedicine. Therefore, we predict that major research advances in morphology control of metal-organic frameworks and porous carbons will facilitate the use of those materials in addressing major needs of the society, especially the grand challenges of energy, health, and environment.

1. Introduction

Porous materials are of high interest for diverse applications ranging from catalysis and separation to gas storage and sensing. These materials can interact with their surrounding not only on their external surface, but throughout the vast internal surface of the pores. By functionalizing the internal and/or external surface, the activity can be tailored to the application. However, a great challenge today is to build materials that translate the functionality at the molecular level effectively to the macroscopic world. To do this, effective transport of reagents to, from, and within porous materials is critical. To overcome this barrier, porous materials will need to be structured with feature sizes from below one micrometre to the millimetre or centimetre scale. In fact, the challenge of morphology control over multiple length scales (Fig. 1) of porous materials is overlooked by researchers so far but is the key to enable groundbreaking real-world applications.

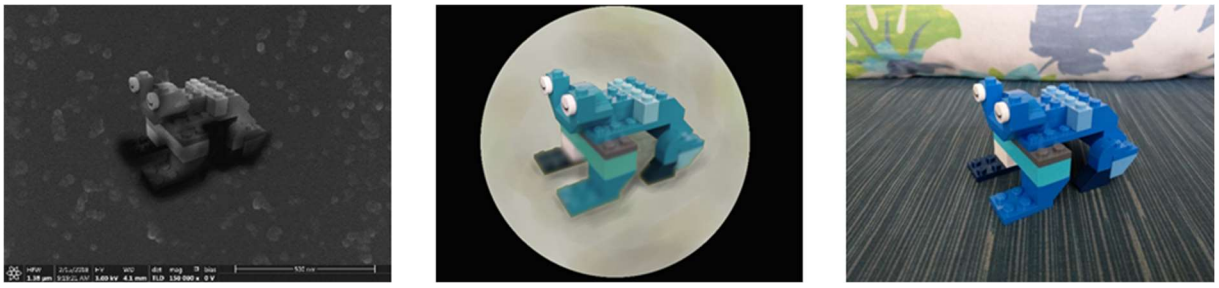

Fig. 1. Illustrating the challenge to synthesise a macroscopic object (*e.g.* toy frog, **right**) with the same morphology at the mesoscale (light microscope image, **middle**) and at the nanoscale (scanning electron microscopy image, **left**).

Recent years have seen a surge in work on materials that are based on reticular chemistry.[1-8] In reticular chemistry, molecular building blocks with controlled shape, geometry, functionality and valence are connected with strong chemical bonds to form porous, crystalline framework structures. Organic building blocks can then be assembled with secondary building units (SBU, *e.g.* metal-oxo clusters) to form extended materials called metal-organic frameworks (MOFs). The nodes and vertices of reticular materials are designed in such a way that they are rigid and directional, which is of great importance as it enables structure prediction and design. The rigidity and directionality of the components also make these materials porous, as free voids in the materials are easily created. These free voids can be post-synthetically modified to add different functionality to the material.[6, 8, 9] The accessibility of the interior of these materials to guests, in addition to the design and functionality aspect, has led to tremendous interest in reticular materials as they are inherently useful for gas adsorption, catalysis, sensing, and drug delivery.[6-8, 10] However, the morphology control of MOF materials beyond their periodic and designed networks is the current key challenge that has to be addressed in order to translate the scientific innovation of reticular chemistry from the lab bench into applicable technologies.[11]

The synthesis of a MOF material always starts with the strategic selection of precursor materials. Besides an organic building block, an inorganic compound providing metal ions is necessary, which most commonly is a metal salt, as it easily dissolves. A relatively new and different approach is the use of metal oxides (MOs). Even though their use is challenging due to low solubility issues and slow and non-homogenous conversion, by carefully optimizing the experimental conditions the MO–to–MOF conversion can be carried out with preserving the morphology of the MO. Thus, the use of MO

precursors, which offers a huge number of different morphologies that can be synthesized with high precision, potentially provides an easy and smart way for the precise synthesis of different MOF morphologies. This strategy opens the door to morphologies that cannot be achieved using reactions based on metal salt precursors or other approaches.

Moreover, the careful carbonization of those MOF materials offers to translate this morphology control to porous carbon.[12, 13] MOF materials could be used as "all-in-one" templates/precursors that contain both inorganic and organic constituents which can be pre-selected for preparation of targeted porous carbon materials, so called MOF-derived carbon (MDC), with specific morphologies and a plethora of applications, *e.g.* in energy storage, catalysis or nanomedicine.[14] MO, MOF and MDC are closely connected, which facilitates synthetic avenues from MO over MOF to MDC with control over morphology from the first building blocks to the final carbon material (Fig. 2). As such, control over MO morphology allows architecture direction over the whole synthesis route. This approach enables additional control over morphology and access to complex material architectures that are challenging to achieve via MOFs alone.

In this review, we summarize the morphology control methods of MOF/MDC with particular emphasis on the use of "MO as primary architecture directing agents". Starting from morphology control of MO itself, we cover the transformation of MO into MOF and finally into MDC. To do so, we categorize the reported MO/MOF/MDC products according to their synthetic strategies and particle morphologies (0D, 1D, 2D, 3D and hierarchical architectures). The synthetic methods, mechanisms, and their advantages and limitations are discussed comprehensively. Morphology controlled MOF and MDC materials have shown already great potential in a number of applications such as batteries, supercapacitors, fuel cells, adsorption, catalysis, sensing, and nanomedicine, which will be addressed as well. Overall, the review describes the avenue from MO over MOF to obtain well-defined MDC for applications.

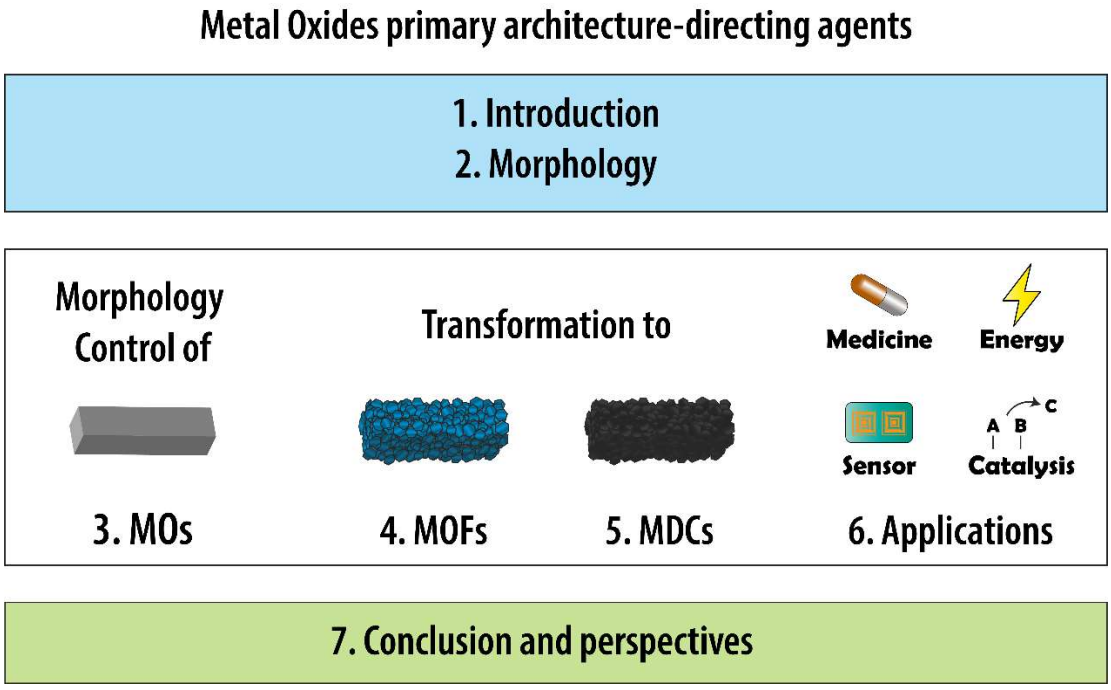

Fig. 2. Outline the article that follows the synthetic avenue from morphology-controlled metal oxides, transformation to MOFs, carbonization, applications and perspectives.

2. Morphology

According to the International Union of Pure and Applied Chemistry (IUPAC), morphology is defined as shape, optical appearance, texture or topography of surface and form of phase domains in materials. The expressions morphology and shape are usually used as synonyms when describing the external structure of nanoparticles and their aggregates.[15, 16] However, the differences between these concepts should be emphasized. The term morphology includes physical size, flatness, roundness, sphericity and aspect ratio of the nanoparticles while the shape considers their appearance without taking into account specific dimensions (Fig. 3).

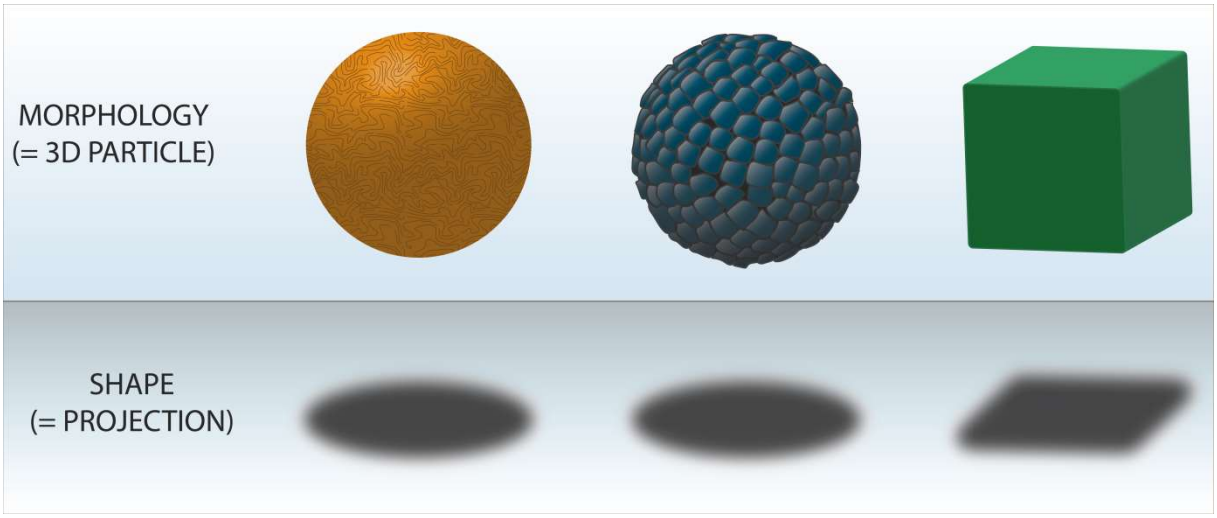

Fig. 3. Top: morphology in form of 3D particles (**left**: smooth surface, **middle**: roughly nanostructure surface, **right**: smooth surface), bottom: shape in form of 2D projection (**left, middle**: spherical, **right**: square).

The concept of morphology may seem intuitive until one attempts to determine the appropriate classification system of particles with regular and irregular shapes employing advanced 2D and 3D microscopy imaging techniques.[17, 18] This system of classification should be as versatile as possible and apply to a wide range of materials. In the case of nanostructures, the greatest difficulty in describing their morphology is that they undergo continuous transformations from one form to another. However, in 1995, Gleiter[19] presented the first classification system of nanostructured materials that was explained in detail by Skorohod *et al.*[20] It was incomplete because it did not include zero-dimensional (0D), one-dimensional (1D), two-dimensional (2D) and three-dimensional (3D) nanostructures *e.g.* fullerenes, tubes, and flowers. Thus, Pokropivny and Skorokhod[21] developed a modified classification system, in which they took into account the above-mentioned nanostructures. Nanomaterials were classified as 0D, 1D, 2D, 3D depending on their specific geometrical dimensions. Fig. 4 shows a schematic representation of various nanostructures and plots of energy dependence versus density of states.[22] It was found that the degree of confinement determines electronic density of state for different types of nanostructures.

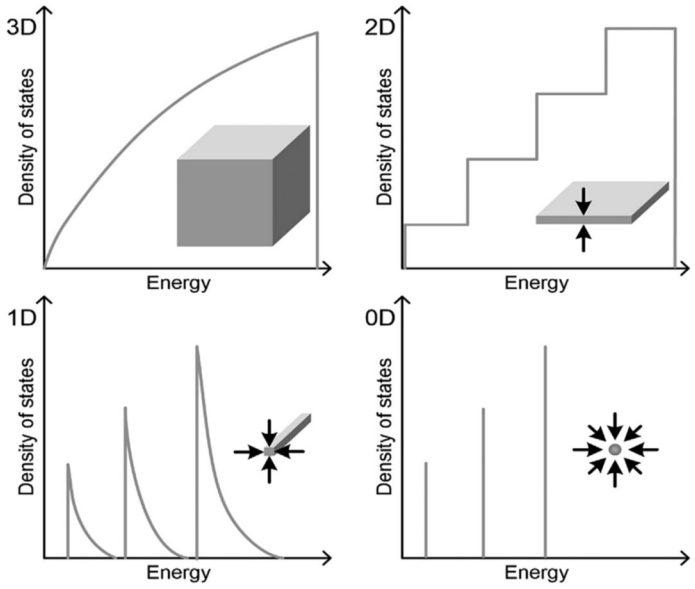

Fig. 4. Electronic density of states for 3D, 2D, 1D nanostructures, and 0D quantum dots. The arrows represent the spatial confinement occurring in each system (Reprinted with permission.[22] Copyright 2018 Elsevier).

2.1. Zero-dimensional nanostructures

Zero-dimensional (0D) nanostructures, *e.g.* quantum dots, spheres, ellipsoids, polyhedra, have all dimensions measured within nanoscale, varying from a few to several dozen nanometers (Fig. 5). They can be amorphous (randomly distributed atoms and molecules) or crystalline (atoms and molecules organized in a defined lattice pattern) and consist of single or more chemical elements.[18, 22-29]

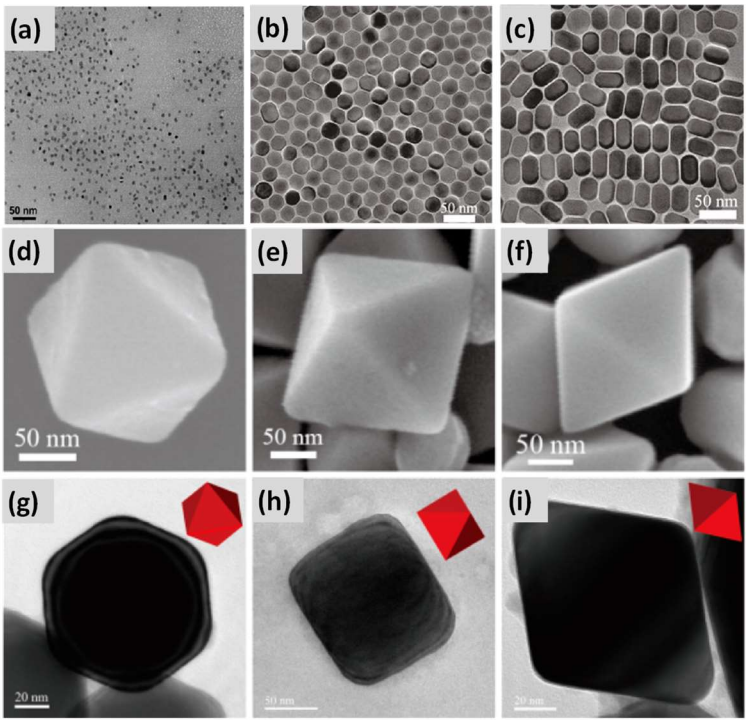

Fig. 5. TEM (a-c, g-i) and SEM (d-f) images of 0D nanostructures: **a)** quantum dots (CdSe/ZnS) (Reprinted with permission.[24] Copyright 2013, Inderscience), **b)** spherical nanoparticles (Mn_3O_4), **c)**

elongated nanocrystals (Mn_3O_4), (Reprinted with permission.[25] Copyright 2010, American Chemical Society), **d, g)** Cu octahedron viewed from [111] axis, **e, h)** Cu octahedron viewed from [112] axis and **f, i)** Cu octahedron viewed from [110] axis (Reprinted with permission.[27] Copyright 2015, American Chemical Society).

Quantum dots with diameters in the range of 2-10 nanometers are shapeless, irregular polyhedra indicating unique electronic properties, which partly result of their high surface-to-volume ratio. In this case, facets are not well-developed. The presence of under-coordinated atoms and high surface energy of quantum dots make them more liable to interactions with the surroundings.[22-24]
Zero-dimensional spheres are formed by reducing the surface energy of various nanomaterials. They exhibit high surface area-to-volume ratio, mechanical strength and good dispersion due to the stabilization of electrostatic charges. Spheres can be created to have well-developed porosity. It is worth noting that spherical morphology is the most stable that occurs in nature. Spheres elongated in one dimension are called ellipsoids. These nanostructures can be unstable because under extreme conditions sharp ends tend to shrink whereas surfaces with smaller curvature grow leading to minimizing surface energy so that they approach spherical geometry.[18, 22, 23, 25] Nanomaterials with specific cubic crystal symmetry, enclosed by (100) facets, typically occur in the form of cubes. The high surface energy of cubes related to the presence of under-coordinated atoms is usually lowered by rounding their edges and vertices. Cubes are often employed as building blocks to generate one-dimensional superstructures having well-defined interparticle orientations and regulated electromagnetic properties.[16, 17] Octahedra together with cubes are the most thoroughly studied nanostructures having interesting physicochemical features. They are composed of eight (111) facets. In 2D microscopic projection, octahedra can be visible as rectangles, rhombuses, hexagons depending on their orientation. In addition, octahedra are considered classic models for testing the surface properties of (111) facets. However, their precise synthesis is quite difficult.[17, 27, 30]

2.2. One-dimensional nanostructures

One-dimensional (1D) nanostructures including rods, wires, tubes, belts, hooks, ribbons, needles, fibers, helices (or spirals) and zigzags, are characterized by the high ratio of one dimension over two other, which are equivalent, and in the nanoscale (length >> width or diameter).[12, 16, 17, 26] Many of them are presented in the literature as acicular-like structures whose length can even reach millimeter range (Fig. 6).[17]

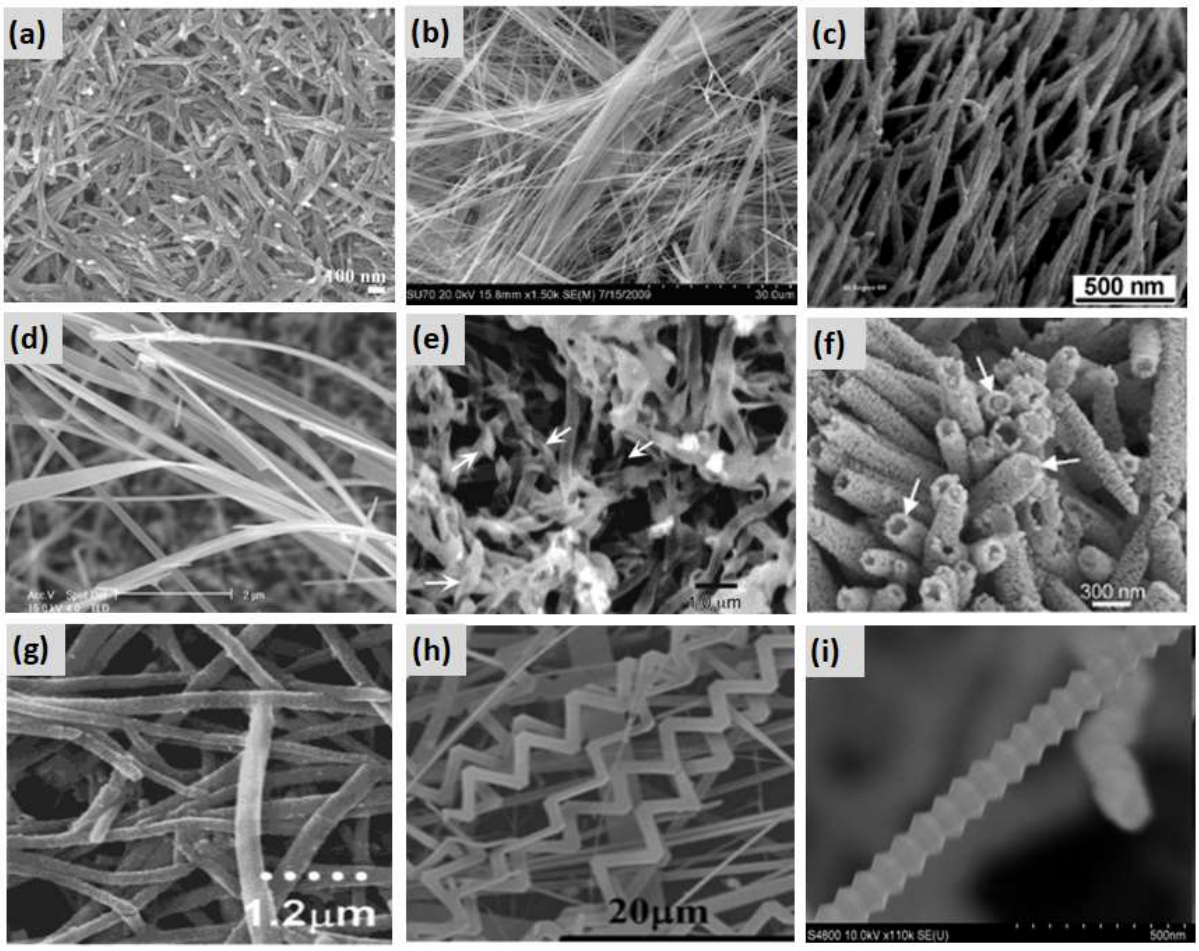

Fig. 6. SEM images of 1D structures: **a)** rods (γ-MnO_2) (Reprinted with permission.[31] Copyright 2012, Elsevier), **b)** wires (δ-$K_xV_2O_5$) (Reprinted with permission.[32] Copyright 2010, American Chemical Society), **c)** large arrays of oriented nanotubes (TiO_2) (Reprinted with permission.[33] Copyright 2003, American Chemical Society), **d)** belts (ZnO) (Reprinted with permission.[34] Copyright 2009, Inderscience Enterprises Ltd), **e)** helical ribbons and the double-layered nanotubes (TiO_2) (Reprinted with permission.[35] Copyright 2002, American Chemical Society), **f)** needles (β-$Co(OH)_2$) (Reprinted with permission.[36] Copyright 2008, John Wiley & Sons), **g)** hollow fibers (TiO_2) (Reprinted with permission.[37] Copyright 2000, American Chemical Society), **h)** zigzag belts (SnO_2) (Reprinted with permission.[38] Copyright 2016, Elsevier), **i)** zigzag (GaN) (Reprinted with permission.[39] Copyright 2016, Elsevier).

Rods exhibiting aspect ratios of 3-5 may occur as aggregates composed of separate building blocks like dots, polyhedra or platelets.[23, 31] Wires have aspect ratios even more than 1000 and they are described by greater flexibility and slenderness compared to rods.[17, 32] The structure of wires is so simple that there is no space for any defects, thus electrons pass through unimpeded. In contrast to rods and wires, tubes have more complex hollow structures and can be single- or multi-walled. Their properties differ depending on how they are rolled up. Belts are extremely thin and flat structures of ribbon shape with the rectangular cross-section. Moreover, they possess high specific surface areas therefore are often used in catalysis and photocatalysis.[16, 17, 26, 40, 41]

Progress in developing new synthesis methods of 1D nanostructures with precisely controlled dimensions, phase purity, morphology, and chemical composition has contributed to their wide application as functional units in the design of solar cells, electronic nanodevices, supercapacitors,

gas sensors or transistors. Xia *et al.*[34] have compiled bottom-up synthetic strategies for fabrication of 1D nanostructures which involve: *(i)* utilization of the intrinsically anisotropic crystallographic structure of a solid to achieve 1D growth, *(ii)* reduction of the seed symmetry by introducing a liquid-solid interface, *(iii)* modification of seed growth by control of supersaturation, *(iv)* capping reagent assisted procedure in order to kinetic control the growth rates of different facets of seeds, *(v)* application of appropriate templates exhibited 1D morphologies to manage the 1D nanostructures creation, *(vi)* 0D nanostructures self-assembly and *(vii)* reducing the size of 1D microstructures. It should be noted that a wide variety of materials can naturally grow into 1D nanostructures which is influenced by highly anisotropic bonding in crystallographic structures. They exhibit distinct optical, thermal, chemical and electronic properties. In addition, 1D nanostructures are interesting systems for studying new phenomena at the nanoscale and dependence of specific physicochemical properties on the shape and dimensions.[34]

2.3. Two-dimensional nanostructures

Two-dimensional (2D) nanomaterials, possessing thickness in the range from a few to tens of nanometers and lateral dimension reaching up to many centimeters, have been a subject of intensive research in the last years.[12, 16, 17, 26, 42] They are described in the literature as single- or multilayered nanostructures with strong bonds in plane and weak van der Waals forces between layers which are often deposited on the surface of various substrates (*e.g.* silicon, nickel sheets, copper foil). 2D nanostructures typically include platelets, sheets, flakes, rings, membranes, walls, prisms, disks, films characterized by unique geometry, well-developed surface area and high surface-to-volume ratio (Fig. 7).[12, 16, 17, 26, 42, 43] In addition, the advantages of 2D nanostructures are also the presence of many active sites, straightforward surface functionalization and possibility to assembly into 3D complex structures. Up to now, 2D nanostructures of graphene, metal oxides, polymers, metal hydroxides, metal dichalcogenides, boron nitride, phosphorene, MXenes and metal organic frameworks have been synthesized with the use of strategies based on extraction, exfoliation, chemical or physical vapor deposition and various wet chemical methods.[36]

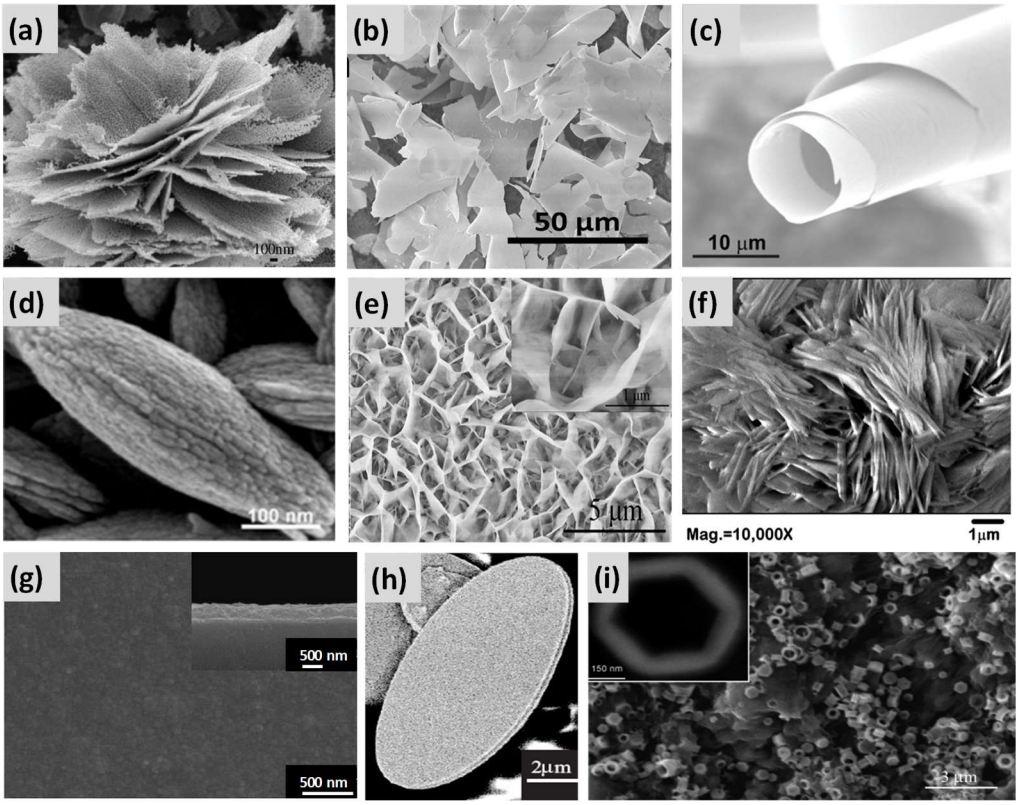

Fig. 7. SEM images of 2D structures: **a)** plates (porous ZnO) (Reprinted with permission.[44] Copyright 2008, John Wiley & Sons), **b)** membranes (Fe_2O_3) (Licensed under CC-BY.[45]), **c)** membranes ($Pd/MnO_x/Pd$) (Licensed under CC-BY.[46]), **d)** mesocrystal disks (Mn_3O_4) (Reprinted with permission.[47] Copyright 2014, John Wiley & Sons), **e)** wall arrays ($Ni(OH)_2$) (Reprinted with permission.[48] Copyright 2015, The Royal Chemical Society), **f)** flakes (ZnO) (Reprinted with permission.[49] Copyright 2013, Elsevier), **g)** dense film (NiO) (Reprinted with permission.[50] Copyright 2010, Elsevier), **h)** diskettes (SnO) (Reprinted with permission.[51] Copyright 2003, John Wiley & Sons), **i)** rings (ZnO) (Reprinted with permission.[52] Copyright 2006, American Chemical Society).

In 2D microscopic images, platelets can appear in the form of flat triangles, rectangles, rhombuses or hexagons which is largely dependent on the crystal lattice and growth direction of materials.[44] Those that have circular or irregular shapes are called disks and discoids.[23, 47] Films and sheets are 2D nanostructures with very high but not well-defined aspect ratios exhibiting superior mechanical properties which include hardness and strength.[42, 43, 50] It is worth noting that during formation of films, their interaction with properly selected substrate determines the initial nucleation and growth. Three basic modes of initial nucleation involve: *(i)* island or Volmer-Weber growth, *(ii)* layer or Frank-van der Merwe growth, and *(iii)* island-layer or Stranski-Krastonov growth. Island growth takes place when the growth species are more strongly bonded to each other than to the substrate as opposed to layer growth mode. In the latter one at first monolayer is completely formed before the deposition of second layer. Island-layer growth is a combination of layer growth and island growth modes.[43] Rings that are one of the least-studied 2D nanostructures can be fabricated by the rupture of platelets in order to generate a hole in the center.[17, 52]

Easy and precise control of 2D nanostructures composition enables exploration and optimization of their functional properties which contributes to the extension of applications in the design of novel sensors, electronic devices, photocatalysts, and reactors.

2.4. Three-dimensional nanostructures

Three-dimensional (3D) nanostructures are described as complex structures assembled from 0D, 1D, 2D or multiscale nanocomponents which have three random dimensions larger than 100 nm. Their examples are multipods, balls (dendritic structures), cones, pillers, and hierarchical structures such as flowers, trees, branches, urchins (Fig. 8).[12, 16, 17, 26, 36, 53, 54] Moreover, both spheres and polyhedra (*e.g.* tetrahedra, cubes, octahedra, prisms) can also be classified into 3D nanostructures if they are polycrystalline and obtained *via* the aggregation of fundamental building blocks including dots, rods or platelets. Compared with 0D spheres and polyhedra, they are characterized by larger sizes and porosity. Their surfaces can be smooth, rough or occupied by various types of adsorbates. 3D spheres and polyhedra often occur in the form of hollow or multilayered structures.[23]

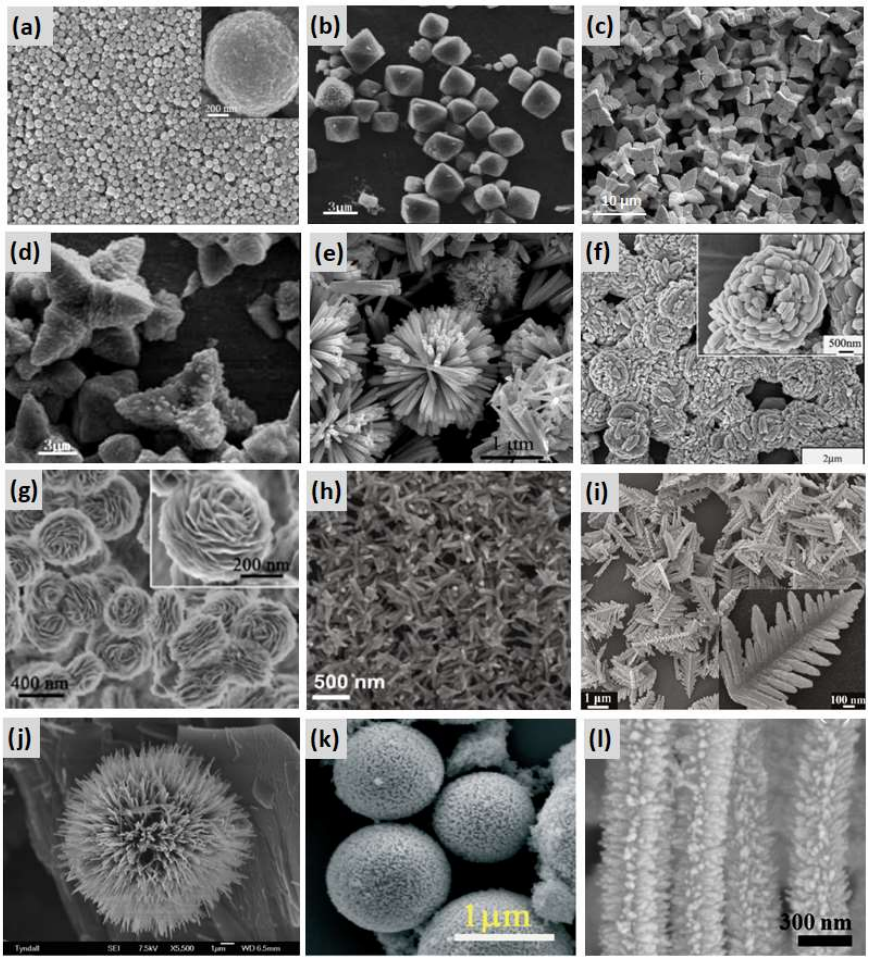

Fig. 8. SEM images of 3D structures: **a)** colloidal spheres (Mn_3O_4) (Reprinted with permission.[25] Copyright 2010, American Chemical Society), **b)** octahedra (Cu_2O), **c)** eightpod cubes (Cu_2O), **d)** six-armed starlike Cu_2O (Reprinted with permission.[55] Copyright 2009, American Chemical Society), **e)** ZnO microsphere consisting of nanorods (Reprinted with permission.[56] Copyright 2009, American Chemical Society), **f)** doughnut-shaped microparticles (ZnO) (Reprinted with permission.[57] Copyright 2005, American Chemical Society), **g)** flowers (β-$Ni(OH)_2$) (Reprinted with permission.[58] Copyright 2014, The Royal Chemical Society), **h)** multipods (Ni) (Reprinted with permission.[54] Copyright 2018, American Chemical Society), **i)** dendritic structures (γ-Fe_2O_3) (Reprinted with permission.[59] Copyright 2011, American Chemical Society), **j)** urchin (VO_x) (Reprinted with permission.[60] Copyright 2006, American Chemical Society), **k)** balls (Mn_2O_3) (Reprinted with permission.[61] Copyright 2016, The Royal Chemical Society), **l)** branches (TiO_2-SnO_2) (Reprinted with permission.[62] Copyright 2013, The Royal Chemical Society).

Multipods, exhibiting high aspect ratio, are composed of large sphere-like cores with long arms of uniform width and rounded ends which extend out from the cores. Most often the number of arms is in the range from 4 to 8. Their length is measured from the tip to the base, whereas the width is determined in the center area of the multipods arms.[23, 54]

Cones have height and diameter of the same order of magnitude. It should be noted that they are mainly made of carbon and take place *e.g.* on the surface of natural graphite.[63] In turn, balls are well-ordered spherical nanostructures possessing dendritic exteriors. They can be formed by the aggregation of small particles, which causes their surface to be rough.[61]

Hierarchical nanostructures are defined as integrated architectures consist of low-dimensional sub-units *e.g.* 0D dots, spheres, 1D wires, rods or tubes, 2D sheets which are arranged in a well-ordered manner. They mimick structures widely found in nature such as trees with trunks and branches, plant flowers composed of petals, and sea urchins whose surface is spiny.[64, 65] Synthesis of materials with hierarchical nanostructures gives the opportunity to precisely adjust their physicochemical properties for specific applications. Flower-like structures having size in the range 100-500 nm consist of several layers of inteconnected petals with relatively small thickness and different shapes.[18, 23, 58, 66] All petals are dense at the cores and radiate from the center of flowers to the outside surface. Their shape and dimensions are very difficult to control during synthesis. Flowers are characterized by high surface-to-volume ratio and demonstrates large number of adsorption sites as well as good charge transfer. This type of architecture can increase the use of nanomaterials in the design of novel catalysts, solar cells, biosensors (detection of conditions such as food infection, diabetes, Parkinson, Alzheimer, etc.), devices, fuel cells and drug delivery agents.[18, 23, 66]

Among the 3D nanostructures, branches have been widely studied due to their straightforward modification and applicability to various types of chemical compounds. They are composed of small arms growing radially from the major frame. Both the morphology and length of branches influence the physicochemical properties of nanomaterials. Many synthetic strategies have been described in the literature for branch-like structures *e.g*. the formation of branches on nanowires backbone by a hydrothermal method or chemical vapor deposition (CVD), and preparation of hyper-branched structures *via* thermal evaporation. Branches that are less densely packed grow depending on pre-deposited seeds. Together with trees, they are examples of fractal structures.[62, 67] Urchin-like structures are covered with radially oriented and interconnected needles of high density. They are a bit similar to multipods, but urchins have a much larger number of arms attached to the spherical cores.[60, 68]

Despite the huge efforts to control the growth mechanism of three-dimensional nanostructures, some fundamental phenomena are not well understood. Therefore exploration of the impact of size and morphology on their physicochemical properties is still required in order to plan the optimal application of these nanomaterials.[12, 16, 17, 26]

3. Morphology control of metal oxides nanostructures

3.1. General aspects

MOs are an important class of inorganic materials with diverse composition and morphology. They are widely used in the design of catalysts,[69-75] sensors,[76-79] solar cells,[80-84] adsorbents of many contaminants,[85-88] drug delivery agents,[89-92] and additives for skincare products[93-96]. Significant efforts over the last years have been focused on the synthesis of MO nanostructures with controlled morphology that exhibit new interesting optical, magnetic, thermal, catalytic properties and thus can

enable novel applications. Unique physicochemical properties of MO nanoparticles originate from their small size, high density of the corner or edge surface sites in conjunction with shape effect.[74, 75, 97] Moreover, the exposed facets of the MO nanocrystals and the high specific surface area can strongly determine their surface chemistry.[97-100]

From the scientific point of view, in order to fully exploit the potential of MO nanomaterials, it is necessary to understand the relation between their shape, size and the resulting properties. Accordingly, the synthesis of uniform oxide nanoparticles with precise control of morphology is crucial to characterize their specific properties. In addition, shape-controlled MO nanocrystals can be fundamental building blocks for the bottom-up assembly of novel nano- and microstructures.[97, 101-103] It should be noted that reducing the particle size of MOs to the nanometric scale causes their properties to be governed by high surface area-to-volume ratio and quantum confinement effects. As such, the atoms at the surface of MO nanoparticles dominate over the internal atoms. Changes in thermodynamic stability associated with decreasing size to nanometer regime can bring about a modification of cell parameters or structural transformations. In some cases, the oxide nanoparticles can be degraded due to interactions with their surrounding environment, high surface free energy, and the large surface curvature.[104] Therefore, to exhibit mechanical or structural stability, the surface free energy of nanoparticles must be lowered. As a result, phases having low stability in bulk materials can become very stable in nanostructures. Additionally, it has been revealed that the electronic structure of oxide nanomaterials could be altered from the continuous electronic bands to the discrete or quantized electronic levels. The size of the nanocrystals has also a significant influence on the electron-transport process.[103-105] Similarly, the shape of the MO nanoparticles plays a key role in the determination of their properties. It depends on the crystalline structure of MO nanomaterials because the growth of primary particles is imposed by the symmetry and dimensionality of the structure. The orientation of the crystal facets can be adjusted with the surface atomic arrangement and coordination.[99] With reducing the particle size, the surface area-to-volume ratio rises and the shape could impart its own effect on the surface structure.[97] Many nanostructures of MOs including spheres, cubes, octahedra, polyhedra, wires, rods, tubes, belts, sheets, platelets and complicated hierarchical structures (*e.g.* flowers, branches) have been reported in the literature. As mentioned in section 2, they are classified as zero-dimensional (0D), one-dimensional (1D), two-dimensional (2D) and three-dimensional (3D).

Controlled synthesis of MO nanostructures is the main strategy for achieving desired shape and size. So far, many valuable reviews[22, 23, 97, 100, 102, 103, 105-107] have described the preparation methods of oxide nanomaterials with tunable morphology, but the topic has not been completely explored. Due to the extensive scope of the synthetic approaches, as well as the diversity of MO nanostructures and composition, a huge challenge is to create a general algorithm that would facilitate the selection of the appropriate method of synthesis and its conditions in order to obtain a specific shape and size of nanoparticles. It is necessary to compile literature data that will allow for a deep analysis of what parameters in the chosen preparation method have the greatest impact on the morphology of MO nanomaterials.

3.2. Synthetic strategies for metal oxide nanostructures with controlled morphology

MO nanomaterials can be fabricated with the use of two general strategies: bottom-up and top-down (Fig. 9).[101, 102, 106] These synthetic strategies differ in the way how a specific nanostructure is created. In the bottom-up approach, MO nanomaterials are obtained from basic building blocks (*e.g.* atoms or molecules) that react and grow in size or self-assemble into a more complex structure. In

contrast, the top-down approach involves breaking down bulk materials (*e.g.* cutting, grinding or etching) to the nanoscale structures.[33] The advantage of the top-down approach is high yield, but it requires expensive, complex and specialized equipment to maintain specific conditions including pressure, temperature or environment. Moreover, it should be noted that the obtained nanostructures often have surface defects and non-uniform shapes which limit their applicability. The control over the size and shape of MO nanoparticles through the top-down strategy is very difficult.[102, 103, 106] Therefore, the bottom-up wet chemical methods are often selected for preparation of MO nanostructures due to their simplicity, reproducibility, low energy consumption, easily available and cheap equipment as well as the theoretical possibility to precise control of all dimensions, morphology, and monodispersity of the products.[22, 23, 102, 106, 107] In the wet chemical syntheses, the nucleation and growth kinetics of the seeds strongly influence the shape of the MO nanostructures. In order to control the size and morphology of the nanocrystals some critical reaction parameters such as temperature, time, precursor and surfactant concentration, the molar ratio of precursor to capping ligand should be precisely adjusted in the crystal nucleation-growth stages.

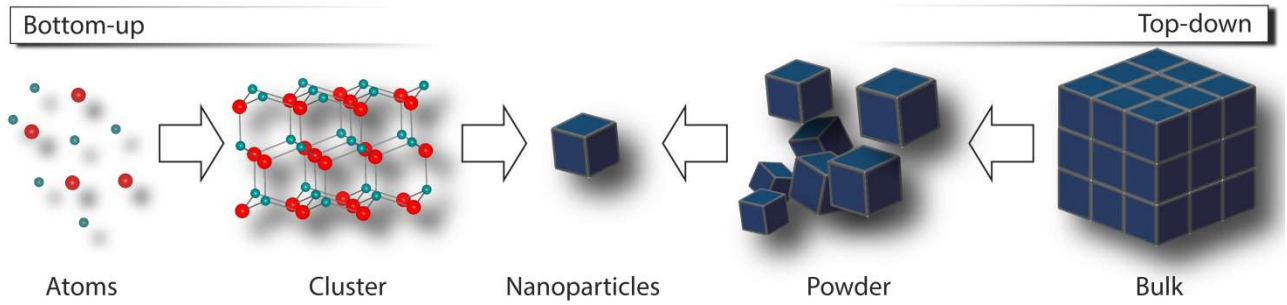

Fig. 9. Bottom-up and top-down synthetic strategies.

Understanding the formation mechanisms of nanoparticles is the key to manipulate the morphology. The creation of nanoparticles can be described by classical Ostwald ripening mechanism, in which the growth of larger particles at the expense of smaller ones is driven by surface energy reduction. This phenomenon is primarily applied to explain the fabrication of thermodynamically stable nanocrystals with nearly spherical shapes.[97, 100] In the case of the controlled self-assembly of nanoparticle building blocks into more complex anisotropic nanostructures, organic capping reagents usually play a crucial role in reducing the activity of the nanocrystal surface. The organic ligand with high nanoparticle binding affinity can promote or adjust an oriented-assembly, driven by the interaction between surface-adsorbed ligands instead of between the particles themselves. The selective adsorption of the capping molecules (*e.g.* fatty acids, alkyl amines, amino acids, trioctylphosphine oxide, block copolymers) onto specific crystal facets of the growing nanoparticles can result in controlling the product morphology.[22, 23, 97, 100, 102, 106, 107]

In recent years, many studies have been dedicated to developing various synthetic approaches that allow the simultaneous control of the size, shape, and monodispersity of MO nanostructures with high potential application in biomedicine, catalysis, optical sensing, and energy conversion technology. In this section, we focused on the presentation of the most important methods of MO synthesis (*e.g.* sol-gel, hydro/solvothermal, biogenic, thermolysis, reverse micelle, electrodeposition, two-phase route, flame spray pyrolysis). Their different aspects such as advantages, limitations and product morphology are presented in Table 1.

Table 1. Synthetic strategies for MO nanostructures with controlled morphology.

Method	Advantages	Limitations	Product morphology	Examples of MOs	Ref.
Sol-gel	• Cost-effective • Reproducible • Simple experimental set-up • Low-temperature operation (<100 °C) • Highly controllable synthesis parameters (concentration of precursor, nature of solvent, pH of the solution, pre and post heat treatment of the materials, aging of the solution, nature of polymer used for condensation) which have significant influence on the morphology and properties of the final product • The possibility of obtaining homogeneous, high quality MO nanostructures • Precise control of phase, shape and size of the MO nanoparticles • Large-scale production	• Time consuming fabrication technique • Little control over porosity of the gel • Formation of significant amounts of chemical waste • Production of partly contaminated nanoparticles • Particle size distribution of MOs can be broad • Low chemical stability of the product	**(0D)** dot **(1D)** tube, tube-array, rod-array, wire-array **(2D)** film, platelet-circle **(3D)** helical ribbon, sphere-hollow, sphere-wall, branch-fractal, flower-wall, flower-urchin, cube-hollow, multipod	TiO_2, V_2O_5, Mn_3O_4, MnO, Co_3O_4, Fe_3O_4, NiO, Cu_2O, ZnO	[107-133]
Hydro/Solvothermal	• Straightforward synthesis procedure • High solubility of the metallic ion precursors in the solvent-contained reactor facilitates the synthesis of highly crystalline oxide nanoparticles • Variety of sizes and shapes of MO nanoparticles can be constructed by adjusting reaction parameters (temperature, pressure, time, specific solvent properties) • The reaction parameters can be tuned to attain satisfactory nucleation and growth rates and particles size distribution. • The possibility of obtaining monodisperse oxide nanoparticles that are highly selective and reproducible in terms of purity, crystallinity and morphologies	• Large scale synthesis is intricate due to relatively high temperature, high pressure and prolonged reaction time • Impossibility of monitoring the reaction process (because is performed in autoclaves) • The high growth rate of the oxide monomers in polarity solvents often results in the formation of large sized oxide particle aggregates with irregular shapes • For controlling the shape and monodispersity of the oxide particles, the addition of the capping molecules to the reaction mixture at high temperature and pressure is achieved • The mechanisms controlling the reactions are not well understood	**(0D)** dot, polyhedron, ellipsoid **(1D)** tube, tube-array, rod, rod-array, rod-assembly, belt, wire, wire-array, wire-porous **(2D)** film-rough, film-wall, film - small patches, platelet-rectangle, platelet-hexagon, platelet-circle, ring **(3D)** flower-multipod, flower-urchin, flower-wall, flower-cluster, sphere-hollow, sphere-porous, sphere-wall-multilayer, branch	TiO_2, V_2O_5, CeO_2, Mn_3O_4, MnO, Co_3O_4, Fe_3O_4, NiO, Cu_2O, ZnO	[97, 102, 106-109, 133-149]
Thermal decomposition (Thermolysis)	• Straightforward synthesis procedure • Short reaction time • Precise control of the oxides particle shape and size by adjustment reaction temperature and time, ratios of the starting reagents, including organometallic compound, surfactant, and solvent	• Excessive use of solvent • Large quantity of initial reagents • Limited yield per batch • Slight change in reaction condition affects size and shape of nanoparticles	**(0D)** dot, octahedron-mono, cube-mono, sphere-mono, sphere-mono-assembly **(1D)** rod, rod-assembly, wire **(2D)** platelet-triangle, platelet-hexagon	TiO_2, MnO, Mn_3O_4, Co_3O_4, CoO, NiO, Cu_2O, ZnO, V_2O_5	[97, 102, 106-149, 150-161]

	• The possibility of performing the production scale-up while maintaining the uniform size and shape of the monodisperse oxide nanoparticles • Separation of the nucleation and growth stages • Nucleation is fast and growth depends on the availability of monomer units		**(3D)** sphere, flower-multipod, cube-hollow-urchin, sphere-hollow-urchin, ranch, multipod-tetrapod		
Reverse micelle (Microemulsions)	• Separation of the nucleation and growth stages • Minimal aggregation of nanoparticles • The possibility of obtaining oxides with narrow particles size distribution • High yield of finer particles synthesis in multi-microemulsion approach in comparison to the single microemulsion approach • Precise control of shape, size, uniformity and dispersity of the metal oxides nanoparticles • Size and dispersity can be tailored by changing type of solvent, the surfactant or co-surfactant, addition of electrolyte, molar ratio water/surfactant, concentration of reagents, • Particle shapes are affected by micellar template, added anions and molecular adsorption	• Synthesis of small quantities of products while consuming relatively large volumes of the reaction solvents • Surfactants are difficult to remove	**(0D)** sphere, cube **(1D)** rod, fibers, belt, needle-like **(2D)** sheet **(3D)** floral petal, florets of cauliflower	CeO_2, TiO_2, V_2O_5, SnO_2, Sb_2O_3, Sb_2O_5, ZnO, Fe_3O_4	[97, 102, 162-172]
Two-phase route	• Straightforward synthesis procedure • Synthesis of metal oxides with good crystallinity and narrow particle size distribution under mild condition • Slow rate of the nucleation and growth stages which occur at the interfaces • Easy control of size and shape of oxide nanoparticles • The shapes of nanocrystals can be tuned by changing the metal precursor concentration, the nature of the capping agents, the reaction temperature and time • Highly recyclable reaction solutions • The possibility of scale-up production	• The low reactive precursors often decrease the reaction rate • The nucleation and growth are typically much weaker compared with the one-phase system	**(0D)** dot, cube, elongated cube, sphere, peanut, teardrop **(1D)** rod	TiO_2, ZrO_2, CeO_2, Mn_3O_4, Sm_2O_3, La_2O_3, Gd_2O_3, NiO, Co_3O_4	[97, 102, 173-178]
Co-precipitation	• Straightforward synthesis procedure • Cost-effective • Simple and rapid preparation • Low-temperature operation • Energy efficient • Does not involve use of organic solvent	• Not applicable to uncharged species • Trace impurities may also get precipitated with the product • Batch-to-batch reproducibility problems • Does not work well if the reactants have very different precipitation rates	**(0D)** sphere **(1D)** rod, needle-like, spindle **(2D)** plate **(3D)** pyramida	MnO_2, Fe_3O_4, SnO_2, ZnO, MgO	[117-125]

	• Easy control of particle size and composition • Various possibilities to modify the particle surface state and overall homogeneity • Suitable for large-scale synthesis • The possibility of obtaining oxides nanoparticles with relatively narrow size distribution	• Ostwald ripening and aggregation, dramatically affect the size, morphology, and properties of the products • Difficult to precisely control the morphology of metal oxides due to the high reaction rate			
Flame spray pyrolysis	• Cost-effective • High production rate • Scalable and high throughput process • Only subsintering temperatures are necessary to form crystallized particles • Production of oxide nanoparticles with a high specific surface area and purity • The morphology of particles can be strictly controlled by adjustment of the precursor concentration, the residence time and temperature	• The poor mechanical stability of nanostructured products • Formation of large aggregates • Particle size distribution of metal oxides can be broad	**(0D)** sphere **(1D)** rod	Al_2O_3, Fe_2O_3, V_2O_5, SnO_2, ZrO_2, Mn_2O_3, WO_3	[188-192]
Electrodeposition	• Cost-effective • Relatively fast • Environmentally friendly • Low-temperature operation limited by boiling point of the electrolyte • Cheap and easily available equipment • The possibility of kinetic and thermodynamic control by adjusting the current passed through the cell and changing the cell potential, respectively • Flexibility in the control of the structure and morphology of metal oxides • Formation of the nanostructures occurs directly in the final substrate, which prevents further agglomeration steps of the nanoparticles • Production of high purity materials	• Unsuitable for large-scale production • Fabrication of poorly ordered products making unequivocal structural characterization difficult • Synthesis can only be carried out on conducting substrates	**(0D)** sphere **(1D)** tube, tube-array, rod, rod-array, needle-like **(2D)** film, platelet **(3D)** floral petal, flower	ZnO, TiO_2, WO_3, V_2O_5, Fe_3O_4, MnO_2, Cu_2O	[108, 109, 193-203]
Biogenic	• Cost-effective • Environmentally friendly • Reduction or elimination of toxic reaction precursors • High production yield • Simple and cheap equipment • High control over the morphology, composition and surface area of the oxide nanoparticles	• The exact mechanism for synthesis of metal oxides nanoparticles need to be elucidated • Low reproducibility • Limitations to scale-up of the production processes	**(0D)** sphere, cuboid **(1D)** spring, ring, helix, comb, wire, rod, needle-like **(2D)** sheet, platelet-rectangle, platelet-triangle **(3D)** flower, urchin, pyramida, cone, bundle	ZnO, Fe_3O_4, UO_2, MnO, TiO_2, CuO, CeO_2, NiO	[109, 204-219]

	• The particle size can be modulated by tuning synthesis parameters (the medium pH, temperature, concentration, incubation time, reaction time), in turn, their morphology by changing the organism (bacteria, fungi, yeast) or plants extracts used as stabilizing or reducing agents	

3.2.1. Sol-gel method

The synthesis of MO nanostructures by the sol-gel method is based upon inorganic polymerization reaction occurring through the solvolysis/condensation mechanism.[23] The main step of this route comprises hydrolysis or alcoholysis of precursors (metal alkoxides, halides) to generate a colloidal solution of metal hydroxide (sol), followed by condensation leading to obtaining metal-oxygen-metal interlocked network (gel). Then the solvent is slowly removed at elevated temperature (60-100 °C). The final product with the desired crystal phase is achieved after thermal treatment causing decomposition of the residual gel.[22, 23, 107-109] It has to be taken into account that the synthesis parameters including concentration of precursor, nature of solvent, pH, pre and post heat treatment strongly determine the morphology, and properties of the MO nanostructures. The sol-gel method allows to control the crystal phase, shape, and size of the materials obtained. Up to now, this synthetic route has been developed to fabricate a wide range of MOs *e.g.* Cu_2O,[110-114] Mn_3O_4,[31, 47, 115] NiO,[116, 117] V_2O_5,[118] Fe_3O_4,[119] Co_3O_4,[120] TiO_2,[35, 37, 121-126] characterized by diverse morphology.

Kuo *et al*.[111] described a simple and rapid seed-mediated strategy for the synthesis of monodispersed Cu_2O nanocubes with sizes varying from 40 to 420 nm. The nanocubes were obtained within 2 h at room temperature. It was found that the combination of $CuSO_4$ precursor and sodium dodecyl sulfate played a key role in the formation of structurally well-defined Cu_2O nanocubes. Pang and Zeng[106] synthesized Cu_2O spheres with uniform diameters in the range of 130-135 nm by facile sol-gel method at room temperature in the presence of hydrazine hydrate as a capping agent. The monodispersity of the spheres permitted the formation of 2D and 3D superlattices. Moreover, cuprous oxide was used as a starting solid precursor in the preparation of hollow spheres of copper sulfide (CuS) and copper selenide (CuSe). Yang and coworkers[107] reported shape-controlled synthesis of well-defined truncated edge polyhedral Cu_2O architectures, including truncated edge cubic and truncated edge octahedral Cu_2O crystals. The concentrations of OH^- and CH_3COO^- ions, the reaction temperature and time were tuned to control the final morphology of the products. Various shapes of materials were achieved *via* selective oxidative etching and preferential growth on different facets of Cu_2O crystals. Huang *et al*.[114] prepared a series of Cu_2O nanocrystals with systematic morphology evolution from cubic to rhombic dodecahedral structures and sizes ranging from 140 to 300 nm at room temperature by mixing an aqueous solution of $CuCl_2$, sodium dodecyl sulfate surfactant, NaOH, and $NH_2OH{\cdot}HCl$ reductant. With increasing the amount of reductant added to the reaction system, the shapes of cuprous oxide changed from cubic to face-raised cubic, edge- and corner-truncated octahedral, all-corner-truncated rhombic dodecahedral, 100-truncated rhombic dodecahedral, and rhombic dodecahedral (Fig. 10).

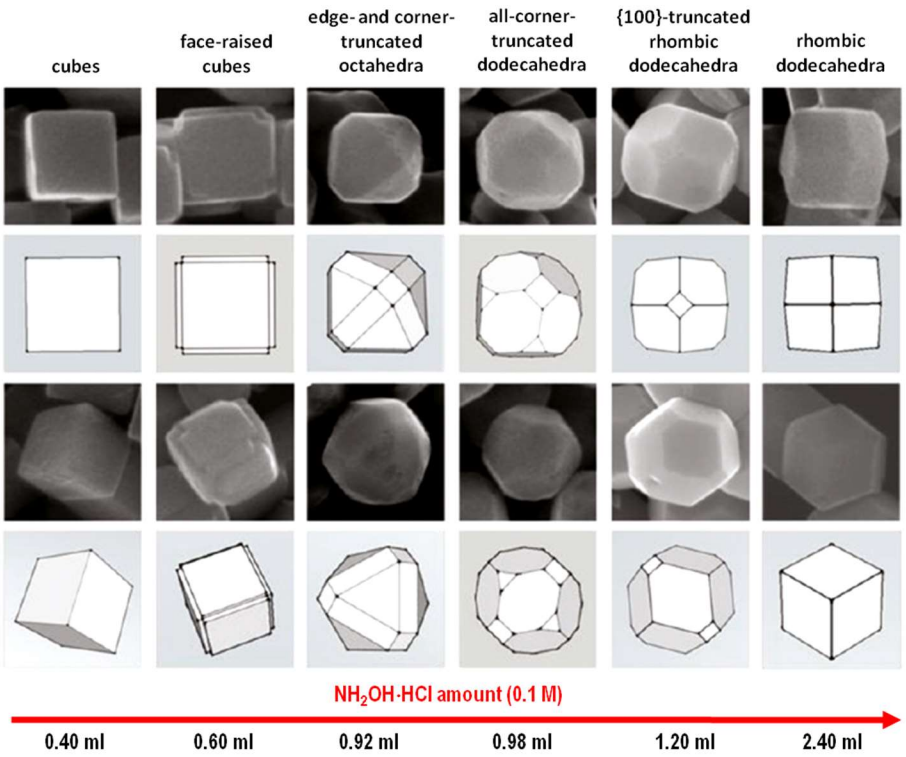

Fig. 10. SEM images and the corresponding schematic drawings of the Cu_2O nanocrystals synthesized with morphology evolution from cubes to rhombic dodecahedra upon increasing the amount of $NH_2OH{\cdot}HCl$ added to the reaction mixture. Two orientations are shown for each particle shape (Reprinted with permission.[114] Copyright 2012, American Chemical Society).

Chen *et al.*[47] demonstrated a versatile synthetic procedure for the fabrication of Mn_3O_4 nanocrystals of different morphology (square nanoplates, mesocrystal nanodisks, nanopolyhedra) at room temperature with the use of manganese(II) acetate tetrahydrate and hydrazine monohydrate. The shape and size of the materials were controlled by adjusting the concentration or ratio of reactants. Synthesis of Mn_3O_4 nanoparticles at room temperature was also realized by mixing the aqueous solution of $MnSO_4$ and Na_2CO_3.[31] Transmission electron microscopy (TEM) images showed a Mn_3O_4 sample consisting of almost spherical agglomerate particles with diameters in the range 50-100 nm. Hydrothermal treatment of Mn_3O_4 nanoparticles in acidic solution at 120 °C for 6 h led to formation of γ-MnO_2 nanorods with uniform diameters of 5-10 nm and lengths of 100-400 nm. Qiao *et al.*[115] designed multi-step preparation of porous double-shelled hollow, solid and yolk-structured Mn_2O_3 spheres at 80 °C for 1 h. The synthetic protocol involved precipitation, controlled oxidation, selective etching and calcination.

Jang and coworkers[110] synthesized various types of NiO nanostructures with flower-, slice-, and spherical shapes *via* sol-gel method. $Ni(CH_3COO)_2{\cdot}H_2O$ and $Ni(NO_3)_2{\cdot}6H_2O$ were used as precursors and ammonium hydroxide, lithium hydroxide, hexamethylene tetramine acted as reagents controlling the reaction conditions. The pore size distributions of NiO changed depending on the morphology of the structure and packing. Nanoslices and nanoparticles had an average pore diameter of 4 and 8 nm, respectively. Bimodal pore size distribution with maxima peaks centered at ~4 and 15 nm was obtained for the nanoflower-shaped NiO.

Karami and Mohammadi[112] presented a very interesting poly(vinyl alcohol) (PVA) based sol-gel method for the fabrication of uniform V_2O_5 nanostructures. In this procedure, the NH_4VO_3 precursor

and PVA were dissolved in an ethanol: water (70:30) mixture to obtain the sol followed by the evaporation of the solvent resulting in a homogeneous polymeric gel. The last stage of the synthesis involved calcination at 560 °C for 3 h. The results indicated that the amount of vanadium salt, gel-forming agent, solvent composition and synthesis additives strongly affected the morphology of the product. As the aforementioned parameters were changed, the shape of V_2O_5 nanostructures evolved from simple spherical nanoparticles to uniform nanoflakes with a mean thickness of 37 nm. The morphology of vanadium pentoxide was controlled by the gel network rigidity.

Kang *et al*.[119] focused on the sol-gel synthesis of Fe_3O_4 and γ-Fe_2O_3 nanoparticles in an aqueous solution without using any surfactant. The Fe_3O_4 nanoparticles were nearly spherical and had a narrow size distribution with an average diameter of 8.5 nm. Their size was smaller than other particles reported in the literature. The oxidation of Fe_3O_4 into γ-Fe_2O_3 was performed by adjusting the pH of the hydrosol to about 3.5 and stirring for 30 min at 100 °C. Applying this procedure needle-like γ-Fe_2O_3 nanoparticles with lengths of 20-50 nm and widths of 4-6 nm were synthesized.

Itteboina and Sau[114] reported the preparation of morphology-controlled Co_3O_4 particles by a sol-gel method employing cobalt(II) chloride hexahydrate, cobalt(II) acetate tetrahydrate, cobalt(II) perchlorate hexahydrate as precursors. The shape of resulting Co_3O_4 particles varied from octahedral to hexagonal and planar with smooth surfaces, sharp edges or corners depending on metal salts, solvents, capping agents used in the synthetic procedure. These parameters played also a crucial role in determining particle size.

Sugimoto *et al*.[121-124] conducted a series of studies focused on the application of the sol-gel method for the fabrication of TiO_2 nanoparticles of different sizes and shapes. Titanium tetraisopropoxide was used as a precursor and different amines including triethanolamine, diethylenetriamine, ethylenediamine, trimethylenediamine, and triethylenetetramine acted as the shape controlling agents. The morphology of TiO_2 nanoparticles evolved from cuboidal to ellipsoidal when synthesis was performed at pH above 11 in the presence of triethanolamine. Using diethylenetriamine at pH above 9.5 led to the formation of ellipsoidal nanoparticles with a high aspect ratio.[124] Tertiary amines, such as trimethylamine and triethylamine promoted the growth of ellipsoidal particles with lower aspect ratios. The shape of the TiO_2 nanoparticles was also changed from round-cornered cubes to sharp-edged cubes employing sodium oleate and sodium stearate. Tuning the growth rate of the crystal planes of TiO_2 *via* specific adsorption of shape controlling agents under different pH conditions allowed obtaining nanoparticles with desired morphology.[124] Kobayashi *et al*.[37] described a sol-gel synthesis of TiO_2 material with a hollow-fiber structure like "macaroni" using *trans*-(1R,2R)-1,2-cyclohexanedi-(11-aminocarbonylundecylpyridinium) hexafluorophosphate, as a template. The process involved the polymerization of titanium tetraisopropoxide and the self-assembly of the amphiphilic compound containing cationic charge moieties. Fibrous TiO_2 materials were formed by the electrostatic interaction between the anionic titania species and the cationic compound serving as a template under basic conditions. In 2003, Gundiah *et al*.[125] applied a tripodal cholamide-based hydrogel as a template to prepare TiO_2 nanotubes. The diameters of the nanotubes were controlled by adopting the appropriate hydrogelator and slightly modifying the gelation conditions.

3.2.2. Hydro/Solvothermal methods

Hydro/solvothermal syntheses involve chemical reactions carried out in water or organic solvents at temperatures above their boiling points and at high pressures.[97, 25, 33, 102, 127-141] All reactants are placed in a sealed vessel (*e.g.* bomb or autoclave). These approaches are suitable for the preparation of MO nanostructures with controlled size and morphology. The most commonly used precursors are

aqueous solutions of salts such as metal chlorides, nitrates, sulphates or acetates. Their hydrothermal treatment can promote hydrolysis reaction.[22, 23, 25, 33, 102, 106, 107, 127-141] The shape, size, and monodispersity of the MO nanostructures can be regulated by tuning the reaction parameters (*e.g.* temperature, time, pressure, specific properties of solvents). It should be noted that the rapid growth of oxide monomers in high-polarity solvents can lead to forming large size particle aggregates. Therefore, to control the morphology and uniformity of MO particles, various surfactants acting as capping agents are introduced into the reaction mixture.[97, 102, 107] In this case, the reaction system always consists of oil, surfactant and aqueous phase. The presence of a surfactant can control the growth of the product.[107]

Li *et al*.[25] prepared Mn_3O_4 nanocrystals with tunable sizes and shapes in the presence of dodecanol and oleylamine surfactants under mild experimental conditions. Manganese(II) nitrate was applied as a precursor. Morphology of Mn_3O_4 evolved from dots to rods and wires depending on concentration of metal salt, employed surfactants, volume of the solvents and reaction time. Additionally, the as-prepared hydrophobic spherical or elongated nanoparticles were assembled into three-dimensional (3D) Mn_3O_4 colloidal spheres using a facile ultrasonication strategy.

Wang *et al*.[131] described the large-scale synthesis of Co_3O_4 nanostructure arrays on nickel foam substrates *via* hydrothermal process at a temperature range of 50-90 °C. In this procedure, different cobalt salts including $CoCl_2{\cdot}6H_2O$, $Co(NO_3)_2{\cdot}6H_2O$ or $Co(CH_3COO)_2{\cdot}4H_2O$ were used as precursors. The shapes of the as-synthesized Co_3O_4 nanostructures were strongly affected by the type of cobalt precursors applied and the growth parameters. Flower-like Co_3O_4 structures composed of hundreds of nanorods with a length of 2-4 μm were formed at 90 °C using $Co(NO_3)_2{\cdot}6H_2O$ as cobalt source. In turn, at 70 °C the nanorod arrays adopted a necklace-like morphology when $CoCl_2{\cdot}6H_2O$ was employed as a precursor. The nanorods consisted of interconnected nanocrystallites similar to those grown at 90 °C (Fig. 11). Two-step synthesis of functional Co_3O_4 with highly ordered structures of different shapes has been demonstrated by Wan and coworkers.[132] Firstly cobalt acetate reacted with ethylene glycol in the presence of poly(vinyl pyrrolidone) (PVP), resulting in a cobalt oxide precursor which was then calcined at 500 °C for 2 h to obtain crystalline Co_3O_4. The morphology of the products was regulated by tuning the reaction conditions (time, initial concentration of $Co(CH_3COO)_2{\cdot}4H_2O$). The shape of Co_3O_4 varied from nanospheres to two-dimensional (2D) nanoplates and 3D cabbage-like hierarchical structures, and finally to microspheres. CoO and Co_3O_4 nanotubes were also prepared by solvothermal treatment of colloidal hydroxide without using any catalyst, surfactant, or template.[133] CoO nanotubes obtained had an outer diameter of 18 nm and an inner diameter of about 7 nm. They were converted to Co_3O_4 nanotubes composed of irregular nanoparticles after annealing at 650 °C in air. It was shown that the duration of solvothermal treatment strongly influenced the morphology of the materials.

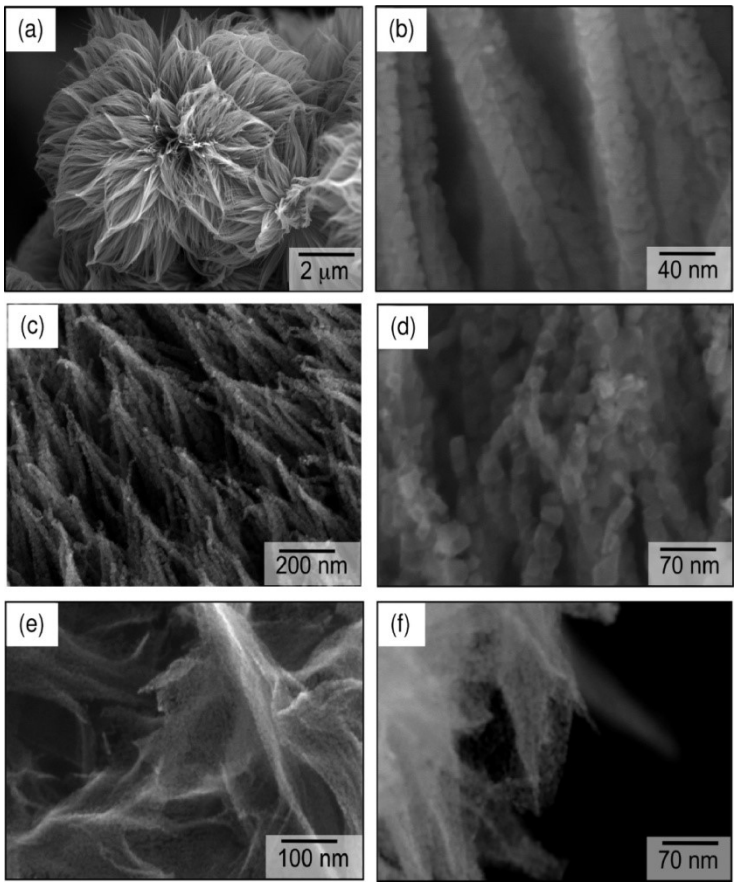

Fig. 11. SEM micrographs of flower-like Co_3O_4 nanostructures achieved at 90 °C using $Co(NO_3)_2 \cdot 6H_2O$ as cobalt source: **a, b)** necklace and **c, d)** net, **e, f)** Co_3O_4 nanostructures obtained from $CoCl_2 \cdot 6H_2O$ precursor at 70 °C and 50 °C, respectively (Reprinted with permission.[131] Copyright 2011, American Chemical Society).

Xia and coworkers[128] described a facile synthetic procedure based on polyol reduction for the fabrication of cuprous oxide nanostructures with well-defined shapes. Sodium chloride was added to the reaction mixture to manipulate the crystal habit and consequently to control the morphology of the product. Polycrystalline colloidal spheres with a mean diameter of 360 nm were synthesized by reducing copper nitrate with ethylene glycol at 140 °C in the presence of PVP. The introduction of a small amount of sodium chloride led to obtaining Cu_2O nanocubes with an average length of 410 nm.

Shang *et al*.[135] reported the fabrication of rose-like NiO nanostructures by calcination of the solvothermally obtained α-$Ni(OH)_2$ with similar morphology. TEM images indicated that the structures were made of flakes with a thickness of about 20 nm. Moreover, the decomposition of α-$Ni(OH)_2$ at 420 °C for 5 h led to the formation of many holes between NiO flakes. Hierarchical porous NiO nanoflowers were also synthesized by Ren and Gao.[136] Firstly high-quality flower-like $Ni(OH)_2$ was obtained using microwave heating of nickel nitrate hydrate in ethanol at 150 °C for 15 min. Then the product was calcined to form NiO nanostructures with well-developed specific surface areas. It was found that the shape of calcined NiO particles originated from the flower-like architecture of the α-$Ni(OH)_2$ precursor. However, the surface of the NiO nanoflowers was rough and grainy. The petals were composed of well-defined nanoparticles with a diameter of 10 nm.

Flower-like ZnO nanostructures were prepared *via* an organic-free hydrothermal method with the use of zinc acetate as a precursor.[137] The morphology of the ZnO nanostructures was strongly affected by reaction temperature and pH of the solution. The typical flower-like ZnO nanostructures

consisted of sword-like ZnO nanorods with width in the range of 60-200 nm and several micrometers in length.

In 2007, He *et al*.[138] presented a simple hydrothermal route performed in the presence of polyethylene glycol 400 (PEG 400) at 150 °C for the synthesis of uniform, single-crystalline Fe_3O_4 nanowires. Ferrous sulphate was selected as a precursor. The nanowires obtained had a narrow size distribution centered at 15 nm and length up to 3 μm. Wan *et al*.[139] prepared uniform single-crystal Fe_3O_4 nanorods *via* a soft template-assisted hydrothermal route at 120 °C for 20 h. In this procedure, ethylenediamine was used as a soft template and benzene as an oil membrane for preventing oxidation of ferrous ions. It was found that as-synthesized product mainly consisted of uniform Fe_3O_4 nanorods with an average diameter of 25 nm and length of 200 nm. A single crystalline triangular Fe_3O_4 nanoprisms employing a direct hydrothermal method in the presence of 1,3-propanediamine (PDA) and ethylene glycol (EG) were fabricated by Li *et al*.[140] The synthesis was carried out in autoclave at 200 °C for 12 h with $FeCl_3{\cdot}6H_2O$ as iron source. Magnetite nanostructures were mainly composed of triangular nanoprisms with average edge length and thickness of 113 nm and 25 nm, respectively. A small fraction of the polyhedral nanoparticles with an average size of 40 nm was also observed. The morphology evolution of the Fe_3O_4 was controlled by tuning the volume ratio of EG to PDA.

Dinh *et al*.[141] developed a versatile solvothermal method for obtaining titania nanocrystals with various shapes including rhombic, truncated rhombic, spherical, dog-bone, truncated and elongated rhombic or bar. In the synthetic protocol, water vapor was applied to accelerate controlled hydrolysis of titanium butoxide to form TiO_2 nanoparticles, while oleic acid and oleylamine were adopted as two distinct capping surfactants. The morphology control of titania was realized by tuning oleic acid: oleylamine ratio and reaction temperature. It was shown that the shape of the TiO_2 evolved from rhombic to truncated rhombic and sphere with increasing ratio of surfactants from 4:6 to 5:5 and 6:4. In turn, when the molar ratio of titanium precursor to oleic acid and oleylamine was changed from 1:6:4 to 2:6:4 the morphology of TiO_2 nanocrystals transformed from spheres to dog-bone.

3.2.3. Thermal decomposition (Thermolysis)

MO nanostructures with desired size and shape can be obtained by thermal decomposition of organometallic compounds in high-boiling, coordinating or non-coordinating organic solvents (*e.g.* 1-octadecene, benzyl ether, phenyl ether, trioctylamine) containing surfactant as a stabilizing agent at high temperature and ambient pressure.[22, 23, 107, 142-153] In this procedure, metal acetylacetonates, acetates, oxalates, cupferronates, alkoxides or carbonyls are often applied as organometallic precursors while fatty acids, aliphatic amines, alkyl phosphonic acids, and alkyl thiols can serve as capping agents.[142-153] The ratio of the starting reagents such as metal-organic salts, solvents, surfactants, and specific reaction conditions (*e.g.* time and temperature) have a direct influence on the obtained morphology. Additionally, the choice of appropriate organometallic compounds and the balance between nucleation and growth stages are important for the synthesis of highly monocrystalline products. MO nanoparticles achieved by thermal decomposition are monodisperse in shape and size. In the thermolysis, the stages of nucleation and growth occur separately, because the preformed nuclei are added to the reaction solution containing the monomers that subsequently grow on the surface of small particles without further nucleation. Consequently, precise control of the morphology of MO nanoparticles is possible.[102, 141-153]

Up to now, facile thermal decomposition method was used to obtain samaria (Sm_2O_3) nanowires and nanoplates.[146] Sm_2O_3 nanowires with a rectangular shape were synthesized by the thermolysis of

hydrated samarium(III) acetate in the presence of a mixture of oleylamine and decanoic acid under argon atmosphere. They had uniform thickness of about 1 nm and width of 2 nm, with lengths of more than 1 μm. Due to the high surface energy, the nanowires generated parallel arrays *via* the self-assemby process. When in the synthesis the oleic acid with oleylamine were used as surfactants, square-shaped Sm_2O_3 nanoplates having a thickness of ~1 nm were formed. Nanoplates of other rare-earth metal oxides, such as La_2O_3, Nd_2O_3, Y_2O_3, and Pr_2O_3, were achieved employing a very similar procedure. Cao *et al*.[147] described the fabrication of Gd_2O_3 nanoplates by thermal decomposition of gadolinium-acetate precursor in hot octadecene containing oleylamine and oleic acid. Evaporation of the solvent during sample preparation for TEM analysis led to the assembly of Gd_2O_3 nanoplates into ribbons of stacked plates.

Hyeon *et al*.[148] described the synthesis of highly crystalline and monodisperse γ-Fe_2O_3 with a size in the range of 4-16 nm by thermal decomposition of iron pentacarbonyl ($Fe(CO)_5$) in the presence of oleic acid. High temperature (300 °C) aging of iron-oleic acid metal complex caused the formation of iron nanoparticles that were transformed in the next step to γ-Fe_2O_3 by controlled oxidation with the use of trimethylamine oxide as a mild oxidant. Moreover, monodisperse γ-Fe_2O_3 nanocrystallites with a particle size of 13 nm can be generated *via* the direct oxidation of $Fe(CO)_5$ with trimethylamine oxide in the presence of oleic acid. In both approaches, it is possible to obtain 2-dimensional or 3-dimensional close-packed superlattice. The authors revealed that during the thermal decomposition of $Fe(CO)_5$ the nucleation occurs at low temperature, whereas the growth derived from the decomposition of the iron oleate complex takes place at a higher temperature. These stages should be separated. A similar procedure was applied for the synthesis of MnO nanorods and nanospheres.[149] These nanostructures were fabricated by thermal decomposition of Mn-surfactant complexes prepared by reacting $Mn_2(CO)_{10}$ with oleylamine at 100 °C. The morphology of the MnO nanoparticles was precisely controlled by tuning the reaction temperature. The one-dimensional nanorods were generated when two surfactants with different stabilizing capabilities were employed under kinetically controlled conditions, such as those requiring rapid thermal decomposition at high temperature (Fig. 12a). Spherical nanoparticles were formed under thermodynamically controlled conditions, *i.e.* corresponding to the slow decomposition of the precursors over a long time. The sizes of MnO nanoparticles were controlled by varying the stabilizing agents (trioctylphosphine, triphenylphosphine). The diameters of MnO nanospheres were in the range of 5 to 40 nm. MnO nanorods had dimensions of 7 nm (diameter) × 33 nm (length) and 8 nm (diameter) × 140 nm (length). Formation of monodisperse MnO nanocrystals by simple heating of manganese(II) stearate in octadecene was systematically studied by Chen *et al*.[150] The authors observed that the shape of manganese(II) oxide nanocrystals (rice, rods, peanuts, needles, dots) can be changed by adding an activation reagent (ocadecanol) or an inhibitor (stearic acid) to the system prior to heating (Fig. 12b, c, d). Zitoun *et al*.[151] reported the application of the thermal decomposition approach for the production of MnO multipods (Fig. 12e, f, g). The $Mn(oleate)_2$ prepared from manganese acetate and sodium oleate was used as a precursor. The mechanism of MnO particles formation involved two stages: *(i)* the nucleation of truncated octahedra or cubes and *(ii)* the growth of homogeneous pods. The rate of the precipitation of multipods strongly determined their overall size and arm lengths.

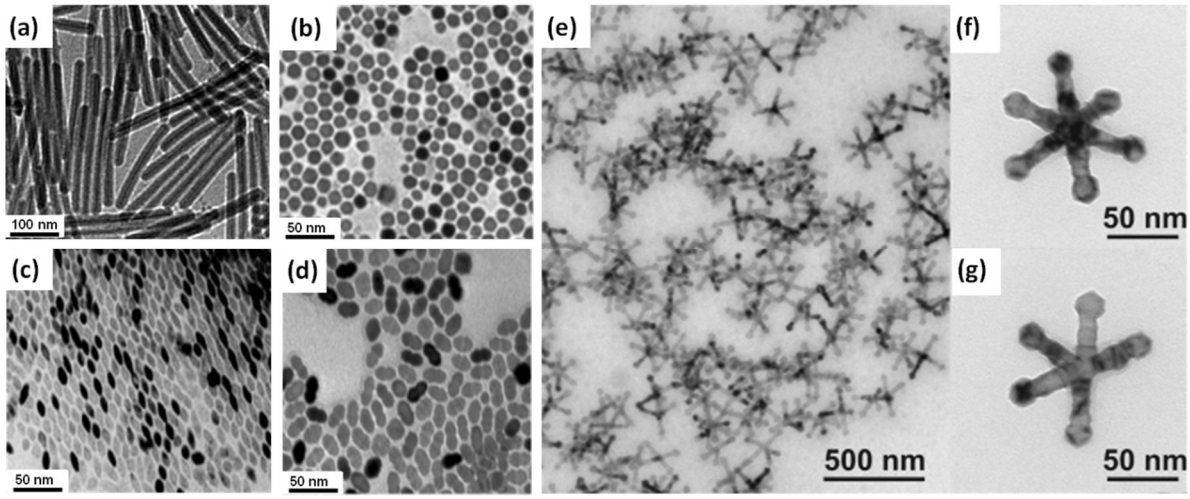

Fig. 12. TEM images of MnO **a)** nanorods (Reprinted with permission.[89] Copyright 2004, American Chemical Society), **b)** dots, **c)** rice, **d)** peanuts (Reprinted with permission.[150] Copyright 2007, American Chemical Society), an assembly of **e)** multipods, **f)** hexapod and **g)** pentapod (Reprinted with permission.[151] Copyright 2005, American Chemical Society).

A significant limitation of the traditional thermolysis is the application of high-cost and toxic organometallic precursors, therefore many research groups have started to develop alternative strategies based on cheaper and less hazardous chemical compounds.[102] Salavati-Niasari *et al*.[152] synthesized Co_3O_4 nanorods by thermal decomposition of inexpensive cobalt oxalate of low toxicity in the presence of triphenylphosphine and oleylamine as surfactants in order to control the morphology. The average length of obtained nanorods determined using TEM was around 500 nm whereas the diameter was about 20 nm. The authors revealed that the external faces of initial nuclei have an impact on the final morphology of the products. Binding of triphenylphosphine and oleylamine to high energy surface as capping molecules can selectively reduce the energy of this face relative to the other external faces. Therefore, the sequent growth takes place along the external faces and 1D nanostructures are formed. Seo *et al*.[153] developed a highly effective one-pot synthetic procedure to synthesize 1-dimensional nanostructures of transition MOs including $W_{18}O_{49}$, TiO_2, Mn_3O_4, V_2O_5 with narrow size distribution. The well-defined nanorods were obtained through a simple reaction of metal chlorides with a mixture of oleic acid and oleylamine surfactants. As a result, stable MO monomers were formed and promoted the anisotropic growth of nanocrystals along the high energy crystallographic direction.

3.2.4. Reverse micelle (microemulsions)

Reverse micelles are the hydrophilic cavities of microemulsions formed from the mixture of surfactant, water, and oil.[97, 154, 155] In 1982 for the first time, they were applied as templates in the preparation of inorganic nanomaterials.[156] The reverse micellar synthesis of nanostructures belongs to wet chemical methods and allows excellent control of size, morphology, uniformity, and dispersity of MO nanoparticles.[157-164] However, the main drawback of this route is the formation of small quantities of products while consuming relatively large volumes of organic solvents.[155]

The most commonly used approach involves mixing two separate microemulsions containing different reactants necessary for the synthesis of the nanostructures. Nucleation occurs at the edges of micelles when the water phase inside gets saturated with reactants. The growth stage begins at

the interface and then shifts into the core of the micelle. It should be noted that the intermicellar exchange limits the growth rate of nanoparticles. Another approach used for the synthesis of nanoparticles is based on the preparation of single microemulsion and then successive diffusion of chemical compounds into the interior of reverse micelles where the proper reaction occurs. The problem with this procedure is that the composition of the microemulsion is gradually changed by adding solutions of different reactants, which causes significant modification of the micelle properties.[155, 157-164]

The morphology of the obtained nanostructures is determined by three main factors: *(i)* micellar template, *(ii)* added anions, and *(iii)* molecular adsorption. A surfactant-water-oil system can create various self-assembly structures such as spheres, cylinders, interconnected cylinders, and planes termed lamellar phase, which can transform into onion-type structures. Therefore, many nanoparticles of different shapes could be grown inside these templates.[97, 102, 154, 155]

Gu *et al*.[160] successfully synthesized one-dimensional mesoporous ceria nanofibers and nanobelts with the use of reverse micelle method. In an applied procedure, $Ce_2(CO)_3$ nanofibers, acting as precursors, were prepared by rapidly pouring the reverse micelles I (Triton X-100, cyclohexane, n-hexacohol, $Ce(NO_3)_3$ hydrous solution) into the reverse micelles II (Triton X-100, n-hexacohol, cyclohexane, NH_4HCO_3 hydrous solution). In the next step, the mixture was aged for 48 h at 30 or 40 °C and then precipitate was dried and calcined to obtain CeO_2 nanostructures. Studies have revealed that the aging temperature is a key parameter to control the morphology of ceria. CeO_2 nanofibers were formed when the aging temperature during synthesis was 30 °C. The diameter of the nanofibers was estimated to be 50-200 nm and the length was more than 50 µm. Performing the aging process at 40 °C resulted in the fabrication of CeO_2 nanobelts with a length of a few tens of micrometers, a width ranging from 0.5 to 5 µm and a thickness varying from 20 to 100 nm. Kuiry *et al*.[161] described the preparation of CeO_2 nanorods by self-assembling the crystalline ceria nanoparticles utilizing a double microemulsion procedure. Microemulsion I consisted of cerium nitrate dissolved in the sodium bis(2-ethylhexyl) sulfosuccinate (AOT)-in-toluene solution, whereas microemulsion II was obtained by adding H_2O_2 to the AOT-in-toluene solution. These microemulsions were mixed and aged for a few weeks. The self-assembly process occured during aging of the sol after the formation of CeO_2 nanoparticles, leading to the gradual evolution of ceria nanorods. The authors proposed a mechanism of this process involving the creation of cylindrical supra-aggregates and their subsequent growth by preferential assembly of ceria nanocrystallites along the longitudinal direction. The nanorods achieved with this procedure had a diameter of 40 nm and a length of 250 nm.

Li *et al*.[162] obtained TiO_2 nanoparticles with controlled morphology and high photoactivity using microemulsion-mediated hydrothermal method. The microemulsion was prepared by introducing Triton-X-100 and water into the mixture of heptane and hexanol. Titanium isopropoxide as precursor was directly added into microemulsion. In this procedure, hydrothermal treatment was carried out for 13 h at different temperatures which had a direct impact on the morphology of TiO_2. As the temperature of the hydrothermal treatment increased, the shape of titania particles changed from spherical into rod-like. The results indicated that spherical particles with diameters 6-10 nm grow into rods along their preferred (101) direction confirming that the microemulsion droplet provides a large space for nuclei growth of titania due to a decrease in the interface strength and an increase in the collision efficiency between droplets at high temperature.

Bumajdad *et al*.[163] synthesized zinc oxide nanostructures with various shapes (spherical, needle-like, acicular) using water-in-n-heptane microemulsion (relatively insensitive towards precursor

incorporation) stabilized by a mixture of cationic (didodecyldimethylammonium bromide) and non-ionic (Brij®35) surfactants. It was found that the molar ratio of Zn precursor to precipitating agent (NaOH) plays a crucial role in the control of morphology and porosity (Fig. 13). Application of a 1:1 molar ratio led to the formation of nanoparticles with a well-organized spherical shape, having an average diameter of 110 nm. At a ratio of 1:2 (Zn: NaOH), the produced zinc oxide nanoparticles preferred a needle-like shape with an average diameter of 70 nm and a length of 1 µm. Using a ratio of 1:4 (Zn: NaOH), the nanoparticles of needle-like morphology changed into an acicular shape with an average diameter of 55 nm. ZnO nanoparticles with irregular shapes were formed when the highest concentration of the precipitating agent was used. This morphology change was attributed to the concentration of OH^- ions which affected the nucleation process.

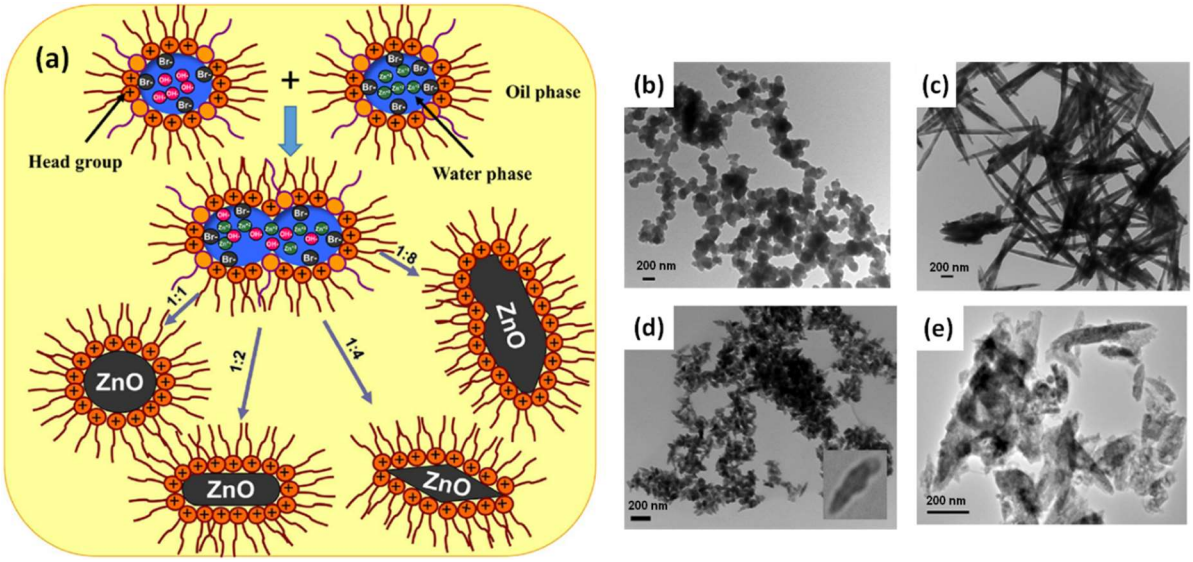

Fig. 13. a) Zn^{2+}, Br^-, and OH^- ion interaction and effect of $[Zn^{2+}]$:$[OH^-]$ ratio on ZnO nanoparticle morphologies. TEM images of ZnO with **b)** spherical, **c)** needle-like, **d)** acicular, and **e)** irregular shapes (Licensed under CC-BY.[163]).

A new modified reverse micelle method was developed to control the morphology of magnetic iron oxide nanocrystals under mild conditions.[164] Magnetic nanocubes were prepared by injecting water to the reaction mixture containing iron(II) acetate and oleylamine in xylene solution. To control the morphology of the iron oxide nanocrystals, oleic acid was added as co-surfactant. Park *et al.*[164] showed that the strong binding affinity of oleylamine to the (100) facet of magnetite structure caused the construction of nanocubes.[164] With decreasing the amount of oleylamine in the synthetic procedure, the cubic shape of iron oxide nanocrystals transformed into a spherical shape. Spherical magnetite nanocrystals with different sizes were also synthesized with the use of a mixture of oleic acid and oleylamine. It is well known that oleic acid strongly binds to the surface of oxide nanocrystals. Therefore, all facets of magnetite nanocrystals surface could be stabilized by this carboxylic acid. Reducing the difference in surface energy of the facet brought about the formation of spherical nanocrystals. Their size was modulated by tuning the amount of oleylamine, maintaining other experimental conditions constant.

3.2.5. Two-phase route

A two-phase synthesis involves the mixing precursors with capping molecules in the reaction medium consisting of water and organic solvents.[97, 102, 165-170] The nucleation and growth stages of MO

nanoparticles occur at the interface of two immiscible liquid phases during thermal treatment. The initial nuclei grow to form capping-assisted oxide nanoparticles which are highly dispersed in the nonpolar organic solvent. Then the product is precipitated by adding excess ethanol or methanol and recovered by centrifugation and decantation. In this method, MO nanocrystals are stabilized in the solution by the organic capping layer adsorbed on their surface. In comparison to the single-phase synthetic approaches, the two-phase strategy also leads to obtaining high crystallinity products under relatively mild conditions, thanks to the presence of the aqueous phase, which increases the speed of the growth process. Due to the slow rate of nucleation and growth occurring at the liquid-liquid interface, it is possible to precisely control the particle size and morphology.[97, 102, 165-170]

Zhao *et al*.[165] described a two-phase synthesis of Mn_3O_4 nanocrystals that were capped with an organic ligand (dodecylamine) and dissolved in a nonpolar solvent. In this synthetic procedure, manganese(II) stearate was used as a precursor. The morphology and size of the product were controlled by changing reaction conditions (*e.g.* time, temperature, activation agent concentration). The results have shown that the cubic nanocrystals were fabricated in the early stages of the anisotropic growth. With increasing the reaction time, the monomer concentration was gradually reduced and the energetically unfavorable cubes transformed into spheres. The Mn_3O_4 nanoparticles obtained at relatively low temperature (120 °C) had cubic shape and the average size of 8 nm, whereas the spheres with a diameter of about 5 nm were synthesized at 180 °C.

Ji and coworkers[160] developed a two-phase approach for the preparation of zirconia nanoparticles with spherical, teardrop, rod and rice shapes. The synthesis was performed by the mixing of zirconium(IV) n-propoxide and oleic acid in the toluene-tert-butylamine-water system and then thermal treatment at a temperature in the range 120-180 °C. It was found that the reaction time, temperature, the nature of the capping agent, and the monomer concentration are key factors for controlling the shape of ZrO_2 nanoparticles. The change of zirconia morphology was the result of both the martensitic transformation and the diffusion mechanism, which influenced the nucleation and growth, respectively.

Nguyen and Do[161] reported different two-phase methods for synthesis of rare earth oxides (Sm_2O_3, CeO_2, Er_2O_3, Gd_2O_3, La_2O_3, Y_2O_3) and transition metal oxides (Mn_3O_4, Cr_2O_3, Co_3O_4, NiO) with controlled size and shape, through the hydrolysis of corresponding inorganic salts or metal-surfactant complexes in the water-toluene system. The advantages of these approaches are mild reaction conditions, high yields, and easy tunability of the product morphology. Depending on the nature of the metal precursors, the nanoparticles obtained had spherical, cubic, peanut, rod or hexagonal shapes. Moreover, it was observed that when the monomer concentration of cerium salts rose from 0.015 to 0.120 M, the shape of CeO_2 nanoparticles changed from nanocubes to elongated nanocubes, what could be associated with an increase in the chemical potential in bulk solution. In turn, the morphology of Co_3O_4 nanoparticles transformed from nanocubes to nanospheres with increasing reaction time up to 24 h at 180 °C because of the differences in chemical potential between different facets of the nanocrystals.

Nguyen *et al*.[168] proposed a low cost and reproducible preparation of samaria spheres and rods from inexpensive Sm_2O_3 powders and various capping long-chain alkyl acids with the use of two-phase hydrothermal method. The shape of nanoparticles was controlled by reaction temperature while the diameters of rods were controlled by the alkyl chain length of capping agents. The Sm_2O_3 nanocrystals synthesis occurred through two mechanisms: Ostwald ripening (nucleation and growth) in the case of spherical nanoparticles generation and the oriented attachment for the formation of rods from nanoparticles.

Pan *et al*.[169] synthesized high-quality nanocrystals of anatase TiO_2 with narrow size distribution employing a two-phase route performed in an autoclave. Titanium(IV) n-propoxide was applied as a precursor, while oleic acid or stearic acid were served as capping agents. The TiO_2 nanocrystals were nearly spherical with an average diameter of 4.5 nm.

A rapid approach for producing colloidal CeO_2 nanocrystals using organic-ligand-assisted supercritical water as a medium was presented by Zhang *et al*.[170] The ceria nanocrystals with uncapped surfaces showed spherical shapes with an average diameter of 7 nm and they were partly aggregated. Adding decanoic acid (molar ratio to ceria precursor 6:1) to the reaction system led to obtaining nanocubes with an average size of 6 nm. The morphology of the nanocrystals was controlled by tuning the interaction between decanoic acid capping molecules and various crystallographic facets of CeO_2.

3.2.6. Co-precipitation method

Co-precipitation is a simple and low-cost method for the preparation of MO nanostructures, in which nucleation, growth, coarsening, and/or agglomeration processes occur simultaneously. Due to the high reaction rate it is difficult to precisely control the morphology of the formed MO nanoparticles.[22, 171, 172] Moreover, the application of the co-precipitation method gives less opportunity to obtain a large variety of nanoparticle shapes compared to other commonly used preparation approaches. Most of them have spherical morphology. It is worth emphasizing that a high surface area-to-volume ratio, good mechanical strength, easy coatings and short pathways for diffusion of different species are the main advantages of metal oxides spheres. Ostwald ripening and aggregation strongly affect the size, morphology, and properties of the resulting product. The co-precipitation method has been employed in the synthesis of MOs such as ZnO,[173, 174] Fe_3O_4,[175] MnO_2,[176] SnO_2,[177] Cu_2O,[178] or MgO[179].

Farahmandjou and Jurablu[113] reported the fabrication of ZnO nanoparticles with the use of zinc nitrate as a precursor and potassium carbonate as a precipitant. It was observed that increasing annealing temperature up to 500 °C transformed the morphology of zinc oxide particles from spherical into pyramidal. The diameters of ZnO nanospheres were in the range of 20-80 nm, whereas pyramid-like shaped ZnO nanoparticles had sizes 40-100 nm. Spherical zinc oxide nanoparticles with diameters varied from 35 to 40 nm were also obtained by Ahamed and Kumar.[114] However, in this case, sodium hydroxide solution was employed as the precipitating medium in the synthetic protocol.

Wu *et al*.[175] described the synthesis of magnetic Fe_3O_4 nanoparticles by low-temperature co-precipitation of Fe(II) and Fe(III) chlorides (Fe^{2+}/Fe^{3+} ratio = 0.5) in NaOH solution. TEM micrographs showed that single spherical nanoparticles with an average size of 6 nm aggregated into tubular clusters.

Chen *et al.*[176] prepared MnO_2 with different crystallographic forms (α, γ) and one-dimensional morphologies *via* a facile quick-precipitation procedure at a low temperature (83 °C) without using any templates or surfactants. The particles of manganese dioxide showed needle-, rod- and spindle-like shapes. Their diameters were 20-50 nm, 40-100 nm, 30-80 nm and lengths of 200-500 nm, 100-200 nm, 70-160 nm, respectively. The formation of unique nanostructures of MnO_2 was dependent on different reaction parameters. The authors revealed that needle- and rod-like products were composed of a few primary nanorods aggregated along the lateral faces.

Tazikeh *et al.*[177] described a fabrication of SnO_2 nanostructures with spherical morphology using tin chloride, Triton X-100, and ammonia precipitant. The obtained nanoparticles possessed diameters

smaller than 100 nm. The slow addition of ammonia to the reaction solution under stirring resulted in the formation of many initial nuclei. Moreover, it was noted that with increasing pH from 6 to 9, the particle sizes of tin oxide decreased.[117]

Park *et al*.[178] found that Cu_2O nanocubes can be easily converted to polycrystalline CuO hollow nanostructures through a sequential dissolution-precipitation process by adding aqueous ammonia solution in air. The morphology of the product was tailored by adjusting the pH value of the reaction solution. It was observed that increasing the pH of the solution led to the formation of hollow cubes, hollow spheres with numerous needle-like branches on the surface, and urchin-like particles (Fig. 14). Magnesium oxide nanoparticles with spherical granules structures and size ranging from 100 nm to 120 nm were also successfully fabricated by co-precipitation method.[179]

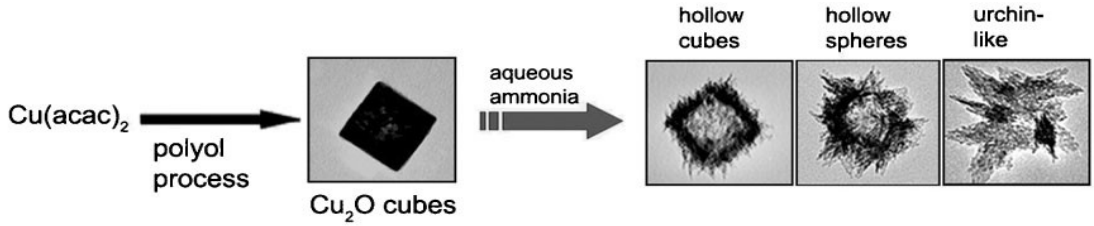

Fig. 14. Overall synthetic scheme of Cu_2O nanocubes and CuO nanostructures (Reprinted with permission.[178] Copyright 2009, John Wiley & Sons).

3.2.7. Flame spray pyrolysis

In recent years, the combustion of the sprayed metal salts solution in the flame has become a promising technique for the rapid and scalable synthesis of nanostructural MOs with size ranging from 1 to 200 nm and extraordinary properties.[180] The formation of MO particles involves four sequential stages: *(i)* precursor spray evaporation/decomposition; *(ii)* nucleation as a result of supersaturation; *(iii)* growth by coalescence and sintering; and *(iv)* particle aggregation and agglomeration. Appropriate selection of metal precursors and solvents with suitable combustion enthalpies, melting/decomposition temperatures and chemical stability plays an important role in the MO particles formation. Nitrates, acetates, acetylacetonates and alkoxides are the most commonly employed precursors in the flame spray pyrolysis process. While many of these metal salts are low-cost and readily available commercially, they do not always yield the homogeneous morphology of resulting metal oxide particles.[180]

Flame spray pyrolysis allows achieving a wide range of nanostructural MOs *i.e.* ZrO_2,[180] Al_2O_3,[180] Fe_2O_3,[181] WO_3,[182] V_2O_5,[183] ZnO[184]. Due to the high temperature (1500-2200 °C) of the synthetic procedure, MO nanostructures exhibit good thermal stability.

Grimm *et al*.[181] synthesized highly dispersed γ-Fe_2O_3 powders with particle sizes down to 5 nm by combustion of iron pentacarbonyl or iron(III) acetylacetonate solutions in an oxyhydrogen flame. The iron oxide primary particles had a spherical shape but were partly agglomerated. Their structure, size, and morphology were predominately determined by the nature of the starting solution and the conditions of the process (*e.g.* temperature and retention time). Spherical nanoparticles have also been obtained in the case of the WO_3 synthesis described by Pokhrel *et al*.[182] Single-crystalline WO_3 nanospheres were fabricated using different tungsten precursors (WCl_6, WCl_4, $W(CO)_6$) with the combination of highly combustible organic solvents such as benzyl alcohol and tetrahydrofuran. The avarage diameters of the particles obtained from all the precursors were found to be ~10 nm. The results have shown that the application of different inexpensive and unusual precursors in the flame

spray pyrolysis technique opens new opportunities for the production of ultrafine single-crystalline MO nanomaterials.

Sel *et al*.[183] reported the application of flame spray pyrolysis for the preparation of orthorhombic vanadium pentoxide (V_2O_5) nanoparticles. In the synthetic protocol, vanadium oxotriisopropoxide dissolved in propionic acid was employed as a precursor. It was observed that spherical primary nanoparticles with the avarage diameter of 20 nm formed chain-like aggregate structures having polydisperse size distribution.

Height *et al*.[184] demonstrated direct synthesis of ZnO nanorods with controlled aspect ratio by flame spray pyrolysis using zinc naphthenate as a precursor and dopant species such as indium acetyl acetonate, stannous 2-ethyl hexanoate and lithium tert-butoxide. It was shown that tin and indium dopants had an influence on formation of specific zinc oxide crystal plane. They were incorporated into certain crystal lattice, thereby disrupting the crystal growth. Nanorod formation was attributed to the higher valency and coordination of indium and tin dopants in comparison to zinc. Lithium, with an equivalent ionic radius to other dopants but lower valency than zinc, does not affect the ZnO morphology. The final rod shape was mainly associated with particle annealing and rearrangement during the flame cooling.

3.2.8. Electrodeposition

Electrochemical methods of synthesis (*i.e.*, electrodeposition - ED, electrophoretic deposition - EPD) can be applied to obtain various MO nanostructures with desired shape and dimensions.[49, 50, 185-193] The reaction occurs at the interface of electrode-electrolyte and does not require elevated temperature. The product is deposited on the electrode surface in the form of a coating or thin film having specific morphology. The film structure can be controlled by changing the bath composition and parameters of the electrochemical processes. Other advantages of these methods include the high growth rate, low cost, and the possibility of using different types of substrates.[49, 50, 185-193]

Lu and Zhou[183] described a fabrication of vanadium oxide films by facile electrochemical deposition method on ITO-coated glass substrates at +2.0 V for 3 min and thermal treatment at 400 °C for 6 h. Vanadium(IV) oxide sulfate was used as a precursor and Triton X-100 polymer surfactant with different concentrations was selected as a templating agent to control the morphology of the nanostructures. Nanorods with diameters of about 62 nm and lengths range of 200-400 nm were synthesized in the presence of 100 mM polymer surfactant. A reduction of Triton X-100 concentration to 50 mM led to formation of irregular vanadium oxide nanoparticles having different diameters of 39 nm. Without using polymer surfactant after thermal treatment irregularly shaped crystal platelets were fabricated. Lu *et al*.[190] also prepared V_2O_5 films by electrodeposition performed at -0.7 V against the reference electrode for 20, 40, and 60 s. It was observed that vanadium oxide thin films deposited for 20 s were relatively smooth and adhered very well onto the substrate. As the deposition time rose to 40 and 60 s, the morphology of the V_2O_5 films transformed from smooth into typical sea-island.

Hassan and Hashim[43] demonstrated that time of the process strongly affected the shape and size of the ZnO nanostructures electrochemically deposited on silicon Si (111) using 0.1 M of $Zn(NO_3)_2{\cdot}6H_2O$ aqueous solutions at room temperature. Zinc oxide nanostructure exhibited a high-quality flakes-like morphology. The authors suggested that during the synthetic procedure Zn^{2+} in the solution moved toward the cathode and condensed to Zn droplets on the silicon. The Zn droplets reacted with hydroxide to form ZnO. Yang *et al*.[191] synthesized zinc oxide nanotube arrays on ITO-coated glass substrates by two-step route. The first step involved the electrodeposition of ZnO nanorod arrays in

a zinc nitrate aqueous solution. Then the core of electrodeposited nanorods was selectively etched using potassium hydroxide solution. It was shown that the sizes of zinc oxide nanorods can be controlled by adjusting the electrochemical parameters. In turn, the concentration of alkali, dissolution time and temperature have an impact on the morphology of ZnO nanotube arrays. With increasing of the KOH concentration, etching time to 2 h and temperature to 90 °C, zinc oxide nanotubes were completely formed and their inner/outer walls surfaces were quite smooth.

Chou *et al*.[192] prepared a porous Co_3O_4 nanostructured thin film by electrochemical deposition on nickel sheets from $Co(NO_3)_2$ aqueous solution and then sintering at 300 °C for 3 h. The morphology of the products was controlled by adjusting of $Co(NO_3)_2$ aqueous solution concentration. Porous Co_3O_4 films were formed from large nanoflakes with 20-30 nm in thickness and several micrometers in length or from small nanoflakes with 30-40 nm in thickness and less than 1 µm in length. A non-porous film with a smooth surface was obtained when the electrodeposition process was carried out in $Co(NO_3)_2$ aqueous solution with the lowest concentration of 0.0125 M (Fig. 15).

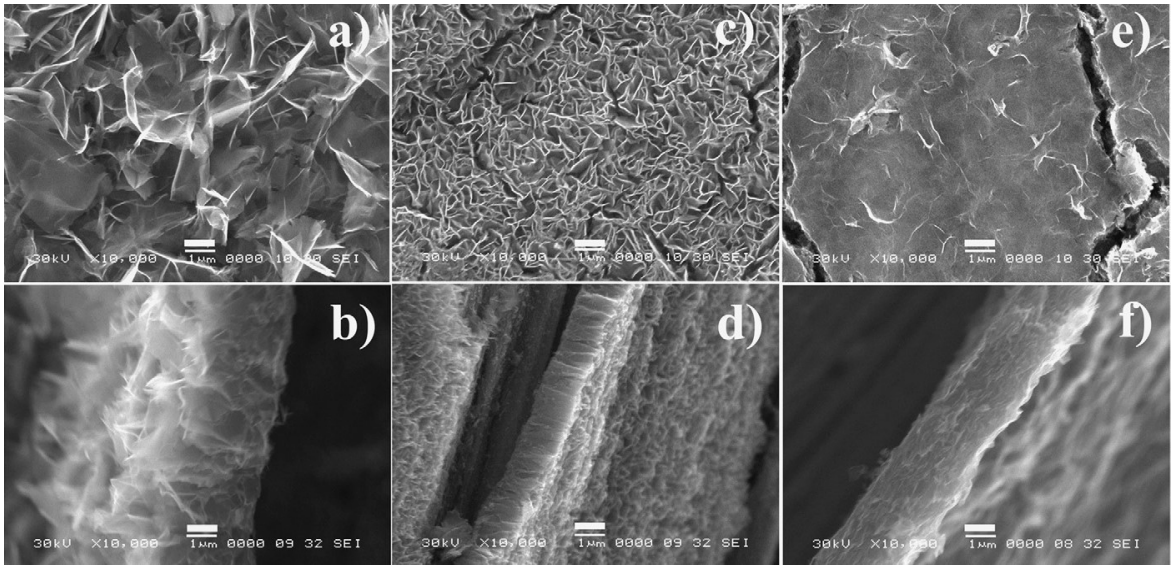

Fig. 15. SEM images of as-prepared Co_3O_4 thin films produced by electrochemical deposition in **a, b)** 0.025M, **c, d)** 0.1M, and **e, f)** 0.0125M $Co(NO_3)_2$, followed by heat-treatment at 300 °C for 3 h (Reprinted with permission.[133] Copyright 2008, Elsevier).

Yuan *et al.*[50] reported a fabrication of hierarchically ordered porous nickel oxide array film by electrodeposition with the use of a monolayer polystyrene spheres template. The framework of porous films consisted of bowls with a diameter of 1 µm, and the interstices between bowls were interconnected by some NiO nanoflakes. In contrast, the film prepared without template exhibited a homogeneous dense structure.

Xiang *et al*.[193] characterized Cu_2O film electrodeposited on copper foil through a self-assembled polystyrene sphere template. It was shown that the Cu_2O film prepared within 10 min exhibited an ordered porous structure. The well-ordered and close-packed hemispherical voids were observed in the film after the removal of the polystyrene sphere template. Moreover, the voids in the Cu_2O film had the same diameter as the polystyrene spheres (about 800 nm). As the deposition time increased to 20 min, the Cu_2O film displayed a similar porous morphology but the diameter of the spherical voids decreased to about 500 nm. Thus, it could be concluded that both the diameter of the

polystyrene spheres and the electrodeposition time had an impact on the geometry of the voids in the Cu_2O film.

3.2.9. Biogenic synthesis

In recent years, the biogenic synthesis of MO nanostructures using microorganisms or plant extracts have been of great interest to many scientists from around the world due to its cost-effectiveness, safety, versatility, mild conditions, and high production yield.[194, 195] Moreover, this approach is environmentally friendly and allows to reduce or eliminate the use of toxic reaction precursors and solvents. In the synthetic procedure bacteria, fungi, yeast, and plant extracts act as reducing or stabilizing agents. The size of the nanostructures can be controlled by adjusting reaction parameters including temperature, time, pH of the solution and the concentration of reactants. The morphology of the nanoparticles can be modulated by a selection of appropriate microorganisms or plant extracts.[194, 195] Biogenic methods have been developed to prepare many MOs including TiO_2,[196, 197] UO_2,[198] ZnO,[195, 199-204] Fe_3O_4,[205-207] CuO[208, 209].

Zhou *et al*.[196] synthesized biomorphic TiO_2 hollow spheres and tubes using two species of bacteria - *Streptococcus thermophilus* and *Lactobacillus bulgaricus* as biotemplates naturally covered with different organic functional groups (*e.g.* carboxyl, ester, amine, hydroxyl groups) which can easily capture cations. The original morphologies of bacteria were retained in the case of titania structures. TiO_2 hollow spheres obtained applying *Streptococcus thermophilus* had a diameter of 500 nm and shell thickness of about 15 nm. It was observed that during calcination at 700 °C some spheres were broken demonstrating their hollow cavities. A rod-shaped *Lactobacillus bulgaricus* was a template in the synthesis of TiO_2 hollow tubes having a diameter in the range 200-300 nm and length of 800 nm. The shell thickness was measured to be 30-40 nm. Jha *et al*.[139] reported the preparation of spherical titania particles assisted with *Lactobacillus sp.* and baker's yeast (*S. cerevisiae*). The nanoparticles showed broad size distributions with average diameters of 25 or 12.5 nm for TiO_2 synthesized in the presence of bacterium and yeast, respectively. The duration of the reaction strongly affected the size disztribution of the nanoparticles.

Suzuki *et al*.[198] described a fabrication of UO_2 nanoparticles from uranium in sediments by reduction with *Desulfosporosinus spp.*, a Gram-positive sulphate-reducing microbe. The uranite nanoparticles were spherical and less than 3 nm in diameter. They occurred as specific aggregates and particle coatings on the bacterial cell surface.

In recent years, many studies have been focused on the biological methods of ZnO nanostructures fabrication employing plant extracts, bacterial strains or fungi. Ali *et al*.[199] applied *Aloe barbadensis Miller* leaf extract with high reducing and capping potential for the biogenic synthesis of zinc oxide nanoparticles of different morphology. $ZnSO_4$ was adopted as a precursor in the synthetic procedure. The ZnO nanoparticles with size varied from 8 to 18 nm showed spherical, oval and hexagonal shapes. Rajiv *et al.*[200] obtained highly stable, spherical and hexagonal ZnO nanoparticles with an antifungal activity employing *Parthenium hysterophorus L.* leaf extract. Their morphology was dependent on the concentration of the plant extract. The spherical and hexagonal nanoparticles were not uniform and had an average size of about 27 and 84 nm, respectively. Nagajyothi *et al.*[143] demonstrated an eco-friendly and inexpensive approach for the formation of zinc oxide nanoparticles from *Coptidis Rhizoma* which is the dried rhizome of *Coptis chinensis Franch*.[201] It was observed that ZnO nanoparticles with the size ranged from 3 to 25 nm were nearly spherical or rod-like shaped. Madan *et al*.[202] reported facile biosynthesis of ZnO nanostructures with diverse shapes performed *via* low-temperature solution combustion using neem (*Azadirachta indica*) extract. It was

found that the morphology successively evolved from mushroom-like superstructures to bullet, nanobuds, aggregated hexagonal-shaped flakes arranged in the form of a cone, bundles and pine-like with increasing the plant extract concentration (2, 4, 6, 10, 15, 20 ml). It was concluded that the shape of the zinc oxide nanostructures can be modulated by tuning the volume of neem extract added to the reaction system during the synthetic procedure. Raliya and Tarafdar[197] prepared monodisperse ZnO nanoparticles from zinc nitrate with the use of extracellular secretions of *Aspergillus fumigatus TFR-8* fungus. The nanoparticles with size in the range of 1-7 nm were oblate spherical and hexagonal. Tripathi *et al*.[204] developed novel eco-friendly biosynthesis of ZnO nanostructures assisted with bacterial strains of *Bacillus licheniformis* MTCC 9555 at ambient temperature. Zinc oxide nanostructures had 3D flower-like morphology. The size of nanoflowers varied from 200 nm to 1 µm and they were composed of several petals with a width of about 40 nm and length of 400 nm. The basic shape of the nanoflowers were rods that agglomerated to form the final material.

Venkateswarlu *et al*.[205] presented a green synthesis of Fe_3O_4 1D nanorods utilizing *Punica Granatum* rind extract, a naturally available agricultural by-product, as a reducing agent. The obtained nanorods had a mean diameter of 40 nm and a length above 200 nm. Other studies of the same team were aimed at the preparation of monodisperse Fe_3O_4 magnetic nanoparticles of spherical shape using plantain peel extract.[206] Byrne *et al*.[207] synthesized magnetite nanoparticles by biogenic method assisted with *Geobacter sulfurreducens*. It was found that the size of the nanoparticles with spherical and square shapes can be controlled within the range of 10-50 nm by tuning the total amount of bacteria introduced to the system at the beginning of the experiment. The higher concentration of bacteria led to decreasing nanoparticle diameters.

In 2019, Singh *et al*.[208] reported the environmentally friendly and low-cost green synthesis of CuO nanoparticles employing *Psidium guajava* leaf extract as reducing and capping agent, and copper acetate monohydrate as a metal precursor. Monodisperse CuO nanoparticles exhibited spherical morphology and uniform size distribution of 2-6 nm. Saravanakumar *et al*.[209] synthesized copper oxide nanoparticles with the use of the cell-free extract of *Trichoderma asperellum* fungus. The size of spherical CuO nanoparticles evenly agglomerated varied from 10 to 190 nm with a mean diameter of 110 nm.

3.3. Morphology control of metal oxides by confinement of growth in solid matrices

The morphology of MO nanostructures can be controlled by confining the growth process of the primary particles in inorganic networks acting as a hard template. In this case, the voids of the solid matrix are filled with target precursors which undergo further transformations. The final material is obtained after removing the template.[210, 211] Therefore, the size and shape of the voids present in the structures of the matrix as well as the type and concentration of the precursor used strongly affect the morphology of the resulting MO nanostructures. The commonly used hard templates for the creation of MO nanostructures are zeolites, polymers, alumina membranes, ordered mesoporous silica and carbons. However, most scientific works consider the use of silica materials as solid matrices due to their well-developed surface areas, high pore volumes and diverse morphologies such as spherical, fibrous, noodle- and rod-like.[210, 211] This section presents an overview of representative examples employing different template approaches.

Rumplecker *et al*.[212] focused on the synthesis of Co_3O_4 nanostructures with the use of two-dimensional (2D) hexagonal SBA-15 and three-dimensional (3D) cubic KIT-6 silica materials as hard templates. It was found that the ordering and the interconnectivity of cobalt oxide nanowires were

strongly determined by the amount of mesoporous silica added into the solution of $Co(NO_3)_2 \cdot 6H_2O$ precursor during the synthetic procedure. When the loading of the solid matrix increased the nanostructures changed from randomly packed, isolated Co_3O_4 nanowires to highly ordered, mesostructured, and fully interconnected networks. Moreover, the application of cubic KIT-6 silica with specific wall thickness and degree of framework interconnectivity as a template allowed to modulate the pore size of mesostructured Co_3O_4 from 3 nm up to 10 nm.

Lakshmi *et al*.[213] reported a general preparation of semiconductor MO nanotubes and fibrils *via* the sol-gel method applying porous alumina and polymeric filter membranes as templates. For TiO_2 nanostructures, the synthetic procedure involved dipping of alumina membrane in a TiO_2 sol obtained by mixing solution of titanium isopropoxide with water, ethanol and hydrochloric acid followed by drying, heating at 400 °C for 24 h and removal of the template. The results have shown that titania tubules were formed when the alumina membrane was immersed in the sol for only 5 s, while solid TiO_2 fibrils were obtained within 60 s. Immersion of template for 25 s led to producing tubules with very thick walls. In all cases, the outside diameter of tubules and fibrils was about 200 nm (the diameter of the pores in the template) and a length of 50 µm (the thickness of the alumina membrane). The morphology of the TiO_2 nanostructures was also controlled by the temperature of the membrane dipping process. Thin-walled TiO_2 tubules and fibrils were fabricated at 5 °C and 20 °C, respectively. Similar methods were applied for the synthesis of 1D nanostructures of other MOs such as MnO_2, V_2O_5, Co_3O_4, ZnO, and WO_3. Limmer *et al*.[214] demonstrated the template-based growth of uniform oxides nanorods (TiO_2, SiO_2, $BaTiO_3$, $Sr_2Nb_2O_7$, and $Pb(Zr_{0.52}Ti_{0.48})O_3$), formed by a combination of the sol-gel process and electrophoretic deposition. These nanostructures with a diameter in the range 125-200 nm and length of 10 µm were arranged parallel to one another over a broad area of the hydrophilic polycarbonate (PC) membrane.

The hard templating method is widely applied to obtain hollow spheres.[215] The size of the inner hollow space can be modulated by a selection of appropriate solid matrix whereas the thickness of the shell by adjusting the concentration of the reactants and changing hydrophilicity of the template surface. Ren *et al*.[216] described a synthesis of uniform hollow titania nanospheres with an average diameter of approximately 80 nm and composed of 7 nm-sized nanoparticles employing quasi-nanosized carbonaceous spheres. Zeng *et al*.[217] also reported a simple hard template strategy for the fabrication of multi-shelled TiO_2 structures with the use of porous polystyrene-divinylbenzene (PS-DVB) spheres as templates. The TiO_2 spheres had smooth surfaces and were connected with each other. It should be noted that the application of the solid matrix does not always limit the final shape of the product to hollow spheres.[215]

In recent years, a lot of consideration has been paid to the application of metal-organic frameworks (MOFs) both as precursors and self-sacrificial templates in the fabrication of MO nanostructures with diverse compositions and morphologies.[218] The advantages of MOFs are the tunability of structural and chemical function, the well-developed specific surface area, high porosity, good structural integrity, and various physicochemical properties.[5, 6, 8, 219, 220] When MOFs are subjected to direct annealing in an oxygen atmosphere, the organic linkers decompose creating pores whereas metal ions oxidize to metal oxides.[218]

Zhang *et al*.[221] described a simple approach to synthesize Co_3O_4 polyhedrons and plates *via* the calcination of two metal formate frameworks (MFFs) with different morphologies. It was shown that the obtained Co_3O_4 samples not only inherited the original shapes of the as-prepared precursors but also were composed of many interconnected nanoparticles. In other studies, Zhao *et al*.[222] revealed

that Co_3O_4 nanostructures retained the rhombic dodecahedral morphology of the ZIF-63 template after thermal treatment at 350 °C for 2 h in air.

Wu *et al*.[223] synthesized porous CuO hollow architectures with octahedral shape by annealing Cu-based metal-organic framework ($[Cu_3(btc)_2]$, btc - benzene-1,3,5-tricarboxylate) templates. It was found that the morphology of the CuO products can be controlled by changing thermal treatment conditions of $[Cu_3(btc)_2]$. When the calcination process was performed at 300 °C, the octahedral shape of the MOF template was well preserved in CuO samples. Moreover, their surface was very rough and contained many holes demonstrating the formation of pores. During calcination at a temperature of 350 °C, some initial octahedra collapsed creating flower-like CuO structures whereas at 400 °C only agglomerates with non-regular shapes were obtained. In 2015, Song *et al*.[224] published a very interesting paper about a green strategy to fabricate CuO superstructures in which octahedral and six-prismatic Cu-MOFs prepared by the hydrothermal method were only immersed and stirred in NaOH solution without further thermal treatment. Novel 3D urchin-like and rod-like CuO superstructures consisted of nanoparticles, nanowires, and nanosheets (Fig. 16). The inner structure of MOFs strongly determined the morphology of hierarchical structures of the prepared CuO.

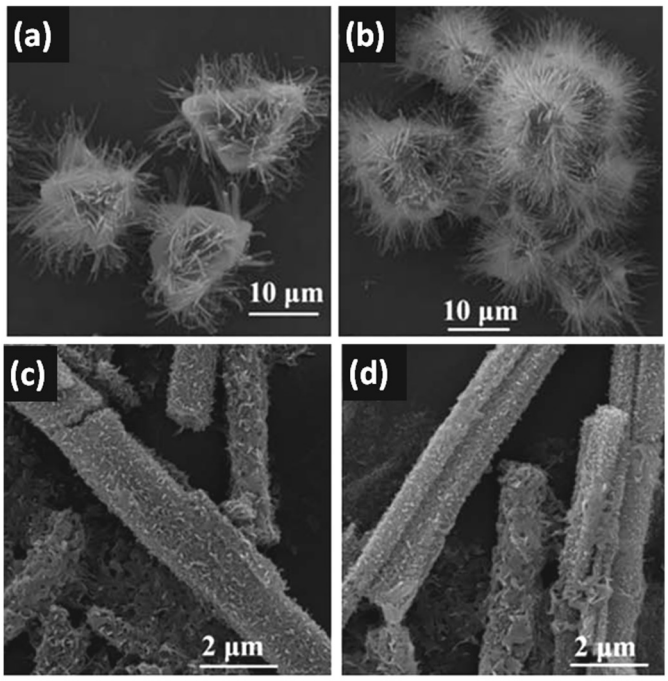

Fig. 16. SEM images of urchin-like CuO superstructures prepared by immersing octahedral Cu-MOFs in 0.1M NaOH at room temperature for **a)** 5 h or **b)** 12 h and SEM images of rod-like CuO superstructures obtained by immersing six-prismatic Cu-MOFs in 0.1M NaOH for **c)** 30 min or **d)** 5 h (Licensed under CC-BY.[224]).

Zhang *et al*.[225] prepared NiO nano/microstructures employing a facile solid-state thermolysis of Ni-based MOF precursor obtained *via* a solvothermal method from p-benzene-dicarboxylic acid (bdc) and $NiCl_2 \cdot 6H_2O$. Nickel oxide samples were composed of porous two-dimensional sheets formed from many uniform nanoparticles. It was observed that temperature and time of the thermolysis had significant impact on the structure and morphology of the products.

4. MO-to-MOF morphology control

Structural designability at the molecular length scale, feasibility of chemical functionalization and accessible high surface area of MOFs are the main reasons they are still intensively studied materials. The wide variety of components, *i.e.*, metallic cations and organic linkers, introduces immense possibilities of constructing new types of crystalline scaffolds with desired features. It allows applying MOFs in different fields, such as adsorption,[226-231] catalysis,[232, 233] separation[228, 234-237] or even chemical sensing[238-242] and drug delivery[243-250].

Although plenty of reports have described the preparation of MOF-derived materials with variety of composition and morphology, there are less syntheses that are focused on morphology control of MOFs exclusively.[251-256] It is difficult to predict in what kind of shape and size the MOF nanomaterial will be obtained, even if the topology of a single MOF unit is predicted, especially after one MOF topology can crystallize in various different structures.[257] In addition, the term `morphology control` is usually used in a misleading way when any homogeneous particles with definable forms are synthesized. In fact, `morphology control` should be used for well-thought out strategies, of which purpose precisely leads to beforehand selected shape and size of the product. It is extremely difficult to achieve this kind of control, especially for structures such as aesthetically captivating and extraordinarily complex. The starting point for `morphology control` is the deep understanding of the involved chemical reactions on a molecular level; only when one is able to gain control over the underlying chemistry it is also possible to really control and dictate the material's morphology. The construction of MOFs usually starts with the strategic selection of precursor materials: inorganic building units (IBUs), which are mostly formed *in situ* from a metal precursor, and organic building units (OBUs), which are commonly polytopic acids or imidazoles. To coordinate ligands to a metal centre and form the IBU, it is necessary to use substrates that provide easily accessible metallic cations. For that, the most common ion sources used are metal salts (*e.g.* nitrates, chlorides), as they easily dissolve in solvent. While this straightforward dissolution often favours MOF nucleation and growth, morphology is mainly dictated by the underlying MOF topology. Strategic pathways, such as top-down synthesis and controlled SBU approaches allow to control these topologies, however they fail to deliberately obtain complex 3-dimensional structures. In contrast, the MO precursor strategy might seem challenging due to low solubility of MOs caused by high lattice enthalpies, however, it has substantial advantages that metal salts cannot provide (Table 2).[257] Firstly, MOs can serve as substructures and templates for the final MOF, differently from metal salts, which dissolve far too easily due to the comparably high solubility. While aggressive reaction conditions facilitating MO dissolution bear similar initial reaction conditions, careful optimizations of the experimental conditions allow to preserve the MO morphology during the MO-to-MOF conversion. Thoroughly balancing of simultaneous MO dissolution and MOF formation enables to take advantage of the comparatively stable MO shape and morphology with it serving as self-sacrificial template. Furthermore, many available deposition and patterning techniques grant endless possibilities of diverse 3-dimensional MO structures, extending the variety of new MOF morphologies.

Table 2. Synthetic strategies from MO to MOF conversion.

Method	Advantages	Limitations	MOF	Ref.
Hydro-/Solvothermal	• Reproducible and easy to conduct • Substrates rarely require surface modification • Homogeneous and lacking in defect products • Microwave radiation shortens time of the reaction significantly	• Requires the precise maintenance of competing diffusion/nucleation rates to preserve product morphology • Often core-shell structures limit cation/ligand diffusion and further MOF growth	ZIF-8, ZIF-7, $Zn_4(Him)(Im)_8$, MOF-5, HKUST-1, MIL-100(Al), MIL-53(Al), MIL-110, V(OH)ndc, Mg-MOF-74	[267, 276, 279, 280, 283, 290-298, 306]
LAG (liquid-assisted grinding)	• Single-step procedure • Short reaction time • Usual by-product is only water • MOF morphology depends on the solvent • Reduced amount of solvent • Possible scale-up • Simple experimental set-up	• Dependable on the supply of mechanical energy • Generation of water coordinates products differing in morphology	$Zn(C_4H_2O_4)$, $Zn(C_4H_2O_4)\cdot nH_2O$, $Mg(H_2O)_4(sal)_2$, $Mg(H_2O)_6(ibu)_2$, $Bi(sal)_n$, $[Cd](INA)_2(OH_2)]\cdot H_2O$	[268, 308-310]
Solvent-free grinding	• Environmentally friendly • Single-step procedure • Usual by-product is only water • Simple experimental set-up	• Highly dependable on the energy supply (thermal and/or mechanical) • Long-time procedure • Generation water-coordinated products differing in morphology	ZIF-8, ZIF-67	[269, 270, 286-289]
Film processing (*e.g.* ALD, electrodeposition) and patterning techniques (*e.g.* CVD, PVD)	• Environmentally friendly (solvent-free) • Adjustable film thickness and density through synthesis parameters	• Thick films limit cation/ligand diffusion and further MOF growth • Expensive for large-scale production	ZIF-8, ZIF-61, ZIF-72, CuBDC	[260, 261, 271, 272, 277, 280]
***In situ* conversion/acid and alkali neutralization**	• Low-cost procedure • Adjustable MOF-crystals size through synthesis parameters • Well-defined and intergrown membranes • Simple experimental set-up	• Thick membranes limit cation/ligand diffusion and further MOF growth	ZIF-8, ZIF-71, HKUST-1, Mg_2(dobpdc), ZIF-67, Co-MOF-74	[273, 274, 284, 299, 303, 307, 311]

4.1. Mechanism

MO-to-MOF conversion rates are subjected to MO composition, morphology (shape and size), surface roughness and pH-dependent surface charge.[257-259] Tuning these MO features enables fabrication of materials with desirable MOF structures, without the need for surface functionalizations like self-assembled monolayers (SAMs).[260, 261] For example, it was found that the formation of $Cu_3(BTC)_2$ (known as HKUST-1) from CuO sheets is easily feasible, whereas no HKUST-1 was obtained when CuO microcrystals were used under the same conditions.[258] Moreover, choosing suitable solvent(s) in solution-based syntheses is as important for the final MOF morphology as selection of proper MO nanoparticle shape and size. This is exemplified for ZnO, with mixtures of octanol and 2-methylimidazole (2-mim or Hmim) not resulting in ZIF-8 formation, whilst ethanol addition amplified MO dissolution and allowed MOF growth.[262] To fully use the advantages of MOs, a good understanding of the reaction kinetics as a crucial variable of MO-to-MOF conversions is important. Hence, to enable targeted and controllable synthesis relations among competing rates are the key for which mechanism dominates: dissolution-crystallization or template-assisted transition, where the latter is instrumental for a controlled MO-to-MOF conversion (Fig. 17).

The rates that govern MO-to-MOF conversion are MO dissolution, metallic cations/ligands diffusion, MOF nucleation, and MOF growth. High MO dissolution rates paired with sufficient diffusion can result in random crystallization within the solution associated to local supersaturations (homogeneous nucleation).[259] In this case, particles grow in the solution without templating effect, working similarly to soluble salts but without accompanying acidic by-products. On the other hand, when the MO dissolution is balanced in a way, that MOF nucleation can occur locally around the substrate (heterogeneous nucleation) without too high diffusion rates, the MO can serve as a self-sacrificial template. This shape preserving mechanism can allow the full transformation of the MO substrate into MOF and hence the perpetuation of the original morphology. The progressive metallic cation-release as a result of the MO dissolution causes a concentration gradient of IBUs from the substrate to the solution, allowing the MOF to maintain on the MO and eventually to entirely replace it. However, to obtain full conversion, rates have to be matched perfectly and most often the result of MO-to-MOF reactions are core-shell-like structures explainable by diffusion limitations as a result of a closed MOF shell around the substrates before total transformation. Accordingly, to receive the entire conversion or a desired core-shell structure respectively, each reaction requires the understanding of the effect of the different reaction parameters on the system as well as the choice of a suitable MO morphology.

It is important to point out that the physicochemical properties of MOFs depend on their nanostructure, which is not observed for bulk-materials.[245, 263] Thus, designing the right route for MOF assembly is a matter of relevance for scaffolding features and application. Reaction conditions and their impact on kinetics vary dependent on the chosen method. Regardless, there is a general aspect for so-called structured-directing agents (SDA) including guest molecules, mineralizers, surfactants and swelling agents.[264] Whereas solvent-free reactions for MOF self-assembly are feasible, it is challenging to fabricate uniform and distinguished MOF nanomaterials that way. For most commonly used solvent-based syntheses main concern is a choice of solvent(s), solvent ratio, precursor concentration ratio and reaction times. All of these factors can be used effectively if the proper temperature during the processes is applied, as well as enhancements such as radiation, sonication or electric field.

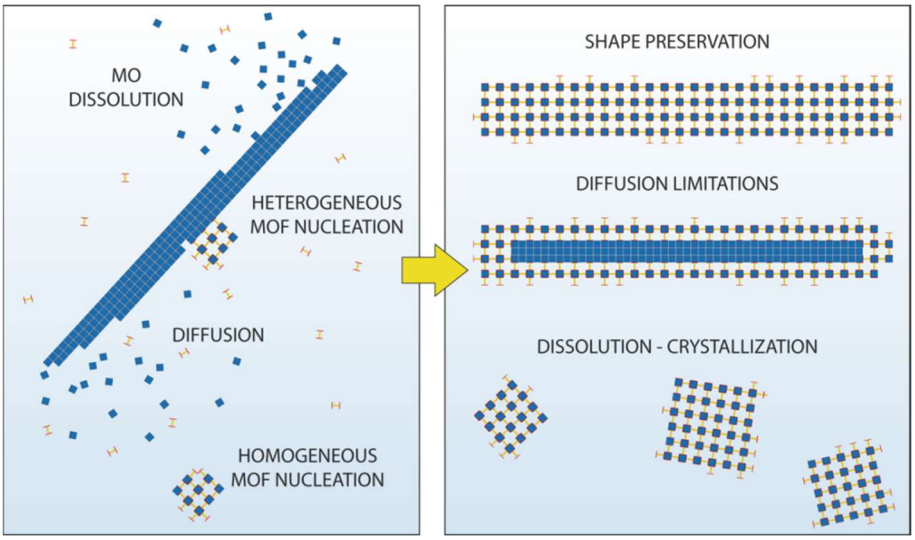

Fig. 17. Graphic representation of IBUs (blue) and OBUs (orange) during different competing rates: MO dissolution, diffusion, heterogeneous and homogeneous MOF nucleation; resulting in MO-to-MOF full conversion (shape preservation), core-shell structure (diffusion limitations) and diverse single-crystals (dissolution-crystallization).

Up to now only a couple of techniques have been proposed for MO-to-MOF preparation, in which MO took part precisely as a self-sacrificial template and metal source. It has to be differentiated from MO utilization for MOF assembly, where the role of MO is only being a non-self-sacrificial substructure for MOF assembly, *i.e.*, inactive MO is passively responsible for surface mounted MOF morphology. However metallic cations are not released from the solid minerals and they do not take part in MOF formation directly. A representative example of such procedure is the heterostructure of Fe_3O_4 covered with ZIF-8. Iron oxide precursor was injected in oil phase as a microreactor, with the metal oxide core being formed in a first step, on top of which in the next step a MOF shell was created, resulting in Fe_3O_4@ZIF-8 composite structures.[265] Another example is introduced by Zhao *et al.*[266] They coated different polymer fibers *via* atomic layer deposition (ALD) technique with a thin layer of Al_2O_3, ZnO, or TiO_2 for nucleation of high-quality HKUST-1 crystals uniformly on top of the fibers surface coatings. MOF was prepared in a solvothermal reaction in a solution of metal salt precursors and the respective organic linker, where MO was not used as a self-sacrificial layer. It was shown that the MOF crystal size depends on the coating used, increasing from ZnO over Al_2O_3 to TiO_2. This is explained through a difference in wettability, surface roughness, and isoelectric point of the different ALD coatings. The so achieved different 'MOF-PP/ALD'-fibers were then investigated for adsorption of hazardous gases like NH_3 or H_2S.

In the following we discuss reports that only used MO as a self-sacrificial template and metal source for the MOF formation.

4.2. ZnO as a metal precursor

One of the first successful MO-to-MOF conversion approaches was reported by Zou *et al.*[267] Zinc wafer was activated by H_2O_2 to form surface-hydroxide layers, on which MOF film was subsequently deposited by hydrothermal reaction. Although this approach was not a direct application of MO, however, it allowed avoiding the use of salt as a metal source and thus it eliminated the problems associated with acidic anions. In the end formation of $Zn_3(BTC)_2$ film exhibited spike-like uniformity

with large scale orders. In the same year Friščić *et al.*[268] used specifically MOs as precursors due to their low-cost and availability. In the single-step neutralisation of MOs with dicarboxylic acids MOF structure was formed, with water as a sole by-product. Their approach based on ZnO and fumaric acid in a liquid-assisted grinding (LAG) reaction led to the formation of the materials varied in morphology by using different grinding liquids *i.e.* ethanol (3D MOF), mixture of ethanol and water with molar ratio 1:1 (2D MOF) and various amount of water (1D zigzag or linear polymers). Interestingly, Lin *et al.*[269] presented formation of ZIF-8 (in their article described as MAF-4) by solvent-free grinding of ZnO or $Zn(OH)_2$. At room temperature substrates did not react, however, after heating at 100 °C for 24 h ZIF-8 was obtained. It was possible to shorten the reaction time to 12 h by heating up the mixture to 180 °C. Powder X-ray diffraction indicated that increasing temperature resulted in sharper and weaker reflexes, which are typical for the guest-free ZIF-8 structure. This method allowed fabrication of high purity ZIF with 100% yield, specific surface area of 1450 $m^2 g^{-1}$ and with relatively homogenous sub-micrometer crystals. In further reports MOFs with higher surface area such as $Zn(mim)_2$ (1961 $m^2 g^{-1}$) and new $Co(mim)_2$ (2070 $m^2 g^{-1}$) were also prepared.[270] Zn and Co imidazoles were obtained in direct acid-base reaction between $ZnO/CoO/Co(OH)_2$. Synthesized ZIF network topologies revealed dependency on the presence of small amounts of co-solvents such as 1-butanol, pyridine or 4-methylpyridine, as well as on the heating rate. Addition of a third species can lower the topological density leading to open-framework compounds. In the case of temperature, the increase enhances ligands deprotonation, which directly leads to homoleptic complexes formation. Heating rate, however, if kept slow provides higher crystallinity of Zn- and Co-derived MOFs, as well as larger size of crystallites.

Stassen *et al.*[260] also focused on ZnO with the aim of the transformation of the resulting two- and three-dimensional MO patterns to ZIF-8 pattern by a convenient two-step procedure *via* sputtering or electrochemical growth, respectively. It was conducted through green solvent-free reaction of ZnO precursor films and patterns with melted organic linker (Hmim). Variation of film thickness and density allowed the control of the ZIF-8 crystal size due to the change of Zn^{2+} supply. In a follow up work uniform ZnO thin films of precisely controlled thickness were deposited using ALD technology, both on a flat substrate and high-aspect-ratio features, which then have been transformed into ZIF-8 using chemical vapour deposition (CVD), providing the linker as a vapour instead of a solution.[271] Different from CVD method, solvothermal transformations need precise matching of MO dissolution and MOF crystallization rates, as slight local differences in dissolution rate, coupled with fast diffusion of the released metal ions can lead to the formation of rough films with many defects. Cross-sectional analysis *via* TEM allowed the study of the MO-to-MOF conversion efficiency: complete transformation could be observed for precursor films of less than 10 nm thickness. Thicker films do not show full transformation because of the diffusion limitations of the organic linker to the oxide and/or of zinc to the growing crystal interface. However, the expansion of around 10 nm film thickness is expected due to the fabrication of highly porous ZIF-8 from the dense ZnO. The thickness increase indicated linkage accordingly to the theoretical value based on the ratio of the crystallographic volume occupied per mol of zinc in MO and MOF.

To show the general applicability of the MOF-CVD approach, ZIF-61 (imidazole) and ZIF-72 (4,5-dichloroimidazole), the Co-based ZIF-67 (using CoO films and Hmim) were deposited under similar experimental conditions, as well as Cu(II)-dicarboxylates using copper hydroxide films as precursor film and fumaric acid and 1,4-H_2BDC as organic linker.[272] A different approach for obtaining ZIF-8 membranes was suggested by Li *et al.*[273] from $Zn(OH)_2$ nanostrands. It is liquid-based synthesis in

which hydroxide and Hmim are left in ethanol and water solution (1:4 by volume) at room temperature for 24 h. To achieve well-defined and intergrown morphology sodium formate was added. It resulted in uniform layer of rhombic ZIF crystals. Increasing alcohol volume in water: ethanol ratio led to smaller and looser packed ZIF-8 crystals. However, using mainly water as a solvent caused formation of more free-standing crystals in the solution, instead on the surface.[274, 275] Out of 900 nm thick precursors 800 nm of ZIF-8 was formed. In the case of the membrane syntheses often diffusion limitation occurs, thus reaction continues to the point of achieving compact structures, which will impede metallic cations and organic linker diffusion.

Zhan *et al.*[276] used ZnO rods to build semiconductor@MOF core-shell heterostructures *via* a self-template synthetic strategy in a solvothermal reaction, whereby the MO templates themselves provided metal ions initiating ZIF-8 growth without the requirement of any surface modifications. The growth process of the ZIF-shell involved firstly growth of ZIF-8 nanoparticles on the MO's surface, which then formed a continuous layer during prolonged reaction time. Similar to Stassen *et al.*[271] a saturation of ZIF-8 growth due to diffusion limitations could be observed. The ZIF-8 shell was found to be very compact without any pinholes and no free-standing ZIF-8 nanoparticles were found at any reaction time under optimized reaction conditions. Changing of the reaction temperature and solvent composition led to huge variations in the quality of the MOF-shell and amount of free-standing ZIF-8 nanoparticles, as the balance between dissolution and coordination rate was disturbed. It has to be noted that, a solvent mixture of DMF and water is crucial because Hmim works both as an etching agent to dissolve ZnO providing Zn^{2+} ions and as a ligand for the ZIF-8 formation. In pure DMF the etching ability of the ligand is too weakened no ZIF-8 formation occurs. Whereas in pure water the dissolution rate dominates, and thus free-standing nanoparticles of dense MOF are the dominant species.

Khaletskaya *et al.*[255] used ALD and magnetron sputtering for localized deposition of MO thin films, which then were converted into thin MOF membranes. The resulting thin films were analysed in cross-sectional view (prepared by focused ion beam [FIB] milling) using TEM, scanning transmission electron microscopy-electron energy loss spectroscopy (STEM-EELS) and energy-dispersive X-ray elemental mapping (STEM-EDX). The film fabrication approach was then extended to amorphous Al_2O_3 layers pre-deposited by ALD, which were converted into a dense homogeneous $[Al(OH)(1,4\text{-ndc})]_n$ film.[255] ZnO particles (as well as functionalized ZnO particles) can be also used as heterogeneous nucleation agents for the rapid growth of a number of different MOFs, such as MOF-5 (terephthalic acid), IRMOF-3 (2-aminoterephthalic acid), IRMOF-8 (2,6-naphthalenedicarboxylic acid) and IFMOF-10 (4,4'-biphenyl dicarboxylic acid) (Fig. 18). In a solution of dissolved metal salt and organic linker, variation of ZnO particle size (micro- and nanoparticles) were immersed leading to different MOF types.[271]

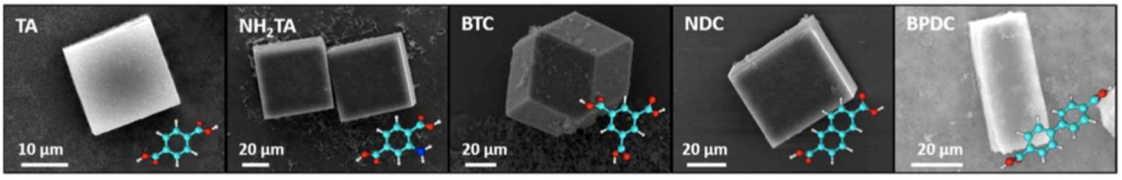

Fig. 18. SEM images of the MOFs prepared with different ligands for 1 h at 95 °C. In the insets: the corresponding ligand structure. From left to right: MOF-5, IRMOF-3, MOF-4, IRMOF-8, and IRMOF-10 (Reprinted with permission.[271] Copyright 2014, American Chemical Society).

It was shown that the use of nano-sized nucleation agents allowed to decrease nucleation time, as well as the temperature required for the MOF synthesis.[277] Further, it was demonstrated that the ZnO seeds-induced rapid MOF formation is not simply driven by an increase in the pH (which facilitates ligand deprotonation) of the bulk reaction solution. When in fact, increasing the number of seeds resulted in faster nucleation, an increased number of MOF crystals but decreased the crystal size were observed. Using paper support and immersing one side in a solution of ZnO nanoparticles and the other side in a solution of dissolved MOF precursors paired with a lateral flow of the solutions induced by capillary forces, led to MOF nucleation at the contact interface. Further, ZnO seeds were used to precisely control the position of MOF crystal formation within microchannels (Fig. 19).

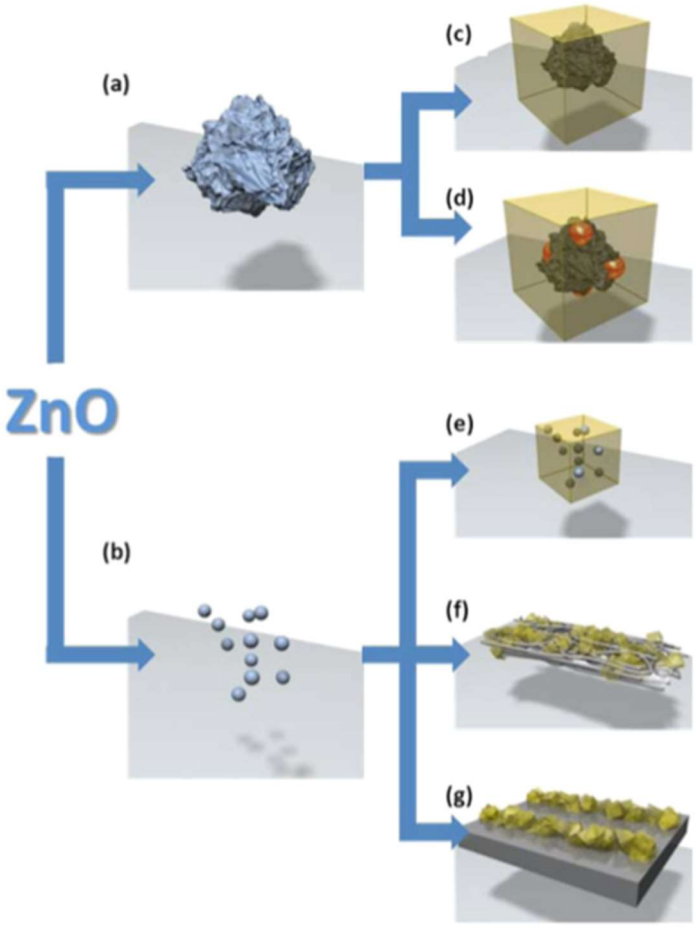

Fig. 19. Outline of the heterogeneous nucleation of MOFs by pure and functionalized ZnO microparticles **a, c, d)** and nanoparticles **b, e, f, g)** demonstrated in this work. ZnO nanoparticles can also be used to induce the growth of MOF crystals on paper and within microfluidic channels as shown in **f)** and **g)**, respectively (Reprinted with permission.[277] Copyright 2014, American Chemical Society).

Meckler *et al.*[278] used the ZnO-to-ZIF conversion to fabricate a layered composite of sub-micron-thick ZIF-7 and ZIF-8 films on polymers of intrinsic microporosity (PIMs). It was found that parameters like temperature, ligand concentration and reaction time failed to give control over film growth and quality, however, changes in solvent composition enabled significant control. Reaction

mixtures of DMF-to-water with up to 50 vol % water yielded relatively smooth and continuous ZIF-8 films, suggesting the formation of many ZIF-8 nuclei and comparatively slow crystal growth. At water content beyond 50 vol %, significantly less ZnO was visible in cross-sectional SEM images and the ZIF-8 grain size increased, resulting in faceted, isolated crystals adhered to the polymer surface instead of a continuous film. Uninterrupted, nearly pure ZIF-8 coatings could be obtained from 15 nm thick ZnO films with 50 vol % water reaction mixtures. Variant preparation of substructure for ZIF-8 was suggested by Al-Kutubi *et al.*[279] They synthesized ZIF-8 thin films on top of an electrochemically grown ZnO rod array. They were fabricated through the deposition of the linker on top of the rod array, with subsequent solvent evaporation to form a thin uniform linker film. Heating the sample in an oven resulted in the formation of a ZIF-8 film on the ZnO arrays. Liu *et al.*[280] prepared a ZIF-8-ZnAl-NO_3 layered double hydroxide (LDH) composite membrane by partial conversion of the ZnAl-NO_3 LDH membrane in a one-step reaction for enhanced H_2/CH_4 separation. Zhang and coworkers[281] converted ZnO to ZIF-8 as precursors/sacrificial template to construct Zn-based nanoarchitecture electrode materials for high energy storage lithium-ion batteries. ZIF-8 was thereby transformed into amorphous carbon framework and ZnO quantum dots in a thermal decomposition process. Del Rio *et al.*[282] used a sacrificial ZnO coating which is transformed into ZIF-8 to create polystyrene–ZnO–ZIF-8 core–double-shell particles with an intermediate shell of residual ZnO. Increasing reaction time and temperature did not show any influence on ZnO conversion into ZIF-8, suggests interrupted growth due to the diffusion limitations after a certain point. Maserati and coworkers[252] studied the formation of M-MOF-74 series (M_2(dobpdc), M = Mg, Mn, Co, Ni, Zn) using different bivalent MOs as precursors in a solvothermal reaction, following a dissolution-crystallization mechanism, with the MO dissolution being the rate-limiting factor.[258] The use of MOs as precursors allowed them to reduce reaction times by several orders of magnitude, achieving MOF formation in a matter of minutes.

Sun *et al.*[283] reported the formation of Zn-derived MOF shells: ZIF-8 and ZIF-71 on ZnO particles as cores, reacting with Hmim and 4,5-dichloroimidazole, respectively. To prevent aggregation of minerals their surfaces were modified with PVP, which additionally promoted retention of the released metallic cations near the template. Three types of colloidal ZnO particles with different size were fabricated: 95 nm, 230 nm and 320 nm. Synthesized MOF product from 95 nm ZnO showed rhombic-dodecahedral shape with 270 nm diameter. TEM and TGA revealed that ZnO remains inside the structure, with 12.8 wt.% of non-converted oxide. It was caused by the small pore apertures present in ZIF, resulting in before mentioned Zn^{2+} diffusion limitations. The sizes of ZnO@ZIF core-shell particles were dependent on the template size, diffusion and nucleation/growth rates, which mainly were influenced by the ratio of water/DMF. Water enhances ZnO dissolution, whereas DMF reduces it. Both, however, if used separately cause heterogeneous nucleation of MOF nanoislands on the mineral core. Solvent effect was investigated manifesting hybrid core-shell particles in aqueous solution. Changing the thickness of ZIF-8 shell was possible with DMF addition. Treatment of reactants with DMF only led to fabrication of partially enshrouded structures, with one or several MOF domains on the mineral template. Furthermore, limited Zn^{2+} diffusion slower than nucleation and growth ended up in surrounding the core with thin ZIF layer and thereby further thickening of the shell was terminated. Size-dependent ZIF formation is linked to the nucleation energy-requirements. It was suggested that lower energy is needed for the growth of ZIF-8 on the oxide surface, than its nucleation. Thus smaller ZnO particles form fewer nucleation sites, ending up with more homogeneous shells. In consequence, if ZnO precursor particle is larger, longer distances have to be overcome between nucleated MOF crystallites and Zn^{2+} from MOF-free sites. Therefore, it is

preferable to form more nuclei on the larger core, leading to intergrown crystal domains. Successful approach of combining MOF from MO with different type of material was introduced by Mazal *et al.*[284] They hybridized MOF-5 and HKUST-1 with polyHIPE by using ZnO and CuO as precursors, respectively. MO nanoparticles embedded into polymer walls formed nanocomposite, which was subjected to organic ligand solution in the solvothermal conditions. TGA and XRD measurements confirmed nearly entire MO-to-MOF conversion into cubic MOF-5 and octahedral HKUST-1. Applying porous polymer without acidic anions stabilized final materials, by avoiding direct exposure of formed MOF crystals to monomeric solution.

There are several proposals of a mechanochemical top-down approach for ZIF-8 synthesis from ZnO grinding with Hmim. Reduction or total solvent absence unlocked novel prospects for prominent composites with MOF. Yue *et al.*[285] synthesized both ZIF-8 nanoparticles and ZIF-8 thin films from the corresponding ZnO nanoscopic precursors through solid-state reactions without the involvement of conventional dissolution processes. According to the authors, this transformation process can be understood as an anion-exchange process, involving the displacement of the lattice oxide anions with imidazolate anions. The dependence of the phase purity on the molar ratios of Hmim to ZnO was shown, *e.g.* producing phase pure ZIF-8 nanoparticles using a molar ratio of 5:2 (Hmim to ZnO).[286] Building upon this work, Yue *et al.*[287] prepared a multi-walled carbon nanotube/zeolitic ZIF-8 composite by a template free 'brick and mortar' method: ZnO nanoparticles were adsorbed onto the surface of the tubes and then reacted with the organic linker. Strong interactions between linker and the carbon surfaces led to the nucleation and the growth of the ZIF-8 crystal solely on the tube's surface. ZnO precursor nanoparticles with an average size of 35 nm and no ZnO signal was observed in XRD measurements after the reaction. Involving new materials in milling during MO-to-MOF transition was suggested by Li *et al.*[288] in 2019. They introduced mechanochemistry-assisted solvent-free synthesis involving incorporation of Pd nanoparticles into the MOF structure for catalycic purposes. Using MO/hydroxide without solvents presence is highly preferable for bulk-synthetic industrial routes. Although it seems efficient it is often difficult to synthesize distinguished in morphology MOF nanomaterials *via* top-down strategies.

4.3. Al_2O_3 as a metal precursor

Besides ZnO another often applied MO for MOF as a substructure and a source of metallic cations is alumina (Al_2O_3). Reboul *et al.*[289] used Al_2O_3 in the form of a two-dimensional honeycomb pattern and a three-dimensional inverse opal structure as a metal reservoir and mesoscale SDA for construction of a mesoscopic MOF architecture (namely, coordination replication). $[Al(OH)(1,4\text{-ndc})]_n$ was formed in a microwave-assisted reaction in an aqueous solution of the organic linker; MIL-100(Al) in a solution of H_3BTC; MIL-53(Al) in a solution of H_2BDC. In 2013 Mao *et al.*[290] presented synthesis of oriented three-dimensional MIL-110 rod arrays on porous anodic aluminum oxide membrane (AAO) in the company of the hetero-metal hydroxide strands, which in this case were made of $Cu(OH)_2$. Hexagonal column structure of the MOF was maintained when $Cu(OH)_2$ strand layer was utilized; the absence of such layer led to sheet-like products only. Inductive coupled plasma emission spectrometry (ICP-AES) indicated remaining copper ions in solution after the procedure, thus in the end pure MIL-110 was formed. Also $Cd(OH)_2$ and $Zn(OH)_2$ were tested as SDAs with the successful outcome. Nevertheless, the density of the MIL-110 rods arrays was highly dependent on the kinds of metal hydroxides used. Most dense were rods after $Cu(OH)_2$ application, less after $Cd(OH)_2$ and the least after $Zn(OH)_2$. Another morphology impactful parameter was the time of the reaction.

Proceeding synthesis for 3 h led to irregular particle layers with Cu. Continuing reaction to thereabouts 6-9 h resulted in dissolving copper-related structures, whilst thick and straight MIL-110 fibers with shrubbery-like morphology were obtained. After 24 h well-oriented rod arrays of the MOF were formed. Selecting a proper solvent was equally important for the material shape and size. For example, using octanol led to sheet-like Cu-BTC belts formation, whereas mixture of DMF and ethanol ended up in occurring small, loosely packed HKUST-1 crystals. Thus, it was concluded that using only water promoted MIL-110 nucleation and further kept material stable without formation of different MOFs impurities, inspite of the presence of other cations than Al^{3+} (*e.g.* Cu^{2+}).[291]

Nahakama *et al.*[292] introduced alumina as a metal source and SDA for fibrous macroscopic architectures of Al(OH)(L), where L is 1,4-naphthalene dicarboxylate (ndc) or 1,4-benzene dicarboxylate (bdc). The synthesis was performed in aqueous solution at 180 °C and for only 1 min because of the acceleration effect of microwave irradiation. Morphology control was conducted by changing the pH of the mixture. Low pH 2.1 highly increased dissolution of the mineral, resulting in small fragmented MOF fibers. At pH 4.0, needle-like „rose thorns" crystals were formed. Slightly higher pH 4.3 led to needles thickening to fibers morphology, whereas rectangular crystals of fibers occurred at pH 5.4. Fabricated Al-derived MOF structures were thicker than Al_2O_3 template due to the lower density and thus bigger volume. Furthermore, the structural deformation phenomenon was noticed when the reaction was continued for 72 h at 400 °C. Block-type crystals of Al(OH)(bdc) transformed from closed-form to open-form, which usually is observed for bulk crystals only.[293]

Bechelany *et al.*[294] made use of the so-called 'reactive seeding' approach, by converting a metal oxide thin film (ZnO/Al_2O_3, deposited uniformly on polymer fibers using ALD) to MOF by solvothermal reaction (using both conventional and microwave-assisted heating) with a simple solution of the organic linker with different concentrations. ZnO coatings were converted into ZIF-8 in a methanolic solution of Hmim with conversion rates of up to 86% for microwave-assisted heated and up to 96% using conventional heating; Al_2O_3 coatings were converted into MIL-53-NH_2 in an aqueous solution of 2-aminoterephthalic acid with conversion rates of up to 66% for microwave-assisted heated and up to 94% using conventional heating. Microwave-assisted reactions did not exhibit influence on crystal morphology or MO conversion regardless of Hmim concentration or the reaction time. Slight influence occurred when different 2-aminoterephthalic acid concentrations were used. Reactions using conventional heating led to non-uniform crystal growth and fibre coverage and showed a high dependency on both, linker concentration and reaction time, which resulted in the increased crystal size and conversion rate.

Li *et al.*[295] utilized three different aluminium compounds, Al_2O_3, $Al(OH)_3$ and boehmite, as stable metal sources for MIL-53(Al) formation *via* hydrothermal synthesis. In comparison to the traditional synthesis with aluminium salt, mineral sources proved sufficiency with higher yields, even if the molar ratio of metal source/organic linkers was lower. Additionally, very common pH decrease caused by protons release from H_2BDC ligands and acidic anions from salt was eschewed. Furthermore, pH remained constant or even slightly basic due to the acid-based neutralization. Each substructure varied in shape and size, thus MOFs morphology was different. After the synthesis, ball-like $Al(OH)_3$ cluster with a size above 100 μm transformed into MIL-53(Al) of which size was less than 5 μm. A lamellar sheet of boehmite was converted to rod-like MOF. At the early stage of conversion, Al_2O_3 blocks were covered with MOF structure, but after 72 h when source material depleted, only crystal rods of MIL-53(Al) were noticeable in SEM images. Interestingly alumina-derived MOF

indicated the highest specific surface area compared to the other substructures. Thus, it could be potentially a better candidate for industrial synthesis when porosity and yield are considered.

4.4. Cu-based sources

An unconventional proposition of preparation of most known copper based MOF, HKUST-1, was presented by Guo *et al.*[296] They prepared an HKUST-1 membrane out of Cu nets (thread diameter and void in size were both 20 µm). The primarily metallic net was crystallized from $Cu(NO_3)_2$, and then oxidized to CuO before hydrothermal synthesis. It was found that the use of CuO was crucial for the continuous Cu^{2+} dissociation and homogeneous HKUST-1 crystallization. SEM image indicated arranging of a defect-free structure of octahedral crystals (5-10 µm) on the net, which formed a 60 µm thick membrane. It led to the conclusion that a transfer of MO-to-MOF preserving morphology is also possible in the case of copper-derivatives.[296, 297] Majano and Pérerez-Ramírez[298] synthesized HKUST-1 through a room temperature procedure in 5 min. Conversion rate of the hydroxide after such short period of time was 82%, whereas full conversion took place after 5 h. Both MOF crystal size and growth were dependent on the initial $Cu(OH)_2$ crystallite size (800 nm-1 µm) for both reaction times. However, morphology changed completely from layered elongated $Cu(OH)_2$ crystals to the MOF octahedrons. It is worth mentioning that the whole procedure was carried out in aqueous-ethanolic solution, without DMF which impedes crystallization kinetics. Okada *et al.*[299] presented HKUST-1 synthesis from $Cu(OH)_2$ tubes. The high rate of the above-mentioned processes aggravates control of $Cu_3(BTC)_2$ size. After 1 s MOF with <200 nm average dimension was formed. At 25 s first octahedral crystals appeared. After 1 min hydroxide tubes became shorter and $Cu_3(BTC)_2$ crystals became larger in size with a rougher surface. At 300 s crystals with 200-400 nm diameter were detectable which kept growing for a total of 1200 s (Fig. 20). After that no changes were observed.

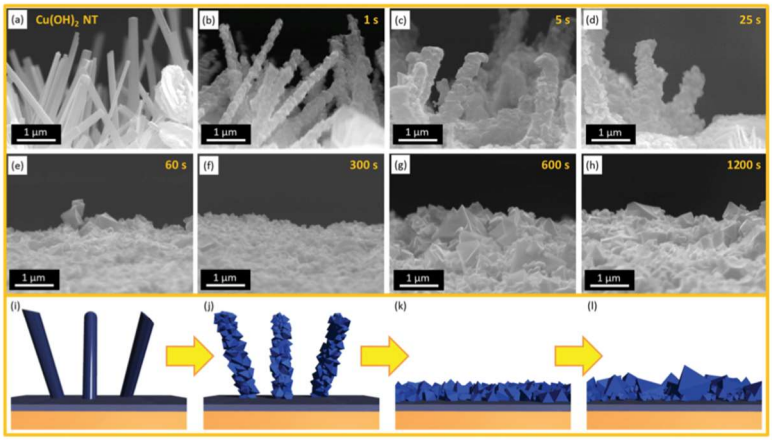

Fig. 20. Evolution of the $Cu(OH)_2$ nanotubes from the original shape was investigated using SEM. **a)** The substrate decorated with $Cu(OH)_2$ nanotubes, once immersed in a 1,3,5-benzenetricarboxylic acid and alcoholic mixture, shows rapid conversion into a crystalline material. **b)** The change can be detected within 1s. **c-h)** Further evolution leading towards the formation of a flat layer of MOF crystals. **i-l)** Schematic representing the key steps in the morphological change during the $Cu_3(BTC)_2$ crystal formation using $Cu(OH)_2$ nanotubes. **i, j)** Change dominated by the pseudomorphic replication. **j-k)** Crystal growth without the conservation of the initial tubular shape. **k, l)** Change dominated by the Ostwald ripening mechanism (Reprinted with permission.[299] Copyright 2014, John Wiley & Sons).

Another preparation of well-established size of $Cu_3(BTC)_2$ was presented by Takahashi's group. MOF crystals were prepared by conversion of $Cu(OH)_2$ belts previously coated on a gold electrode.[300] The ratio of ethanol: water has high impact on $Cu_3(BTC)_2$ crystals size due to co-solvent polarity (dielectric constant), which affects ligand deprotonation. Higher hydroxide conversion of MOF and larger octahedral crystals from several hundred to over than 3 μm were obtained in 2:5 ratio (ethanol: water). In more ethanolic mixture (5:2 ethanol: water) smaller crystals were formed. This observation implies that crystallization is dominated specifically by Ostwald ripening. More polar solvents like water (dielectric constant - 80.1) increase acidity of a mixture due to the enhanced proton release from organic linkers. Less polar ethanol (dielectric constant - 24.5) limits deprotonation, which further leads to decrease in $Cu(OH)_2$ dissolution rate and thus shorter diameter of $Cu_3(BTC)_2$.

In 2017 Falcaro *et al.*[301] prepared centimetre-scale, aligned two- and three-dimensional MOF films directly from a $Cu(OH)_2$ substrate. Following a heteroepitaxial growth mechanism, the synthesis was facilitated by precise matching of the structure metrics of the organic linker and the lattice parameters of the metal hydroxide substrate. MOF crystals being oriented in one direction, the out-of-plane one, have been previously synthesized using liquid phase epitaxy, however, MOF crystals being orientated in all three directions have not been demonstrated. Orientation along all three crystallographic axes could be achieved by conversion of a crystalline metal hydroxide surface.

Zhang and Zeng[302] proposed applying Cu_2O as a metal source for HKUST-1 formation in a solution based synthesis with co-solvents of DMF/ethanol, which indicated nanoscale „domain growth" mechanism. After MO dissolution the starting solution became heterogeneous in metallic cations, however, the presence of oxygen in the medium allowed converting oxidation state of Cu^{I} to Cu^{II} *via* the following reaction: $2Cu_2O + O_2 + 8H^+ \rightarrow 4Cu^{2+} + 4H_2O$. Oxidized copper ions were able to react with organic linker to form crystallites, which in time aggregated, producing larger MOF domains. Using Cu_2O cubes with uniform size and shape (average edge size of 60 nm) led to the formation of 3D networks of nanocrystal MOF domains (~20 nm). It was stated that for successful MO conversion into MOF networks it is necessary to provide a specific concentration of PVP (*e.g.* 0.48 g/L) as a structure-directing agent. Also the polar co-solvents affected organic ligand dissociation and oxidative dissolution of ions from mineral. Under the optimized reaction temperature and time, it was possible to generate HKUST-1 with hierarchical porosity. Further investigation on the shape and size control demonstrated that ratios of metal oxide/organic linker and solvent/co-solvent are crucial for crystallization process and thus morphology of the final product. It was found that the required ratio of Cu_2O/H_3BTC and water/ethanol for fibers was 1:76 and 1:0.43 respectively; for rod-like crystals was 1:38 and 1:1.2 respectively. Further decrease of organic ligand amount to 1:19 ratio led to the growth of thin nanosheets with a rectangular shape.[303]

4.5. Other MOs as metal reservoirs

Concept of MO-derived MOFs was further investigated for only several oxides such as V_2O_5, MgO, MnO, Bi_2O_3, CoO, NiO, and CdO. Vanadium PCPs, due to their porosity and electronic properties, can be applied in separation, sensing, and catalysis. First approach of vanadium based polycrystalline macrostructures $[V(OH)ndc]_n$ fabricated from V_2O_5 was introduced by Reboul and coworkers.[304] PCPs were obtained in short 10 min microwave treatment from a water solution of V_2O_5 and naphthalene dicarboxylic acid (H_2ndc), in the presence of ascorbic acid as a reductant. Ascorbic acid not only changed the oxidation state of vanadium from V^{V} to V^{III}, but also improved the solubility of the

mineral.[259] Combination of applied radiation and mineral precursor ended up in covering the entire surface of oxide with nuclei. V_2O_5-derived MOFs showed rod-like shape and had smaller and more uniform particle size than VCl_3-derived ones.

Wang *et al.*[305] presented a new synthetic strategy for Mg-MOF-74 films from MgO using solvothermal conditions. Magnesium nitrate salts were *in situ* produced during synthesis, notwithstanding MgO was used as a seeding agent hooked onto Al_2O_3 substructure. MgO released Mg^{2+} ions, and promoted both nucleation and growth of MOF thin films. The resulting MOF membranes demonstrated no defects in their structure, despite the presence of nitrate ions. The effect of the amount of the mineral precursor on the morphology of MOF was investigated by Maserati and his group in 2017.[306] With different ratio of MgO to H_4dobpdc [4,4'-dihydroxy-(1,1'-biphenyl)-3,3'-dicarboxylic acid] they presented two synthetic routes for nanocrystals (16:1) or microcrystals (2:1). In the case of not fully converted MgO to MOF, acetic acid was used as a mild etchant to separate product from MO. The final morphology of the two products was rod-like. These rods revealed an average cross-section crystallite size of ~12 nm, and a greater surface area than bulk structures. Another interesting approach used seemingly mechanochemically inert MgO in one step LAG method. Grinding MO with carboxylic acid drug derivatives, such as ibuprofen or salicylic acid in the presence of water led to complex self-assemblies process. It involved coordination to water molecules with subsequent acid-base neutralisation and molecular inclusion. In 2010 Chow *et al.*[307] synthesized a series of diverse MOF networks *via* the same method by varying the amount of water coordinated to the Mg^{2+} centre. Similarly to previous structures bismuth subsalicylate MOF was synthesized by using ion- and liquid-assisted grinding (ILAG). The environmentally friendly method using Bi_2O_3 as a metal source and coordinating drugs allowed preparation of novel metallodrugs. The volume of solvent had a high impact on the final network, thus hydrated 2D crystal structure varied dependently on the water coordinates.[308] To reduce the amount of water coordinates and to avoid temperature treatment it is feasible to conduct LAG procedure also in non-aqueous solution *e.g.* in DMF. Such example was obtained by Wang and coworkers for CdO-derived MOF.[309] Milling CdO with isonicotinic acid (HINA) led to the formation of interpenetrated diamondoid network of $[Cd(INA)_2(OH_2)]\cdot DMF$. MO-to-MOF conversion efficiency in this case is very small leaving loads of unreacted CdO.

Three-dimensional and mesoporous ZIF-67, Co-MOF-74 and Ni-MOF-74 hybrid arrays were successfully synthesized by Cai *et al.*,[310] by using self-sacrificial CoO and NiO arrays on Ni foam with Hmim and 2,5-dihydroxyterephthalic acid as the organic linkers. Firstly MO precursor on Ni foam was prepared. Next, it was placed in the mixture of water, ethanol and DMF with 2,5-dihydroxyterephtalic acid as linker. Poor solubility of MOs at times can be still `too fast`, thus for shape-preservation procedure it needs to be lowered. In this case using only water led to too fast dissociation and nucleation in the solution, whereas for morphology control epitaxial growth is required. Hence, the addition of ethanol slowed reaction down and enabled well-defined MOF formation, meaning slow rate of dissolution was important for morphology control for this material. ZIF-67 morphology was directed by changing the pristine shape of the mineral, *e.g.* applying CoO wires led to rods formation, whereas CoO walls formed CoO@ZIF-67 walls. Presented growth mechanism revealed the phenomenon of shell thickening in spite of complete core surrounding. After 12 h of reaction, the size of CoO core/ZIF-67 shell changed from 100/40 nm to 53/180 nm. Continuation of the reaction led to core corrosion, but it did not stop further ZIF-shell formation. It means that organic linkers were able to deprotonate themselves and enhances CoO dissolution, on

top of that they could easily penetrate ZIF pores and add up to its structure. Interestingly, replacing CoO with Co_3O_4 did not lead to formation of ZIF-67 on the oxide Co_3O_4.[311]

The solution-mediated techniques are rather expensive and environmentally unfriendly. These problems prompted Friščić *et al.*[311, 312] to develop an „accelerated ageing method", which imitates geological biomineralization (mineral weathering/mineral neogenesis). MOF materials are generated from the exposure of minerals (*e.g.* MgO, MnO, NiO, CoO, CuO, PbO) to organic molecules (oxalate ligands) without solvent. Motillo *et al.*[307] also introduced „accelerated aging" for ZIF-67 and ZIF-8 preparation.[313, 314] This technique enabled forming ZIFs from CoO and ZnO, however it took many days (up to 11 days in some cases) to gain any hybrid structure. Additionally, beside linkers (Hmim or HEtim) salts additives are needed, such as $(NH_4)_2SO_4$, $KHSO_4$, $(H_2Im)_2SO_4 \cdot H_2O$, (Hcaf)(HSO_4), (Hcaf)$(HSO_4)\cdot H_2O$ or $(H_2BIm)_2(SO_4)$, which for the morphology control purposes can be unreasonable, if once stated acidic by-products might occur or no well-defined shape and size of the final material is fabricated.

5. Controlling morphology of metal-organic frameworks-derived carbon

Since the pioneering work by Xu and coworkers[315] in 2008, MOF-derived carbon (MDC) has been of particular research interest for the past decade.[14, 316-321] The characteristic features of MOFs, such as high surface area, designable uniform pore size and structures, highly ordered and chemically homogeneous structures,[6, 322] are partially transferred to derived carbons, so that MDCs can have tailored physicochemical properties which are difficult to be realized by other porous carbons. MOFs are now considered as "all-in-one" templates/precursors that contain both inorganic and organic constituents which can be pre-selected for preparation of targeted carbon materials.[323] Inorganic metal species function as sacrificial porogens, catalysts for *in situ* graphitization, and active components that are useful for energy storage and heterogeneous catalysis.[324-326] Organic ligands serve as mainly carbon and heteroatom sources, as well as pore forming agents. They decompose to gaseous products and/or cross-link to form porous (heteroatom-doped) amorphous carbon. *In situ* generated gas outflux can sometimes create additional mesopores and even macropores.[327-329] The well-defined periodic arrangement of metal nodes and organic motifs in MOF often leads to a homogeneous distribution of metal or metal oxide nanoparticles in carbon matrix.[320, 330] This feature even allows preparation of single atomic metal catalysts and metal-N-C active sites throughout the whole structures, which is useful for various applications.[331]

MOFs can be further functionalized, either by guest incorporation into the porous MOF hosts or post-synthetic modification of MOFs, to achieve improved MDC material performance.[332] For instance, secondary carbon sources (furfuryl alcohol, glucose, phenolic resins) and heteroatom sources (dicyanamide for nitrogen, glyphosine and triarylphosphine for phosphorus, and dimethyl sulfoxide for sulfur) can significantly improve the textural- and electronic-properties of MDCs, respectively.[319] Addition of secondary metal ions and other inorganic precursors enables preparation of diverse metallic and multi-metallic nanocatalysts.[320, 330] The reaction between MOF and sulfur, selenium, or phosphorus containing chemicals at high temperature leads to formation of carbon composites with metal chalcogenides and phosphides.[333, 334] Apart from MOF precursors, the final properties and structures of MDCs can also be controlled by simply varying pyrolysis conditions such as temperature, ramping rate, retention time, and gas atmosphere.[335-338]

Another important key advantage of MDCs is controllable particle morphologies ranging from simple 0D, 1D, 2D to complex 3D and hierarchical architectures. Carbon morphology control is

essential to understanding the fundamental morphology–performance relationships and therefore could provide new insights for the rational design of carbon materials that are highly desired in real world applications.[339] Morphology control also expands the scope of possible applications of carbons to cutting edge biomedical, energy, and environmental technologies.[316-321] In this respect, MDC is highly advantageous due to the straightforward pseudomorphic transformation of the parent MOF morphology into MDCs. In addition, complex yet well-defined 3D hierarchical architectures can be realized by MOF deposition on the external templates with predefined structures and morphologies. The pre-synthesized MOFs can also be processed into desired morphologies through various top-down fabrication techniques (refer to section 4).

Although some excellent reviews on morphology and size control of MOFs,[264, 340-342] preparation of MOF-derived materials,[253, 334, 343, 344] and applications of MDCs[316-321] have been published, however, a comprehensive overview on controlling morphologies of MDCs is still missing. This MDC section covers the carbonization mechanism, morphology control methods, and future outlook, so that general trends and future direction of MDC can be sketched. We focus on strategies for MDC morphology control, with particular emphasis on "solid metal oxides as primary architecture directing agents (*i.e.*, reactive external templates)" for MDC preparation.

5.1. Carbonization mechanism

The main scope of this section is to provide key information on thermal transformation mechanism of MOFs into carbons upon heat treatment under inert gas atmosphere. For the other metal-based nanomaterials, such as MOF-derived metal oxides, carbides, chalcogenides, and phosphides, the readers can refer to various reviews in the literature.[323, 334, 345] The factors that affect the physicochemical properties of MDCs will be discussed with particular emphasis on the role of metal ions, organic ligands and pyrolysis conditions.

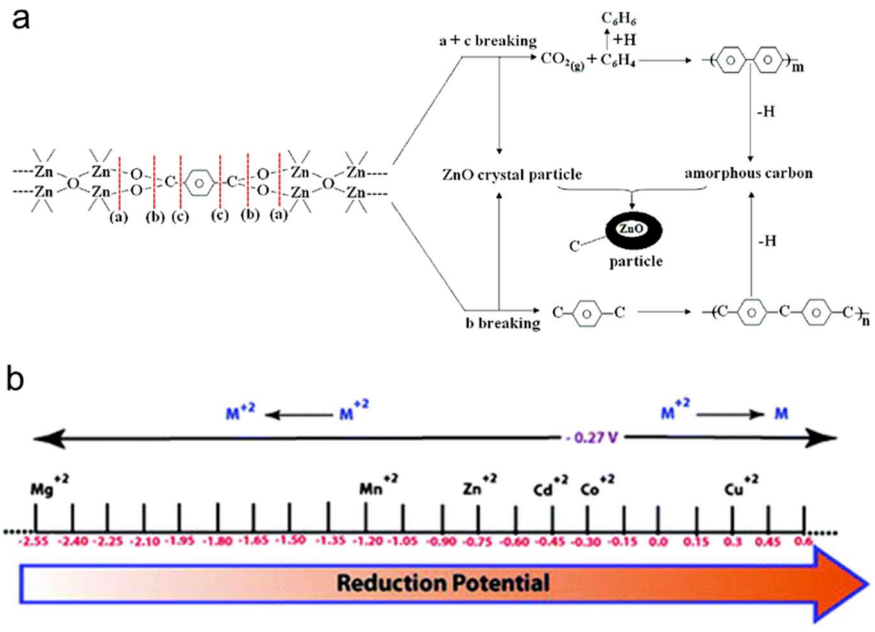

Fig. 21. a) Proposed thermal decomposition mechanism of MOF-5 (Reprinted with permission.[335] Copyright 2010, American Chemical Society). **b)** The effect of reduction potential of metal atoms present in the MOFs on the formation of the metal/metal oxide nanoparticles (Reprinted with permission.[346] Copyright 2012, The Royal Society of Chemistry).

Investigating thermal stability of MOFs is the first step to understand their thermal transformation mechanisms. Thermal stability and MOF decomposition profiles were traced by thermogravimetric analysis, temperature programmed-mass spectrometry,[335, 347] and pyrolysis-gas chromatography/mass spectrometry[329]. Zhang *et al.*[335] systematically investigated the decomposition of MOF-5 ($Zn_4O(BDC)_3$, BDC=1,4-benzenedicarboxylate)) for the first time. The guest solvents vaporized, and then MOF-5 started to decompose at temperature >400 °C. The decomposition products were identified as CO, CO_2, and benzene without any other hydrocarbons. Fig. 21a shows the proposed MOF-5 decomposition mechanism, consisting of (a) Zn-O bond breaking between Zn_4O cluster and carboxylic group, (b) O-C bond breaking of carboxylic group, and (c) C-C bond breaking between carboxylic group and benzene ring. MOF-5 decomposed through either (*a* + *c*) breaking (75%) or *b* breaking (25%). Both pathways work cooperatively to form CO_2, ZnO nanoparticles, and benzene-derived carbon species, thereby resulting in ZnO/amorphous carbon composites. Carbothermal reduction of ZnO to Zn metals started at 750 °C, accompanying the release of CO and CO_2 gas (ZnO + C → Zn + CO or CO_2).[347] Subsequent heating at higher temperature (*e.g.*, 900 °C) led to vaporization of *in situ* formed Zn metals. This process is analogous to the chemical activation and produces a large number of micropores in MDCs. The kinds of metal ions and organic ligands significantly influence the coordination strength and thermal stability of MOFs, and therefore their transformation behaviors. For instance, the carbonization process of ZIF-8 - the representative example of robust MOFs with high thermal stability - begins at >600 °C, releasing methyl side groups followed by nitrogen and vaporized Zn metals at higher temperature. Thus, the framework decomposition and carbonization rate of ZIF was relatively slower than those of carboxylate ligand-based MOFs.[336]

Two major components of MOFs, metal ions and organic ligands work cooperatively in determining the properties of the final MDCs. Metal species act as sacrificial pore forming agents, catalysts for *in situ* graphitization, and active components for target applications. During the pyrolysis of MOFs, the metal ions/clusters converted to either MOs or metals. Das *et al.*[346] suggested a standard reduction potential of metal ions as a criterion to predict formation of metal or MOs in the carbon matrix (Fig. 21b). The threshold reduction potential was proposed as -0.27 V. The metal ions (*e.g.*, Co, Ni, Cu) with reduction potential >-0.27 V form pure metal nanoparticles, while those <-0.27 V (*e.g.*, Mg, Al, Mn, Zn, Cr) combine with the oxygen of the organic ligands to form metal oxide nanoparticles during the thermolysis under N_2 at 900 °C. The Gibbs free energy of oxidation of metals can also help to estimate the temperature needed for carbothermal reduction of specific oxides.[348] The Ellingham diagram - widely used in extractive metallurgy - shows the relationship between the formation free energy of oxides *versus* temperature, so that the stability of oxides and the associated reduction temperature can be derived.[348] *In situ* generated metal nanoparticles play multiples roles in controlling the properties of MDCs. Volatile Zn is easily vaporized during carbonization >900 °C, leaving a number of pores (mostly micropores but even meso- and macropores) and thereby greatly increasing the porosity and specific surface area of MDCs. On the other hand, metallic Co, Ni, and Fe can induce catalytic graphitization, increasing the degree of graphitization of carbon frameworks. The controlled pyrolysis of such metal containing MOFs enabled formation of oriented-carbon nanotube (CNT) assemblies,[325] and porous graphene[349, 350]. To achieve synergistic effects from each metal component, bimetallic or multi-metallic MOFs were designed and used as precursors for direct preparation of functional MDCs.[351, 352] The residual metal species either contribute to formation of additional pores through chemical etching[353] or work as active catalysts for specific applications.[324]

Organic ligands work as porogens as well as carbon and heteroatom sources (*e.g*., imidazolate and NH_2-functionalized ligands). During pyrolysis under inert atmosphere, they decomposed to gaseous products and condensed/cross-linked to form (heteroatom-doped) amorphous carbon. This process typically leads to formation of random mesopores in MDCs, yet can be modified to afford foam-like macroporous structures as well. Kitagawa and coworkers[327] reported a ligand-assisted foaming process by using MOFs constructed by Zn^{2+} and ligands with nitro group substituents. During carbonization, the nitro group rapidly decomposed/released a large amount of NO_2 which act as foaming agents to create hierarchically porous carbon networks. Recently, Zhao *et al.*[328] reported a similar foaming effect in Zn-based triazole-rich energetic MOFs. Kim *et al.*[329] utilized labile, thermally less stable aliphatic carboxylate ligands as mesopore-forming agents. Aliphatic ligands were first transformed to organic substances with high boiling point (even higher than 550 °C) and then subsequently evaporated to generate numerous mesopores throughout the whole carbon matrix.[337, 338] In addition, the inherent characteristics of ligands greatly influence the textural properties of the resulting MDCs. Kurungot and coworkers[354] directly carbonized various Zn-MOFs with different ligand aromaticity, such as MOF-2, MOF-5, Zn-BTC (Zn-1,3,5-benzenetricarboxylic acid), Zn-NDC (Zn-2,6-naphthalene dicarboxylic acid), Zn-PAA (Zn-1,4-phenylenediacetic acid), Zn-ADA (Zn-1,3-adamantanediacetic acid) and observed that the surface area of MDCs increases with increasing the aromaticity of the MOF precursors.

Several attempts have been made to correlate the properties of parent MOFs with those of daughter MDCs, yet there is no general consensus on such relations. Earlier studies suggested that the porous structures and surface area of MDCs are mostly inherited from MOF precursors.[316] For instance, Lim *et al.*[355] carbonized a series of Zn based MOFs with different structures and compositions, and found a linear correlation between Zn/C ratio of MOF precursors and the surface area of resulting MDCs (*i.e.*, the higher the Zn/C ratio, the larger the surface area). However, this finding was difficult to be generalized, because many other factors (metal ions, ligands, bond strength, framework topology, MOF preparation methods) were not considered. Recently, Moon and coworkers[323] made a more comprehensive survey of the literature, and found that there are no apparent trends between the surface area of MOFs and MDCs, nor between the Zn/C ratio of MOFs and surface area of MDCs.

Instead, it was suggested that the physicochemical properties of MDCs are highly dependent on the pyrolysis condition (temperature, ramping rate, and retention time).[323] Indeed, the same parent MOFs can be transformed to daughter carbons with significantly different physicochemical properties by controlling the pyrolysis conditions, in agreement with a number of previous literature.[315, 336, 353, 356-358] The high temperature carbonization could enhance the porosity at the expense of carbon yield and loss of heteroatom species. In addition, as demonstrated by Hwang *et al*.[337], even the nonporous MOFs can be converted to MDCs with controllable large surface area, nitrogen content and pore structures by simply varying the pyrolysis temperature (550-1000 °C) and the removal method of *in situ* generated Zn porogens. The porosity of MDCs can also be tuned by changing the ramping rates and retention time.[338] Slow ramping rate and long retention time at 750 °C (5 °C min^{-1}, 6 h) promoted the aggregation of Zn species which contribute to increase in mesopore volume. Fast ramping rate and short retention time at 1000 °C (10 °C min^{-1}, 1 h) rapidly removed *in situ* generated Zn metal, leading to formation of micropore-dominant carbon.

The carbonization mechanisms are highly dependent on the kinds of metal ion-organic ligand pairs and their coordination strength, as well as pyrolysis conditions. The physicochemical properties of

daughter MDCs are not only partially inherited from parent MOFs but also greatly affected by the multiple factors as aforementioned. The relationship between the nature of the parent MOF and that of daughter MDC still remains rather controversial. Therefore, it is highly recommended to investigate the underlying thermal transformation mechanisms to prepare MDCs with desired properties (*e.g.*, surface area, pore size, pore volume, degree of graphitization, and heteroatom doping level). The universal trends/rules that govern the thermal transformation process and associated pore formation mechanism are ongoing subjects of research.

5.2. Strategies for morphology control of MOF-derived carbon

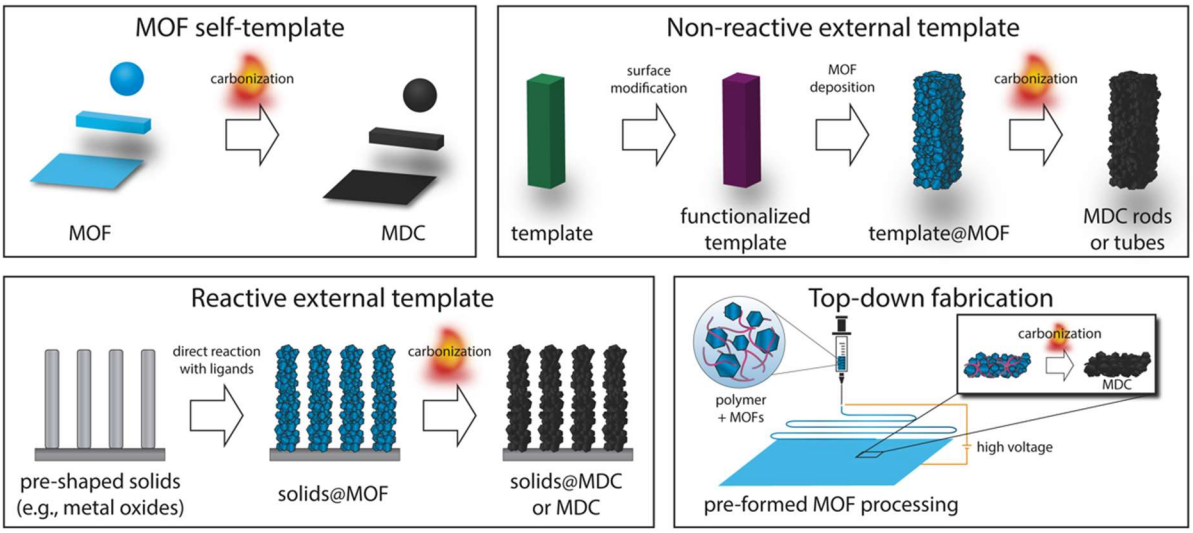

Fig. 22. Strategies for morphology control of MOF-derived carbon. **a)** MOF self-template method, **b)** Non-reactive external template method, **c)** Reactive external template method and **d)** Top-down fabrication.

We categorize the reported MDC literature into the following four general morphology control strategies: 1) MOF itself as a self-template, 2) non-reactive external template method, 3) reactive external template method, and 4) top-down fabrication method (Fig. 22 and Table 3). In the MOF self-template method, the morphologies of parent MOFs are inherited to daughter MDCs without the assistance of other templates or microfabrication techniques. Higher level of morphology control can be achieved by integrating MOFs with external templates with predefined structures and morphologies. This external template method can be further divided into two categories, non-reactive and reactive ones. The former mainly relies on the coordination between the surface functional groups of templates and the metal ions; thus surface modification is usually required to induce preferential MOF deposition on non-reactive templates. The latter uses insoluble solid matters (*e.g.*, metal oxides) as reactive self-sacrificial templates. The solid MOs function as metal ion reservoirs and specific nucleation sites, which directly react with the solid/liquid/gas phase organic ligands at the interfaces. Finally, the pre-synthesized MOFs are utilized as building blocks for various top-down processing techniques to prepare MOF/MDC with desired morphologies. Based on these four categories, we further sub-divided the MDCs according to their dimensions, *i.e.*, 0D (dot, polyhedra, hollow- and multi-shelled polyhedra), 1D (rods and tubes), 2D (sheets, ribbons, sandwiches), 3D and hierarchical morphologies (arrays, superstructures, hierarchical architectures),

and discuss their formation mechanism as well as their thermal transformation process. We place particular emphasis on ‘solid MOs as reactive external templates’, and comprehensively review the available literature on this strategy as a versatile tool to obtain complex yet sophisticated carbon architectures with multiple levels of hierarchies (see also section 4).

Table 3. Synthetic strategies for MDC nanostructures with controlled morphology.

Method	Advantages	Limitations	Product morphology	Examples of templates	Ref.
MOF self-template	• Straightforward synthesis procedure (without the need of additional templates or processing techniques) • Simple experimental set-up • Preparation of homogeneous, high quality MOF/MDC is possible • The possibility for large-scale production • The secondary components (either inorganic or organic species) can be incorporated into the pores of MOFs and thus MDCs • Controllable MDC morphologies and physicochemical properties by changing thermal transformation process	• Morphologies of MDCs are mostly restricted to a few simple single crystal morphologies of parent MOFs • Difficult to prepare MOF/MDC with complex morphologies • Difficult to predict MOF morphology because of insufficient understanding on a standard growth unit of MOFs • Partial or complete collapse of morphology (particle shrinkage and deformation) during pyrolysis • Particle agglomeration during pyrolysis • Partial loss of ordered pore structures of MOF • In some cases low carbonization yield	**(0D)** dot, polyhedral, hollow sphere, multi-shelled structures **(1D)** rods, tubes **(2D)** sheets, leaf, platelet **(3D)** dandelion, honeycomb, diatom, chestnut nanorod superstructures, flower superstructures	ZIF-8, ZIF-67, ZIF-L, MOF-1, MOF-5, MOF-74, MIL-88, $Zn_2[bdc]_2[DABCO]$, $(Al(OH)(1,4\text{-}NDC)\cdot 2H_2O)$, PPF-3, Mn-bdc	[325, 326, 336, 337, 359-380]
Non-reactive external template	• Straightforward control over the size and morphology of MDC • Morphology that is difficult to obtain from MOF self-template is achievable • MDC remains relatively well-dispersed without significant structural/morphological deformation because of the stabilization by external templates • External templates either generate internal voids through their removal or contribute as functional components in the final MDC composites	• Time-consuming multi-step procedures • Surface functionalizations/modifications are usually necessary • The reaction parameters should be tuned to attain controllable nucleation and growth on templates • Inhomogeneous MOF deposition (formation of undesired bulk MOFs in solution) • Insufficient control of MOF thickness • Only a few MOFs can be directly grown on the non-reactive external templates, and their detailed growth mechanism is not fully understood	**(0D)** core-shell**,** hollow, single-holed hollow sphere **(1D)** wires,rods, tubes **(2D)** sheet, sandwich-like **(3D)** arrays (wires, tubes grown on condutive substrates), 3D ordered macroporous structures	PS and silica beads, Te nanowires, CNTs, MoO_3 nanorods, graphene oxide, metal foam/mesh/foil, carbon cloth, melamine sponge, Preformed MIL-88	[389-397, 400-408, 425]
Reactive external template	• Reactive external template provides additional advantages as well as those of non-reactive external template • Reactive external templates function as architecture directing agent, cation reservoirs, and specific nucleation sites at the same time • Additional metal ion source and surface functionalization are not needed	• Time-consuming multi-step procedures • The balance between the release rate of metal ions from the solid matters and the coordination rate of metal ions with ligands should be controlled • The reaction parameters should be tuned to attain controllable nucleation and growth on templates • Inhomogeneous MOF deposition (formation of	**(0D)** hollow sphere, hollow polyhedral **(1D)** wires, tubes, hierarchical tubes **(2D)** sheets, honeycombe-like flakes, plates **(3D)** flowers,urchin-like,arrays	ZnO, CoO, NiO, $Cu(OH)_2$, cobalt oxalate, cobalt carbonate hydroxide, PAN/metal acetate, layered double-metal hydroxide, and solid	[281, 310, 333, 415-424, 426-435

	• The possibility to create complex morphologies with multiple levels of structural hierarchies which are difficult to obtained from the other MOF-mediated routes • Well-established morphology control of metal oxides can be transferred to MDCs • Cheap solid precursors from large-scale industrial production or earth-abundant natural minerals are available	undesired bulk MOFs in solution) • Insufficient control of MOF thickness • Chemical composition of parent metal oxides is restricted to a few substances, mostly Zn and Co based ones • Considerable lack of understanding of underlying growth kinetics and thermodynamics	(wires, tubes grown on conductive substrates),	precursors grown on carbon cloth, metal foam/mesh/foil, fluorine doped tin oxide glass	
Top-down fabrication	• A wide variety of techniques (chemical etching, exfoliation, microfabrication such as electrospinning and 3D printing) are available • Pre-synthesized MOFs can be processed into desired morphologies • Separation of the MOF preparation and the MOF shaping • Any kinds of MOFs with various combinations can be applied in microfabrication • The possibility of obtaining MDCs with unique structures and morphologies	• Chemical etching is dependent on the stability of specific MOFs against the etchant solution • Exfoliations are only applicable to a few layer-structured MOFs; construction of high-quality 2D MOFs and their conformal transformation are challenging • Development of low cost, high yield, and versatile top-down methods is highly desired	**(0D)** hollow polyhedra, adamantine-like **(1D)** rods, tubes, **(2D)** sheet**,** paper,necklace-like paper, stacks, nanoribbon **(3D)** printed mesh architectures	Chemically etched ZIF-8 and ZIF-67, electrospun ZIF-8, ZIF-67, and MIL-88, exfoliated MOFs, 3D printed Co-MOF	[373, 438-452]

5.2.1. Conformal transformation of MOF self-template

The inherent crystal morphologies of MOFs can be transferred to the derived MDCs, namely, conformal transformation or pseudomorphic transformation. The morphologies of MDCs are inherited from MOFs without the use of additional templates and processing techniques, *i.e.*, MOF self-templating method. This approach is simple, straightforward and economical. Despite of considerable progress in morphology and size control of MOF,[340] morphologies of MDCs are still rather restricted to a few simple single crystal morphologies such as polyhedra, rods, and sheets.

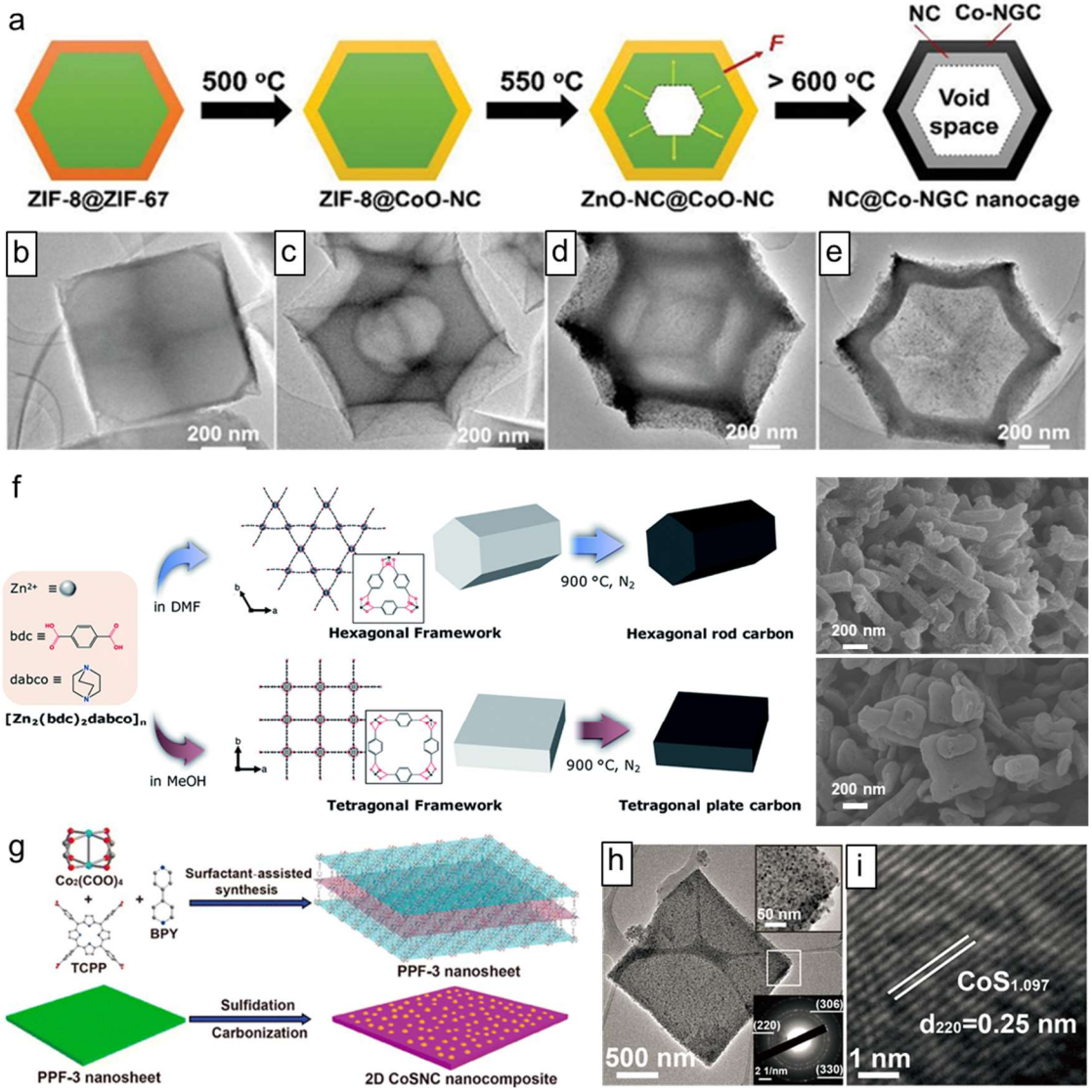

Fig. 23. Carbon derived from MOF self-templates. **a-e)** 0D hollow N-doped microporous carbon@Co-N-doped graphitic carbon (NC@Co-NGC) nanocages prepared by external rigid-shell-induced outward contraction (Reproduced with permission.[359] Copyright 2017, John Wiley & Sons). **f)** Solvent mediated selective synthesis of 1D and 2D MOFs and their transformation to nanoporous carbons (Licensed under CC-BY[360]). **g)** Surfactant assisted synthesis of 2D porphyrin paddlewheel framework-3 (PPF-3) nanosheets and their derived CoS/N-doped carbon nanosheets and **h, i)** the corresponding TEM images of the sample (Reproduced with permission.[361] Copyright 2016, American Chemical Society).

Zero-dimensional carbons: Direct carbonization of MOFs can produce MDCs with different 0D morphologies such as polyhedra, dot, hollow, and multi-shelled structures. Polyhedral ZIFs are by far the most widely used MOFs for conformal transformation because of their high thermal stability.[336, 362] Thus, most common morphologies of MDCs are polyhedra (hexahedral, octahedral, and dodecahedral shape). Carbon dots can also be prepared by pyrolysis of small ZIF-8 nanoparticles <20 nm at 500 °C in Ar flow for 10 h.[363]

Particular attention has been paid to hollow and multi-shelled MDCs.[364] ZIF-67 is commonly used as single precursor for direct preparation of hollow graphitic carbons. The formation of highly active Co metal nanocatalysts *via* controlling pyrolysis temperature and gas atmosphere is the key to obtain hollow N-doped CNT particles (N-CNTs). Xia *et al.*[365] converted ZIF-67 to hollow N-CNTs through the pyrolysis under reducing H_2/N_2 gas atmosphere in a wide temperature range (600-900 °C). H_2 rapidly generated highly active Co metal nanoparticles which catalyzed the growth of N-CNTs. Because of the preferential surface-enrichment of Co metal, the subsequent catalytic growth direction of N-CNTs is from inside to outside, resulting in formation of hollow structures. Controlled low temperature pyrolysis of various Co-MOFs (at near the decomposition temperature of MOFs (430 °C) for 8 h under Ar flow) led to hollow N-CNTs assemblies.[325] *In situ* generated reducing gas turned the surface Co ions/clusters to uniformly distributed metallic Co nanoparticles which resulted in similar inside-to-outside growth of N-CNTs.

Heterogeneous contraction during thermal treatment is a simple and efficient strategy for preparation of hollow particles.[364] Liu *et al.*[359] synthesized hollow N-doped microporous carbon@Co-N-doped graphitic carbon (NC@Co-NGC) nanocages *via* external rigid-shell-induced outward contraction (Fig. 23a). The difference in thermal stability between ZIF-8 core and ZIF-67 shell (ZIF-8@ZIF-67) precursor is the key factor. The less stable ZIF-67 shell decomposed first to form rigid shells of CoO/carbon around ZIF-8 cores above 500 °C. The strong connection between CoO/carbon and ZIF-8 provided an outward adhesive force to pull the ZIF-8-derived carbon to adhere on the CoO/carbon shell. Following carbonization at 800 °C and catalytic CNT growth on Co metals resulted in hollow nanocages with NC@Co-NGC shells (Fig. 23b-e). This strategy is also applicable to the other types of rigid shells, such as silica[366] and polymer[367]. Recently, multilayer solid ZIFs, prepared by stepwise multiple epitaxial growths on preformed ZIF-seed, were converted to multishell hollow metal@NC with precisely controlled shell number and composition.[368]

One-dimensional carbons: MOFs with intrinsic 1D crystal morphologies were the straightforward choice of precursors for carbon nanorods and nanotubes. However, there are only a few 1D MOFs available, such as M-BTC (M = Mn, Zn),[369, 370] Fe-MIL-88,[371] and Al-MOF ($Al(OH)(1,4\text{-}NDC)\cdot 2H_2O$)[326]. Interestingly, carbonization and HF etching of Al-MOF led to spongy-like carbon nanorods made up of randomly assembled nanosheets having tunable large surface area and pore volume.[326]

Anisotropic 1D MOFs can be prepared by a coordination modulation in which certain monodentate modulators (*e.g.* monocarboxylic acid) competitively interact with organic ligands and by that change the coordination equilibrium and promote/suppress the relative growth rates of MOF-crystal faces.[372] Zn-MOF-74 nanorods were synthesized by using salicylic acid as a coordination modulator, and then conformally transformed to 1D carbon nanorods.[373] Different from conventional modulators, the solvent itself can function as both a structure directing agent isolating particular MOF polymorph and a crystal modulator controlling the aspect ratio of nanorods (Fig. 23f).[360] In an ambient temperature synthesis of $[Zn_2(BDC)_2DABCO]_n$ (DABCO = 1,4-diazabicyclo[2.2.2]octane),

dimethylformamide (DMF) and methanol induced the selective formation of the kinetic polymorph with 1D hexagonal rod morphology. Addition of methanol decreased the rate of nucleation and thus led to formation of larger rod-MOFs. Methanol also suppressed the crystal growth along Zn-DABCO [001] directions by forming hydrogen bonds with nucleophilic DABCO ligand, thereby inducing the morphology change from 1D hexagonal rods to 2D nanoplatelets. Thus, 1D hexagonal rods with different size and aspect ratio can be easily prepared. The structure formation has also significant effect on electrochemical applications (refer to section 6).

Two-dimensional carbons: 2D MOFs are usually prepared by top-down (exfoliation of layered bulk MOFs; kindly refer to section 5.2.4) or bottom-up approaches (surfactant or coordination modulator-assisted anisotropic crystal growth). Only a few 2D MOFs, such as ZIF-L with 2D leaf-like morphology (a polymorph of ZIF-8)[374] and recently developed 2D Zn-hexamine coordination frameworks[375] were employed as precursors for N-doped porous carbon nanosheets.

Surfactants and coordination modulators have been widely used to regulate the growth of bulk crystals into anisotropic 2D morphologies. Cao *et al.*[361] reported a surfactant assisted synthesis of 2D porphyrin paddlewheel framework-3 (PPF-3) nanosheets and their derived CoS/N-doped carbon nanosheets (Fig. 23g-i). PVP attached on the surface of MOF, promoted the anisotropic growth of MOFs and finally formation of nanosheets with tunable thickness. Because of relatively low thermal stability and significant framework shrinkage during carbonization, the 2D square-like morphology was only retained when sufficiently thick (ca. 40 nm) MOF nanosheets were used. Ultrathin PPF-3 < 10 nm was completely destroyed after carbonization. However, this approach may not be suitable for large-scale synthesis because of high cost of porphyrin ligands. He and coworkers[376] developed a high-yield (> 65%) synthesis of ultrathin MOF/MDC nanosheets (ca. 2.5 nm) by using low-cost ligand sources (benzimidazole and sodium acetate). Sodium gluconate modulators restricted the growth of the layered MOFs in the direction perpendicular to the layers. Likewise, Mn-BDC nanosheets were prepared by simply adding monodentate benzoate modulator into the synthesis solution of bulk Mn-BDC cubes.[377]

Three-dimensional and hierarchical carbon: For preparation of 3D and hierarchical architectures, several novel approaches based on controlling thermal transformation process and MOF crystallization pathway have been reported in recent years. Xiong and coworkers[378] reported formation of 3D dandelion-like CoO@C spheres through the pyrolysis of metal-organic layers with 2D framework topologies. Upon thermal annealing, the ligand-bridges decomposed to form 1D chain of CoO_6 octahedra which in turn converted to 1D nanowires. Meanwhile, morphology evolution proceeded from flake-like crystals to dandelion-like spheres comprised of 1D nanowire arrays through thermally induced recrystallization and self-assembly. However, this approach needs specific MOF with special 2D topologies and therefore lacks versatility as it is not applicable to other MOFs.

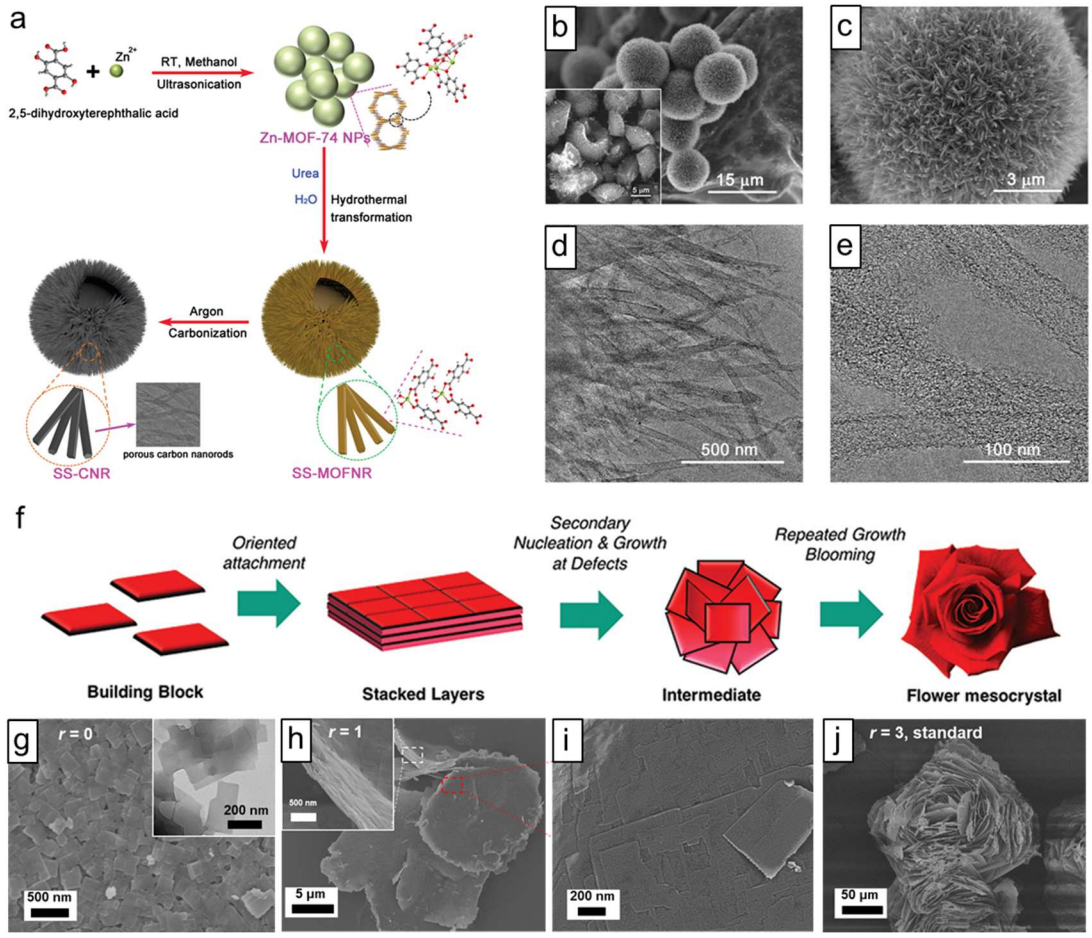

Fig. 24. 3D Carbon derived from MOF self-templates. **a)** Fabrication of spherical carbon nanorods superstructures (SS-CNR). **b, c)** SEM and **d, e)** TEM images of SS-CNR (Reproduced with permission.[379] Copyright 2019, John Wiley & Sons). **f)** Suggested formation of flower Zn-NTA (nitrilotriacetic acid) mesocrystals. **g-j)** SEM images of ZnNTA mesocrystals prepared under different HNO_3/NTA (*r*) (Reproduced with permission.[337] Copyright 2019, John Wiley & Sons).

Guest incorporation can change thermal transformation mechanisms and create new synergistic effects that induce dramatic morphological transformation. Guest@MOF has shown great potential as a versatile precursor to achieve hierarchical carbon structures. In 2016, Zhu *et al.*[380] explored this concept for the first time, and developed honeycomb-like porous carbons with embedded Co_9S_8 nanoparticles. Decomposition of encapsulated thiourea and cobalt chloride within the MOF not only led to formation of Co_9S_8 nanoparticles but also released a large amount of N, S-containing gases which induced heteroatom doping and expansion of the pores. Smoukov and coworkes[381] found that carbonization of molybdate@HKUST-1 yielded natural diatom-like carbons with multi-level hierarchies, (*i*) outermost polyhedral boundaries (15 μm) composed of (*ii*) webs (0.5-1 μm), (*iii*) fibers inside the diatom (100 nm in diameter), and *iv*) mesopores (20 nm). Upon pyrolysis, Cu migrated to the outer surface of carbons due to weak Cu-C interactions, while Mo stayed in the carbon matrix due to strong Mo-C interactions. A small fraction of Cu in proximity to Mo can synergistically catalyze the growth of web- and fiber-like carbon nanostructures, which cannot be achieved by Cu or Mo alone. Thus, the fibers grew only inside of the carbon cages. The surface accumulated Cu could not contribute to fiber formation and left mesopores after acid washing.

Of particular interest in this research area is the development of hierarchical carbons with well-defined 3D superstructures, which can show novel collective properties that are considerably better than the sum of their parts. However, the examples as such are still very rare. Xu and coworkers[379] fabricated a spherical superstructure of carbon nanorods with hierarchical pores (Fig. 24a). In a hydrothermal reaction condition, the presynthesized spherical Zn-MOF-74 ($Zn_2(C_8H_4O_6)$) nanoparticles were firstly transformed into $Zn(H_2O)_2(C_8H_4O_6)$ nanorods having different crystal structures, and then self-organized to chestnut-like-superstructures. The use of Zn-MOF-74 (a precursor), water (a solvent), urea (a crystal modulator) was critical for controlled dissolution and recrystallization to obtain the final 3D superstructures with radially oriented 1D nanorods (Fig. 24b-e). Very recently, Hwang *et al.*[337] reported hierarchically porous 3D flower-like carbon superstructures through direct thermal transformation of bio-inspired MOF mesocrystals (Fig. 24f). The initially formed 2D nanosheet acted as a primary building block that underwent oriented attachment and mesoscale assembly. The secondary nucleation and growth on the preformed layers resulted in formation of 3D flower-like mesocrystals composed of 2D nanosheets. Nitric acid-mediated kinetics control enabled the morphogenesis from 2D nanosheets to 3D flower-like superstructures with controllable particle size and dimensions (Fig. 24g-j). Finally, the mesocrystals were converted into porous carbon materials.

Challenges and opportunities: The use of MOFs as sole precursor for MDCs still suffers from the following problems. High temperature thermal transformation often leads to a partial or complete collapse of the original MOF morphology, and is sometimes accompanied by particle agglomerations and loss of ordered pore structure. These drawbacks could be partially overcome by stabilizing MOFs with the well-defined external templates, which will be discussed in the following sections. In this regard, development of thermally stable MOFs with various compositions and structures (other than ZIFs) is highly desired. Furthermore, direct fabrication of MOF with multiple levels of structural hierarchy still remains a great challenge because of single crystalline nature of MOFs and incomplete understanding of their crystallization mechanism. In a classical crystallization theory, the crystal morphologies likely reflect the replication/amplification of the unit cells. Although the SBU concept has been well established to predict/determine the framework topologies, however, SBUs cannot be simply considered as growth units because they are oriented in the network in a complicated way.[382] Therefore, further understandings on a standard growth unit of MOFs and associated crystallization mechanism are highly required.

To circumvent this issue, a nonclassical crystallization pathway for morphology control of MOFs has been recently proposed.[337, 383] Natural mineralization often follows this pathway to create sophisticated 3D mesocrystals *via* particle-mediated growth and attachment, as observed in various biominerals (*e.g.*, bone, nacre, sea urchins).[384, 385] Mesocrystal is a kind of superstructure consisting of individual nanoparticles in crystallographic register with defined order.[384, 385] Inspired by nature, Schmidt and coworkers[383] reported double hydrophilic block copolymer-mediated morphogenesis of MOF mesocrystals with high level of structure control, such as kinetic formation of MOF mesocrystals and their recrystallization to MOF mesocrystals with thermodynamic structure, as well as hybridization of two distinct MOFs. This approach opens a new avenue for morphogenesis of MOFs and thus possibly MDCs. Along this line, we also believe that *in situ* hybridization of MOF and other components into single architectures (*e.g.*, MOF-MOF, MOF-polymers)[352, 386-388] is a promising

strategy for morphology control of MDCs, by controlling the MOF architectures themselves and/or by changing the thermal transformation process.

5.2.2. Non-reactive external templates

In situ growth of MOFs on external templates can mitigate some of the inherent drawbacks of the MOF self-template method. The most obvious advantage of the external template is the straightforward control over the size and morphology of resulting carbon materials. In addition, MDC can remain relatively well-dispersed without significant aggregation because the parent MOFs are anchored and stabilized on the external templates during thermal transformation. External templates either generate internal voids through their removal or contribute as functional components in the final MDC composites. In the case of non-reactive external template, surface modification is usually required to increase the interaction/affinity with metal ions and therefore to achieve homogeneous and uniform MOF coating. For example, functionalization with carboxyl/sulfonyl groups or polymers (*e.g.*, PVP) is conducted before MOF deposition.

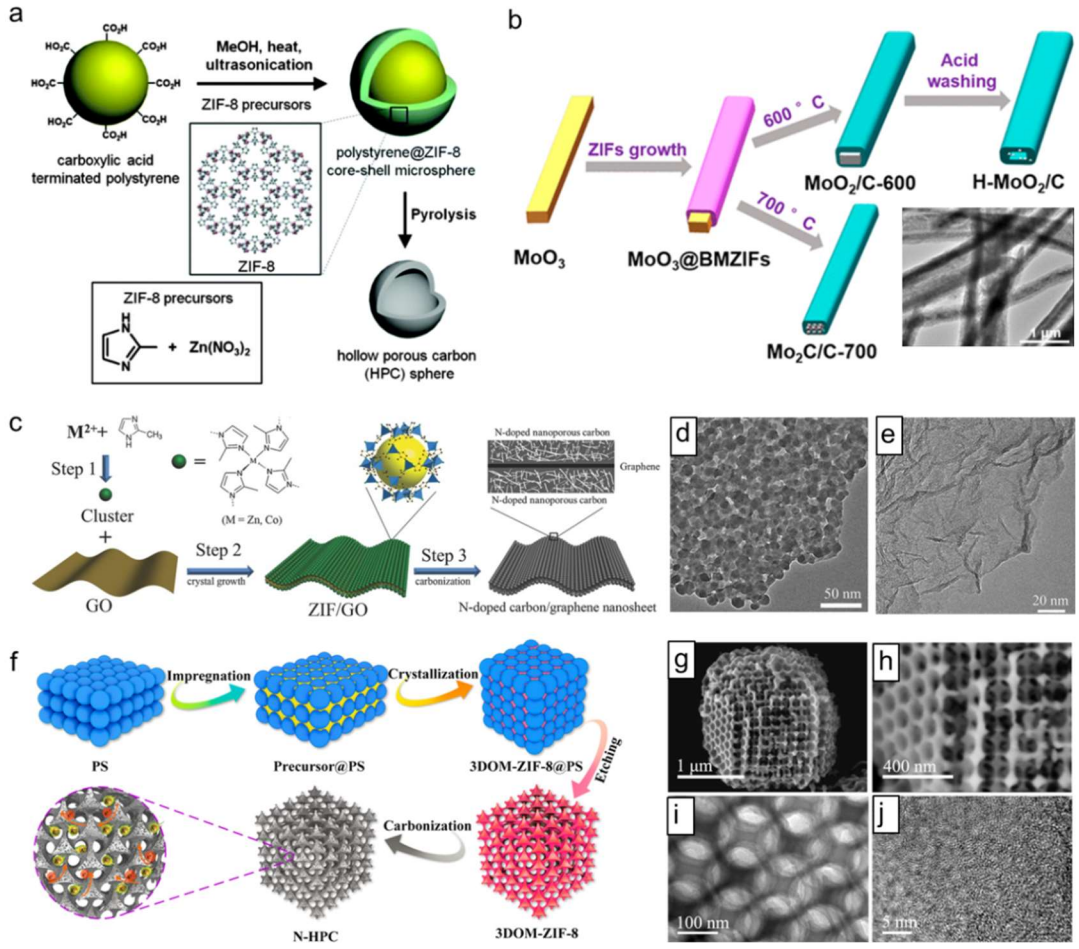

Fig. 25. Carbon derived from MOF/non-reactive external templates. **a)** Schematic representation for synthesis of 0D hollow carbon from PS@ZIF-8 (Reprinted with permission.[389] Copyright 2014, The Royal Chemical Society). **b)** 1D carbon coated Mo-based nanocomposites from PVP-modified MoO_3@bimetallic ZIFs (Reproduced with permission.[390] Copyright 2018, American Chemical Society). **c)** 2D porous carbon nanosheets from ZIF/GO sandwiches and **d, e)** their TEM images (Reproduced with permission.[391] Copyright 2015, John Wiley & Sons). **f)** Schematic diagram for three-dimensional

ordered macroporous ZIF-8 single crystal-derived nitrogen-doped hierarchical porous carbon and corresponding SEM **g, h)** and TEM **i, j)** images at different magnification (Reprinted with permission.[392] Copyright 2019, American Chemical Society).

Zero-dimensional carbons: Typically, carboxylate (or PVP)-terminated poly(styrene) (PS) beads[389] were mixed with a solution of metal ions/organic ligands to obtain core-shell PS@MOF microspheres (Fig. 25a). Surface carboxyl groups interacted with metal ions and initiated the growth of MOFs. The resulting PS@MOF hybrids were subjected to carbonization under inert gas atmosphere, during which the MOF shell transformed to porous carbon and the PS core decomposed to form hollow interiors. Several PS@ZIF-8,[389, 393] PS@ZIF-67,[394] PS@MIL-101/ZIF67[395] were used for preparation of hollow carbon spheres with or without metal nanoparticles embedded in the carbon shell. Interestingly, fast pyrolysis of PS@ZIF-67 at rapid heating rate (> 5 °C min^{-1}) yielded "single-holed" hollow carbon spheres.[394] Thermal decomposition of PS core generated a strong hydrocarbon gas outflux which created a large single hole in each shell. Zhang *et al.*[395] prepared MIL-101/ZIF-67 composites shells on PS spheres (PS@MIL-101/ZIF-67) by functionalizing the surfaces of both PS spheres and MIL-101(Fe) nanoparticles with PVP. Thus, the preformed secondary MIL-101 could be homogeneously distributed within the dual-MOF nanoshells. The following pyrolysis produced CoFe alloy@N-doped hollow carbon spheres.

One-dimensional carbons: 1D template-directed growth of MOFs and their transformation to 1D carbon nanofibers and hollow nanotubes were demonstrated. Yu and coworkers[396] utilized ultrathin tellurium nanowires (TeNWs) as hard templates to induce *in situ* growth and assembly of ZIF-8. Without surface modification, TeNWs were directly immersed in methanolic Zn^{2+}/2-methylimidazole (Hmim) solution at ambient temperature, leading to formation of TeNWs@ZIF-8. The concentrations of TeNWs and reactants were precisely controlled to inhibit solution phase growth of bulk ZIF-8. Porous carbon tubules were obtained after pyrolysis at 1000 °C, during which TeNWs were completely vaporized to form hollow interiors. ZIF-8 derived carbons can also be grown on CNTs.[397] For controllable ZIF-8 deposition, CNTs were treated with a mixture of nitric acid and sulfuric acid at 80 °C to generate the surface carboxylic groups which serve as nucleation sites for ZIF-8 growth. Subsequent pyrolysis at 1000 °C yielded N-doped porous carbons/CNT with controllable large surface area. By using PVP-modified MoO_3 nanorods as templates, Tian *et al.*[390] synthesized a series of 1D Mo-based carbon nanorods and nanotubes (Fig. 25b). Amide carbonyl groups of PVP can form weak coordination interactions with metal ions in solution and allow uniform ZIF coating on MoO_3 nanorods. Controlled pyrolysis at different temperature resulted in either carbothermal reduction to form MoO_2/C or reaction with carbon to form Mo_2C/C nanorods. The inner MoO_2 species were dissolved and dispersed into the porous carbon matrix by HCl washing, leading to formation of hollow MoO_2/C nanotubes.

Two-dimensional carbons: Scalable synthesis of high quality 2D MOFs have been considered as a difficult task and thus only a few 2D MOFs are available for preparation of MDCs so far. This problem can be largely alleviated by using 2D external templates. Graphene has been most extensively used as 2D template because of its excellent thermal, electrical and mechanical properties. As nicely reviewed by Zheng *et al.*[398] and Liu *et al.*[399], a wide variety of MOF/graphene composites have been prepared to combine the advantages of individual components. ZIF-derived graphene based N-doped

porous carbon was prepared by the *in situ* growth of ZIF-8 on graphene oxide (GO) sheets.[400] PVP functionalization facilitated the uniform nucleation of ZIF-8, resulting in formation of the dispersive 2D sandwich-like ZIF-8/GO composites. Without the use of PVP, the surface deposition of ZIF-8 was incomplete and inhomogeneous. Excess Hmim ligand was also necessary for the uniform ZIF growth on GO. Finally, thermal annealing of ZIF-8/GO at 800 °C in Ar flow generated N-doped porous carbon sheets.

ZIF-8/GO sandwiches can also be prepared by controlling the addition sequence of the precursors without any surface modification of GO (Fig. 25c-e).[391] In the proposed synthetic route, GO dispersion was added to Zn ions/Hmim ligands solution where ZIF clusters were already formed. The cluster readily attached to the GO layer due to a strong interaction between metal ions of cluster and the oxygen functional groups from GO. The uniform deposition of clusters and their confined growth to ZIF nanocrystals on GO surface allowed formation of ZIF-8/GO sandwiches with ZIF nanocrystals (20 nm) fully covering the GO. ZIF-derived carbon acted as a spacer to alleviate the significant agglomeration of GO during high-temperature treatment. In contrast, when Zn salts in methanol were firstly added to the GO solution, the Zn ions were located both on GO and in the solution because of insufficient numbers of oxygen groups in GO to capture all the Zn ions. This inhomogeneous nucleation resulted in the mixture of discrete ZIF-8 crystals and ZIF-8/GO composites.

Three-dimensional and hierarchical carbon: 3D carbon arrays, derived from MOF nanowires grown on various conductive substrates (*e.g.,* metal foam/mesh/foil, carbon cloth, and CNT fibers) are the most common examples of external templated materials.[401-404] The substrates provide additional functions such as high electronic conductivity, mechanical stability, and flexibility. Such 3D aligned architectures are of particular interest in electrochemical applications, as they can provide large electrochemical surface area which facilitate electrolyte penetration and diffusion of ionic species, and avoid the use of extra polymeric binders or conductive additives.[405] In 2014, Qiao and coworkers[401] fabricated MOF-derived Co_3O_4/carbon porous nanowire arrays for the first time. Co-NDC with a layered crystalline structure was directly grown on Cu foil through a hydrothermal reaction at 80 °C for 20 h, and then converted to Co_3O_4/carbon hybrid arrays with high surface area (251 m^2 g^{-1}) and large carbon content (52.1 wt%) *via* pyrolysis at 600 °C under a N_2 atmosphere. Inspired by this pioneering work, researchers have developed a wide variety of 3D carbon-based arrays by employing different combinations of substrates and MOFs.[402-404] Instead of arrays, surface-mounted MOF (SURMOF), typical MOF thin films prepared by layer-by-layer growth process, was employed as precursor for 3D hierarchical carbon.[406] A ZIF-67 thin film was grown on hydroxyl-group-terminated 3D macroporous melamine sponge and then converted to vertically aligned N-doped CNTs *via* pyrolysis at various temperature 700-1000 °C.

Preformed MOFs are also promising external templates that enrich the possible particle morphologies of MDCs. Different from typical MOF-on-MOF epitaxial growth, PVP-modified MOFs can be directly integrated with other MOFs *via in situ* assembly and growth. Guan *et al.*[407] introduced PVP-functionalized MIL-88B (Fe) nanorods into the reactant solution of ZIF-8, and obtained uniform MIL-88B@ZIF-8 particles in which a number of 1D MIL-88B nanorods were co-assembled and encapsulated in ZIF-8 polyhedron (*i.e.*, MOF-in-MOF). This dual-MOF with tailored morphologies and compositions enabled preparation of hierarchically structured Fe_3C@N-CNT assemblies confined in a porous carbon matrix.

Shen *et al.*[408] developed a novel approach toward single-crystal ordered macroporous ZIF-8 (Fig. 25f). ZIF-8 precursors (Zn salt and Hmim) were filled into 3D ordered PS sphere-monoliths, and then soaked in $CH_3OH/NH_3{\cdot}H_2O$ mixed solvent. $NH_3{\cdot}H_2O$ induced rapid crystallization of the precursors while CH_3OH stabilized the precursors and adjusted the balance between nucleation versus growth of ZIF-8. 3D-ordered macroporous (3DOM) ZIF-8 was liberated from PS templates by repeated soaking in tetrahydrofuran. PS templates imposed unique shaping and templating effects which guided the morphological evolution of 3DOM-ZIF-8 into a tetrakaidekahedron, in contrast to typical rhombic dodecahedra. In the following work, Zhou *et al.*[392] reported 3DOM-ZIF-8-derived hierarchically porous N-doped carbons as high performance anode materials in potassium ion battery (Fig. 25g-j).

Challenges and opportunities: Non-reactive external template methods usually rely on time-consuming and laborious multi-step procedures, including preparation of templates (sometimes their bottom-up assembly into specific shape), surface modification, MOF deposition, carbonization, and template removal (if necessary). Another challenge in this process is the uniform MOF deposition with a controlled thickness. Non-reactive external templates lack the interaction sites that can tightly bind the metal ions. Part of adsorbed metal ions can diffuse into the ligand solution to form bulk MOFs. Thus, it is difficult to confine heterogeneous growth on the surface of templates exclusively. To date, only a few MOFs can be directly coated on the templates and their detailed growth mechanism is not fully understood yet. Thus, the exploration of new synthetic approaches for direct construction of MOF on external templates will be the important subject of future research. In addition, development of new templates with predesigned morphologies and multi-level hierarchical structures (*e.g.*, reactive external templates) is of urgent importance.

5.2.3. Reactive external templates

Pre-shaped, solid state MOs can be transformed into morphology conserved carbons *via* MOF as intermediate precursors (*i.e.*, reactive external template method or solid-to-MOF-to-carbon pathway).[259] Different from typically used solvent-soluble metal salts, the solvent-insoluble solid precursors can perform multiple roles in MOF/carbon synthesis. (1) Architecture directing agents (templates): the morphologies of solid precursors are replicated to the derived MOF and the final carbon materials. (2) Cation reservoirs (metal ion source): solid precursors provide metal ions by slowly dissolving themselves with the assistance of solvents and organic ligands under specific condition, or directly react with organic ligands in solvent-free conditions. Thus, additional metal ion source is not needed. (3) Specific reaction sites for heterogeneous nucleation: the growth of MOF/carbon is localized/confined on the surface of solid precursors. Tedious surface modification steps typically needed in non-reactive external template methods are no longer required. (4) Functional components enhancing physical/chemical properties of the final carbon products. Typical synthesis procedures consist of mainly three steps: preparation of shaped-metal oxides, conversion to desired MOFs by reacting with organic ligands, and thermal transformation into the carbon or carbon-based composites.

The key advantage of the reactive template method (*e.g.,* MOs as self-sacrificing templates) lies in its ability to create complex morphologies with multiple levels of structural hierarchies. There are a wide variety of well-established approaches for controlling morphologies of MOs from nano- to micro- to macro-scopic length scales (refer to section 3).[210, 211, 409-414] In addition, the MOs can be directly grown onto various functional substrates and host materials, and pre-installed on specific

locations before their transformation into MOFs. These capabilities enable the preparation of patterned MOFs in a spatially controlled manner, which in turn lead to formation of sophisticated, higher-order carbon architectures such as 3D arrays and multi-dimensional hierarchical assemblies.

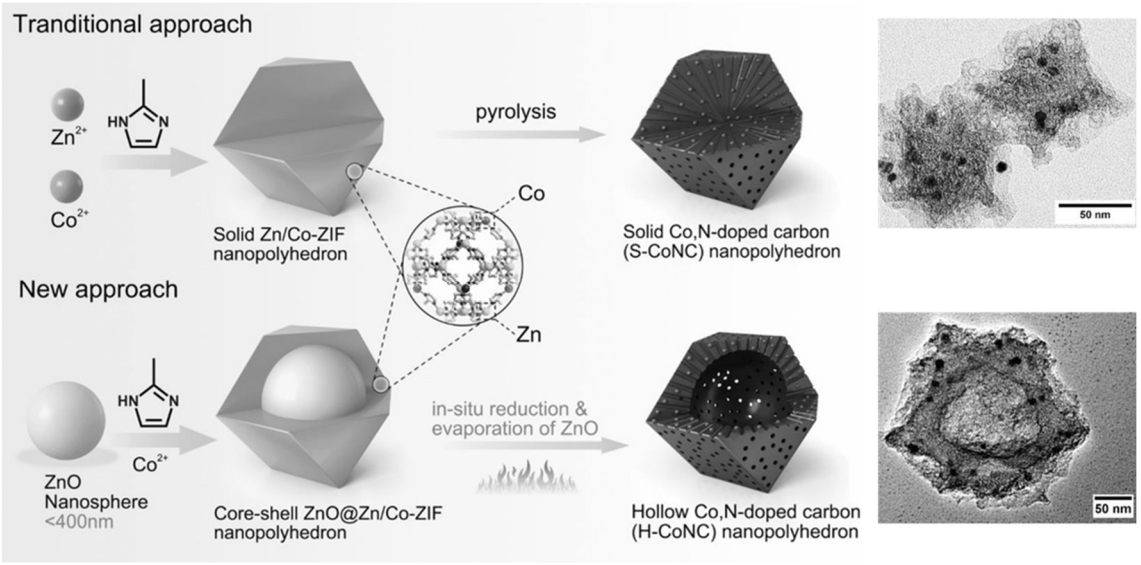

Fig. 26. 0D ZnO nanosphere directed synthesis of S-CoNC and H-CoNC (Reproduced with permission.[415] Copyright 2017, John Wiley & Sons).

Zero-dimensional carbons: Song *et al.*[415] demonstrated a synthesis of 0D hollow Co and N co-doped carbon nanopolyhedra (H-CoNC) by using ZnO nanospheres as self-sacrificing templates. Zn/Co-ZIF shell epitaxially grew on the surface of ZnO nanospheres in a mixed solvent of DMF/H_2O (3:1 v/v ratio) at 50 °C. The ZnO@ZIF precursors were converted to H-CoNC after carbonization at 900 °C in the N_2 atmosphere and HCl washing. For comparison, solid Co and N-codoped carbon nanopolyhedra (S-CoNCs) without hollow cavity was prepared by pyrolysis of conventional bimetallic Zn/Co-ZIF (Fig. 26). It was revealed that the ZnO mediated-strategy had several advantages over the template-free conformal transformation. *In situ* evaporation of the excess Zn species during pyrolysis can *i*) etch the carbon shell and enlarge the pores, leading to formation of well-developed hierarchical pore system ranging from 9 nm to 290 nm; *ii*) help to retain more Co and N contents in carbon frameworks. In addition, the excess Zn supply could break the tradeoff between Zn and Co content, which is observed in the conventional S-CoNC. Thus, the Co and N contents increased with an increase of the ZnO/ZIF mass ratio; and *iii*) allow more homogenous Co-N_x distribution throughout the structures. The XPS depth profile analysis revealed that the chemical distributions of Co and N in the H-CoNC remained constant from the outer shell to inner core, whereas the concentration gradient was observed in S-CoNC. As a result, the H-CoNC showed excellent materials properties superior to those of S-CoNC, for instance, enlarged hierarchical pores (9-290 *vs.* 20-160 nm), high Co (0.97 *vs.* 0.35 wt%) and nitrogen content (9.75 *vs.* 3.24 at%), and homogenously distributed Co-N_x sites. Similarly, Chai *et al.*[416] prepared the hollow N-doped carbon materials through multiple transformation steps from amorphous Zn-BTC coordination polymers to ZnO microspheres to ZnO@ZIF-8 to final hollow N-doped carbon spheres. Hollow carbons with 25 nm-thin walls comprised of highly porous carbon polyhedrals were elaborately constructed.

The direct chemical bonding of organic ligand and MOs under "solvent-free" condition has been developed to prepare carbon coated MOs. Mai and coworkers[417] reported SnO_2/Co@carbon *via* thermal solid phase reaction of hollow $CoSn(OH)_6$ cubes and excess 1,4-benzenedicarboxylic acid. The coordination reaction occurred at the exterior surface of the $CoSn(OH)_6$ cubes at 300 °C, and the un-reacted organic ligands vaporized at 320 °C under air. The uniformly coated MOFs were converted to carbon shell after pyrolysis under Ar atmosphere. Similarly, N-rich carbon wrapped $CoSnO_3$ particles were prepared by heating a mixture of $CoSnO_3$ and Hmim in a Teflon-lined autoclave at 200 °C for 24 h without the solvents.[418] Upon heating, the Hmim was melted and impregnated into the $CoSnO_3$, and reacted with Co^{2+} to form ZIF-67 at the both internal and external surface of the $CoSnO_3$ nanoboxes. The original morphologies were well-retained after MOF growth and carbonization at 500 °C under Ar atmosphere. As the amount of Hmim increased, the carbon (7.5-24.6 at%) and nitrogen content (2.4-7.6 at%) increased accordingly. This strategy eliminates the solvent-related synthesis steps (*e.g.*, washing, separation, drying) and associated problems (*e.g.*, uncontrollable MOF growth in the bulk solution), therefore could be an attractive alternative for MOF/carbon coating on various MO substrates.

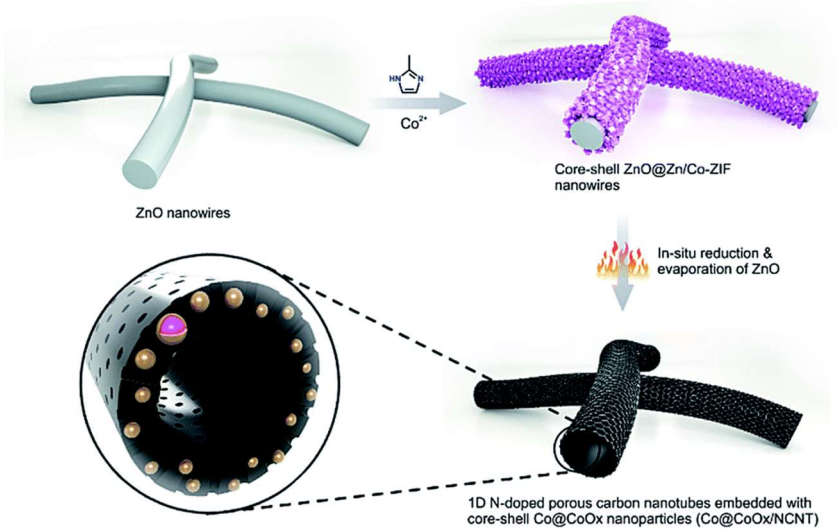

Fig. 27. 1D ZnO nanowires directed synthesis of Co@CoO_x/NCNTs. The magnified view indicates the existence of core–shell Co@CoO_x nanoparticles embedded in the porous carbon nanotube (Reprinted with permission.[419] Copyright 2017, The Royal Society of Chemistry).

One-dimensional carbons: 1D N-doped porous carbon nanotubes embedded with core-shell Co@CoO_x nanoparticles (Co@CoO_x/NCNTs) were prepared by one step carbonization of bimetallic ZnO@Zn/Co-ZIF nanowires at 900 °C for 2 h under a N_2 atmosphere (Fig. 27).[419] Here the ZnO nanowires (ZnONWs) acted as templates, Zn^{2+} ion sources and specific nucleation sites for bimetallic Zn/Co-ZIF growth. In addition, *in situ* evaporation of Zn during pyrolysis mitigated the undesired aggregation of the carbon particles and generated hierarchical pore structures as well as tubular morphology. Notably, ZnONW also plays a crucial role for *in situ* formation of Co@CoO_x nanoparticles by providing the excess oxygen species which directly reacted with metallic Co nanoparticles during one-step pyrolysis. In the conventional ZIF pyrolysis, such Co@CoO_x core-shell structures can be prepared only after additional heat treatment under an oxidizing gas atmosphere.

The other types of metal containing 1D-solid matters have been employed for directing the growth of MOF and carbonaceous materials. Starting from cobalt oxalate microtubes, Ahn *et al.*[420] synthesized the Co- and N-doped 1D carbon microtubes composed of hollow nanospheres and CNTs. Due to the presence of oxalate species, the formation of ZIF-67 nanocrystals was largely retarded and confined in the cobalt oxalate microtubes. The cobalt species selectively reacted with Hmim in an ethanol solution for various conversion times, which greatly affected the final tubular morphologies. As the conversion time increased from 4 to 24 h, the diameter, the surface roughness, and the aspect ratio of carbon microtubes increased. *In situ* formed Co metallic species during pyrolysis at 800 °C catalyzed the growth of tiny CNTs, and left behind hollow nanospheres after HCl etching.

Chen *et al.*[421] used electrospun poly(acrylonitrile) (PAN)/cobalt acetate ($Co(Ac)_2$) nanofibers for fabrication of hierarchical CNT/hollow Co_3O_4 microtubes. The proposed multi-step routes consist of multiple steps, *i.e.*, the surface growth of ZIF-67 nanocrystals on PAN/$Co(Ac)_2$ nanofibers in an ethanolic Hmim solution, dissolution of the PAN/$Co(Ac)_2$ core in DMF, thermal annealing in Ar (95%)/H_2(5%) atmosphere at 750 °C, and calcination in air at 360 °C. Two-step reduction-oxidation treatments are important for the generation of unique hierarchical structures. Ar/H_2 treatment completely reduced the CoO_x species to Co metals which led to formation of multiwalled CNTs throughout the microtubes. Following mild oxidation treatment converted Co solid nanoparticles into Co_3O_4 hollow nanoparticles with size of 15-30 nm due to Kirkendall effect. The resulting hierarchical microtubes were composed of hollow CNT/Co_3O_4 nanoparticles with inner diameters of 3.2/10.5 nm, respectively.

In a similar manner, PAN/$Zn(Ac)_2$/$Co(Ac)_2$@bimetallic Zn/Co-ZIF nanofibers were also prepared to obtain N-doped 1D carbon hollow tubules with tunable porosity and a large fraction of graphitic layers.[422] The PAN/$Zn(Ac)_2$/$Co(Ac)_2$ core turned into carbon/ZnO/Zn_xCo, which was then etched away *via* carbothermal reduction and evaporation. *In situ* TEM study during carbonization confirmed that the formation of ZnO - derived from $Zn(Ac)_2$ - was only localized in the fiber core. This preparation process enabled the selective etching of the carbon core, which leads to numerous internal voids. Therefore, the final porous/hollow structures were largely influenced by the amount of $Zn(Ac)_2$ in the initial precursor solution. Indeed, the morphology changes from solid fibers to hollow tubules even with a few carbon nanosheet-shells were clearly observed with increasing the amount of $Zn(Ac)_2$.

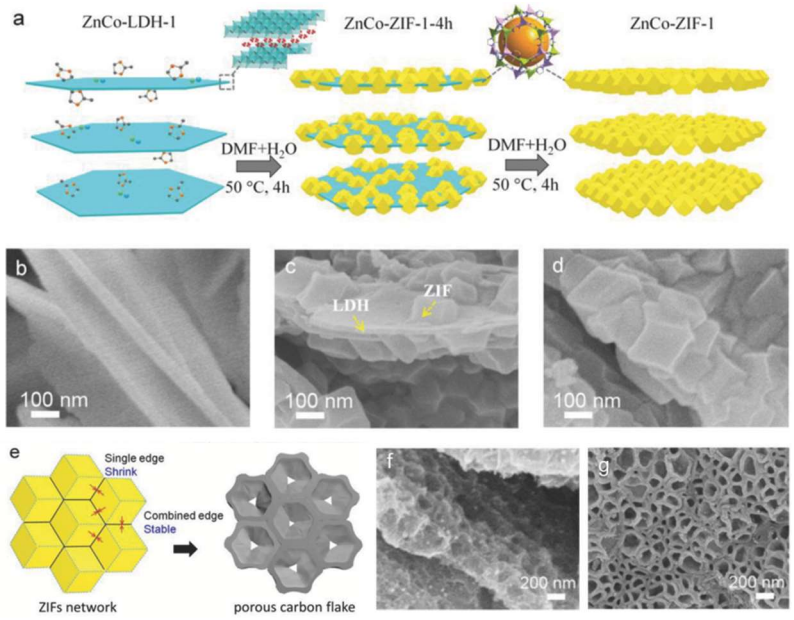

Fig. 28. 2D ZnCo-LDH derived synthesis of 2D ZIF and carbon flakes. **a)** Schematic illustration of the synthesis of ZIF networks. SEM images of **b)** ZnCo-LDH-1, **c)** ZnCo-ZIF-1-4h, and **d)** ZnCo-ZIF-1. **e)** Schematic illustration of the pore formation mechanism. SEM images of **f, g)** 2D honeycomb-like carbon flakes (Reproduced with permission.[423] Copyright 2018, John Wiley & Sons).

Two-dimensional carbons: 2D porous ZnO nanosheet was the first choice to demonstrate the preparation of 2D ZIF-8 and carbon materials with hierarchical porosity.[424] On the other hand, layered double-metal hydroxide (LDH) and metal hydroxide have great potential as 2D scaffolds and self-sacrificial metal ion sources for *in situ* MOF growth as well. LDHs inherently possess a plentiful amount of coordinatively unsaturated metal sites on their surface, providing specific anchoring sites for MOF deposition. Indeed, *in situ* ZIF-67 deposition to CoAl-LDH nanoplatelets was demonstrated by Wei and coworkers.[425] In their contribution, however, surface Co ions in CoAl-LDH served as preferential nucleation sites only and additional Co source was needed for controllable ZIF-67 growth.

The use of LDH as true reactive external template was demonstrated by Yamauchi and coworkers[423] for preparation of 2D honeycomb-like carbon flakes. ZnCo-LDHs with a lateral size/thickness of 1 µm/10 nm were dispersed in mixed solvent of DMF/H_2O (9:1 v/v ratio), and subsequently underwent transformation to ZnCo-ZIFs through the reaction with Hmim at 50 °C. ZIF polyhedrals with a diameter of 100 nm began to grow on the flat surface of ZnCo-LDH after 4 h, and they formed densely packed flake-like networks after 8 h (Fig. 28a-d). The Zn/Co molar ratio in parent ZnCo-LDH was comparable to that in daughter ZnCo-ZIF, suggesting the homogeneous reaction between dissolved metal ions and Hmim. 2D-interconnected carbon flakes with abundant honeycomb-like macropores were produced *via* carbonization at 800 °C and acid etching, during which ZnCo-ZIF suffered from inhomogeneous framework shrinkage (Fig. 28e-g). This shrinkage is closely related to tightly packed networks of ZIF polyhedrons. The connected edges that intimately adhere with adjacent polyhedrons were stable and well-retained during carbonization. In contrast, the exposed single edges without intimate contact with the others were unstable and shrank toward the edge sides, thereby leading to formation of honeycomb-like macropores. This formation strategy was also applicable to ZnCo-LDH with a different molar ratio and other layered metal hydroxide

($Zn_5(OH)_8(NO_3)_2$, $Co(OH)_2$), allowing the preparation of carbon flakes with similar morphologies and honeycomb structures but with different specific surface area (226-860 $m^2 g^{-1}$), pore volume (0.75-1.45 $cm^3 g^{-1}$), nitrogen content (1.1-12.9 at%), and degree of graphitization.

Three-dimensional and hierarchical carbon: The methods to process MOs into complex morphologies and architectures are better established than those of MOFs, and thus could enrich the structure engineering tools for the MOF-derived carbonaceous materials. Along this line, Song *et al.*[426] employed pre-shaped ZnO templates with different morphologies (*i.e.*, nanowires (1D), nanoplates (2D), and nanoflowers (3D)) as architecture directing agents for general dimension-controlled synthesis of hollow carbons. A versatile approach to synthesize core-shell ZnO@ZIF-8@Zn/Co (or Fe)-ZIF was presented. ZnO@ZIF-8 was easily prepared by adding Hmim to ZnO suspension. However, in the case of bimetallic Zn/Co-ZIF shell growth, the sequence of precursor addition plays a crucial role in determining the final crystal morphologies. The simultaneous addition of Co salt and Hmim to the ZnO suspension led to rapid formation of $Co(Hmim)_4^{2+}$ complex in the bulk solution (pathway 1 in Fig. 29a). The released Zn^{2+} directly reacted with the $Co(Hmim)_4^{2+}$ and Hmim to form $Co_xZn_{1-x}(Hmim)_4^{2+}$, rather than $Zn(Hmim)_4^{2+}$ complex. As a result, Zn/Co-ZIF nucleated either in bulk solution or on the rugged surface of ZnO. With increasing the reaction time, Zn/Co-ZIF grew to 0D polyhedra by continuously extracting the Zn^{2+} ions from ZnO until its full dissolution. Because of this inhomogeneous and uneven growth process, part of the ZnO was encapsulated by the Zn/Co-ZIF layers, resulting in formation of ZnO@Zn/Co-ZIF polyhedrons (Fig. 29b). In contrast, one-by-one addition of Hmim followed by Co salt led to controlled epitaxial growth of ZIFs on ZnO templates (pathway 2 in Fig. 28a). The ZIF-8 seed layers ~ 40 nm were rapidly formed on the surface of ZnO within a short time <10 min. Subsequent addition of Co salt induced the formation of $Co_xZn_{1-x}(Hmim)_4^{2+}$ specifically on the ZIF-8 layers, and therefore Zn/Co-ZIF uniformly nucleated and deposited onto the ZnO. The secondary Zn/Co-ZIF layers prohibited the complete dissolution of inner ZnO templates, forming the ZnO@ZIF-8@Zn/Co-ZIF heterostructures (Fig. 29c). The resulting ZnO@ZIF hybrids were transformed to hollow carbon/metal composites *via* one-step pyrolysis at 900 °C under N_2 atmosphere. ZnO was carbothermally reduced and evaporated upon pyrolysis, leaving hollow inner structures and macropores. Co and Fe metals catalyzed the formation of graphitic carbon and remained well-dispersed in the form of nanoparticles (Co) or single atoms (Fe). The particle morphologies inherited from parent ZnO templates (1D nanowires, 2D nanoplates, 3D nanoflowers) were well-preserved without significant deformation (Fig. 29d-f).

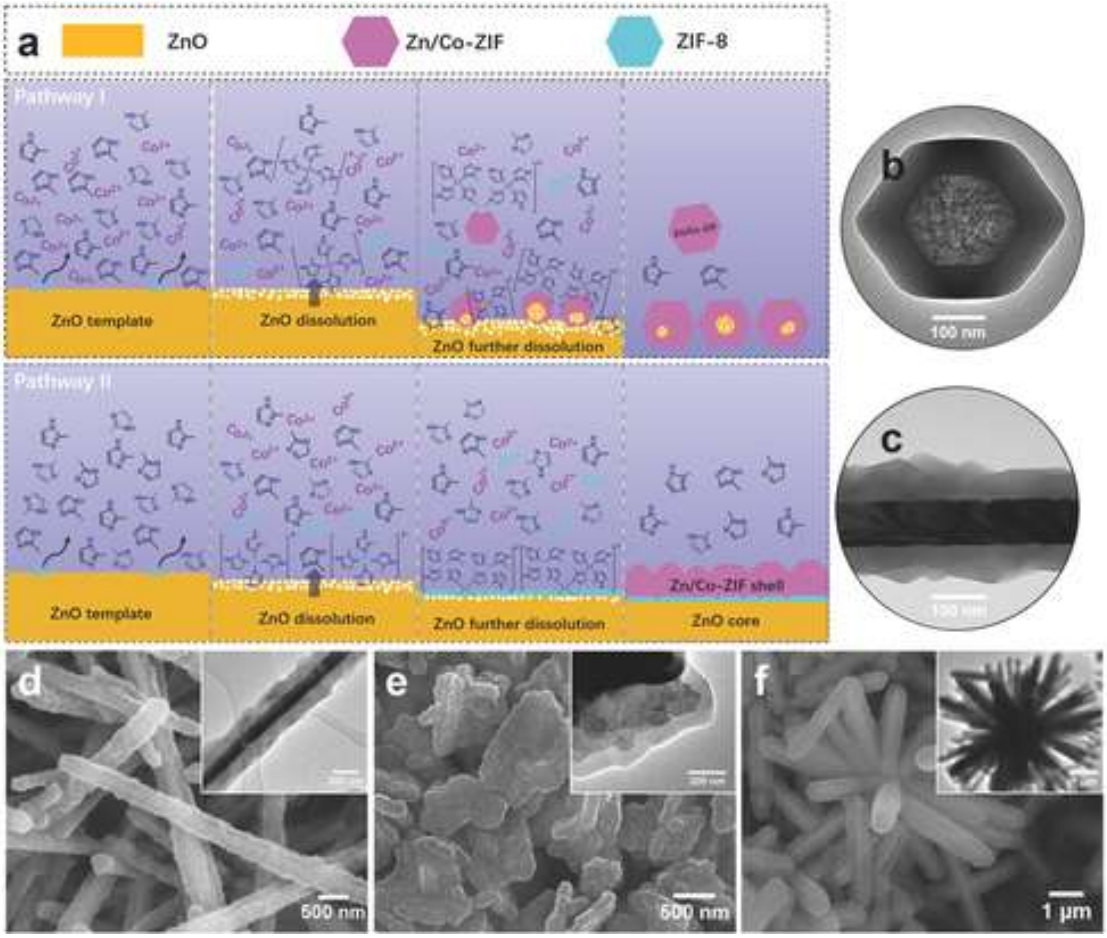

Fig. 29. Dimension controlled ZnO directed synthesis of hollow carbons. **a)** Schematic representation of the growth of bimetallic Zn/Co-ZIF using ZnONW as a template under different precursor addition sequences. TEM images of **b)** ZnO@Zn/Co-ZIF nanopolyhedron and **c)** core–shell ZnONW@ZIF-8@Zn/Co-ZIF. SEM images and the corresponding TEM images (inset) of **d)** 1D ZnONW@ZIF-8@Zn/Co-ZIF, **e)** 2D ZnONP@ZIF-8@Zn/Co-ZIF, and **f)** 3D ZnONF@ZIF-8@Zn/Co-ZIF. The products were collected at a reaction temperature of 45 °C after 2 h reaction (Reprinted with permission.[426] Copyright 2018, John Wiley & Sons).

Urchin-like nanorods of cobalt carbonate hydroxide (UNR CCH) were also utilized as architecture directing agents to prepare urchin-like nanotubes of Co single atoms/nitrogen doped carbon (UNT Co SAs/N-C).[427] UNT ZIF-67 superstructures were firstly prepared by hydrothermal reaction of UNR CCH powders with Hmim in Teflon-lined autoclave at 150 °C, followed by HCl washing. They were subjected to thermal treatment at 500 °C in a sealed vacuum environment, which can facilitate the formation of well-dispersed Co single atoms. Therefore, multidimensional hierarchical tubes comprised of carbon dodecahedron with embedded Co SAc were successfully synthesized.

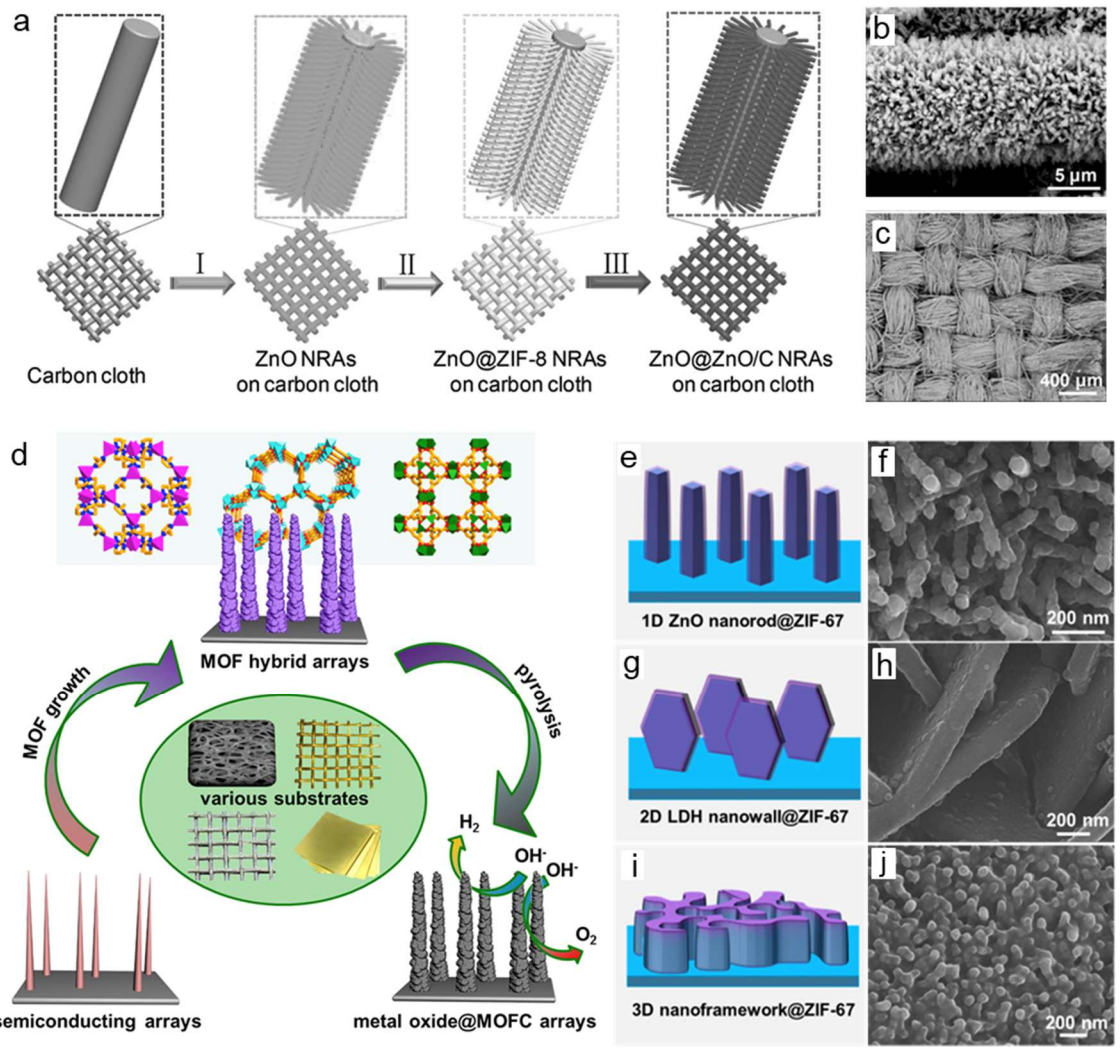

Fig. 30. 3D carbon array structures. **a)** Schematic illustrating the synthesis procedures of ZnO@ZnO QDs/C core–shell NRAs on carbon cloth. **b, c)** High and low magnifications of core–shell ZnO@ZnO QDs/C NRAs grown on flexible carbon cloth (Reproduced with permission.[281] Copyright 2015, John Wiley & Sons). **d)** Schematic illustration showing the fabrication of MO@MOF hybrid arrays and their derived MO@MOFC arrays on the 3D conductive matrix (Reprinted with permission.[310] Copyright 2017, Elsevier). Electrosynthesis of ZIF-67 on Ni-foam supported **e, f)** 1D ZnO nanorod, **g, h)** 2D LDH nanowall, and **i, j)** CoNi-alloy (Reproduced with permission.[428]).

The MO and hydroxide arrays with different morphologies and compositions can be grown on a wide variety of substrates (*e.g.*, carbon cloth, metal foam/mesh/foil, and fluorine doped tin oxide (FTO) glass) by means of hydrothermal reaction, electrochemical deposition and *etc.*[405] They are readily described in a number of literature examples and therefore can be used as versatile self-sacrificing architecture directing agents to realize 3D carbon arrays with complex morphologies and unique multi-functions.[281, 310, 428-431] For instance, 3D architectures ensure the facile mass transport ability and the easy accessibility to catalytic active sites, and also support the MOFs to maintain their structural integrities without significant particle aggregation/collapse during thermal transformation. The substrates enhance the mechanical stability, and serve as a consecutive conductive network for fast electron/ion transport. As a result, such 3D integrated carbon composites have been popularly

adopted as binder-free, conductive additive-free self-supported electrodes in energy storage and conversion devices, such as flexible supercapacitor, electrochemical water splitting, Zn-air battery, Li and Na ion battery.[281, 310, 405, 428-431]

In 2015, Duan and coworkers[281] described the integration of metal oxide array and conductive substrate for the first time to develop ZnO@ZnO quantum dots (QD)/C core-shell nanorod arrays (NRA) on flexible carbon cloth (Fig. 30a-c). ZnO NRAs with the diameter/length of 300 nm/4.5-7 μm were vertically grown on carbon cloth by hydrothermal deposition route, and further served as sacrificial template and Zn ion source for ZIF-8 shell growth. They reacted with Hmim ligand in a mixed solvent of DMF/H_2O (3:1 v/v ratio) at 70 °C, yielding ZnO@ZIF-8 NRAs. Thermal annealing under N_2 gas flow at 650 °C led to formation of ZnO@ZnO QD/C with multi-dimensional hierarchical architectures. Starting from identical ZnO@ZIF-8 NRA on carbon cloth, the same group also fabricated N-doped carbon bubbles supported on carbon tube arrays *via* catalytic deposition of ethanol and reduction-evaporation process.[429] The ethanol vapour penetrated the ZIF-8 shell to access the surface of ZnO core where the catalytic ethanol decomposition-carbon deposition occurred at high temperature (500-800 °C). During this process the continuous ZIF-8 shell layer cracked into discrete ZIF-8 nanocrystals. Following H_2/Ar gas reduction at 800 °C rapidly generated nano-sized Zn metals, which were completely removed by evaporation without additional acid etching. This process directly converted the ZnO@C@ZIF-8 to hollow carbon tubes@N-doped carbon bubbles. Yang *et al.*[430] further employed the ZnO@ZIF-8 NRAs as versatile precursors for fabrication of other types of hybrid materials with tailored chemical structures and compositions. ZnO@C@CoNi-LDH arrays were prepared by pyrolysis of ZnO@ZIF-8 and subsequent electrochemical deposition of CoNi-LDH nanoplatelets on the external surface of ZnO@C. In parallel, Fe_2O_3@C NRAs were synthesized by converting ZnO@ZIF-8 to $Fe(OH)_3$@ZIF-Fe through Zn-Fe cationic exchange in aqueous solution at room temperature, followed by pyrolysis in N_2 atmosphere at 450 °C. The resulting ZnO@C@CoNi-LDH and Fe_2O_3@C were used as self-supported electrodes for fabrication of asymmetric flexible all-solid-state supercapacitors.

Solid cobalt materials (cobalt carbonate hydroxide (CCH) and cobalt oxide) were integrated with conductive metal substrates to prepare similar 3D architectures having different chemical compositions. ZIF-67 was directly grown on well-aligned CCH nanorods in Hmim/H_2O/triethylamine solution. Subsequent treatments of oxidation, sulfurization, carbonization and phosphorization gave rise to hierarchically structured Co_3O_4@X composites (where X = Co_3O_4, CoS, C, and CoP).[333] Huang *et al.*[432] modified this procedure to prepare CoP nanoarray wrapped by N, P-doped carbon on Ti foil. Instead of CCH arrays, Wang *et al.*[433] used hierarchical CoO nanowires on Ni foam to synthesize CoO@ZIF-67 and in turn CoO@N-doped carbons.

Jiang and coworkers[310] demonstrated fabrication of a series of well-defined MOF arrays/carbons grown onto various substrates (Fig. 30d). Different kinds of solid metal arrays (CoO, NiO and Cu(OH_2) were directly grown on diverse substrates (Ni foam, Cu mesh, Cu foil, and Fe mesh) by a hydrothermal method, then reacted with related organic ligands to form ZIF-67, Co-MOF-74 and HKUST-1. Pyrolysis under N_2 gas flow at 500 °C yielded the corresponding metal oxide@carbon on substrates with well-retained 3D array architectures. The authors found that the choice of appropriate solvents and solid metal precursors is critical for controlled MOF growth. For instance, the dissolution of CoO in ethanol is too slow to provide enough Co^{2+} ions for ZIF-67 formation, while that in water is too fast to confine the ZIF-67 nucleation on CoO nanorods exclusively. Furthermore, the use of Co_3O_4 instead of CoO only led to poorly defined heterostructures, possibly because of its

limited dissolution under the given synthesis condition. The successful preparation of CoO@ZIF-67 was achieved by using the mixed solvent of ethanol and water (1:1 v/v ratio). Therefore, it was revealed that the balance between the MO dissolution and MOF precipitation rate is crucial for the preparation of desired hybrid MOF/carbon arrays, which is also important for applications in hydrogen evolution reaction (HER) (refer to section 6).

Despite of these progresses, a versatile approach for continuous MOF deposition with controllable thickness and dimension is still considerably lacking. One possible strategy to overcome this challenge is electrodeposition of MOF on shape-controlled MO/conductive substrates. Shao and coworkers[428] demonstrated electrosynthesis of ZIF films on commercial conductive substrates (FTO glass, carbon fiber cloth, and Ni foam) (Fig. 30e-j). ZIF-8, ZIF-67 and bimetallic Zn/Co-ZIFs with various molar ratios and thickness were electrochemically deposited on the conductive substrates (working electrodes). OH^- generated from H_2O on the working electrodes rapidly reacted with $M(Hmim)_4^{2+}$ complex to form $M(mim)_2$ solids within tens of seconds at ambient temperature. The authors also reported electrodeposition of ZIFs to the nanostructured solid metal arrays with different morphologies (1D ZnO nanorod array, 2D CoAl-LDH nanowall array and 3D CoNi-alloy nanoframework), and their thermal transformation to hierarchically structured CNTs. In addition, electrodeposition could be highly attractive for the case in which direct growth of MOF is not possible because of the incompatibility between conductive substrate and MOF. For instance, Feng *et al.*[434] demonstrated electrodeposition of $Co(OH)_2$ on a carbon fiber paper to deposit ZIF-67 in a controlled manner, which is not achievable by direct MOF growth method. Very recently, Chen *et al.*[435] vertically grew 2D Co-LDH nanosheets on HNO_3-treated carbon cloth *via* a fast electrodeposition process, and utilized them as self-sacrificial templates that underwent coordination reaction with Hmim in H_2O/MeOH (1:1.5 v/v ratio) to induce ZIF-67 crystal growth and associated structural reconstruction. ZIF-67 dodecahedra tended to grow/graft on the top of the nanosheets, resulting in formation of 2D ZIF-67 nanosheets grafted with 3D ZIF-67 dodecahedra (2D/3D ZIF-67). They were transformed into ultrafine Co nanoparticle embedded 2D N-doped porous carbon nanosheets and 3D hollow N-doped porous carbon polyhedron, respectively.

Solution phase MOF deposition often involves the precise choice of solvents, solid metal precursors, substrates, ligands, and reaction temperature as well as potential risks for substrate corrosion and contamination. These factors can impose limitations on controlling thickness and morphology of the MOF layer. To address this issue, solvent-free MOF growth techniques such as hot pressing,[436] steam assisted conversion,[437] and chemical vapour deposition (MOF-CVD)[271] have been developed in recent years. MOF-CVD has shown promise as a versatile method that conformally transforms complex 3D structures into continuous MOF films with uniform and controlled thickness by simply exposing the substrate to ligand vapour at moderate temperature (*e.g.,* 100 °C). Inspired by this, Young *et al.*[431] reported MOF-CVD mediated synthesis of MOF arrays on carbon cloth. Hydrothermally grown ZnO and $Co(CO_3)_{0.5}(OH)\cdot 0.11H_2O$ arrays were exposed to Hmim vapour in a Teflon-line autoclave at various temperatures (90-120 °C) and for various times (3-24 h) to deposit ZIF layers with controlled thickness. Two-step carbonization and oxidation treatments led to their conversion to MO/carbon composites (*e.g.*, Co_3O_4/N doped carbon arrays on carbon cloth).

Challenges and opportunities: The reactive external template methods usually rely on multi-step procedures and thus are rather complicated and costly. However, the associated disadvantages could be largely compensated by development of multi-functional, high-value added carbon materials that

are otherwise not accessible. The fast and economical routes for fabrication of sophisticated architectures would be highly appreciated in the future. Solid precursors from large-scale industrial production or earth-abundant natural minerals are attractive low-cost raw materials. In addition, to date, the chemical composition of parent MOs is restricted to a few substances, mostly Zn and Co based ones. Many others still remain unexplored because of the lack of general criteria that govern the solid-to-MOF transformation. In the case of solution phase syntheses, the balance between the release rate of metal ions from the solid matters and the coordination rate of metal ions with ligands is critical for the controlled MOF growth. The solvent composition and reaction temperature also need to be optimized to localize the MOF nucleation only at the surface of MOs. However, the understanding of underlying growth kinetics and thermodynamics are still considerably lacking. In this regard, the high throughput methods are needed to rapidly screen the potential solid precursors and to establish the suitable transformation conditions. Taken together, there are still great opportunities to develop multi-functional carbonaceous materials constructed by hierarchically assembled multi-component building blocks (MO, MOFs, carbon, and substrates) through the reactive external template methods.

5.2.4. Carbon derived from top-down processed MOF

The aforementioned three strategies control the bottom-up assembly of metal ions and organic ligands in combination with various templates and substrates. In contrast, top-down processing uses the 'pre-synthesized MOFs' as building blocks for microfabrication (*e.g.,* electrospinning,[438] 3D printing[439]), chemical etching[440] and exfoliation[441] to obtain desired morphologies. Thanks to the recent progress in the development of new processing technologies and the nano-MOFs, top-down MOF fabrication has become more easily accessible, thereby boosting the development of MOF-derived carbonaceous materials with unique structures and morphologies.

Zero-dimensional carbons: Chemical etching is a typical top-down approach to generate voids inside of solids. In recent years, controlled etching of preformed MOF crystals has attracted great interest as a means to prepare meso/macroporous MOF, hollow MOF, and complex multi-shelled MOF,[364] opening up new opportunities for preparation of void-engineered carbon materials. Zhang *et al.*[440] reported MOF nanobubbles with monocrystalline frameworks and their transformation to hollow carbons *via* pyrolysis (Fig. 31a). By simply immersing the preformed ZIF-8 in tannic acid solution for 5 min, hollow ZIF-8 nanobubbles with thin shell of 15 nm were obtained. Tannic acid acts as both etching agent and surface protecting layer. It releases free H^+ ions which can destroy the framework. Tannic acid itself is too large to penetrate into the MOF and thus adsorbs on the exposed surface of MOFs only, protecting the outer part from complete etching. In this way, the free H^+ ions selectively etch the inner core of MOFs, generating hollow ZIF-8 nanobubbles. Of particular advantage of etching strategy is its ability to maintain inherent single-crystalline nature of parent MOFs, ensuring a highly ordered crystallographic orientation. Although other hollow MOFs have been prepared by direct growth/assembly of MOFs on spherical templates, they are comprised of a number of aggregated MOF nanocrystals (*i.e.*, polycrystalline) with ill-defined particle orientation and non-uniform size. In contrast, the etching-derived ZIF-8 nanobubbles retain monocrystalline nature as well as uniform and smooth surface which cannot be obtained from the conventional template methods. Moon and coworkers[442] synthesized adamantine shaped, hierarchically micro- and macro-porous, N-doped carbon nanoframes *via* acid etching of ZIF-8 in an aqueous xylenol orange

tetrasodium salt/HCl solution. Preferential etching along <211> direction led to formation of unique adamantine-like particle shape.

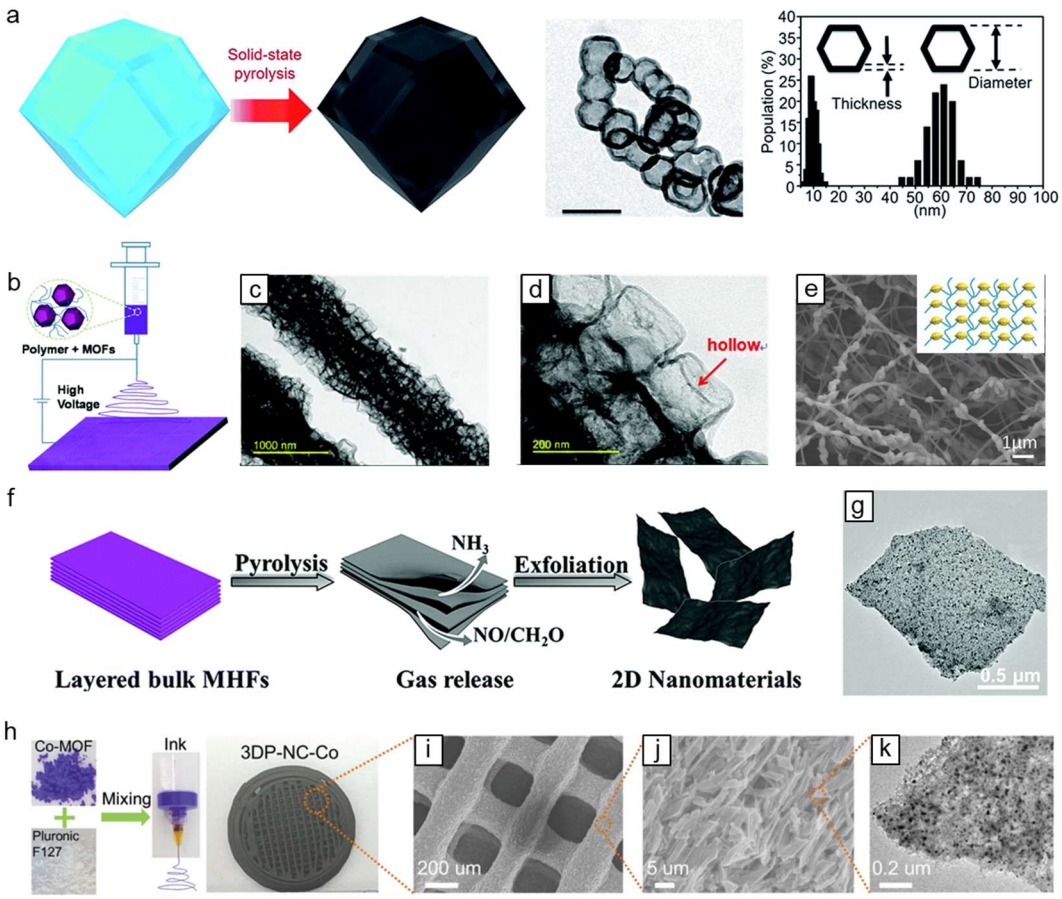

Fig. 31. Carbon derived from top-down processing of MOFs. **a)** Acid etching derived synthesis of 0D carbon nanobubbles (Licensed under CC-BY[440]). **b)** Electrospinning of 1D MOF-based nanofibers from the precursor solution of preformed MOF nanoparticles and polymers fibers (Reproduced with permission.[438] Copyright 2018, The Royal Society of Chemistry). **c, d)** Electrospun ZIF-8/PAN-derived 1D porous carbon fibers (Reproduced with permission.[443] Copyright 2017, The Royal Society of Chemistry). **e)** Electrospun MIL-88@PAN-derived carbon necklace papers (Reproduced with permission.[444] Copyright 2018, John Wiley & Sons). **f)** Thermal exfoliation/carbonization of layered bulk metal-hexamine frameworks to 2D carbon materials (Reprinted with permission.[445] Copyright 2018, The Royal Chemical Society). **h)** The 3D printing diagram, and **i-k)** 3D printed nitrogen doped mesoporous carbon flakes with embedded Co nanoparticles (Reproduced with permission.[439] Copyright 2019, John Wiley & Sons).

One-dimensional carbon: Electrospinning is a simple and straightforward top-down approach for production of 1D nanofibers, and is by far the most extensively used method for processing MOFs/MDCs into 1D nanowires and nanotubes (Fig. 31b).[438] In addition, the nanofibers can be directly deposited onto certain substrates or processed into functional textiles and free-standing papers. Combining with a large variety of nano-MOFs, electrospinning has a great potential in development of a number of new 1D porous carbon and carbon-based composite materials. Typical fabrication steps involve: *i*) preparation of the precursor solutions of preformed nano-MOFs and polymers, *ii*) electrospinning to MOF-based nanofibers, and *iii*) carbonization. The intimate

interaction between MOFs and polymeric binders is necessary to maintain the structural integrity of 1D nanofibers with uniformly distributed/confined MOF nanocrystals. For this purpose, the polymers with functional moieties that can interact/coordinate with the exposed metal ions on the surface of MOFs have been widely used (*e.g.,* PVP,[446] PAN,[443, 447] poly(vinyl alcohol) (PVA)[448]). For instance, the surface Zn^{2+} ions in ZIF-8 can coordinate with the C≡N moieties abundantly present in PAN,[443] which enables homogeneous and uniform distribution of ZIF-8 nanocrystals in the PAN matrix. Upon pyrolysis, PAN-derived carbons were generated at the early stage of thermal transformation, tightly encapsulating ZIF-8 nanocrystals to change their pyrolysis behavior. Because of the strong cohesive interfacial interaction between ZIF-8 and PAN-derived carbon, ZIF-8 decomposed with significant shrinkage from inside to outside, thereby generating uniform mesopores or hollow structures (Fig. 31c, d). In addition, several functional 1D porous carbon materials have been prepared from ZIF-8, ZIF-67 and bimetallic Zn/Co-ZIF.[443, 446, 448, 449] Interestingly, MOF (ZIF-67 and MIL-88) nanoparticles strung on the thin PAN fibers can be fabricated by carefully controlling the electrospinning conditions (Fig. 31e).[444] The PAN strings bridged the MOF joints and well-entangled to form interconnected network, which led to formation of free standing carbon necklace papers after pyrolysis under N_2 atmosphere.

Two-dimensional carbons: Top-down synthesis of MOF nanosheets relies on the exfoliation of layer-structured bulk MOFs.[441] The weak interlayer interactions, *e.g.*, van der Waals forces, hydrogen bonding, π-π stacking, can be broken by sonication, mechanical- and chemical-exfoliation. Although the exfoliated MOF nanosheets have shown promise in a myriad of applications,[441] however, they are rarely exploited for fabrication of 2D nanocarbons mainly because of the high cost and low yield of exfoliation methods, as well as structural collapse/restacking of nanosheets during carbonization. Recently, facile thermal exfoliations of layered MOFs into 2D N-doped carbon nanosheets[445] and graphene stacks[450] were reported. Fast pyrolysis (ramping rate >5 °C min^{-1}) rapidly generated a large amount of gases which exfoliated/converted the layered bulk metal-hexamine frameworks to 2D carbon materials (Fig. 31f).[445] Zhang *et al.*[450] carbonized the MOF crystals with stacked 2D lamellar structures at 500 and 900 °C for 1 h with a slow ramping rate (1 °C min^{-1}). During this mild thermal treatment, the gradual structural rearrangements occurred from MOF 2D subunits to 2D nanocarbon stacks. Xia *et al.*[451] prepared N-doped porous graphene by thermal exfoliation of ZIF-L in the presence of LiCl/KCl salts under inert atmosphere at 700-900 °C. The LiCl/KCl salts acted as exfoliator and etching agent. The metal ions from molten salt (>369 °C) inserted into the crystal layers first, and then induced thermal exfoliation and formation of micro- and mesopores *via* vaporization at higher temperature (>700 °C). Final 2D ultrathin carbon nanosheets were obtained after removal of residual metal salts and impurities through acid washing. Alternatively, Xu and coworkers[373] combined the conformal transformation of MOF with chemical exfoliation to obtain few-layered graphene 2D nanoribbons. The MOF-derived solid carbon nanorods were exfoliated to two- to six-layered graphene nanoribbons through a KOH-assisted sonochemical treatment and thermal activation at 800 °C. This novel strategy enabled the preparation of high-quality graphene nanoribbons with high yield (>75%) and purity (>90%), which are higher than those obtained from the exfoliation of CNTs.

Three-dimensional carbons: 3D printing, also known as additive manufacturing, has attracted significant attention both in industry and academia.[452] It allows direct fabrication of prototype-objects and patterns based on the digitally controlled deposition of successive layers of material.

Recently, this technology was successfully applied for manufacturing 3D complex structures of MOF-embedded polymers[453] and MOF-derived hierarchically porous carbon frameworks[439]. The printable ink was firstly prepared by mixing the Co-MOF (leaf-shape ZIF polymorph) and Pluronic F127 triblock copolymer in water, and then printed as fine filament layers to form 3D Co-MOF framework (Fig. 30g).[439] The 3D-printed mesh architectures enabled a uniform shrinkage to retain a good mechanical stability without cracking during carbonization at 800 °C. The resulting 3D carbon frameworks have hierarchical pore system (200 μm pores from inter-weaved filaments, meso- and micropores from Co-MOF-derived carbon flakes), uniformly embedded Co nanoparticles, high electric conductivity and mechanical stability (Fig. 31h-j).

Challenges and opportunities: Top-down processing opens up new possibilities toward the designable MDC architectures. Chemical etching enables the preparation of single-crystalline MDCs with tailored pore structures, yet is highly dependent on the stability of MOFs against the etchant solution. Exfoliations are mostly applicable to a few layer-structured MOFs. The construction of high-quality 2D MOFs and their conformal transformation without aggregation, restacking and structural collapse still remain great challenges. Therefore, development of low-cost, high yield, and versatile top-down methods is highly desired. Integrations of MOFs with microfabrication technologies are attractive approaches to obtain MDCs with sophisticated morphologies. For instance, the use of emerging technologies, *e.g.*, biomimetic 4D printing,[454] may allow programmed fabrication of bio-inspired complex 3D architectures that are pre-encoded with unique functions.

6. Applications

6.1. General aspects

The control of material morphology as well as understanding processes associating with material application is extremely important due to the inherent connection between physical and chemical properties. The whole purpose of demonstrating noteworthy affinity between seemingly different materials (MO, MOF and porous carbon) ultimately has to convey to their utility. We must accentuate that besides chemical designability (*e.g.* chemical composition) of materials, the physical designability (*e.g.* morphology) of materials is another essential factor. Physical designability of porous materials gives the opportunity to improve the material performance *via* design of the physical form rather than altering the chemical component, for instance, chitin assemblies build butterfly wings with nanostructures to impart hydrophobicity for a fly in rain and at the same time glaring colours to discourage predators. It is baffling to create a general scheme that directly links material's specific shape and size with its physical properties as both are mutually connected with the chemical composition. However, it is doable to show some pros and cons in certain applicability cases. For instance, it has been suggested that size of nanomaterial particles has a strong influence on their toxicity, more specifically smaller particles might be more toxic per mass-based concentration.[455] It led straight away to biomedical applications whereas particles surrounding such as cells, tissues or topical use can determine what nanomaterial size is required.[456] The size of particles is also significant in catalysis, where along with the lowering the size, the number of the active sites increases, which is desired for catalyst efficiency.[457] All in all, the application of porous materials is usually highly affected by the structuring and the morphology of the material, as both affects the optical properties, conductivities of electrons and ions, and the diffusion of gasses and

liquids through the materials that have a significant impact on larger scale application for gas storage, membranes and their use for chemical transformations, be it as a catalyst itself or as a support for such.

6.2. MOF applications

MOF nanoparticles and their more complex structures found application in many areas such as adsorption,[226, 458] separation,[459] catalysis,[460, 461] sensing,[462] optics,[463-465] magnetics,[466] drug delivery,[467] bioimaging,[468, 469] tribology,[470] patterning,[242] as well as data-,[471] energy-[251] and gas-[472] storage. Generally, for each application homogeneity of nanocrystals is mainly required. Nevertheless, to broaden detailed information about the dependency of morphology and implementation, it is important to present and distinguish how *e.g.* length of rods or size of globules affects processes parameters they are used in. Thus, here we report examples of different applications of MOF materials that are affected by both the shape and size of their particles.

MOFs are well known due to their porosity and high specific surface areas, thus they are a natural choice of materials for adsorption and separation.[473] Size and morphology are also valid for such processes, especially in terms of kinetics.[474] Homogeneous and smaller particles are usually more preferred to minimize diffusion limitations,[475] also along with that adsorption equilibrium time decreases.[476] Non-spherical anisotropic crystals are more required when it is necessary to obtain proper orientation in films or membranes.[477] Peculiar shapes are often less stable, whereas for sorption procedures defect-free surfaces are mostly needed.[280] Thicker films are usually more rigid, but they permeate much less gas or liquid. For that it has to be considered the synthesis of MOF-membranes with thickness less than 100 nm.[478]

The shape of the MOF crystals could have also an impact on the application of membranes in adsorption and separation processes. Some of them have a tendency to agglomerate which leads to a decrease in membrane selectivity. Thus, a compromise must be involved between choosing sophisticated or durable membrane without defects, such as pinholes or cracks,[479, 480] which ends up in either better selectivity or permeability.[481] An interesting example of how tuning MOF crystals morphology affected membrane applicability was presented by Zuo and Chung.[482] Their goal was to obtain nature-mimetic hydrophobic membrane for seawater desalination, by covering pristine ceramic tube surface with NH_2-MIL-53(Al). Depending on the source two different types of crystals were fabricated, flower-like and ordered nanocrystals (Fig. 32). The first one characterized with high aspect ratio which promotes the effective membrane surface area, but they were poorly aligned. The second MOF morphology made of small crystals were more suited for set goal since nanocrystals were small enough to cover whole surface leading to less defect probability. The influence of the MOF crystal morphology is particularly noticeable in MMMs composites (mixed-matrix membranes), consisted of MOF particles in a polymer matrix. Rodenas *et al*.[483] introduced copper-based MOF (CuBDC) with different morphologies like nanosheets and bulk crystals into the matrix. The prepared composites exhibited very different efficiency in CO_2/CH_4 separation. More uniform dispersion of nanosheets in the form of lamellae-like structure showed higher separation factors.

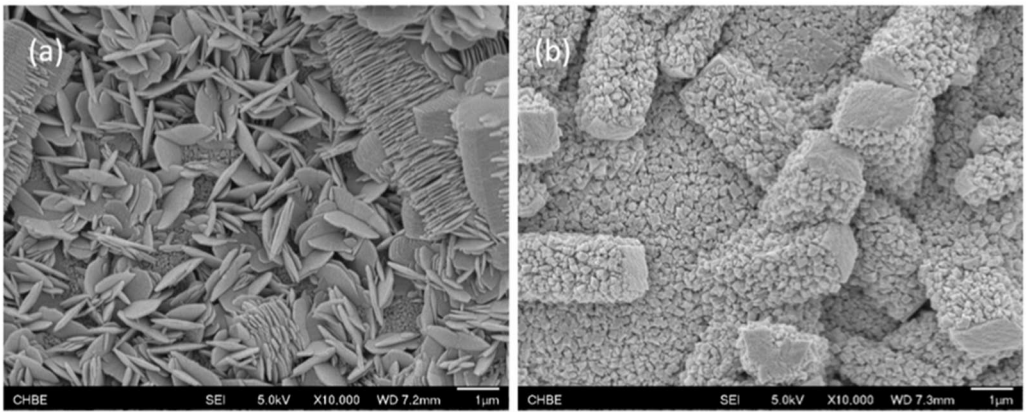

Fig. 32. Flower-like (left) and ordered nanocrystals (right) morphology of NH_2-MIL-53(Al) of the second growth tubes for seawater desalination (Licensed under CC-BY.[482]).

MOF storage capabilities are strictly the result of well-developed specific surface area and morphology ensuing from the crystalline facets. Gases, drug particles, pollutants or electrolytes differ in particle size. Due to the wide range of MOF crystal shapes, it is possible to control pore accessibility and dictate the way how such particles will be adsorbed, dispersed, bonded and stabilized. In the research of Li *et al.*[484] it was presented how sulfur performance in Li-S batteries was improved by using ZIF-8 with different sizes. In the range between 20 nm to 1 μm, smallest MOF particles were most efficient with sulfur implementation, however best cycling stabilization was achieved with average ones (~200 nm). Most beneficial dimensions of the particles were called *'golden size',* which definitely are difficult to discover and match with proper utility, nevertheless it should be fundamental for every conducted research. In another studies, it was suggested that define morphology made of MOF crystals can improve gas storage. Zr- and Cr-MOF within electrospun nanofibers revealed higher loadings towards H_2 and N_2, than single crystals.[485]

Bioapplication of MOF is mainly focused on drug delivery, but also on cancer cell targeting.[486] For the sake of biocompatibility, non-toxicity and safe decomposition of the selected OBIs and IBUs, they must be precisely investigated towards metabolic processes and other biocompounds reactivity. Besides the composition, undoubtedly morphology of the drug carrier has to be considered. It can enhance the dispersion of the API (active pharmaceutical ingredient), stabilize API-MOF system but also have an impact on materials motion in human body fluids. The comparison of loading anti-cancer drug oridonin into nano- and micro-sized MOF-5 revealed higher capacities and later better drug release from the smaller particles.[487] In the research presented by Lin *et al.*[488] nanoplates of DBP-UiO (Hf-porphyrin based MOF) exhibited exceptional behavior in photodynamic therapy for head and neck cancer. Results suggested that specific MOF morphology and porosity was helpful in reactive oxygen species generation, and further cancerous tissue atrophy.

Atomically dispersed active sites are the major MOFs attribute for their exquisite catalytic performance including heterogeneous catalysis,[489, 490] photo- and electrocatalysis (*i.e.*, water splitting,[491, 492] CO_2 reduction,[493, 494] organic transformations,[495] and oxygen reduction reactions[496]). To increase catalytic activity of materials enhancing their surface area is the key and can be executed in two ways: synthesizing either very small nanoparticles or super-thin films.[497] Also changing the shape of the MOF shell in the core-shell structures *via* modulating kinetic factors (nucleation/dissolution) enables unusual size selectivity of the products in many catalytic processes.[498] When it comes to

applying 2D materials such as nanosheets in catalysis, features like rigidity, porosity and smoothness are highly dependent on their thickness. Jia *et al*.[499] presented bivalent CoFe-MOF with thickness of 1.3 nm. By adjusting membrane or film thickness it became possible to create suitable catalysts for specific purposes. It is surprising that thicker films containing mesopores in the structure are less catalytically active than non-porous thin film. Ultrathin films made of only a few atomic layers have easily accessible active sites, which is crucial in electrocatalysis. However, such thin sheets are more potent to damage or disperse in various solvents. Additionally, ultrathin films are lacking roughness, thus they are much smoother than thick membranes and often the development of porous network in their structure is not observed. Han *et al.*[500] presented the influence of Zn-MOFs [$Zn_3(BTC)_2(H_2O)_3$] morphology on electrochemical reduction of CO_2 to CH_4. The shape of materials achieved varied from rod-like to sheet-like and spherical. Sheet-like Zn-MOF had most beneficial influence on current density, increasing it mostly due to its largest electroactive surface area. Therefore, it was the most efficient in the reduction process. Another morphology-dependent case of MOF application was the photodegradation of methylene blue by coordination polymer Prussian white (PW).[501] Specific shape of the hollow cubic structures increased decomposition of the organic dye comparing to cubic crystals almost 3 times after 5 min and 2.5 time after 25 min (Fig. 33)

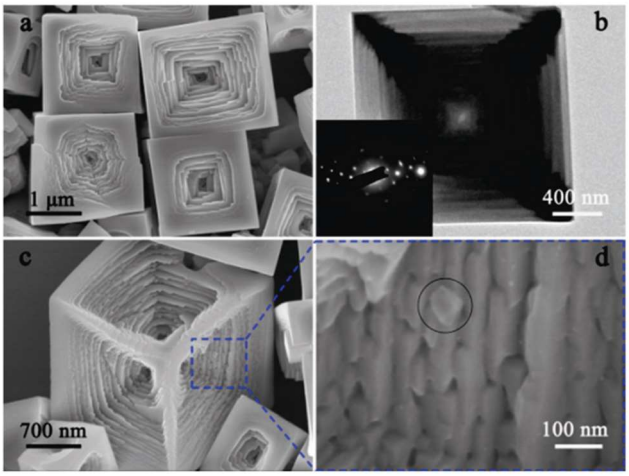

Fig. 33. a) FESEM image of the sample prepared following a typical procedure. **b)** TEM and **c, d)** high magnification FESEM images of a single hierarchical PW crystals. Inset: selected area electron diffraction (SAED) pattern taken from the edge section. (Reprinted with permission.[501] Copyright 2014, The Royal Chemical Society).

For electrochemistry and sensing MOF materials are perfect not only because of their porosity which allows ion storage and transport but also electrochemical stability and guest/host interactions.[502] Once again low-dimensional crystallites favor increasing electrodes surface area to shorten diffusion paths. For instance, Zhou *et al.*[503] presented 2D few-layer structure of NiCo-MOF and black phosphorus, which simplified charge transfer and increased battery efficiency. Dependably on usage, rigid or flexible MOFs are more required. Chemical and mechanical stability are important especially when it comes to operating devices where the dangerous short circuit may occur. Choosing short and rigid linkers with redox-inactive nodes reinforce the MOF material, and with obtaining the proper size of the nanoparticles all together it can amplify stability. It is particularly necessary for electrodes where dendrite formation happens. However, flexibility and malleability are handy in

systems where materials' volume expands and contracts. In this situation long and stretchy ligands that can form crystals with the smallest structural tensions are preferable.[504]

Formerly, bulky MOF materials limited their applicability in highly sensitive sensors. Now, when it is feasible to obtain single nanocrystals it became possible to use them in detecting very small molecules.[505] Morsali *et al.*[506] compared bulk sample and plate-like nanocrystals of $[Zn(OBA)(H_2DPT)_{0.5}]\cdot DMF$ (TMU-34) for Al(III) sensing. Nanomaterial exhibited not only faster response but also a higher detection limit. The plurality of ligands and cations allows to creating MOF crystals with the required composition and morphology that will be able to trap a nanoparticle with a simultaneous reaction in the form of a structural change. For example, rare bundle-like morphology of Eu based MOF was used as a platform to detect styrene volatile vapors.[507] Fluorescent MOFs are an interesting case, proving how sensitive these materials can be. It was suggested that the response to the stimulus may be changing the distance between nodes by shortening/lengthening the linkers, and as the result changing MOF fluorescence.[508] Similarly like in previous applications, the size of the nanoparticles matters in sensing. It was presented by Nenoff *et al.*[509] for I_2 detection by using diverse MFM-300(X) materials (X= Al, Fe, In or Sc with biphenyl-3,3',5,5'-tetracarboxylate as linker). The amount of adsorbed and then polarized I_2 molecules were different dependably on the quantum size and morphology of MFM-300, which ultimately led to the distinct electrochemical response.

6.3. MOF-derived Carbon applications

As already mentioned in the preceding sections, MDCs are of significant interest for various applications, *e.g.* electrochemical energy storage, electrocatalysis, nanomedicine or sensing. Especially, the opportunity to tailor the obtained carbon material *via* the precursor morphology*, i.e.*, in 0D, 1D, 2D and 3D, has a profound effect on materials properties and applicability. As such the approach going from solids-to-MOF-to carbon is an effective way to introduce additional versatility in the finally obtained carbon structures.

In energy-related applications, high specific surface area is one of the required features of MDC electrode materials because it considerably influences charge and discharge rates, which are a significant performance indicator in modern energy storage.[316] Moreover, through tailoring the structure of MDCs pores that mediate ion access to electrodes, exchange kinetics can be improved. For example, the ratio of micropores to mesopores is crucial to ameliorate electrochemical properties of MDCs[321] or the accessibility of active sites[510]. The morphology of MDCs has also significant impact on the overall efficiency of energy-related devices as the material needs to sequester charge carrying species.[510] Therefore, 2D nanostructures are of interest due to their high surface area and good compatibility with device integration.[339] In addition, MDCs contain residual metal ions that can have a positive effect on performance but might also interfere with catalytic reactions at the surface.[511]

The well-developed surface area of materials is especially important in catalysis and sensing because it affects reaction rates and sensitivity.[512] One of the possible approaches to maximize the number of the active sites on solid catalysts is to lower the size of the their particles.[513] Additionally, the morphology of materials has a significant influence on molecular transport at the surface in diffusion-controlled processes. As such, tuning the shape of the catalyst particles can remarkably alter the catalytic activity and selectivity due to the significant variations in the surface atomic configurations. Especially for catalysis, spherical structures are advantageous because of short pathways for the diffusion of species, dispersion enhancement and easy attachment to supports.

Moreover, catalyst nanoparticles with an anisotropic morphology can greatly mediate the reaction properties by selectively exposing desired crystal facets.[514] The morphology can affect the mechanism of the metal-support interaction as well, which is one of the most fundamental issues in heterogeneous catalysis. In nanomedicine, drug loading and designed release show a significant relation to high surface area.[515] Additionally, pore structures, sizes and connections can be utilized to modulate and design release characteristics.[516] Spherical systems are of particular use as they minimize viscous effects and can be functionalized homogenously. Moreover, for smaller particles with higher surface-to-volume ratio, therapeutic amounts of drugs can be loaded on their surfaces.[517] Nevertheless, shape-anisotropic nanoparticles have been found to exhibit specific interactions with biological cells depending on particle morphology.[518] Furthermore, metal ions in the final product can be useful for photothermal therapy and diagnostic tasks, *e.g.* imaging and sensing.

Adsorption is one of the classical applications of MOFs and MDCs, which is mainly related to their porosity and surface chemistry.[316, 519] Surface chemistry can be easily tailored *via* MO/MOF compositions. It should be noted that especially nitrogen-doped MDCs are promising adsorbents for gases including H_2 and CO_2.[316] The pore connectivity and sizes, as well as morphology of carbon materials have also impact on the rate of adsorption and its selectivity.

Carbon materials are often used in the design of supercapacitors that are of particular interest in portable electronics.[321, 520] The capacitance and energy density of supercapacitors relies to a significant extent on porosity and surface area of the utilized electrode material. Moreover, pore sizes and structures have a profound influence on supercapacitor activity, where the utilization of well-defined precursors, *i.e.* MOFs have a tremendous impact.[521-523] In regard of future applications as device, the development of appropriate supercapacitors is of utmost importance. In order to tackle that challenge, Shao and coworkers[430] fabricated flexible carbon-based electrodes as mentioned in section 5.2.3. To obtain a supercapacitor two nanorod arrays were generated and combined, namely ZnO@C@CoNi-LDH (as anode) and Fe_2O_3@C (as cathode). The nanorod array itself served as template to obtain high surface areas including abundant and accessible active sites. After addition of PVA-KOH as solid electrolyte a flexible supercapacitor was designed. A high energy density of 1.078 mW h cm^{-3} was obtained with an outstanding cycling stability of 95% capacity retention over 10,000 cycles. In a similar way, Wang and coworkers[524] assembled a flexible supercapacitor from MOF-derived nanocarbon arrays on carbon cloth (Fig. 34 a, b). Finally, active MnO_2 or Bi_2O_3 were deposited on the carbon substrate. A 2D Cu-MOF-based approach was developed by Li *et al.*[209] A 2D MOF was synthesized from Cu^{2+} and 1,4-bis(2-methyl-imidazol-1-yl)butane) as ligand to afford stacked lamella. Subsequently, the material was calcined, etched with HCl and activated by KOH to obtain carbon nanosheets with ultrahigh porosity (BET surface area of 2491 m^2 g^{-1}). The defined layers with interspace of the MOF precursor were translated into the final carbon material, which was reflected in an excellent specific capacitance (260.5 F g^{-1} at 0.5 A g^{-1}) and energy density (18.38 Wh kg^{-1}). A correlation between morphology and capacitance was investigated by Schmidt and coworkers.[360] Plate-like 2D MOFs and rod-like hexagonal MOFs were synthesized as described in section 5.2.1 and carbonized to form the respective 2D or rod-like carbon structures. The performance of the material in supercapacitors was evaluated. Interestingly, a distinct difference in volumetric capacitance was observed, while the specific capacitance was almost the same for both carbon structures. This result shows that even the overall shape of the carbon has an influence on performance, which is a good starting point for future developments of more sophisticated architectures.

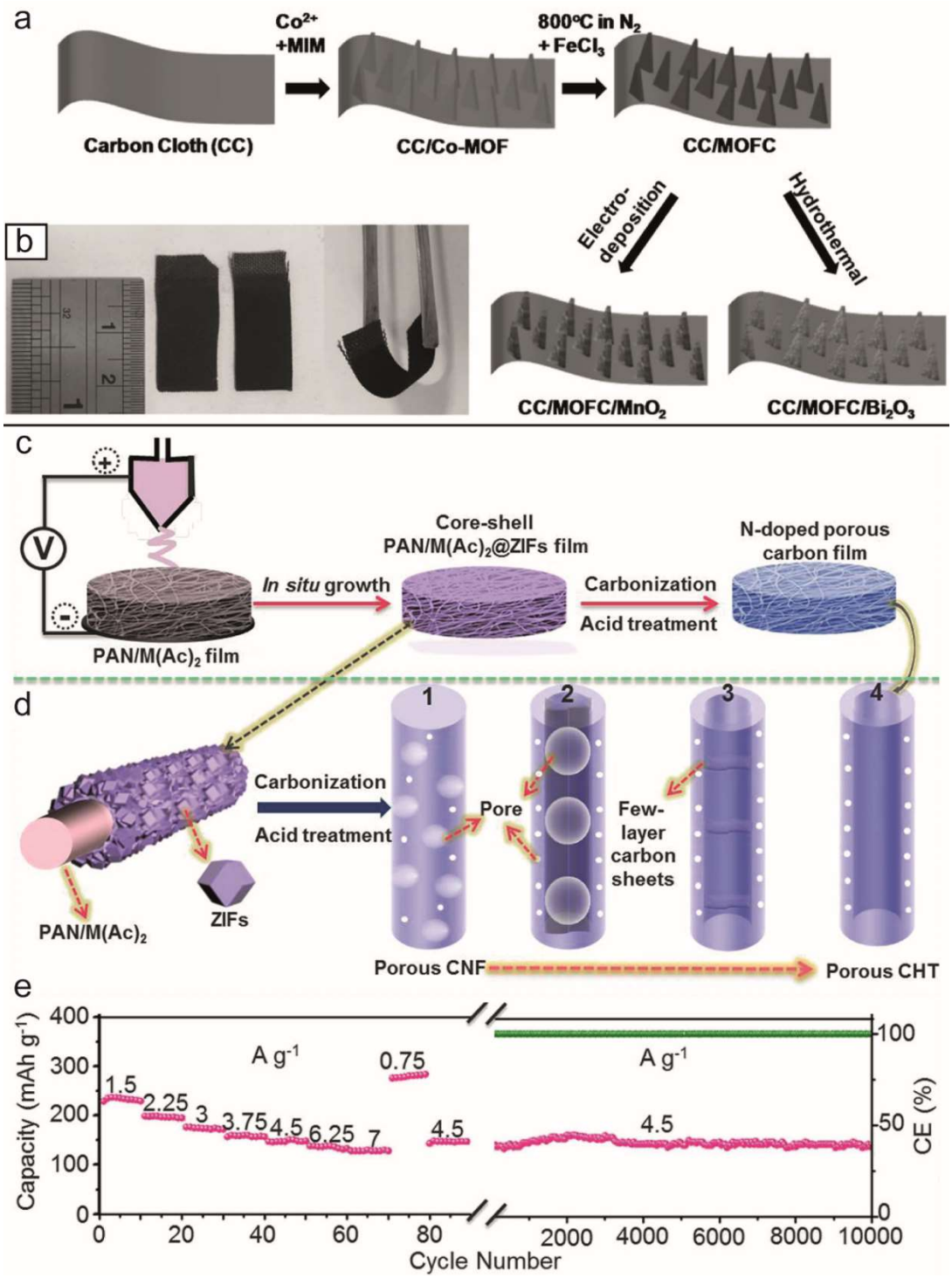

Fig. 34. a) Fabrication process of the MDC-decorated electrodes: MnO_2 as cathode and Bi_2O_3 as anode are directly grown on the CC/MDC surface and **b)** two photos showing the size and flexibility of the electrodes (Reprinted with permission.[524] Copyright 2018, John Wiley & Sons). **c, d)** Schematic illustration 1D nanocarbon synthesis from porous N-doped CNFs to CHTs with enlarged graphene interlayer spacing and **e)** rate capability and cycling performance (Reproduced with permission.[422] Copyright 2017, Elsevier).

In addition to supercapacitors, batteries constitute another important type of device in electrochemical energy storage. Here, carbon materials are frequently utilized as electrode materials as well. Similar to supercapacitors, porosity, morphology and high surface area are the key issues to obtain superior charge/discharge characteristics. Nevertheless, one of the major challenges is long-term stability and high performance at high current rates.[522] Especially, Zn-based batteries are frequently investigated.[525, 526] Sun and coworkers[527] fabricated a hierarchical electrode material based on MnO_2 nanorods for Zn-batteries. At first MnO_2 nanorods were synthesized *via* hydrothermal method and coated with PVP as a support for MOF synthesis. Subsequently, ZIF-8 was formed on the surface of PVP and carbonized *via* thermal treatment in the final step that led to a partial reduction of MnO_2 to a porous MnO_x structure. The porous MnO_x structure facilitated ion transport and acted as a buffer space to alleviate volume expansion/contraction during discharge/charge processes, which is a significant feature for long-term stability. Meanwhile, the MOF-derived N-doped carbon enabled efficient electron transport. For electrochemical performance, Zn was utilized as anode and MnO_x@N-C as cathode as well as reference materials (MnO_2 and MnO_y). Due to the porous structure and conductive carbon network, superior electrochemical properties, *e.g.* cycling stability, high capacity and rate capability, were observed. In depth studies on the charge/discharge mechanism showed that the superior performance at high rates is due to the short length of ion diffusion and rapid electron transfer. In addition to Zn batteries, Li-ion batteries belong to the most important types of batteries.[528, 529] Thus, Duan and coworkers[281] studied MOF-derived anodes for Li-ion batteries, as described in section 5.2.3. The resulting ZnO@ZnO quantum dots/carbon core-shell nanorod arrays on flexible carbon cloth showed high specific capacities and rate capabilities, which was ascribed to the porous shell layer and single-crystal ZnO core. In the area of sodium batteries, Goodenough and coworkers[422] employed nitrogen-doped carbon anodes formed from MOF precursors (Fig. 34c-e, section 5.2.3). At first, PAN was combined with zinc acetate/cobalt acetate and nanofibers were obtained *via* electrospinning (PAN/$M(Ac)_2$ film). After introduction of hmim, a ZIF network was formed on the nanofiber surface (PAN/$M(Ac)_2$@ZIF film) and the whole composite material was carbonized to undergo a transition from carbon nanofibers (CNF) to carbon hollow tubules (CHT). Finally, the N-doped carbon material was utilized as anode in a sodium battery with excellent rate capability, high capacity (up to 346 mAh g^{-1}) and cycle performance (over 10,000 cycles). The superior performance was attributed to the structural features. For example, the enlarged spacing of carbon layers facilitated effective Na^+ storage, while the high surface area and porous structure enabled short diffusion distance for Na^+ ions. Thus, sufficient contact between active material and electrolyte was introduced for a fast charge-transfer process. Moreover, the long-aspect ratio of tubular structures improves 1D electron transport and electrical percolation. The presence of defects in MDC further assists Na^+ diffusion from outer to inner carbon for a rapid activation of the whole carbon material.

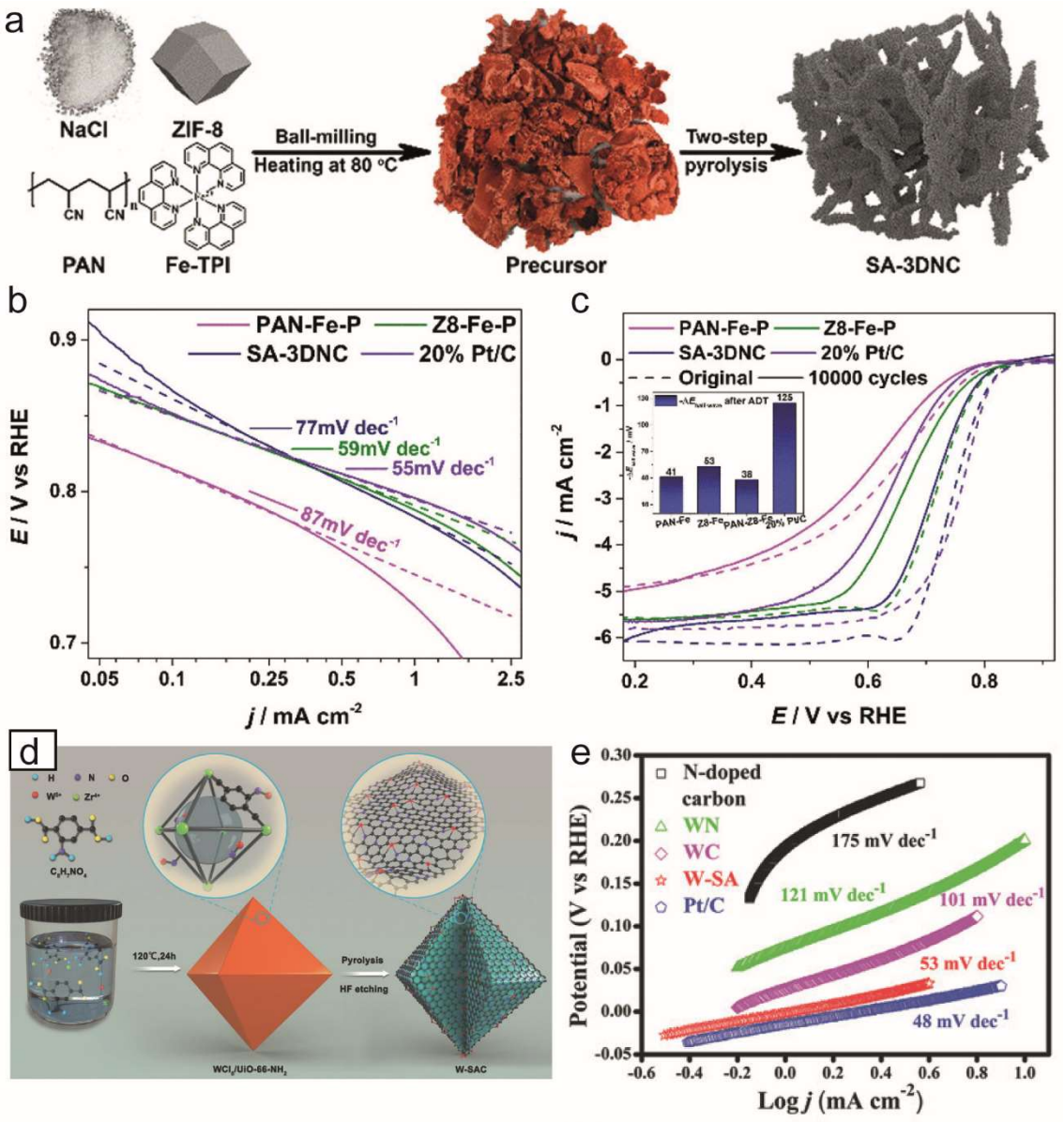

Fig. 35. a) Preparation of SA-3DNC for ORR catalysis in acidic media, **b)** Tafel plots of SA-3DNC and references (20% Pt/C, Z8-Fe-P, PAN-Fe-P) and **c)** linear scan voltammetry plots of SA-3DNC and references (20% Pt/C, Z8-Fe-P, PAN-Fe-P) before and after the 10,000-cycle durability test. (Reprinted with permission.[530] Copyright 2019, American Chemical Society) **d)** Illustration of formation of porous N-doped carbon with single W atoms (W-SAC) and Tafel plots of the W-SA (Reprinted with permission.[531] Copyright 2019, John Wiley & Sons).

In the realm of electrochemical energy conversion, fuels cells and proton exchange membrane fuel cells (PEMFCs) play a significant role. One of the main challenges in PEMFCs is the sluggish kinetics and high overpotential of the ORR as well as electrode durability.[532] A solution to the problem, albeit an expensive one, is the utilization of Pt as catalyst. One option to improve catalyst activity is to tailor the catalytic interfaces, *e.g.* the support material or the grain size of catalytic particles as well as their distribution.[533] For example, increased surface area and conductivity of the carbon support can have a profound influence on catalyst activity.[319] A bimetallic catalyst based on Pt/Ni was reported by Zhao

and coworkers.[534] MOF-5 derived carbons with well-developed surface area (1453-3174 m^2g^{-1}) were used as support materials for subsequent deposition of Pt and Ni through modified polyol methods. At last the ORR activity was investigated, showing a significant increased activity compared to commercial Pt/C, which might be of interest for PEMFC. Due to the significant expense of Pt, many researchers are looking into cheap, earth-abundant alternatives. Liao and coworkers[535] fabricated a MDC electrode for PEMFC. Ferrocene was introduced into ZIF-8 *via* evaporation and carbonized to a porous N-doped carbon with embedded single Fe atoms. Subsequently, PEMFCs were assembled and the performance evaluated showing excellent results in cathodic ORR in H_2/O_2 systems (current density of 1100 mA cm^{-2} at 0.6 V and power density of 775 mW cm^{-2}), while decent performance was also observed in and H_2/air systems. Although the catalyst durability was higher than the literature references, improvements are still needed to reach industrial standards. Very recently, Zhao and coworkers[530] prepared an ORR catalyst *via* multi component ball milling approach (Fig. 35a-c). PAN and ZIF-8 as carbon precursors were combined with NaCl and Fe-tris-1,10-phenanthroline (Fe-TPI) as morphological modulator and Fe-source, respectively. The precursor was pyrolyzed to obtain a carbon material consisting of microporous nanosheets, embedded macropores and dispersed Fe-N_4 sites (SA-3DNC). The obtained catalysts showed exceptional activity in PEMFC at high current density and improved durability, which was attributed to the hierarchical pore structure of PAN-based carbon.

In contrast to the ORR that is utilized in fuel cells, electrochemical water splitting is an important process to generate hydrogen, *i.e.* HER on cathode and oxygen evolution reaction (OER) on anode.[536, 537] Here also MOF-derived carbon is utilized frequently to improve the electrocatalytic process due to conductivity from carbon and catalytic centres from metal ions.[538, 539] As mentioned in section 5.2.3 Jiang and coworkers[310] introduced a method to fabricate well-aligned MOF arrays and turned them into self-standing electrodes. The porous N-doped carbon arrays with incorporated Ni and CoO were utilized for HER and OER. A superior performance compared to reference materials *e.g.* CoO@CoNC on Ni foam was observed. Moreover, the catalytic material showed only negligible deactivation in OER and HER after 3000 cycles. The improved electrocatalytic performance was attributed to the porous nanoarray electrode architecture, *in situ* carbon incorporation, increased accessibility of active sites, accelerated release of gas bubbles, robust structure as well as improved mass and charge transport. Single W atoms on N-doped carbon were utilized by Wang and coworkers for HER (Fig. 35d, e).[531] A UiO-66-NH_2-based MOF was formed from WCl_5, 2-amino-benzenedicarboxylic acid and $ZrCl_4$. After pyrolysis and HF etching, well-defined porous N-doped carbon with homogenously dispersed W atoms (W-SAC) was obtained, which was subsequently used as an electrode in HER. In the electrochemical investigation a small overpotential was found with an overall activity similar to Pt/C. DFT calculation showed that the $W_1N_1C_3$ unit played the most important role in HER performance, which opens up new opportunities for further improvement in the future.

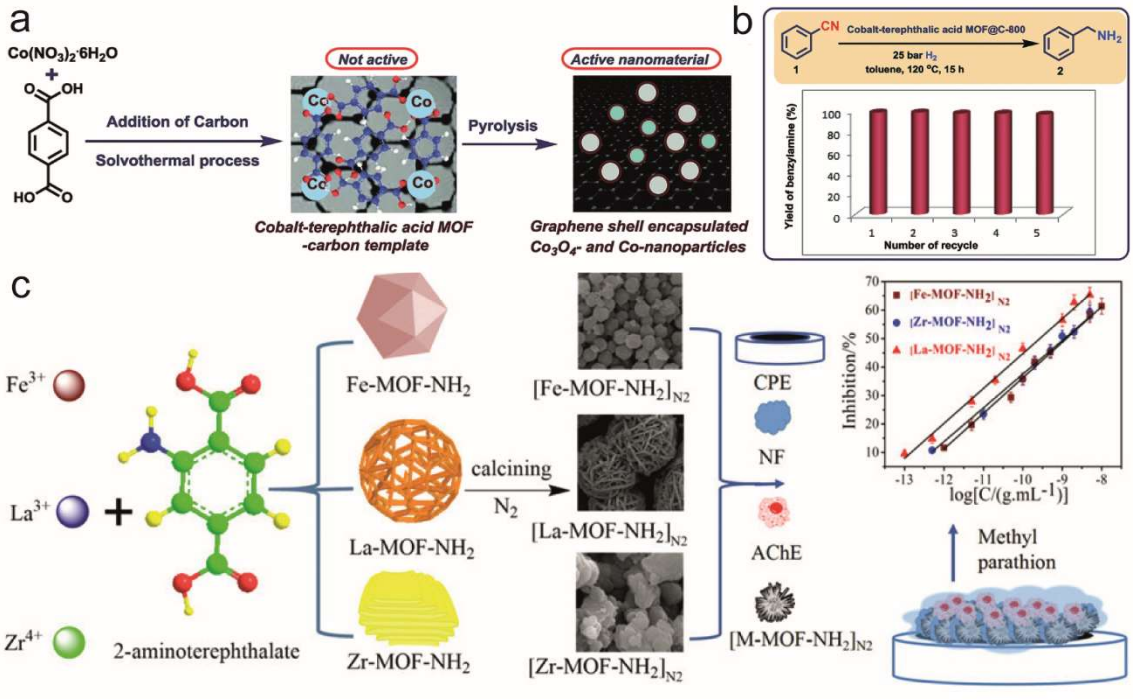

Fig. 36. a) Preparation of graphene encapsulated cobalt oxide- and cobalt-nanoparticles supported on carbon by the pyrolysis of cobalt-terephthalic acid MOF-carbon template and **b)** the recycling of cobalt-terephthalic acid MOF@C-800-catalyst for the hydrogenation of benzonitrile to benzylamine (Reaction condition: 5 mmol benzonitrile, 250 mg catalyst, (3.8 mol% Co), 20 mL toluene, 25 bar H_2, 5 bar NH_3, 120 °C, 16 h) (Licensed under CC-BY[540]). **c)** Schematic formation of Fe, La and Zr-MOFs, calcination to obtain MDC, formation of AChE-modified electrodes and their inhibition curves for methyl parathion (Reproduced with permission.[541] Copyright 2018, American Chemical Society).

MOFs are well-known for their catalytic activity,[542-544] which also counts for MDCs. Jagadeesh and coworkers[540] used a Co-MOF as template to form an efficient carbon catalyst for hydrogenation of benzonitrile (Fig. 36a,b). A Co-BDC MOF was pyrolyzed to obtain activated carbon catalyst with embedded Co_3O_4- and Co-nanoparticles. The catalyst did not require nitrogen doping could be utilized on a large gram scale and recycled in a versatile way. Qian and coworkers[545] applied a Ni-based MOF to synthesize a carbon-based hydrogenation catalyst. A Ni-BTC MOF was pyrolyzed and used for the reduction of 4-nitrophenol with a significant catalytic efficiency. Finally, the catalysts could be recovered with a magnet, which allowed easy recycling. Zhao and coworkers[546] combined graphitic carbon nitride (g-CN) with ZIF-8 derived carbon for enhanced photocatalysis. At first ZIF-8 particles were carbonized and deposited on the g-CN 2D surface. Next, visible light induced photocatalytic degradation of bisphenol A was studied. An improved catalytic activity was attributed to the enhanced light harvesting and efficient interfacial charge separation between g-C_3N_4 and ZIF-8-derived carbon. Such a catalyst is of significant interest for waste water remediation as it can be used to degrade small molecule pollutants, *i.e.* drug residues or residues from agriculture.

One of the common applications of MOFs is sensing.[470, 547, 548] Both enzymatic and non-enzymatic sensors are described in the literature. Moreover, carbon materials derived from MOFs are utilized in sensing as well, which can be ascribed to several factors.[549-551] On one hand, MDC presents a defined environment for analytes that might be useful for the selectivity of the sensor. On the other hand,

the defined environment enables a precise deposition and implementation of the (bio)recognition site, *e.g.* a reactive group or enzyme. Finally, the high surface area of MOFs and MDCs allows increasing number and rate of interactions with the analyte, which leads to improved sensitivity. As such, improved structural control has a profound influence on sensor performance, *i.e.* sensitivity and selectivity, which also leads the direction for future improvements. Thus, the MDC approach allows specific tailoring of the environment for the respective sensing application, *e.g.* with respect to analyte concentration, presence of competing analytes and rate of analysis. Dong and coworkers[541] described MDC nanocomposites for enzyme immobilization (Fig. 36c). Fe^{3+}, Zr^{4+} and La^{3+} were combined with 2-aminoterephthalate to form three MOFs. After carbonization, acetylcholinesterase was immobilized in the carbon/MOF structures to perform biosensing of methyl parathion. The La^{3+}-derived structures showed the best performance, which was deduced to their hierarchical and highly porous architecture. As such, increased amounts of enzyme could be immobilized, electron transfer enhanced and diffusion length of the analyte on the electrode surface shortened. Therefore, biosensors with a linear detection range for concentrations from 1.0×10^{-13} to 5×10^{-19} g mL^{-1} and the lowest detection limit of 5.8×10^{-14} g mL^{-1} were fabricated. A non-enzymatic glucose sensor was described by Fransaer and coworkers.[552] HKUST-1 was grown on a Cu-foam substrate and pyrolyzed to obtain carbon particles with embedded Cu nanoparticles on the Cu-substrate. The fabricated electrode showed high sensitivity, low detection limit and good stability for the non-enzymatic detection of glucose. The superior performance was benefitted from the hierarchical structure of the electrode, the synergistic effect of Cu and carbon as well as their close contact. A molecularly imprinted sensor was presented by Ma and coworkers.[553] On a glassy carbon electrode, carbon nanotubes and MOF-5 derived carbon were deposited. After cleaning, pyrrole was electropolymerized on the carbon surface in the presence of cysteine to obtain molecular imprinting for the cysteine molecule. The sensors could be utilized for enantioselective detection of cysteine enantiomers and then regenerated *via* an overoxidation process and pH adjustment.

Nanomedicine is another important area of applications for MOFs.[554-556] Hence, MDCs found some application in nanomedicine as well with particular areas as controlled drug delivery, bio-imaging and photothermal therapy.[515] The MDCs bring several features that are useful for nanomedicine. For example, improved drug loading and delivery due to well-developed surface area, tunable pore size and functionalizable surface. Metal incorporation enables therapeutic effects, *e.g.* photothermal energy conversion. In addition, the combination with fluorescent material facilitates diagnostic tasks, like imaging and sensing. MDCs provide promising supports to combine diagnostic and therapeutic tasks in one system. Liu and coworkers[557] described the sonodynamic therapy *via* MDC. ZIF-8 was coated with mesoporous SiO_2 to prevent aggregation, pyrolyzed and etched to obtain mesoporous carbon nanoparticles. The key for sonodynamic therapy was the porphyrin-like metal centers formed during the pyrolysis process. Next, the sonodynamic therapy was studied *in vitro* and *in vivo*. The particles were introduced into tumor tissues *via* the enhanced permeability and retention effect. Upon irradiation with ultrasound reactive oxygen species were generated, *e.g.* singlet O_2 as well as hydroxyl radicals that have the therapeutic effect to induce tumor cell apoptosis. Due to the high surface area and pore structure a strong cavitation effect in combination with ultrasound was observed that greatly enhanced the sonodynamic therapy efficiency. In the realm of drug delivery, Yamauchi and coworkers[558] studied ZIF-8 derived carbon nanoparticles as intracellular carriers. A significant loading of *cis*-platin drug as well as a zero-order release profile in the first 20 h were observed. The carbon nanoparticles exhibited excellent biocompatibility even at doses above 100 µg

mL^{-1} and intracellular uptake was observed in HepG2 cells. Fan *et al.*[559] described MDC nanosheets for bacteria eradication and anti-infective therapy (Fig. 37). ZIF-8 was grown on GO sheets, carbonized subsequently to obtain Zn^{2+}-doped carbon on graphene and finally oxidation led to ZnO on graphene. Next, poly(*N*-isopropylacrylamide) was grafted on the surface to introduce photothermal response and obtain the final therapeutic material (TRB-ZnO@G). Overall, the obtained materials entailed three modes to eradicate bacteria, *i.e.* Zn^{2+} release, mechanical cutting of the cell membrane due to the sheet like structure and photothermal hyperthermia *via* NIR irradiation. In the area of bioimaging an example of MDC was described by Xu and coworkers.[363] Carbon nanodots were formed *via* carbonization of ZIF-8 precursors. Fluorescent particles were obtained and used for cell imaging, which is an important application in biomedical diagnostics and cell biology. Water and gas purification is a major issue in environmental technology[560] in which carbon materials found application.[561] For efficient adsorbents a high surface area and surface chemistry are needed, which can be implemented *via* the MOF precursor.

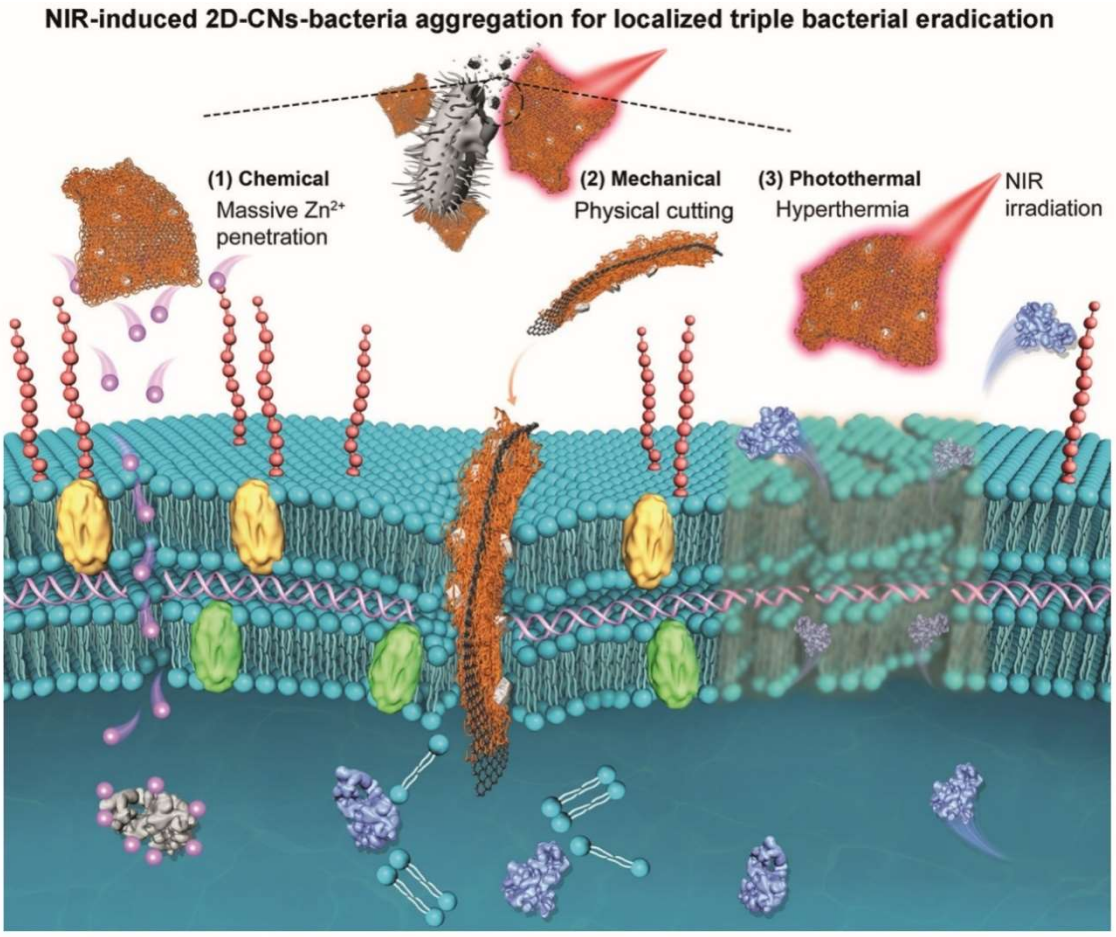

Fig. 37. Proposed sustained and localized (chemical, mechanical, and photothermal) triple antibacterial activities of TRB-ZnO@G (Reproduced with permission.[559] Copyright 2019 American Chemical Society.)

Yamauchi and coworkers[562] utilized Co-MOF as precursor for carbon adsorbents. ZIF-67 was synthesized and carbonized to obtain microparticles. The formed particles were tested in the removal of methylene blue from aqueous solution, which showed a significant adsorption capacity

(up to 500 mg g^{-1}) and an overall incorporation of 99.9% after 24 h. Moreover, the methylene blue loaded particles could be separated from the water easily *via* magnetic field. The adsorption of CO_2 was studied by Li and coworkers.[563] MOF-5 was synthesized and combined with urea to form N-doped porous carbon materials. Efficient CO_2 capture was observed (3.7 mmol g^{-1} at 0 °C and 1 atm), which was ascribed to the high surface area and the introduced functional groups. The interaction of CO_2 and the carbon structure was studied *via* DFT, showing the interaction with pyridinic, pyrrolic and amino functions that give rise to the high CO_2 adsorption performance.

The carbon materials have useful properties that enable various applications. Moreover, these properties can be enhanced *via* structuring and synthetic control.[564] An approach starting from well-defined and tailorable materials like MOFs facilitates a broad variety of properties and applications, even more so if the palette of morphologies is increased by MO-derived MOFs templating. Due to the formidable structural control enabled that way, in-depth investigations of structure-property relationships become viable. Overall, it is obvious that MOFs, MO-derived MOFs and MO/MOF combinations are significant tools to fabricate tailor-made carbon materials for various applications. Certainly, important developments in the field can be expected in the future.

7. Conclusion and perspectives

Structural and morphological control over multiple length scales is one of the most fascinating and important goal of modern solid state and material chemistry. Chemists have learned how to control chemical and structural features with atomic precision and thus the properties of a large variety of porous materials. The chemical control over porous molecular structures of MOF materials has reached a level of sophistication that allows for a wide spectrum of applications. Such porous materials can be developed in the form of films, membranes, monoliths, submicron particles or powders that offer many different physicochemical properties that are obtained by combining their porous texture (accessibility, pore volume, specific surface area, surface area to volume ratio) with the intrinsic characteristics of the matrix (mechanical properties, adsorption, chemical functionality, *etc*.). Although these hybrid materials have unprecedented degree of structural and functional tunability, which should lead to breakthroughs in many key technologies, they are so little considered in industry so far.

In general, structuring porous materials (*i.e.* morphology control at different length scales) gives the opportunity to improve the material performance *via* design of the physical form rather than altering the chemical component. Besides the unique chemical designability of MOF materials at the molecular and nano length scale we wish to foster a pronounced attention for the creation of architectures at the mesoscopic/macroscopic scale by the development of innovate bottom-up and/or top-down strategies in order to increase the physical designability of those materials.

This aspect was taken into consideration by using MO as a precursor for synthesizing MOF structures, as they provide new opportunities for morphology control of MOF/MDC. Thereby, MOs play multiple roles, including architecture directing agents (templates), cation reservoirs (metal ion source), preferential reaction sites for heterogeneous nucleation, and functional components in the final composite materials. As we have shown in this review the morphology control of MO materials at various length scales is extremely high and sophisticated, an impressive plethora of symmetrical and asymmetrical 0D, 1D, 2D, 3D, and hierarchical architectures can be precisely synthesized. In

addition, MOs can be easily integrated with various functional substrates and host materials, and pre-installed on specific locations to make desired patterns.

Starting from morphology control of MO itself, the transformation of MO into MOF and finally MDC enables unprecedented structures and morphologies. As the predefined structures and morphologies of MOs can be transferred to MOFs and MOF derivatives, the MO-to-MOF conversion strategy will enable the preparation of MOF/MDCs with a high level of morphological diversities. Of particular advantage in this approach is the ability to fabricate complex morphologies with multiple levels of structural hierarchies which may be otherwise difficult to achieve.

In turn, morphology controlled MDCs have shown great potential in a number of applications such as supercapacitors, batteries, fuel cells, catalysis, sensing, nanomedicine and adsorption. In energy related applications surface area is a major feature for MDC electrode materials as it significantly influences charge and discharge rates - one of the major performance indicators in modern energy storage. MDCs are of particular utility for tailored porosity and pore structures that mediate ion access to electrodes and allow to improve exchange kinetics. The morphology of MDCs has a significant influence on the overall efficiency of energy related devices especially when the volume of the device is relevant. In catalysis and sensing, surface area is of particular importance for high accessibility of the active centres of catalysts or sensors. Therefore, high reaction rates and sensitivity can be introduced. Moreover, the material morphology has a remarkable impact on molecular transport around the surface, which is a way to regulate diffusion-controlled processes. The pore structure is of considerable interest for tailoring substrate specificity or sensor selectivity, *e.g.* to allow pore access for specific molecules only.

In nanomedicine drug loading and designed release show a significant relation to the well-developed surface area and pore structure, allowing the design of release characteristics through structural tailoring by means of functionalization. Furthermore, in the scaffold incorporated metal ions can be utilized directly for photothermal therapy and enable application in diagnostic tasks, *e.g.* imaging and sensing. The MDC systems are a promising approach for theranostics. The classical application of adsorption is mainly related to surface area and surface chemistry of MDCs. This feature can be easily tailored *via* MO/MOF compositions. With the specificity of adsorption being closely related to surface chemistry and pore structures, respectively, MOF precursors allow the transfer of designed adsorption processes. Regarding the relation of MO/MOF/MDC with the aforementioned applications, a deep understanding of structure-property relationships is missing so far, where future research will have a significant impact. Although considerable progress has been made in this research field over the past decade, there are still many challenges and limitations that need to be resolved in the future.

In-depth understanding of kinetical and thermodynamical aspects of MO-to-MOF conversion are highly required for the preservation of the morphology of the parent material, with many competing rates influencing the conversion kinetics and hence the transition mechanism (dissolution crystallization *vs* template-assisted transition). In particular, the balance between the release rate of metal ions from MO and the coordination rate of metal ions with ligands is critical for controlled MOF deposition on MOs. The other reaction parameters (*e.g.*, solvent composition, temperature and pH) as well as the inherent nature of MOs (*e.g.*, chemical composition, morphology, size, surface roughness and surface charge) also greatly affect the MO-to-MOF conversion. As a result, only a few MOs (*e.g.*, ZnO, CoO_x, CuO_x) are widely utilized for fabrication of 'typical' MOFs so far, such as ZIF, MIL and HKUST-1. A combination of theoretical calculations and experimental approaches is highly

desired to expand the range of possible MOs. High throughput methods would allow for rapid screening of potential solid precursors and help to establish the suitable transformation conditions.

At the moment MO-to-MOF conversion strategy is still rather complicated and expensive hampering large scale applications. Development of fast and economical conversion pathways would be highly appreciated and a considerable driver for the development of the field. Direct conversion of low-cost raw materials (*e.g.*, earth-abundant bio-minerals, solids from large-scale industrial production) into value-added MOF products will attract great attention, both in academia and industry.

Higher level of control over morphology, size and composition of MOF/MDC is greatly desirable. A considerable part of the literature relies on the use MO nanorod-array grown on 2D substrates to form 3D architectures. Future research should focus on development of sophisticated 3D architectures constructed by various building blocks (MO, MOFs, carbon, and substrates). For instance, bio-inspired complex hierarchical architectures that are pre-encoded with unique functions are of great interest. In addition, controllable design and integration of different kinds of MO/MOF/MDC are essential to achieve collective and synergistic effect from the individual components for target applications. However, in many cases, the parent MOs remain in the final composite materials after transition to MOF or MDC, but barely contribute to performance enhancement. They merely occupy the volume of the composites (devices), and this dead volume is a significant problem in applications where volumetric performance is relevant, *e.g.* in portable electronics. In this regard, precise material design is desired to merge the advantage of each component into one hybrid material.

In addition, the relationships between MOF/MDC morphologies and their properties further need to be established. Although a wide variety of MOF/MDC with different compositions and morphologies are reported, there are no systematic investigation of the morphology-property relationship. To study the effect of morphology on MOF/MDC properties, all the other factors, *e.g.* crystallinity, particle size, porosity, surface area, configuration of carbon and heteroatom, doping level, degree of graphitization and more, should remain constant. However, those factors are often mutually interconnected with the morphology itself, so it is challenging to investigate the “true morphology effect” exclusively. Thus, systematic and precise morphology control is highly required to understand how MOF/MDC morphology really affects the materials properties in order to optimize the application performance.

As highlighted in this review, morphology control (physical designability of materials) is an effective and versatile way to control the intrinsic physical and chemical characteristics of materials without changing their chemical compositions. Therefore, we believe that precise morphology control could add a new dimension to the range of possible applications for MOF and MDC. As such, MO-to-MOF and MOF-to-MDC conversion strategy will play a decisive role, because it enables direct access to complex morphologies that are difficult to achieve otherwise. Although considerable advancements have been achieved in recent years, this research field is still in its infancy, and there are still great opportunities to be explored in the future. We expect that this review will provide a general overview of the previous contribution, so that the future direction of morphology control can be foreseen. Further research in the future is going to unravel new breakthroughs in the development of MOF/MDC with defined structures and morphologies that are pre-designed for target applications and device fabrications.

Conflicts of interest

There are no conflicts to declare.

Acknowledgements

Dr. Joanna Goscianska and Aleksander Ejsmont would like to thank the National Science Centre, Poland (project SONATA-12 no: 2016/23/D/NZ7/01347) for financial support.

Abbreviations

3DOM	3D-ordered macroporous
Ac	acetate
AChE	acetylcholinesterase
ADA	1,3-adamantanediacetic acid
ALD	atomic layer deposition
AOT	sodium bis(2-ethylhexyl)sulfosuccinate
BDC	1,4-benzenedicarboxylate
BET	Brunauer-Emmett-Teller
BTC	1,3,5-benzenetricarboxylate
CC	carbon cloth
CCH	cobalt carbonate hydroxide
CHT	carbon hollow tubules
CNF	carbon nanofibers
CNT	carbon nanotube
CPE	carbon paste electrode
CVD	chemical vapour deposition
DABCO	1,4-diazabicyclo[2.2.2]octane
DC	dissolution-crystallization
DFT	density functional theory
DMF	dimethylformamide
dopbdc	4,4’-dihydroxy-(1,1’-biphenyl)-3,3’-dicarboxylic acid
DVB	divinylbenzene
ED	electro deposition
EDX	energy-dispersive X-ray spectroscopy
EPD	electrophoretic deposition
Fe-TPI	Fe-tris-1,10-phenanthroline
FTO	fluorine doped tin oxide
G	graphene
g-CN	graphitic carbon nitride
GO	graphene oxide
Hcaf	caffeine

H-CoNC	hollow Co and N co-doped carbon nanopolyhedra
HER	hydrogen evolution reaction
HEtim	2-ethylimidazole
HIPE	high internal phase emulsion
HKUST	Hong Kong University of Science and Technology
Hmim	2-methylimidazole
IBU	inorganic building unit
IRMOF	isoreticular MOF
ITO	indium doped tin oxide
k	kinetic rate
KIT	Korea Institute of Technology
LAG	liquid-assisted grinding
LDH	layered double-metal hydroxide
MDC	MOF-derived carbon
MFF	metal formate framework
MIL	Materials Institute Lavoisier
MO	metal oxide
MOF	metal-organic framework
NC	N-doped carbon
NDC	2,6-naphthalene dicarboxylic acid
NF	Nickel foam
NGC	N-doped graphitic carbon
NIR	near infrared
NRA	nanorod arrays
NTA	nitrilotriacetic acid
NW	nanowires
OBU	organic building unit
OER	oxygen evolution reaction
ORR	oxygen reduction reaction
PAA	1,4-phenylenediacetic acid
PAN	poly(acrylonitrile)
PDA	1,3-propanediamine
PEG	poly(ethylene glycol)
PEMFC	proton exchange membrane fuel cell
PIMs	polymers of intrinsic microporosity
PPF	porphyrin paddlewheel framework
PS	poly(styrene)
PVA	poly(vinyl alcohol)
PVP	poly(*N*-vinylpyrrolidone)
QD	quantum dots
SA-3DNC	three-dimensional carbon networks with atomically dispersed Fe−N_4 active sites
SAM	self-assembled monolayer
SBA	Santa Barbara Amorphous

SBU	secondary building unit
S-CoNCs	solid Co and N-codoped carbon nanopolyhedra
SDA	structure directing agent
SEM	scanning electron microscopy
SP	shape-preservation
SS-CNR	spherical carbon nanorods superstructures
STEM-EELS	scanning transmission electron microscopy-electron energy loss spectroscopy
SURMOF	surface-mounted MOF
TEM	transmission electron microscopy
TeNW	tellurium nanowires
TGA	thermogravimetric analysis
THF	tetrahydrofuran
TRB	thermoresponsive brushes
UiO	Universitet i Oslo
UNR CCH	urchin-like nanorods of cobalt carbonate hydroxide
UNT	urchin-like nanotubes
W-SAC	N-doped carbon with homogenously dispersed W atoms
XPS	X-ray photoelectron spectroscopy
ZIF	zeolitic imidazolate framework

Reference

1. M. Peplow, *Nature*, 2015, **520**, 148-150.
2. J. R. ILong and O. M. Yaghi, *Chem. Soc. Rev.*, 2009, **38**, 1213-1214.
3. H.-C. Zhou, J. R. Long and O. M. Yaghi, *Chem. Rev.*, 2012, **112**, 673-674.
4. H.-C. Zhou and S. Kitagawa, *Chem. Soc. Rev.*, 2014, **43**, 5415-5418.
5. G. Maurin, C. Serre, A. Cooper and G. Férey, *Chem. Soc. Rev.*, 2017, **46**, 3104-3107.
6. H. Furukawa, K. E. Cordova, M. O'Keeffe and O. M. Yaghi, *Science*, 2013, **341**, 1230444.
7. A. G. Slater and A. I. Cooper, *Science*, 2015, **348**, aaa8075.
8. R. Freund, U. Lächelt, T. Gruber, B. Rühle and S. Wuttke, *ACS Nano*, 2018, **12**, 2094-2105.
9. Y. V. Kaneti, S. Dutta, M. S. A. Hossain, M. J. A. Shiddiky, K. L. Tung, F. K. Shieh, C. K. Tsung, K. C. W. Wu and Y. Yamauchi, *Adv. Mater.*, 2017, **29**, 1700213.
10. S. Canossa, Z. Ji and S. Wuttke, *Adv. Funct. Mater.*, 2019, DOI: 10.1002/adfm.201908547.
11. A. Azhar, Y. Li, Z. Cai, M. B. Zakaria, M. K. Masud, M. S. A. Hossain, J. Kim, W. Zhang, J. Na and Y. Yamauchi, *Bull. Chem. Soc. Jpn.*, 2019, **92**, 875-904.
12. J. Tang, R. R. Salunkhe, H. Zhang, V. Malgras, T. Ahamad, S. M. Alshehri, N. Kobayashi, S. Tominaka, Y. Ide and J. H. Kim, *Sci. Rep.*, 2016, **6**, 30295.
13. Y. V. Kaneti, J. Zhang, Y.-B. He, Z. Wang, S. Tanaka, M. S. A. Hossain, Z.-Z. Pan, B. Xiang, Q.-H. Yang and Y. Yamauchi, *J. Mater. Chem. A*, 2017, **5**, 15356-15366.
14. C. Wang, J. Kim, J. Tang, M. Kim, H. Lim, V. Malgras, J. You, Q. Xu, J. Li and Y. Yamauchi, *Chem*, 2019, DOI: 10.1016/j.chempr.2019.09.005.
15. A. D. McNaught and A. D. McNaught, *Compendium of chemical terminology*, Blackwell Science Oxford, 1997.
16. M. Grzelczak, J. Pérez-Juste, P. Mulvaney and L. M. Liz-Marzán, *Chem. Soc. Rev.*, 2008, **37**, 1783-1791.
17. K. W. Powers, M. Palazuelos, B. M. Moudgil and S. M. Roberts, *Nanotoxicology*, 2007, **1**, 42-51.

18. J. N. Tiwari, R. N. Tiwari and K. S. Kim, *Prog. Mater. Sci.*, 2012, **57**, 724-803.
19. H. Gleiter, *Acta Mater.*, 2000, **48**, 1-29.
20. V. Skorokhod, A. Ragulya and I. Uvarova, *Kyiv: Academperidica*, 2001.
21. V. V. Pokropivny and V. V. Skorokhod, *Mater. Sci. Eng. C*, 2007, **27**, 990-993.
22. D. Nunes, A. Pimentel, L. Santos, P. Barquinha, L. Pereira, E. Fortunato and R. Martins, *Metal Oxide Nanostructures: Synthesis, Properties and Applications*, Elsevier, 2018.
23. L. Qiao and M. T. Swihart, *Adv. Colloid Interface Sci.*, 2017, **244**, 199-266.
24. K. Pathakoti, H. M. Hwang, X. Wang and W. G. Aker, *Int. J. Nanotechnol.*, 2013, **10**, 1093-1108.
25. P. Li, C. Nan, Z. Wei, J. Lu, Q. Peng and Y. Li, *Chem. Mater.*, 2010, **22**, 4232-4236.
26. A. M. Kaczmarek and R. Van Deun, *Chem. Soc. Rev.*, 2013, **42**, 8835-8848.
27. S.-C. Lu, M.-C. Hsiao, M. Yorulmaz, L.-Y. Wang, P.-Y. Yang, S. Link, W.-S. Chang and H.-Y. Tuan, *Chem. Mater.*, 2015, **27**, 8185-8188.
28. C. Zhu, X. Mu, P. A. van Aken, J. Maier and Y. Yu, *Adv. Energy Mater.*, 2015, **5**, 1401170.
29. J. Y. Baek, H.-W. Ha, I.-Y. Kim and S.-J. Hwang, *J. Phys. Chem. C*, 2009, **113**, 17392-17398.
30. Y. Li, H. Tan, X. Y. Yang, B. Goris, J. Verbeeck, S. Bals, P. Colson, R. Cloots, G. Van Tendeloo and B. L. Su, *Small*, 2011, **7**, 475-483.
31. X. Zhang, P. Yu, D. Zhang, H. Zhang, X. Sun and Y. Ma, *Mater. Lett.*, 2013, **92**, 401-404.
32. C. J. Patridge, T.-L. Wu, C. Jaye, B. Ravel, E. S. Takeuchi, D. A. Fischer, G. Sambandamurthy and S. Banerjee, *Nano Lett.*, 2010, **10**, 2448-2453.
33. Z. R. Tian, J. A. Voigt, J. Liu, B. McKenzie and H. Xu, *J. Am. Chem. Soc.*, 2003, **125**, 12384-12385.
34. W. Gao and Z. Li, *Int. J. Nanotechnol.*, 2009, **6**, 245-257.
35. J. H. Jung, H. Kobayashi, K. J. C. Van Bommel, S. Shinkai and T. Shimizu, *Chem. Mater.*, 2002, **14**, 1445-1447.
36. X. W. Lou, D. Deng, J. Y. Lee, J. Feng and L. A. Archer, *Adv. Mater.*, 2008, **20**, 258-262.
37. S. Kobayashi, K. Hanabusa, N. Hamasaki, M. Kimura, H. Shirai and S. Shinkai, *Chem. Mater.*, 2000, **12**, 1523-1525.
38. F. K. Butt, C. Cao, W. S. Khan, M. Safdar, X. Fu, M. Tahir, F. Idrees, Z. Ali, G. Nabi and D. Yu, *CrystEngComm*, 2013, **15**, 2106-2112.
39. G. Suo and J. Li, *J. Alloys Compd.*, 2016, **674**, 16-20.
40. Y. Xia, P. Yang, Y. Sun, Y. Wu, B. Mayers, B. Gates, Y. Yin, F. Kim and H. Yan, *Adv. Mater.*, 2003, **15**, 353-389.
41. X.-Y. Yang, L.-H. Chen, Y. Li, J. C. Rooke, C. Sanchez and B.-L. Su, *Chem. Soc. Rev.*, 2017, **46**, 481-558.
42. X. Liu, T. Ma, N. Pinna and J. Zhang, *Adv. Funct. Mater.*, 2017, **27**, 1702168.
43. B. Viswanath, P. Kundu, B. Mukherjee and N. Ravishankar, *Nanotechnology*, 2008, **19**, 195603.
44. Z. Jing and J. Zhan, *Adv. Mater.*, 2008, **20**, 4547-4551.
45. X. Liu, W. Si, J. Zhang, X. Sun, J. Deng, S. Baunack, S. Oswald, L. Liu, C. Yan and O. G. Schmidt, *Sci. Rep.*, 2014, **4**, 7452.
46. X. Lu, J. Deng, W. Si, X. Sun, X. Liu, B. Liu, L. Liu, S. Oswald, S. Baunack and H. J. Grafe, *Adv. Sci.*, 2015, **2**, 1500113.
47. C. Chen, H. Jian, K. Mai, Z. Ren, J. Wang, X. Fu, C. Fan, C. Sun, G. Qian and Z. Wang, *Eur. J. Inorg. Chem.*, 2014, **2014**, 3023-3029.
48. T. Yu, X. Cheng, X. Zhang, L. Sui, Y. Xu, S. Gao, H. Zhao and L. Huo, *J. Mater. Chem. A*, 2015, **3**, 11991-11999.
49. N. K. Hassan and M. R. Hashim, *J. Alloys Compd.*, 2013, **577**, 491-497.
50. Y. F. Yuan, X. H. Xia, J. B. Wu, J. L. Yang, Y. B. Chen and S. Y. Guo, *Electrochem. Commun.*, 2010, **12**, 890-893.

51. Z. L. Wang, *Adv. Mater.*, 2003, **15**, 432-436.
52. Y. Peng, A.-W. Xu, B. Deng, M. Antonietti and H. Cölfen, *J. Phys. Chem. B*, 2006, **110**, 2988-2993.
53. J. Mei, T. Liao, G. A. Ayoko, J. Bell and Z. Sun, *Prog. Mater. Sci.*, 2019.
54. P. N. Vakil, D. A. Hardy and G. F. Strouse, *ACS Nano*, 2018, **12**, 6784-6793.
55. H. Liu, W. Miao, S. Yang, Z. Zhang and J. Chen, *Crystal Growth&Design*, 2009, **9**, 1733-1740.
56. Y. Zhang, J. Xu, Q. Xiang, H. Li, Q. Pan and P. Xu, *J. Phys. Chem. C*, 2009, **113**, 3430-3435.
57. J. Liang, J. Liu, Q. Xie, S. Bai, W. Yu and Y. Qian, *J. Phys. Chem. B*, 2005, **109**, 9463-9467.
58. X. Ma, J. Liu, C. Liang, X. Gong and R. Che, *J. Mater. Chem. A*, 2014, **2**, 12692-12696.
59. G. Sun, B. Dong, M. Cao, B. Wei and C. Hu, *Chem. Mater.*, 2011, **23**, 1587-1593.
60. C. O'Dwyer, D. Navas, V. Lavayen, E. Benavente, M. A. Santa Ana, G. Gonzalez, S. B. Newcomb and C. M. Sotomayor Torres, *Chem. Mater.*, 2006, **18**, 3016-3022.
61. S. Ghosh, P. Kar, N. Bhandary, S. Basu, S. Sardar, T. Maiyalagan, D. Majumdar, S. K. Bhattacharya, A. Bhaumik and P. Lemmens, *Catal. Sci. Technol.*, 2016, **6**, 1417-1429.
62. S. Park, S. Lee, S. W. Seo, S.-D. Seo, C. W. Lee, D. Kim, D.-W. Kim and K. S. Hong, *CrystEngComm*, 2013, **15**, 2939-2948.
63. G. Brinkmann and N. Van Cleemput, *Discrete Appl. Math.*, 2011, **159**, 1528-1539.
64. M. Fang, G. Dong, R. Wei and J. C. Ho, *Adv. Energy Mater.*, 2017, **7**, 1700559.
65. M. R. Alenezi, S. J. Henley, N. G. Emerson and S. R. P. Silva, *Nanoscale*, 2014, **6**, 235-247.
66. B. I. Kharisov, *Recent Pat. Nanotech.*, 2008, **2**, 190-200.
67. P. Madhusudan, Y. Wang, B. N. Chandrashekar, W. Wang, J. Wang, J. Miao, R. Shi, Y. Liang, G. Mi and C. Cheng, *Appl. Catal. B: Environ.*, 2019, **253**, 379-390.
68. X. Song, C. Huang, Y. Qin, H. Li and H. C. Chen, *J. Mater. Chem. A*, 2018, **6**, 16205-16212.
69. J. C. Védrine, *ChemSusChem*, 2019, **12**, 577-588.
70. Q. Zhang, H.-Y. Wang, X. Jia, B. Liu and Y. Yang, *Nanoscale*, 2013, **5**, 7175-7183.
71. Y. Li and W. Shen, *Chem. Soc. Rev.*, 2014, **43**, 1543-1574.
72. Y. Zhou, Y. Li and W. Shen, *Chem. Asian J.*, 2016, **11**, 1470-1488.
73. Y. Qu and X. Duan, *Chem. Soc. Rev.*, 2013, **42**, 2568-2580.
74. X. Mou, X. Wei, Y. Li and W. Shen, *CrystEngComm*, 2012, **14**, 5107-5120.
75. I. Lee, F. Delbecq, R. Morales, M. A. Albiter and F. Zaera, *Nat. Mater.*, 2009, **8**, 132.
76. Z. Li, H. Li, Z. Wu, M. Wang, J. Luo, H. Torun, P. Hu, C. Yang, M. Grundmann and X. Liu, *Mater. Horiz.*, 2019, **6**, 470-506.
77. B. Zhang and P.-X. Gao, *Front. Mater.*, 2019, **6**, 55.
78. Y.-F. Sun, S.-B. Liu, F.-L. Meng, J.-Y. Liu, Z. Jin, L.-T. Kong and J.-H. Liu, *Sensors*, 2012, **12**, 2610-2631.
79. E. Comini and G. Sberveglieri, *Mater. Today*, 2010, **13**, 36-44.
80. A. Kubacka, M. Fernandez-Garcia and G. Colon, *Chem. Rev.*, 2011, **112**, 1555-1614.
81. M. Adachi, Y. Murata, J. Takao, J. Jiu, M. Sakamoto and F. Wang, *J. Am. Chem. Soc.*, 2004, **126**, 14943-14949.
82. D. Sengupta, P. Das, B. Mondal and K. Mukherjee, *Renew. Sustain. Energy Rev.*, 2016, **60**, 356-376.
83. M. Dürr, S. Rosselli, A. Yasuda and G. Nelles, *J. Phys. Chem. B*, 2006, **110**, 21899-21902.
84. K. Sivula, F. Le Formal and M. Grätzel, *ChemSusChem*, 2011, **4**, 432-449.
85. M. Nagpal and R. Kakkar, *Sep. Purif. Technol.*, 2019, **211**, 522-539.
86. R. Bhateria and R. Singh, *J. Water Process Eng.*, 2019, **31**, 100845.
87. R. Gusain, K. Gupta, P. Joshi and O. P. Khatri, *Adv. Colloid Interface Sci.*, 2019, 102009.
88. M. A. Islam, D. W. Morton, B. B. Johnson, B. Mainali and M. J. Angove, *J. Water Process Eng.*, 2018, **26**, 264-280.
89. M. Martínez-Carmona, Y. Gun'ko and M. Vallet-Regí, *Nanomaterials*, 2018, **8**, 268.
90. Z. Assadi, G. Emtiazi and A. Zarrabi, *J. Mol. Liq.*, 2018, **250**, 375-380.

91. X. Huang, X. Zheng, Z. Xu and C. Yi, *Int. J. Pharm.*, 2017, **534**, 190-194.
92. A. K. Kodoth, V. M. Ghate, S. A. Lewis and V. Badalamoole, *Int. J. Biol. Macromol.*, 2018, **115**, 418-430.
93. P.-J. Lu, S.-C. Huang, Y.-P. Chen, L.-C. Chiueh and D. Y.-C. Shih, *J. Food Drug Anal.*, 2015, **23**, 587-594.
94. C.-L. Kuo, C.-L. Wang, H.-H. Ko, W.-S. Hwang, K.-m. Chang, W.-L. Li, H.-H. Huang, Y.-H. Chang and M.-C. Wang, *Ceram. Int.*, 2010, **36**, 693-698.
95. M. J. Osmond and M. J. McCall, *Nanotoxicology*, 2010, **4**, 15-41.
96. S. Yabe and T. Sato, *J. Solid State Chem.*, 2003, **171**, 7-11.
97. T.-D. Nguyen, *Nanoscale*, 2013, **5**, 9455-9482.
98. C. Burda, X. Chen, R. Narayanan and M. A. El-Sayed, *Chem. Rev.*, 2005, **105**, 1025-1102.
99. J.-P. Jolivet, S. Cassaignon, C. Chanéac, D. Chiche, O. Durupthy and D. Portehault, *C. R. Chimie*, 2010, **13**, 40-51.
100. T.-D. Nguyen and T.-O. Do, *Nanocrystal*, 2011, **2**, 55-84.
101. H.-D. Yu, M. D. Regulacio, E. Ye and M.-Y. Han, *Chem. Soc. Rev.*, 2013, **42**, 6006-6018.
102. C. T. Dinh, T. D. Nguyen, F. Kleitz and T. O. Do, *Controlled Nanofabrication: Advances and Applications*, CRC Press, 2012.
103. J. Park, J. Joo, S. G. Kwon, Y. Jang and T. Hyeon, *Angew. Chem., Int. Ed.*, 2007, **46**, 4630-4660.
104. S. K. Tripathi, R. Kaur and M. Rani, *Solid State Phenomena*, **222**, 67-97.
105. Y. w. Jun, J. s. Choi and J. Cheon, *Angew. Chem., Int. Ed.*, 2006, **45**, 3414-3439.
106. A. V. Nikam, B. L. V. Prasad and A. A. Kulkarni, *CrystEngComm*, 2018, **20**, 5091-5107.
107. T. Guo, M.-S. Yao, Y.-H. Lin and C.-W. Nan, *CrystEngComm*, 2015, **17**, 3551-3585.
108. C. J. Brinker and G. W. Scherer, *Sol-gel science: the physics and chemistry of sol-gel processing*, Academic press, 2013.
109. S. Thiagarajan, A. Sanmugam and D. Vikraman, *Recent Applications in Sol-Gel Synthesis*, 2017, 1-17.
110. W. Z. Wang, G. H. Wang, X. S. Wang, Y. J. Zhan, Y. K. Liu and C. L. Zheng, *Adv. Mater.*, 2002, **14**, 67-69.
111. C. H. Kuo, C. H. Chen and M. H. Huang, *Adv. Funct. Mater.*, 2007, **17**, 3773-3780.
112. M. Pang and H. C. Zeng, *Langmuir*, 2010, **26**, 5963-5970.
113. S. Sun, F. Zhou, L. Wang, X. Song and Z. Yang, *Crystal Growth & Design*, 2009, **10**, 541-547.
114. W.-C. Huang, L.-M. Lyu, Y.-C. Yang and M. H. Huang, *J. Am. Chem. Soc.*, 2011, **134**, 1261-1267.
115. Y. Qiao, Y. Yu, Y. Jin, Y.-B. Guan and C.-H. Chen, *Electrochim. Acta*, 2014, **132**, 323-331.
116. S.-I. Kim, J.-S. Lee, H.-J. Ahn, H.-K. Song and J.-H. Jang, *ACS Appl. Mater. Interfaces*, 2013, **5**, 1596-1603.
117. T. Kavitha and H. Yuvaraj, *J. Mater. Chem.*, 2011, **21**, 15686-15691.
118. H. Karami and A. Mohammadi, *Int. J. Electrochem. Sci*, 2015, **10**, 7392-7408.
119. Y. S. Kang, S. Risbud, J. F. Rabolt and P. Stroeve, *Chem. Mater.*, 1996, **8**, 2209-2211.
120. R. Itteboina and T. K. Sau, *Mater. Today: Proceedings*, 2019, **9**, 458-467.
121. T. Sugimoto, K. Okada and H. Itoh, *J. Colloid Interface Sci.*, 1997, **193**, 140-143.
122. T. Sugimoto and X. Zhou, *J. Colloid and Interface Sci.*, 2002, **252**, 347-353.
123. T. Sugimoto, X. Zhou and A. Muramatsu, *J. Colloid Interface Sci.*, 2002, **252**, 339-346.
124. T. Sugimoto, X. Zhou and A. Muramatsu, *J. Colloid Interface Sci.*, 2003, **259**, 53-61.
125. G. Gundiah, S. Mukhopadhyay, U. G. Tumkurkar, A. Govindaraj, U. Maitra and C. N. R. Rao, *J. Mater. Chem.*, 2003, **13**, 2118-2122.
126. A. Biswas, A. Corani, A. Kathiravan, Y. Infahsaeng, A. Yartsev, V. Sundstrom and S. De, *Nanotechnology*, 2013, **24**, 195601.
127. A. R. Armstrong, G. Armstrong, J. Canales, R. García and P. G. Bruce, *Adv. Mater.*, 2005, **17**, 862-865.
128. A. Q. Pan, H. B. Wu, L. Zhang and X. W. D. Lou, *Energy Environ. Sci.*, 2013, **6**, 1476-1479.

129. G. Liu, Q. Deng, H. Wang, S. Kang, Y. Yang, D. H. L. Ng, W. Cai and G. Wang, *Chem. Eur. J.*, 2012, **18**, 13418-13426.
130. A. G. Roca, L. Gutiérrez, H. Gavilán, M. E. F. Brollo, S. Veintemillas-Verdaguer and M. del Puerto Morales, *Adv. Drug Deliv. Rev.*, 2018.
131. H. Wang, L. Zhang, X. Tan, C. M. B. Holt, B. Zahiri, B. C. Olsen and D. Mitlin, *J. Phys. Chem. C*, 2011, **115**, 17599-17605.
132. A.-M. Cao, J.-S. Hu, H.-P. Liang, W.-G. Song, L.-J. Wan, X.-L. He, X.-G. Gao and S.-H. Xia, *J. Phys. Chem. B*, 2006, **110**, 15858-15863.
133. L. Zhuo, J. Ge, L. Cao and B. Tang, *Crystal Growth & Design*, 2008, **9**, 1-6.
134. M. H. Kim, B. Lim, E. P. Lee and Y. Xia, *J. Mater. Chem.*, 2008, **18**, 4069-4073.
135. S. Shang, K. Xue, D. Chen and X. Jiao, *CrystEngComm*, 2011, **13**, 5094-5099.
136. Y. Ren and L. Gao, *J. Am. Ceram. Soc.*, 2010, **93**, 3560-3564.
137. H. Zhang, D. Yang, X. Ma, Y. Ji, J. Xu and D. Que, *Nanotechnology*, 2004, **15**, 622.
138. K. He, C.-Y. Xu, L. Zhen and W.-Z. Shao, *Mater. Lett.*, 2007, **61**, 3159-3162.
139. J. Wan, X. Chen, Z. Wang, X. Yang and Y. Qian, *J. Cryst. Growth*, 2005, **276**, 571-576.
140. X. Li, Z. Si, Y. Lei, J. Tang, S. Wang, S. Su, S. Song, L. Zhao and H. Zhang, *CrystEngComm*, 2010, **12**, 2060-2063.
141. C.-T. Dinh, T.-D. Nguyen, F. Kleitz and T.-O. Do, *ACS Nano*, 2009, **3**, 3737-3743.
142. K. X. Yao, X. M. Yin, T. H. Wang and H. C. Zeng, *J. Am. Chem. Soc.*, 2010, **132**, 6131-6144.
143. Y. Li, M. Afzaal and P. O'Brien, *J. Mater. Chem.*, 2006, **16**, 2175-2180.
144. M. V. Kovalenko, M. I. Bodnarchuk, R. T. Lechner, G. Hesser, F. Schäffler and W. Heiss, *J. Am. Chem. Soc.*, 2007, **129**, 6352-6353.
145. P. D. Cozzoli, M. L. Curri, A. Agostiano, G. Leo and M. Lomascolo, *J. Phys. Chem. B*, 2003, **107**, 4756-4762.
146. T. Yu, J. Joo, Y. I. Park and T. Hyeon, *J. Am. Chem. Soc.*, 2006, **128**, 1786-1787.
147. Y. C. Cao, *J. Am. Chem. Soc*, 2004, **126**, 7456-7457.
148. T. Hyeon, S. S. Lee, J. Park, Y. Chung and H. B. Na, *J. Am. Chem. Soc.*, 2001, **123**, 12798-12801.
149. J. Park, E. Kang, C. J. Bae, J.-G. Park, H.-J. Noh, J.-Y. Kim, J.-H. Park, H. M. Park and T. Hyeon, *J. Phy. Chem. B*, 2004, **108**, 13594-13598.
150. Y. Chen, E. Johnson and X. Peng, *J. Am. Chem. Soc.*, 2007, **129**, 10937-10947.
151. D. Zitoun, N. Pinna, N. Frolet and C. Belin, *J. Am. Chem. SOc.*, 2005, **127**, 15034-15035.
152. M. Salavati-Niasari, N. Mir and F. Davar, *J. Phys. Chem. Solids*, 2009, **70**, 847-852.
153. J.-w. Seo, Y.-w. Jun, S. J. Ko and J. Cheon, *J. Phy. Chem. B*, 2005, **109**, 5389-5391.
154. I. H. Lone, N. R. E. Radwan, J. Aslam and A. Akhter, *Curr. Nanosci.*, 2019, **15**, 129-136.
155. V. Uskoković and M. Drofenik, *Surf. Rev. Lett.*, 2005, **12**, 239-277.
156. M. Boutonnet, J. Kizling, P. Stenius and G. Maire, *Coll. Surf.*, 1982, **5**, 209-225.
157. A. Kumar, A. Saxena, A. De, R. Shankar and S. Mozumdar, *Rsc Adv.*, 2013, **3**, 5015-5021.
158. Y. Liu, C. Zheng, W. Wang, Y. Zhan and G. Wang, *J. Cryst. Growth*, 2001, **233**, 8-12.
159. N. Pinna, M. Willinger, K. Weiss, J. Urban and R. Schlögl, *Nano Lett.*, 2003, **3**, 1131-1134.
160. F. Gu, Z. Wang, D. Han, C. Shi and G. Guo, *Mater. Sci. Eng. B*, 2007, **139**, 62-68.
161. S. C. Kuiry, S. D. Patil, S. Deshpande and S. Seal, *J. Phys. Chem. B*, 2005, **109**, 6936-6939.
162. X. Li, W. Zheng, G. He, R. Zhao and D. Liu, *ACS Sustainable Chem. Eng.*, 2013, **2**, 288-295.
163. A. Bumajdad and M. Madkour, *Nanoscale Res. Lett.*, 2015, **10**, 19.
164. B. Park, B. H. Kim and T. Yu, *J. Colloid Interface Sci.*, 2018, **518**, 27-33.
165. N. Zhao, W. Nie, X. Liu, S. Tian, Y. Zhang and X. Ji, *Small*, 2008, **4**, 77-81.
166. N. Zhao, D. Pan, W. Nie and X. Ji, *J. Am. Chem. Soc.*, 2006, **128**, 10118-10124.
167. T.-D. Nguyen and T.-O. Do, *J. Phy. Chem. C*, 2009, **113**, 11204-11214.
168. T.-D. Nguyen, D. Mrabet and T.-O. Do, *J. Phy. Chem. C*, 2008, **112**, 15226-15235.
169. D. Pan, N. Zhao, Q. Wang, S. Jiang, X. Ji and L. An, *Adv. Mater.*, 2005, **17**, 1991-1995.

170. J. Zhang, S. Ohara, M. Umetsu, T. Naka, Y. Hatakeyama and T. Adschiri, *Adv. Mater.*, 2007, **19**, 203-206.
171. A. V. Rane, K. Kanny, V. K. Abitha and S. Thomas, in *Synthesis of Inorganic Nanomaterials*, Elsevier, 2018, pp. 121-139.
172. X. Xia, Y. Zhang, D. Chao, C. Guan, Y. Zhang, L. Li, X. Ge, I. M. Bacho, J. Tu and H. J. Fan, *Nanoscale*, 2014, **6**, 5008-5048.
173. M. Farahmandjou and S. Jurablu, *Int. J. Bio-Inorg. Hybr. Nanomater.*, 2014, **3**, 179-184.
174. A. J. Ahamed and P. V. Kumar, *J. Chem. Pharm. Res.*, 2016, **8**, 624-628.
175. W. Wu, X. H. Xiao, F. Ren, S. F. Zhang and C. Z. Jiang, *J. Low Temp. Phys.*, 2012, **168**, 306-313.
176. S. Chen, J. Zhu, Q. Han, Z. Zheng, Y. Yang and X. Wang, *Cryst. Growth & Des.*, 2009, **9**, 4356-4361.
177. S. Tazikeh, A. Akbari, A. Talebi and E. Talebi, *Mater. Sci.-Poland*, 2014, **32**, 98-101.
178. J. C. Park, J. Kim, H. Kwon and H. Song, *Adv. Mater.*, 2009, **21**, 803-807.
179. S. Stankic, S. Suman, F. Haque and J. Vidic, *J. Nanobiotechnol.*, 2016, **14**, 73.
180. W. Y. Teoh, R. Amal and L. Mädler, *Nanoscale*, 2010, **2**, 1324-1347.
181. S. Grimm, M. Schultz, S. Barth and R. Muller, *J. Mater. Sci.*, 1997, **32**, 1083-1092.
182. S. Pokhrel, J. Birkenstock, M. Schowalter, A. Rosenauer and L. Mädler, *Cryst. Growth & Des.*, 2009, **10**, 632-639.
183. S. Sel, O. Duygulu, U. Kadiroglu and N. E. Machin, *Appl. Surf. Sci.*, 2014, **318**, 150-156.
184. M. J. Height, L. Mädler, S. E. Pratsinis and F. Krumeich, *Chem. Mater.*, 2006, **18**, 572-578.
185. M. J. Lawrence, A. Kolodziej and P. Rodriguez, *Cur. Opin. Electrochem.*, 2018, **10**, 7-15.
186. C. A. C. Sequeira, *Organic & Medicinal Chem.*, 2018, **5**, 555660.
187. D. Khudhair, A. Bhatti, Y. Li, H. A. Hamedani, H. Garmestani, P. Hodgson and S. Nahavandi, *Mater. Sci. Eng. C*, 2016, **59**, 1125-1142.
188. D. Ramimoghadam, S. Bagheri and S. B. A. Hamid, *J. Magn. Magn. Mater.*, 2014, **368**, 207-229.
189. Y. Lu and X. Zhou, *Thin Solid Films*, 2018, **660**, 180-185.
190. Y.-R. Lu, T.-Z. Wu, C.-L. Chen, D.-H. Wei, J.-L. Chen, W.-C. Chou and C.-L. Dong, *Nanoscale Res. Lett.*, 2015, **10**, 387.
191. J. Yang, Y. Lin, Y. Meng and Y. Liu, *Ceram. Int.*, 2012, **38**, 4555-4559.
192. S.-L. Chou, J.-Z. Wang, H.-K. Liu and S.-X. Dou, *J. Power Sources*, 2008, **182**, 359-364.
193. J. Y. Xiang, X. L. Wang, X. H. Xia, L. Zhang, Y. Zhou, S. J. Shi and J. P. Tu, *Electrochim. Acta*, 2010, **55**, 4921-4925.
194. N. Zikalala, K. Matshetshe, S. Parani and O. S. Oluwafemi, *Nano-Structures & Nano-Objects*, 2018, **16**, 288-299.
195. H. Agarwal, S. V. Kumar and S. Rajeshkumar, *Resource-Efficient Technol.*, 2017, **3**, 406-413.
196. H. Zhou, T. Fan, J. Ding, D. Zhang and Q. Guo, *Optics Express*, 2012, **20**, A340-A350.
197. A. K. Jha, K. Prasad and A. R. Kulkarni, *Colloids Surf. B.*, 2009, **71**, 226-229.
198. Y. Suzuki, S. D. Kelly, K. M. Kemner and J. F. Banfield, *Nature*, 2002, **419**, 134.
199. K. Ali, S. Dwivedi, A. Azam, Q. Saquib, M. S. Al-Said, A. A. Alkhedhairy and J. Musarrat, *J. Colloid Interface Sci.*, 2016, **472**, 145-156.
200. P. Rajiv, S. Rajeshwari and R. Venckatesh, *Spectrochim. Acta A: Mol. Biomol. Spectrosc.*, 2013, **112**, 384-387.
201. P. C. Nagajyothi, T. V. M. Sreekanth, C. O. Tettey, Y. I. Jun and S. H. Mook, *Bioorg. Med. Chem. Lett.*, 2014, **24**, 4298-4303.
202. H. R. Madan, S. C. Sharma, D. Suresh, Y. S. Vidya, H. Nagabhushana, H. Rajanaik, K. S. Anantharaju, S. C. Prashantha and P. S. Maiya, *Spectrochim. Acta A: Mol. Biomol. Spectrosc.*, 2016, **152**, 404-416.
203. R. Raliya and J. C. Tarafdar, *Agri. Res.*, 2013, **2**, 48-57.

204. R. M. Tripathi, A. S. Bhadwal, R. K. Gupta, P. Singh, A. Shrivastav and B. R. Shrivastav, *J. Photochem. Photobio. B.*, 2014, **141**, 288-295.
205. S. Venkateswarlu, B. N. Kumar, B. Prathima, Y. SubbaRao and N. V. V. Jyothi, *Arabian J. Chem.*, 2019, **12**, 588-596.
206. S. Venkateswarlu, Y. S. Rao, T. Balaji, B. Prathima and N. V. V. Jyothi, *Mater. Lett.*, 2013, **100**, 241-244.
207. J. M. Byrne, N. D. Telling, V. S. Coker, R. A. D. Pattrick, G. Van Der Laan, E. Arenholz, F. Tuna and J. R. Lloyd, *Nanotechnology*, 2011, **22**, 455709.
208. J. Singh, V. Kumar, K.-H. Kim and M. Rawat, *Environ. Res.*, 2019, **177**, 108569.
209. K. Saravanakumar, S. Shanmugam, N. B. Varukattu, D. MubarakAli, K. Kathiresan and M.-H. Wang, *J. Photochem. Photobio. B.*, 2019, **190**, 103-109.
210. Y. Liu, J. Goebl and Y. Yin, *Chem. Soc. Rev.*, 2013, **42**, 2610-2653.
211. A. H. Lu and F. Schüth, *Adv. Mater.*, 2006, **18**, 1793-1805.
212. A. Rumplecker, F. Kleitz, E.-L. Salabas and F. Schüth, *Chem. Mater.*, 2007, **19**, 485-496.
213. B. B. Lakshmi, C. J. Patrissi and C. R. Martin, *Chem. Mater.*, 1997, **9**, 2544-2550.
214. S. J. Limmer, S. Seraji, Y. Wu, T. P. Chou, C. Nguyen and G. Z. Cao, *Adv. Funct. Mater.*, 2002, **12**, 59-64.
215. Y. Boyjoo, M. Wang, V. K. Pareek, J. Liu and M. Jaroniec, *Chem. Soc. Rev.*, 2016, **45**, 6013-6047.
216. H. Ren, J. Sun, R. Yu, M. Yang, L. Gu, P. Liu, H. Zhao, D. Kisailus and D. Wang, *Chem. Sci.*, 2016, **7**, 793-798.
217. Y. Zeng, X. Wang, H. Wang, Y. Dong, Y. Ma and J. Yao, *Chem. Commun.*, 2010, **46**, 4312-4314.
218. M.-L. Hu, M. Y. Masoomi and A. Morsali, *Coord. Chem. Rev.*, 2019, **387**, 415-435.
219. H.-C. Zhou, J. R. Long and O. M. Yaghi, *Journal*, 2012.
220. H.-C. J. Zhou and S. Kitagawa, *Chemical Society Reviews*, 2014, **43**, 5415-5418.
221. L. Zhang, H. Song, G. Xu, W. Wang and L. Yang, *J. Solid State Chem.*, 2019, **276**, 87-92.
222. J. Zhao, Z. Tang, F. Dong and J. Zhang, *Mol. Catal.*, 2019, **463**, 77-86.
223. R. Wu, X. Qian, F. Yu, H. Liu, K. Zhou, J. Wei and Y. Huang, *J. Mater. Chem. A*, 2013, **1**, 11126-11129.
224. Y. Song, X. Li, C. Wei, J. Fu, F. Xu, H. Tan, J. Tang and L. Wang, *Sci. Rep.*, 2015, **5**, 8401.
225. F. Zhang, D. Jiang and X. Zhang, *Nano-Structures & Nano-Objects*, 2016, **5**, 1-6.
226. Y. He, W. Zhou, G. Qian and B. Chen, *Chem. Soc. Rev.*, 2014, **43**, 5657-5678.
227. X. Han, S. Yang and M. Schröder, *Nat. Rev. Chem.*, 2019, **3**, 108-118.
228. K. Adil, Y. Belmabkhout, R. S. Pillai, A. Cadiau, P. M. Bhatt, A. H. Assen, G. Maurin and M. Eddaoudi, *Chem. Soc. Rev.*, 2017, **46**, 3402-3430.
229. N. S. Bobbitt, M. L. Mendonca, A. J. Howarth, T. Islamoglu, J. T. Hupp, O. K. Farha and R. Q. Snurr, *Chem. Soc. Rev.*, 2017, **46**, 3357-3385.
230. S. Ma and H.-C. Zhou, *Chem. Commun.*, 2010, **46**, 44-53.
231. Y. Lin, C. Kong, Q. Zhang and L. Chen, *Adv. Energy Mater.*, 2017, **7**, 1601296.
232. S. M. J. Rogge, A. Bavykina, J. Hajek, H. Garcia, A. I. Olivos-Suarez, A. Sepúlveda-Escribano, A. Vimont, G. Clet, P. Bazin and F. Kapteijn, *Chem. Soc. Rev.*, 2017, **46**, 3134-3184.
233. C. S. Diercks, Y. Liu, K. E. Cordova and O. M. Yaghi, *Nat. Mater.*, 2018, **17**, 301-307.
234. B. Li, H.-M. Wen, W. Zhou and B. Chen, *J. Phy. Chem. Lett.*, 2014, **5**, 3468-3479.
235. X. Zhao, Y. Wang, D. S. Li, X. Bu and P. Feng, *Adv. Mater.*, 2018, **30**, 1705189.
236. Z. Kang, L. Fan and D. Sun, *J. Mater. Chem. A*, 2017, **5**, 10073-10091.
237. M. S. Denny Jr, J. C. Moreton, L. Benz and S. M. Cohen, *Nat. Rev. Mater.*, 2016, **1**, 16078.
238. L. E. Kreno, K. Leong, O. K. Farha, M. Allendorf, R. P. Van Duyne and J. T. Hupp, *Chem. Rev.*, 2011, **112**, 1105-1125.
239. A. Chidambaram and K. C. Stylianou, *Inorg. Chem. Front.*, 2018, **5**, 979-998.

240. W. P. Lustig, S. Mukherjee, N. D. Rudd, A. V. Desai, J. Li and S. K. Ghosh, *Chem. Soc. Rev.*, 2017, **46**, 3242-3285.
241. I. Stassen, N. Burtch, A. Talin, P. Falcaro, M. Allendorf and R. Ameloot, *Chem. Soc. Rev.*, 2017, **46**, 3185-3241.
242. P. Falcaro, R. Ricco, C. M. Doherty, K. Liang, A. J. Hill and M. J. Styles, *Chem. Soc. Rev.*, 2014, **43**, 5513-5560.
243. S. Wuttke, M. Lismont, A. Escudero, B. Rungtaweevoranit and W. J. Parak, *Biomaterials*, 2017, **123**, 172-183.
244. T. Simon-Yarza, A. Mielcarek, P. Couvreur and C. Serre, *Adv. Mater.*, 2018, **30**, 1707365.
245. S. Wang, C. M. McGuirk, A. d'Aquino, J. A. Mason and C. A. Mirkin, *Adv. Mater.*, 2018, **30**, 1800202.
246. W. Chen and C. Wu, *Dalton Trans.*, 2018, **47**, 2114-2133.
247. J. An, S. J. Geib and N. L. Rosi, *J. Am. Chem. Soc.*, 2009, **131**, 8376-8377.
248. M. Zhang, Z.-Y. Gu, M. Bosch, Z. Perry and H.-C. Zhou, *Coord. Chem. Rev.*, 2015, **293**, 327-356.
249. A. M. Fracaroli, P. Siman, D. A. Nagib, M. Suzuki, H. Furukawa, F. D. Toste and O. M. Yaghi, *J. Am. Chem. Soc.*, 2016, **138**, 8352-8355.
250. A. Zimpel, N. Al Danaf, B. Steinborn, J. Kuhn, M. Höhn, T. Bauer, P. Hirschle, W. Schrimpf, H. Engelke and E. Wagner, *ACS Nano*, 2019, **13**, 3884-3895.
251. X. Zhang, A. Chen, M. Zhong, Z. Zhang, X. Zhang, Z. Zhou and X.-H. Bu, *Electrochem. Energy Rev.*, 2019, **2**, 29-104.
252. S. Yang, L. Peng, S. Bulut and W. L. Queen, *Chem. Eur. J.*, 2019, **25**, 2161-2178.
253. H. B. Wu and X. W. D. Lou, *Sci. Adv.*, 2017, **3**, eaap9252.
254. Q. Wu, J. Liang, J.-D. Yi, D.-L. Meng, P.-C. Shi, Y.-B. Huang and R. Cao, *Dalton Trans.*, 2019.
255. A. Indra, T. Song and U. Paik, *Adv. Mater.*, 2018, **30**, 1705146.
256. X.-C. Xie, K.-J. Huang and X. Wu, *J. Mater. Chem. A*, 2018, **6**, 6754-6771.
257. G. Zheng, Z. Chen, K. Sentosun, I. Pérez-Juste, S. Bals, L. M. Liz-Marzán, I. Pastoriza-Santos, J. Pérez-Juste and M. Hong, *Nanoscale*, 2017, **9**, 16645-16651.
258. Y. Guo, Y. Mao, P. Hu, Y. Ying and X. Peng, *ChemistrySelect*, 2016, **1**, 108-113.
259. G. Zhan and H. C. Zeng, *Chem. Commun.*, 2017, **53**, 72-81.
260. I. Stassen, N. Campagnol, J. Fransaer, P. Vereecken, D. De Vos and R. Ameloot, *CrystEngComm*, 2013, **15**, 9308-9311.
261. K. Khaletskaya, S. Turner, M. Tu, S. Wannapaiboon, A. Schneemann, R. Meyer, A. Ludwig, G. Van Tendeloo and R. A. Fischer, *Adv. Funct. Mater.*, 2014, **24**, 4804-4811.
262. S. Li, W. Zhang, Y. Zhu, Q. Zhao and F. Huo, *Cryst. Growth & Des.*, 2015, **15**, 1017-1021.
263. M. Lismont, L. Dreesen and S. Wuttke, *Adv. Funct. Mater.*, 2017, **27**, 1606314.
264. N. Stock and S. Biswas, *Chem. Rev.*, 2012, **112**, 933-969.
265. M. Faustini, J. Kim, G.-Y. Jeong, J. Y. Kim, H. R. Moon, W.-S. Ahn and D.-P. Kim, *J. Am. Chem. Soc.*, 2013, **135**, 14619-14626.
266. J. Zhao, M. D. Losego, P. C. Lemaire, P. S. Williams, B. Gong, S. E. Atanasov, T. M. Blevins, C. J. Oldham, H. J. Walls and S. D. Shepherd, *Adv. Mater. Interfaces*, 2014, **1**, 1400040.
267. X. Zou, G. Zhu, I. J. Hewitt, F. Sun and S. Qiu, *Dalton Trans.*, 2009, 3009-3013.
268. T. Friščić and L. Fábián, *CrystEngComm*, 2009, **11**, 743-745.
269. J.-B. Lin, R.-B. Lin, X.-N. Cheng, J.-P. Zhang and X.-M. Chen, *Chem. Commun.*, 2011, **47**, 9185-9187.
270. M. Lanchas, D. Vallejo-Sanchez, G. Beobide, O. Castillo, A. T. Aguayo, A. Luque and P. Román, *Chem. Commun.*, 2012, **48**, 9930-9932.
271. I. Stassen, M. Styles, G. Grenci, Hans V. Gorp, W. Vanderlinden, Steven D. Feyter, P. Falcaro, D. D. Vos, P. Vereecken and R. Ameloot, *Nat. Mater.* , 2015, **15**, 304.
272. M. S. Yao, W. X. Tang, G. E. Wang, B. Nath and G. Xu, *Adv. Mater.*, 2016, **28**, 5229-5234.
273. J. Li, W. Cao, Y. Mao, Y. Ying, L. Sun and X. Peng, *CrystEngComm*, 2014, **16**, 9788-9791.

274. L. Lin, T. Zhang, H. Liu, J. Qiu and X. Zhang, *Nanoscale*, 2015, **7**, 7615-7623.
275. Y. Pan, Y. Liu, G. Zeng, L. Zhao and Z. Lai, *Chem. Commun.*, 2011, **47**, 2071-2073.
276. W.-w. Zhan, Q. Kuang, J.-z. Zhou, X.-j. Kong, Z.-x. Xie and L.-s. Zheng, *J. Am. Chem. Soc.*, 2013, **135**, 1926-1933.
277. E. Zanchetta, L. Malfatti, R. Ricco, M. J. Styles, F. Lisi, C. J. Coghlan, C. J. Doonan, A. J. Hill, G. Brusatin and P. Falcaro, *Chem. Mater.*, 2014, **27**, 690-699.
278. S. M. Meckler, C. Li, W. L. Queen, T. E. Williams, J. R. Long, R. Buonsanti, D. J. Milliron and B. A. Helms, *Chem. Mater.*, 2015, **27**, 7673-7679.
279. H. Al-Kutubi, A. Dikhtiarenko, H. R. Zafarani, E. J. R. Sudhölter, J. Gascon and L. Rassaei, *CrystEngComm*, 2015, **17**, 5360-5364.
280. Y. Liu, J. H. Pan, N. Wang, F. Steinbach, X. Liu and J. Caro, *Angew. Chem., Int. Ed.*, 2015, **54**, 3028-3032.
281. G. Zhang, S. Hou, H. Zhang, W. Zeng, F. Yan, C. C. Li and H. Duan, *Adv. Mater.*, 2015, **27**, 2400-2405.
282. M. del Rio, C. Palomino Cabello, V. Gonzalez, F. Maya, J. B. Parra, V. Cerdà and G. Turnes Palomino, *Chem. Eur. J.*, 2016, **22**, 11770-11777.
283. Y. Sun, Q. Zhang, X. Xu, L. Zhang, Z. Wu, J. Guo and G. Lu, *Eur. J. Inorg. Chem.*, 2016, **2016**, 3553-3558.
284. M. Mazaj, N. Z. Logar, E. Žagar and S. Kovačič, *J. Mater. Chem. A*, 2017, **5**, 1967-1971.
285. Y. Yue, Z.-A. Qiao, X. Li, A. J. Binder, E. Formo, Z. Pan, C. Tian, Z. Bi and S. Dai, *Cryst. Growth Des.*, 2013, **13**, 1002-1005.
286. Y. Yue, N. Mehio, A. J. Binder and S. Dai, *CrystEngComm*, 2015, **17**, 1728-1735.
287. Y. Yue, B. Guo, Z.-A. Qiao, P. F. Fulvio, J. Chen, A. J. Binder, C. Tian and S. Dai, *Micropor. Mesopor. Mater.*, 2014, **198**, 139-143.
288. X.-C. Li, Z. Zhang, W. Xiao, S. Deng, C. Chen and N. Zhang, *J. Mater. Chem. A*, 2019.
289. J. Reboul, S. Furukawa, N. Horike, M. Tsotsalas, K. Hirai, H. Uehara, M. Kondo, N. Louvain, O. Sakata and S. Kitagawa, *Nat. Mater.*, 2012, **11**, 717-723.
290. Y. Mao, H. Huang, Y. Liu, L. Shi, W. Cao, J. Li, L. Sun and X. Peng, *CrystEngComm*, 2013, **15**, 5591-5593.
291. R. Ranjan and M. Tsapatsis, *Chem. Mater.*, 2009, **21**, 4920-4924.
292. M. Nakahama, J. Reboul, K.-i. Kamei, S. Kitagawa and S. Furukawa, *Chem. Lett.*, 2014, **43**, 1052-1054.
293. T. Loiseau, C. Serre, C. Huguenard, G. Fink, F. Taulelle, M. Henry, T. Bataille and G. Férey, *Chem. Eur. J.*, 2004, **10**, 1373-1382.
294. M. Bechelany, M. Drobek, C. Vallicari, A. A. Chaaya, A. Julbe and P. Miele, *Nanoscale*, 2015, **7**, 5794-5802.
295. Z. Li, Y. n. Wu, J. Li, Y. Zhang, X. Zou and F. Li, *Chem. Eur. J.*, 2015, **21**, 6913-6920.
296. H. Guo, G. Zhu, I. J. Hewitt and S. Qiu, *J. Am. Chem. Soc.*, 2009, **131**, 1646-1647.
297. J. Kim, S. Lee, J. Kim and D. Lee, *Adv. Funct. Mater.*, 2019, **29**, 1808466.
298. G. Majano and J. Pérez-Ramírez, *Adv. Mater.*, 2013, **25**, 1052-1057.
299. K. Okada, R. Ricco, Y. Tokudome, M. J. Styles, A. J. Hill, M. Takahashi and P. Falcaro, *Adv. Funct. Mater.*, 2014, **24**, 1969-1977.
300. K. Okada, S. Sawai, K. Ikigaki, Y. Tokudome, P. Falcaro and M. Takahashi, *CrystEngComm*, 2017, **19**, 4194-4200.
301. P. Falcaro, K. Okada, T. Hara, K. Ikigaki, Y. Tokudome, A. W. Thornton, A. J. Hill, T. Williams, C. Doonan and M. Takahashi, *Nat. Mater.*, 2017, **16**, 342.
302. G. Zhan and H. C. Zeng, *Chem. Commun.*, 2016, **52**, 8432-8435.
303. G. Zhan and H. C. Zeng, *Adv. Funct. Mater.*, 2016, **26**, 3268-3281.
304. J. Reboul, K. Yoshida, S. Furukawa and S. Kitagawa, *CrystEngComm*, 2015, **17**, 323-330.
305. N. Wang, A. Mundstock, Y. Liu, A. Huang and J. Caro, *Chem. Eng. Sci.*, 2015, **124**, 27-36.

306. L. Maserati, S. M. Meckler, J. E. Bachman, J. R. Long and B. A. Helms, *Nano Lett.*, 2017, **17**, 6828-6832.
307. E. H. H. Chow, F. C. Strobridge and T. Friščić, *Chem. Commun.*, 2010, **46**, 6368-6370.
308. A. Delori, T. Friščić and W. Jones, *CrystEngComm*, 2012, **14**, 2350-2362.
309. P. Wang, G. Li, Y. Chen, S. Chen, S. L. James and W. Yuan, *CrystEngComm*, 2012, **14**, 1994-1997.
310. G. Cai, W. Zhang, L. Jiao, S.-H. Yu and H.-L. Jiang, *Chem*, 2017, **2**, 791-802.
311. M. J. Cliffe, C. Mottillo, R. S. Stein, D.-K. Bučar and T. Friščić, *Chem. Sci.*, 2012, **3**, 2495-2500.
312. F. Qi, R. S. Stein and T. Friščić, *Green Chem.*, 2014, **16**, 121-132.
313. C. Mottillo, Y. Lu, M.-H. Pham, M. J. Cliffe, T.-O. Do and T. Friščić, *Green Chem.*, 2013, **15**, 2121-2131.
314. J. A. Sayer and G. M. Gadd, *Mycological Research*, 1997, **101**, 653-661.
315. B. Liu, H. Shioyama, T. Akita and Q. Xu, *J. Am. Chem. Soc.*, 2008, **130**, 5390-5391.
316. W. Chaikittisilp, K. Ariga and Y. Yamauchi, *J. Mater. Chem. A*, 2013, **1**, 14-19.
317. W. Yang, X. Li, Y. Li, R. Zhu and H. Pang, *Adv. Mater.*, 2019, **31**, 1804740.
318. X. Li, S. Zheng, L. Jin, Y. Li, P. Geng, H. Xue, H. Pang and Q. Xu, *Adv. Energy Mater.*, 2018, **8**, 1800716.
319. L. Yang, X. Zeng, W. Wang and D. Cao, *Adv. Funct. Mater.*, 2018, **28**, 1704537.
320. K. Shen, X. Chen, J. Chen and Y. Li, *ACS Catal.*, 2016, **6**, 5887-5903.
321. R. R. Salunkhe, Y. V. Kaneti, J. Kim, J. H. Kim and Y. Yamauchi, *Acc. Chem. Res.*, 2016, **49**, 2796-2806.
322. O. M. Yaghi, M. O'keeffe, N. W. Ockwig, H. K. Chae, M. Eddaoudi and J. Kim, *Nature*, 2003, **423**, 705-714.
323. K. J. Lee, J. H. Lee, S. Jeoung and H. R. Moon, *Acc. Chem. Res.*, 2017, **50**, 2684-2692.
324. S. Zheng, X. Li, B. Yan, Q. Hu, Y. Xu, X. Xiao, H. Xue and H. Pang, *Adv. Energy Mater.*, 2017, **7**, 1602733.
325. J. Meng, C. Niu, L. Xu, J. Li, X. Liu, X. Wang, Y. Wu, X. Xu, W. Chen, Q. Li, Z. Zhu, D. Zhao and L. Mai, *J. Am. Chem. Soc.*, 2017, **139**, 8212-8221.
326. T. Uemura, N. Uchida, A. Asano, A. Saeki, S. Seki, M. Tsujimoto, S. Isoda and S. Kitagawa, *J. Am. Chem. Soc.*, 2012, **134**, 8360-8363.
327. K. Kongpatpanich, S. Horike, Y.-i. Fujiwara, N. Ogiwara, H. Nishihara and S. Kitagawa, *Chem. Eur. J.*, 2015, **21**, 13278-13283.
328. R. Zhao, Z. Liang, S. Gao, C. Yang, B. Zhu, J. Zhao, C. Qu, R. Zou and Q. Xu, *Angew. Chem., Int. Ed.*, 2019, **58**, 1975-1979.
329. T. K. Kim, K. J. Lee, J. Y. Cheon, J. H. Lee, S. H. Joo and H. R. Moon, *J. Am. Chem. Soc.*, 2013, **135**, 8940-8946.
330. Y.-Z. Chen, R. Zhang, L. Jiao and H.-L. Jiang, *Coord. Chem. Rev.*, 2018, **362**, 1-23.
331. Z. Liang, C. Qu, D. Xia, R. Zou and Q. Xu, *Angew. Chem., Int. Ed.*, 2018, **57**, 9604-9633.
332. H. Yang and X. Wang, *Adv. Mater.*, 2018, 1800743.
333. J. Zhou, Y. Dou, A. Zhou, R.-M. Guo, M.-J. Zhao and J.-R. Li, *Adv. Energy Mater.*, 2017, **7**, 1602643.
334. Y. V. Kaneti, J. Tang, R. R. Salunkhe, X. Jiang, A. Yu, K. C. W. Wu and Y. Yamauchi, *Adv. Mater.*, 2017, **29**, 1604898.
335. L. Zhang and Y. H. Hu, *J. Phys, Chem. C*, 2010, **114**, 2566-2572.
336. S. Gadipelli and Z. X. Guo, *ChemSusChem*, 2015, **8**, 2123-2132.
337. J. Hwang, R. Walczak, M. Oschatz, N. V. Tarakina and B. V. K. J. Schmidt, *Small*, 2019, **15**, 1901986.
338. S. Jeoung, S. H. Sahgong, J. H. Kim, S. M. Hwang, Y. Kim and H. R. Moon, *J. Mater. Chem. A*, 2016, **4**, 13468-13475.
339. J. Tang and Y. Yamauchi, *Nat. Chem.*, 2016, **8**, 638-639.

340. S. Furukawa, J. Reboul, S. Diring, K. Sumida and S. Kitagawa, *Chem. Soc. Rev.*, 2014, **43**, 5700-5734.
341. Y. Luo, M. Ahmad, A. Schug and M. Tsotsalas, *Adv. Mater.*, 2019, 1901744.
342. M. Majewski, H. Noh, T. Islamoglu and O. Farha, *J. Mater. Chem. A*, 2018, **6**, 7338-7350.
343. S. Dang, Q.-L. Zhu and Q. Xu, *Nat. Rev. Mater.*, 2017, **3**, 17075.
344. B. Y. Guan, X. Y. Yu, H. B. Wu and X. W. Lou, *Adv. Mater.*, 2017, **29**, 1703614.
345. R. R. Salunkhe, Y. V. Kaneti and Y. Yamauchi, *ACS Nano*, 2017, **11**, 5293-5308.
346. R. Das, P. Pachfule, R. Banerjee and P. Poddar, *Nanoscale*, 2012, **4**, 591-599.
347. S. J. Yang, T. Kim, J. H. Im, Y. S. Kim, K. Lee, H. Jung and C. R. Park, *Chem. Mater.*, 2012, **24**, 464-470.
348. L. Oar-Arteta, T. Wezendonk, X. Sun, F. Kapteijn and J. Gascon, *Mater. Chem. Front.*, 2017, **1**, 1709-1745.
349. K. J. Lee, Y. J. Sa, H. Y. Jeong, C. W. Bielawski, S. H. Joo and H. R. Moon, *Chem. Commun.*, 2015, **51**, 6773-6776.
350. Q. Li, P. Xu, W. Gao, S. Ma, G. Zhang, R. Cao, J. Cho, H.-L. Wang and G. Wu, *Adv. Mater.*, 2014, **26**, 1378-1386.
351. Y.-Z. Chen, C. Wang, Z.-Y. Wu, Y. Xiong, Q. Xu, S.-H. Yu and H.-L. Jiang, *Adv. Mater.*, 2015, **27**, 5010-5016.
352. J. Tang, R. R. Salunkhe, J. Liu, N. L. Torad, M. Imura, S. Furukawa and Y. Yamauchi, *J. Am. Chem. Soc.*, 2015, **137**, 1572-1580.
353. M. Hu, J. Reboul, S. Furukawa, N. L. Torad, Q. Ji, P. Srinivasu, K. Ariga, S. Kitagawa and Y. Yamauchi, *J. Am. Chem. Soc.*, 2012, **134**, 2864-2867.
354. H. B. Aiyappa, P. Pachfule, R. Banerjee and S. Kurungot, *Cryst. Growth Des.*, 2013, **13**, 4195-4199.
355. S. Lim, K. Suh, Y. Kim, M. Yoon, H. Park, D. N. Dybtsev and K. Kim, *Chem. Commun.*, 2012, **48**, 7447-7449.
356. A. Aijaz, N. Fujiwara and Q. Xu, *J. Am. Chem. Soc.*, 2014, **136**, 6790-6793.
357. G. Srinivas, V. Krungleviciute, Z.-X. Guo and T. Yildirim, *Energy Environ. Sci.*, 2014, **7**, 335-342.
358. S. J. Yang, S. Nam, T. Kim, J. H. Im, H. Jung, J. H. Kang, S. Wi, B. Park and C. R. Park, *J. Am. Chem. Soc.*, 2013, **135**, 7394-7397.
359. S. Liu, Z. Wang, S. Zhou, F. Yu, M. Yu, C.-Y. Chiang, W. Zhou, J. Zhao and J. Qiu, *Adv. Mater.*, 2017, **29**, 1700874.
360. J. Hwang, R. Yan, M. Oschatz and B. V. K. J. Schmidt, *J. Mater. Chem. A*, 2018, **6**, 23521-23530.
361. F. Cao, M. Zhao, Y. Yu, B. Chen, Y. Huang, J. Yang, X. Cao, Q. Lu, X. Zhang, Z. Zhang, C. Tan and H. Zhang, *J. Am. Chem. Soc.*, 2016, **138**, 6924-6927.
362. N. Cheng, L. Ren, X. Xu, Y. Du and S. X. Dou, *Adv. Energy Mater.*, 2018, **8**.
363. A. J. Amali, H. Hoshino, C. Wu, M. Ando and Q. Xu, *Chem. Eur. J.*, 2014, **20**, 8279-8282.
364. Z.-X. Cai, Z.-L. Wang, J. Kim and Y. Yamauchi, *Adv. Mater.*, 2019, **31**, 1804903.
365. B. Y. Xia, Y. Yan, N. Li, H. B. Wu, X. W. Lou and X. Wang, *Nat. Energy*, 2016, **1**, 15006.
366. C. Liu, X. Huang, J. Wang, H. Song, Y. Yang, Y. Liu, J. Li, L. Wang and C. Yu, *Adv. Funct. Mater.*, 2018, **28**, 1705253.
367. S. Yang, L. Peng, P. Huang, X. Wang, Y. Sun, C. Cao and W. Song, *Angew. Chem., Int. Ed.*, 2016, **55**, 4016-4020.
368. H. Chen, K. Shen, Y. Tan and Y. Li, *ACS Nano*, 2019, **13**, 7800-7810.
369. X. Li, G. Xu, J. Peng, S. Liu, H. Zhang, J. Mao, H. Niu, W. Lv, X. Zhao and R. a. Wu, *ACS Appl. Mater. Interfaces*, 2018, **10**, 11896-11906.
370. F. Zheng, G. Xia, Y. Yang and Q. Chen, *Nanoscale*, 2015, **7**, 9637-9645.
371. N. Wu, D. Xu, Z. Wang, F. Wang, J. Liu, W. Liu, Q. Shao, H. Liu, Q. Gao and Z. Guo, *Carbon*, 2019, **145**, 433-444.

372. T. Tsuruoka, S. Furukawa, Y. Takashima, K. Yoshida, S. Isoda and S. Kitagawa, *Angew. Chem., Int. Ed.*, 2009, **48**, 4739-4743.
373. P. Pachfule, D. Shinde, M. Majumder and Q. Xu, *Nat. Chem.*, 2016, **8**, 718.
374. W. Xia, J. Li, T. Wang, L. Song, H. Guo, H. Gong, C. Jiang, B. Gao and J. He, *Chem. Commun.*, 2018, **54**, 1623-1626.
375. S. Liu, J. Zhou and H. Song, *Adv. Energy Mater.*, 2018, **8**, 1800569.
376. K. M. Zhao, S. Q. Liu, G. Y. Ye, Q. M. Gan, Z. Zhou and Z. He, *J. Mater. Chem. A*, 2018, **6**, 2166-2175.
377. L. Kong, J. Zhu, W. Shuang and X.-H. Bu, *Adv. Energy Mater.*, 2018, **8**, 1801515.
378. F. Wu, S. Zhang, B. Xi, Z. Feng, D. Sun, X. Ma, J. Zhang, J. Feng and S. Xiong, *Adv. Energy Mater.*, 2018, **8**, 1703242.
379. L. Zou, M. Kitta, J. Hong, K. Suenaga, N. Tsumori, Z. Liu and Q. Xu, *Adv. Mater.*, 2019, **31**, 1900440.
380. Q.-L. Zhu, W. Xia, T. Akita, R. Zou and Q. Xu, *Adv. Mater.*, 2016, **28**, 6391-6398.
381. T. Wang, H.-K. Kim, Y. Liu, W. Li, J. T. Griffiths, Y. Wu, S. Laha, K. D. Fong, F. Podjaski, C. Yun, R. V. Kumar, B. V. Lotsch, A. K. Cheetham and S. K. Smoukov, *J. Am. Chem. Soc.*, 2018, **140**, 6130-6136.
382. A. Umemura, S. Diring, S. Furukawa, H. Uehara, T. Tsuruoka and S. Kitagawa, *J. Am. Chem. Soc.*, 2011, **133**, 15506-15513.
383. J. Hwang, T. Heil, M. Antonietti and B. V. K. J. Schmidt, *J. Am. Chem. Soc.*, 2018, **140**, 2947-2956.
384. M. Jehannin, A. Rao and H. Cölfen, *J. Am. Chem. Soc.*, 2019, **141**, 10120-10136.
385. F. C. Meldrum and H. Cölfen, *Chem. Rev.*, 2008, **108**, 4332-4432.
386. T. Kitao, Y. Zhang, S. Kitagawa, B. Wang and T. Uemura, *Chem. Soc. Rev.*, 2017, **46**, 3108-3133.
387. S. Furukawa, K. Hirai, Y. Takashima, K. Nakagawa, M. Kondo, T. Tsuruoka, O. Sakata and S. Kitagawa, *Chem. Commun.*, 2009, 5097-5099.
388. B. V. K. J. Schmidt, *Macromol. Rapid Commun.*, 2020, **41**, 1900333.
389. H. J. Lee, S. Choi and M. Oh, *Chem. Commun.*, 2014, **50**, 4492-4495.
390. W. Tian, H. Hu, Y. Wang, P. Li, J. Liu, J. Liu, X. Wang, X. Xu, Z. Li, Q. Zhao, H. Ning, W. Wu and M. Wu, *ACS Nano*, 2018, **12**, 1990-2000.
391. J. Wei, Y. Hu, Y. Liang, B. Kong, J. Zhang, J. Song, Q. Bao, G. P. Simon, S. P. Jiang and H. Wang, *Adv. Funct. Mater.*, 2015, **25**, 5768-5777.
392. X. Zhou, L. Chen, W. Zhang, J. Wang, Z. Liu, S. Zeng, R. Xu, Y. Wu, S. Ye, Y. Feng, X. Cheng, Z. Peng, X. Li and Y. Yu, *Nano Lett.*, 2019, **19**, 4965-4973.
393. S. Choi, H. J. Lee and M. Oh, *Small*, 2016, **12**, 2424-2431.
394. B. Y. Guan, L. Yu and X. W. Lou, *Adv. Sci.*, 2017, **4**, 1700247.
395. S. L. Zhang, B. Y. Guan and X. W. Lou, *Small*, 2019, **15**, 1805324.
396. W. Zhang, Z.-Y. Wu, H.-L. Jiang and S.-H. Yu, *J. Am. Chem. Soc.*, 2014, **136**, 14385-14388.
397. L. Ge, Y. Yang, L. Wang, W. Zhou, R. De Marco, Z. Chen, J. Zou and Z. Zhu, *Carbon*, 2015, **82**, 417-424.
398. Y. Zheng, S. Zheng, H. Xue and H. Pang, *Adv. Funct. Mater.*, 2018, **28**, 1804950.
399. X. W. Liu, T. J. Sun, J. L. Hu and S. D. Wang, *J. Mater. Chem. A*, 2016, **4**, 3584-3616.
400. H.-x. Zhong, J. Wang, Y.-w. Zhang, W.-l. Xu, W. Xing, D. Xu, Y.-f. Zhang and X.-b. Zhang, *Angew. Chem., Int. Ed.*, 2014, **53**, 14235-14239.
401. T. Y. Ma, S. Dai, M. Jaroniec and S. Z. Qiao, *J. Am. Chem. Soc.*, 2014, **136**, 13925-13931.
402. J. Zhou, Y. Dou, A. Zhou, L. Shu, Y. Chen and J.-R. Li, *ACS Energy Lett.*, 2018, **3**, 1655-1661.
403. H. Zhang, T. Wang, A. Sumboja, W. Zang, J. Xie, D. Gao, S. J. Pennycook, Z. Liu, C. Guan and J. Wang, *Adv. Funct. Mater.*, 2018, **28**, 1804846.

404. J. Zhao, H. Li, C. Li, Q. Zhang, J. Sun, X. Wang, J. Guo, L. Xie, J. Xie, B. He, Z. Zhou, C. Lu, W. Lu, G. Zhu and Y. Yao, *Nano Energy*, 2018, **45**, 420-431.
405. J. Liu, D. Zhu, Y. Zheng, A. Vasileff and S.-Z. Qiao, *ACS Catal.*, 2018, **8**, 6707-6732.
406. G. Jia, W. Zhang, G. Fan, Z. Li, D. Fu, W. Hao, C. Yuan and Z. Zou, *Angew. Chem., Int. Ed.*, 2017, **56**, 13781-13785.
407. B. Y. Guan, L. Yu and X. W. Lou, *Energy Environ. Sci.*, 2016, **9**, 3092-3096.
408. K. Shen, L. Zhang, X. Chen, L. Liu, D. Zhang, Y. Han, J. Chen, J. Long, R. Luque and Y. Li, *Science*, 2018, **359**, 206-210.
409. N. D. Petkovich and A. Stein, *Chem. Soc. Rev.*, 2013, **42**, 3721-3739.
410. D. Gu and F. Schüth, *Chem. Soc. Rev.*, 2014, **43**, 313-344.
411. J. Hwang, C. Jo, K. Hur, J. Lim, S. Kim and J. Lee, *J. Am. Chem. Soc.*, 2014, **136**, 16066-16072.
412. C. Jo, J. Hwang, W.-G. Lim, J. Lim, K. Hur and J. Lee, *Adv. Mater.*, 2018, **30**, 1703829.
413. S. Kim, I. Jeong, J. Hwang, M. J. Ko and J. Lee, *Chem. Commun.*, 2017, **53**, 4100-4103.
414. J. Hwang, S. Kim, U. Wiesner and J. Lee, *Adv. Mater.*, 2018, **30**, 1801127.
415. X. Song, L. Guo, X. Liao, J. Liu, J. Sun and X. Li, *Small*, 2017, **13**, 1700238.
416. L. Chai, L. Zhang, X. Wang, L. Xu, C. Han, T.-T. Li, Y. Hu, J. Qian and S. Huang, *Carbon*, 2019, **146**, 248-256.
417. Q. He, J. Liu, Z. Li, Q. Li, L. Xu, B. Zhang, J. Meng, Y. Wu and L. Mai, *Small*, 2017, **13**, 1701504.
418. G. Zou, H. Hou, G. Zhao, P. Ge, D. Yin and X. Ji, *J. Mater. Chem. A*, 2018, **6**, 4839-4847.
419. C. Lin, S. S. Shinde, Z. Jiang, X. Song, Y. Sun, L. Guo, H. Zhang, J.-Y. Jung, X. Li and J.-H. Lee, *J. Mater. Chem. A*, 2017, **5**, 13994-14002.
420. S. H. Ahn and A. Manthiram, *Small*, 2017, **13**, 1603437.
421. Y. M. Chen, L. Yu and X. W. Lou, *Angew. Chem., Int. Ed.*, 2016, **55**, 5990-5993.
422. Y. Chen, X. Li, K. Park, W. Lu, C. Wang, W. Xue, F. Yang, J. Zhou, L. Suo, T. Lin, H. Huang, J. Li and J. B. Goodenough, *Chem*, 2017, **3**, 152-163.
423. J. Wang, J. Tang, B. Ding, Z. Chang, X. Hao, T. Takei, N. Kobayashi, Y. Bando, X. Zhang and Y. Yamauchi, *Small*, 2018, **14**, 1704461.
424. B. Ding, J. Wang, Z. Chang, G. Xu, X. Hao, L. Shen, H. Dou and X. Zhang, *ChemElectroChem*, 2016, **3**, 668-674.
425. Z. Li, M. Shao, L. Zhou, R. Zhang, C. Zhang, M. Wei, D. G. Evans and X. Duan, *Adv. Mater.*, 2016, **28**, 2337-2344.
426. X. Song, S. Chen, L. Guo, Y. Sun, X. Li, X. Cao, Z. Wang, J. Sun, C. Lin and Y. Wang, *Adv. Energy Mater.*, 2018, **8**, 1801101.
427. X. Sun, S. Sun, S. Gu, Z. Liang, J. Zhang, Y. Yang, Z. Deng, P. Wei, J. Peng, Y. Xu, C. Fang, Q. Li, J. Han, Z. Jiang and Y. Huang, *Nano Energy*, 2019, **61**, 245-250.
428. Z. Li, J. Cui, Y. Liu, J. Li, K. Liu and M. Shao, *ACS Appl. Mater. Interfaces*, 2018, **10**, 34494-34501.
429. Z. Tang, G. Zhang, H. Zhang, L. Wang, H. Shi, D. Wei and H. Duan, *Energy Storage Mater.*, 2018, **10**, 75-84.
430. Q. Yang, Z. Li, R. Zhang, L. Zhou, M. Shao and M. Wei, *Nano Energy*, 2017, **41**, 408-416.
431. C. Young, J. Wang, J. Kim, Y. Sugahara, J. Henzie and Y. Yamauchi, *Chem. Mater.*, 2018, **30**, 3379-3386.
432. X. Huang, X. Xu, C. Li, D. Wu, D. Cheng and D. Cao, *Adv. Energy Mater.*, 2019, **9**, 1803970.
433. D. Wang, B. Yan, Y. Guo, L. Chen, F. Yu and G. Wang, *Sci. Rep.*, 2019, **9**, 5934.
434. S. Feng, X. Li, J. Huo, Q. Li, C. Xie, T. Liu, Z. Liu, Z. Wu and S. Wang, *ChemCatChem*, 2018, **10**, 796-803.
435. Z. Chen, Y. Ha, H. Jia, X. Yan, M. Chen, M. Liu and R. Wu, *Adv. Energy Mater.*, 2019, **9**, 1803918.
436. Y. Chen, S. Li, X. Pei, J. Zhou, X. Feng, S. Zhang, Y. Cheng, H. Li, R. Han and B. Wang, *Angew. Chem., Int. Ed.*, 2016, **55**, 3419-3423.

437. Q. Shi, Z. Chen, Z. Song, J. Li and J. Dong, *Angew. Chem., Int. Ed.*, 2011, **50**, 672-675.
438. C. Wang, Y. V. Kaneti, Y. Bando, J. Lin, C. Liu, J. Li and Y. Yamauchi, *Mater. Horiz.*, 2018, **5**, 394-407.
439. Z. Lyu, G. J. Lim, R. Guo, Z. Kou, T. Wang, C. Guan, J. Ding, W. Chen and J. Wang, *Adv. Funct. Mater.*, 2019, **29**, 1806658.
440. W. Zhang, X. Jiang, Y. Zhao, A. Carné-Sánchez, V. Malgras, J. Kim, J. H. Kim, S. Wang, J. Liu, J.-S. Jiang, Y. Yamauchi and M. Hu, *Chem. Sci.*, 2017, **8**, 3538-3546.
441. M. Zhao, Y. Huang, Y. Peng, Z. Huang, Q. Ma and H. Zhang, *Chem. Soc. Rev.*, 2018, **47**, 6267-6295.
442. S. Jeoung, I. T. Ju, J. H. Kim, S. H. Joo and H. R. Moon, *J. Mater. Chem. A*, 2018, **6**, 18906-18911.
443. C. Wang, C. Liu, J. Li, X. Sun, J. Shen, W. Han and L. Wang, *Chem. Commun.*, 2017, **53**, 1751-1754.
444. M. Du, K. Rui, Y. Chang, Y. Zhang, Z. Ma, W. Sun, Q. Yan, J. Zhu and W. Huang, *Small*, 2018, **14**, 1702770.
445. S. Liu, J. Zhou and H. Song, *Chem. Commun.*, 2018, **54**, 9825-9828.
446. Q. Lai, Y. Zhao, Y. Liang, J. He and J. Chen, *Adv. Funct. Mater.*, 2016, **26**, 8334-8344.
447. C. Wang, J. Kim, M. Kim, H. Lim, M. Zhang, J. You, J.-H. Yun, Y. Bando, J. Li and Y. Yamauchi, *J. Mater. Chem. A*, 2019, **7**, 13743-13750.
448. G. Lee, Y. D. Seo and J. Jang, *Chem. Commun.*, 2017, **53**, 11441-11444.
449. C.-L. Zhang, B.-R. Lu, F.-H. Cao, Z.-Y. Wu, W. Zhang, H.-P. Cong and S.-H. Yu, *Nano Energy*, 2019, **55**, 226-233.
450. G.-P. Hao, C. Tang, E. Zhang, P. Zhai, J. Yin, W. Zhu, Q. Zhang and S. Kaskel, *Adv. Mater.*, 2017, **29**, 1702829.
451. W. Xia, J. Tang, J. Li, S. Zhang, K. C.-W. Wu, J. He and Y. Yamauchi, *Angew. Chem., Int. Ed.*, 2019, **58**, 13354-13359.
452. K. Fu, Y. Yao, J. Dai and L. Hu, *Adv. Mater.*, 2017, **29**, 1603486.
453. O. Halevi, J. M. R. Tan, P. S. Lee and S. Magdassi, *Adv. Sustainable Syst.*, 2018, **2**, 1700150.
454. A. S. Gladman, E. A. Matsumoto, R. G. Nuzzo, L. Mahadevan and J. A. Lewis, *Nat. Mater.*, 2016, **15**, 413.
455. S. L. Harper, J. L. Carriere, J. M. Miller, J. E. Hutchison, B. L. S. Maddux and R. L. Tanguay, *ACS Nano*, 2011, **5**, 4688-4697.
456. M. Safaei, M. M. Foroughi, N. Ebrahimpoor, S. Jahani, A. Omidi and M. Khatami, *TrAC Trends Anal. Chem.*, 2019.
457. Y. Li and W. Shen, *Nanocatalysis: Synthesis and Applications*, Wiley Online Library, 2013.
458. S. A. A. Razavi, M. Y. Masoomi, T. Islamoglu, A. Morsali, Y. Xu, J. T. Hupp, O. K. Farha, J. Wang and P. C. Junk, *Inorg. Chem.*, 2017, **56**, 2581-2588.
459. J.-R. Li, R. J. Kuppler and H.-C. Zhou, *Chem. Soc. Rev.*, 2009, **38**, 1477-1504.
460. P. Valvekens, D. Jonckheere, T. De Baerdemaeker, A. V. Kubarev, M. Vandichel, K. Hemelsoet, M. Waroquier, V. Van Speybroeck, E. Smolders and D. Depla, *Chem. Sci.*, 2014, **5**, 4517-4524.
461. C. Wang, J. Kim, V. Malgras, J. Na, J. Lin, J. You, M. Zhang, J. Li and Y. Yamauchi, *Small*, 2019, **15**, 1900744.
462. S. A. A. Razavi, M. Y. Masoomi and A. Morsali, *Ultrason. Sonochem.*, 2017, **37**, 502-508.
463. A. Qiao, H. Tao, M. P. Carson, S. W. Aldrich, L. M. Thirion, T. D. Bennett, J. C. Mauro and Y. Yue, *Opt. Lett.*, 2019, **44**, 1623-1625.
464. X. Jiang, L. Zhang, S. Liu, Y. Zhang, Z. He, W. Li, F. Zhang, Y. Shi, W. Lü and Y. Li, *Adv. Opt. Mater.*, 2018, **6**, 1800561.
465. J. Li, Y. Ren, C. Qi and H. Jiang, *Chem. Commun.*, 2017, **53**, 8223-8226.
466. G. M. Espallargas and E. Coronado, *Chem. Soc. Rev.*, 2018, **47**, 533-557.

467. P. Horcajada, C. Serre, G. Maurin, N. A. Ramsahye, F. Balas, M. Vallet-Regi, M. Sebban, F. Taulelle and G. Férey, *J. Am. Chem. Soc.*, 2008, **130**, 6774-6780.
468. W. J. Rieter, K. M. L. Taylor, H. An, W. Lin and W. Lin, *J. Am. Chem. Soc.*, 2006, **128**, 9024-9025.
469. H.-S. Wang, *Coord. Chem. Rev.*, 2017, **349**, 139-155.
470. F.-F. Wang, Z. Liu and Z.-L. Cheng, *Mater. Lett.*, 2019, **248**, 222-226.
471. B. Li, H. M. Wen, Y. Cui, W. Zhou, G. Qian and B. Chen, *Adv. Mater.*, 2016, **28**, 8819-8860.
472. P. K. Allan, P. S. Wheatley, D. Aldous, M. I. Mohideen, C. Tang, J. A. Hriljac, I. L. Megson, K. W. Chapman, G. De Weireld and S. Vaesen, *Dalton Trans.*, 2012, **41**, 4060-4066.
473. S. N. Wijenayake, N. P. Panapitiya, S. H. Versteeg, C. N. Nguyen, S. Goel, K. J. Balkus Jr, I. H. Musselman and J. P. Ferraris, *Ind. Eng. Chem. Res.*, 2013, **52**, 6991-7001.
474. D. Tanaka, A. Henke, K. Albrecht, M. Moeller, K. Nakagawa, S. Kitagawa and J. Groll, *Nat. Chem.*, 2010, **2**, 410.
475. D. Schneider, D. Mehlhorn, P. Zeigermann, J. Kaerger and R. Valiullin, *Chem. Soc. Rev.*, 2016, **45**, 3439-3467.
476. T. G. Glover and B. Mu, *Gas Adsorption in Metal-organic Frameworks: Fundamentals and Applications*, CRC Press, 2018.
477. B. Seoane, J. Coronas, I. Gascon, M. E. Benavides, O. Karvan, J. Caro, F. Kapteijn and J. Gascon, *Chem. Soc. Rev.*, 2015, **44**, 2421-2454.
478. L. M. Robeson, *J. Memb. Sci.*, 2008, **320**, 390-400.
479. D. Bradshaw, A. Garai and J. Huo, *Chem. Soc. Rev.*, 2012, **41**, 2344-2381.
480. S. Qiu, M. Xue and G. Zhu, *Chem. Soc. Rev.*, 2014, **43**, 6116-6140.
481. H. B. Park, J. Kamcev, L. M. Robeson, M. Elimelech and B. D. Freeman, *Science*, 2017, **356**, eaab0530.
482. J. Zuo and T.-S. Chung, *Water*, 2016, **8**, 586.
483. T. Rodenas, I. Luz, G. Prieto, B. Seoane, H. Miro, A. Corma, F. Kapteijn, F. X. L. i Xamena and J. Gascon, *Nat. Mater.*, 2015, **14**, 48-55.
484. J. Zhou, X. Yu, X. Fan, X. Wang, H. Li, Y. Zhang, W. Li, J. Zheng, B. Wang and X. Li, *J. Mater. Chem. A*, 2015, **3**, 8272-8275.
485. J. Ren, N. M. Musyoka, P. Annamalai, H. W. Langmi, B. C. North and M. Mathe, *Int. J. Hydrogen Energy*, 2015, **40**, 9382-9387.
486. B. A. Lakshmi and S. Kim, *Mater. Sci. Eng. C*, 2019, 110091.
487. G. Chen, J. Luo, M. Cai, L. Qin, Y. Wang, L. Gao, P. Huang, Y. Yu, Y. Ding and X. Dong, *Molecules*, 2019, **24**, 3369.
488. K. Lu, C. He and W. Lin, *J. Am. Chem. Soc.*, 2014, **136**, 16712-16715.
489. L. Zhu, X.-Q. Liu, H.-L. Jiang and L.-B. Sun, *Chem. Rev.*, 2017, **117**, 8129-8176.
490. A. H. Chughtai, N. Ahmad, H. A. Younus, A. Laypkov and F. Verpoort, *Chem. Soc. Rev.*, 2015, **44**, 6804-6849.
491. Y. Kataoka, K. Sato, Y. Miyazaki, K. Masuda, H. Tanaka, S. Naito and W. Mori, *Energy Environ. Sci.*, 2009, **2**, 397-400.
492. S. Lin, Y. Pineda-Galvan, W. A. Maza, C. C. Epley, J. Zhu, M. C. Kessinger, Y. Pushkar and A. J. Morris, *ChemSusChem*, 2017, **10**, 514-522.
493. Y. Fu, D. Sun, Y. Chen, R. Huang, Z. Ding, X. Fu and Z. Li, *Angew. Chem., Int. Ed.*, 2012, **51**, 3364-3367.
494. N. Kornienko, Y. Zhao, C. S. Kley, C. Zhu, D. Kim, S. Lin, C. J. Chang, O. M. Yaghi and P. Yang, *J. Am. Chem. Soc.*, 2015, **137**, 14129-14135.
495. M. A. Nasalevich, M. G. Goesten, T. J. Savenije, F. Kapteijn and J. Gascon, *Chem. Commun.*, 2013, **49**, 10575-10577.
496. M. Lions, J. B. Tommasino, R. Chattot, B. Abeykoon, N. Guillou, T. Devic, A. Demessence, L. Cardenas, F. Maillard and A. Fateeva, *Chem. Commun.*, 2017, **53**, 6496-6499.

497. A. Kirchon, L. Feng, H. F. Drake, E. A. Joseph and H.-C. Zhou, *Chem. Soc. Rev.*, 2018, **47**, 8611-8638.
498. L. Luo, W.-S. Lo, X. Si, H. Li, Y. Wu, Y. An, Q. Zhu, L.-Y. Chou, T. Li and C.-K. Tsung, *J. Am. Chem. Soc.*, 2019.
499. J. Xu, X. Zhu and X. Jia, *ACS Sustain. Chem. Eng.*, 2019, **7**, 16629-16639.
500. X. Kang, Q. Zhu, X. Sun, J. Hu, J. Zhang, Z. Liu and B. Han, *Chem. Sci.*, 2016, **7**, 266-273.
501. F.-X. Bu, M. Hu, L. Xu, Q. Meng, G.-Y. Mao, D.-M. Jiang and J.-S. Jiang, *Chem. Commun.*, 2014, **50**, 8543-8546.
502. A. E. Baumann, D. A. Burns, B. Liu and V. S. Thoi, *Commun. Chem.*, 2019, **2**, 1-14.
503. J. Jin, Y. Zheng, S.-z. Huang, P.-p. Sun, N. Srikanth, L. B. Kong, Q. Yan and K. Zhou, *J. Mater. Chem. A*, 2019, **7**, 783-790.
504. M. Kriesten, J. V. Schmitz, J. Siegel, C. E. Smith, M. Kaspereit and M. Hartmann, *Euro. J. Inorg. Chem.*, 2019, **2019**, 4700-4709.
505. P. Kumar, A. Deep and K.-H. Kim, *TrAC Trends Anal. Chem.*, 2015, **73**, 39-53.
506. S. A. A. Razavi, M. Y. Masoomi and A. Morsali, *Ultrason. Sonochem.*, 2018, **41**, 17-26.
507. L. Feng, C. Dong, W. Jiang, X. Gu, M. Xiao, C. Li, Z. Ning and D. Gao, *J. Mater. Sci. Mater. Electron.*, 2019, **30**, 19247-19253.
508. J. Lei, R. Qian, P. Ling, L. Cui and H. Ju, *TrAC Trends Anal. Chem.*, 2014, **58**, 71-78.
509. L. J. Small, R. C. Hill, J. L. Krumhansl, M. E. Schindelholz, Z. Chen, K. W. Chapman, X. Zhang, S. Yang, M. Schröder and T. M. Nenoff, *ACS Appl. Mater. Interfaces*, 2019, **11**, 27982-27988.
510. H. Zhang, X. Liu, Y. Wu, C. Guan, A. K. Cheetham and J. Wang, *Chem. Commun.*, 2018, **54**, 5268-5288.
511. Q. Ren, H. Wang, X.-F. Lu, Y.-X. Tong and G.-R. Li, *Adv. Sci.*, 2018, **5**, 1700515.
512. K. Shen, X. Chen, J. Chen and Y. Li, *ACS Catal.*, 2016, **6**, 5887-5903.
513. A. M. Molenbroek, S. Helveg, H. Topsøe and B. S. Clausen, *Top. Catal.*, 2009, **52**, 1303-1311.
514. Y. Li, Q. Liu and W. Shen, *Dalton Trans.*, 2011, **40**, 5811-5826.
515. Y. Zhang, L. Yang, L. Yan, G. Wang and A. Liu, *Coord. Chem. Rev.*, 2019, **391**, 69-89.
516. P. Horcajada, R. Gref, T. Baati, P. K. Allan, G. Maurin, P. Couvreur, G. Férey, R. E. Morris and C. Serre, *Chem. Rev.*, 2012, **112**, 1232-1268.
517. C. He, D. Liu and W. Lin, *Chem. Rev.*, 2015, **115**, 11079-11108.
518. J. A. Champion, Y. K. Katare and S. Mitragotri, *J. Control. Release*, 2007, **121**, 3-9.
519. B. N. Bhadra, A. Vinu, C. Serre and S. H. Jhung, *Materials Today*, 2019, **25**, 88-111.
520. L. Borchardt, M. Oschatz and S. Kaskel, *Mater. Horiz.*, 2014, **1**, 157-168.
521. D. Sheberla, J. C. Bachman, J. S. Elias, C.-J. Sun, Y. Shao-Horn and M. Dincă, *Nat. Mater.*, 2016, **16**, 220.
522. L. Wang, Y. Han, X. Feng, J. Zhou, P. Qi and B. Wang, *Coord. Chem. Rev.*, 2016, **307**, 361-381.
523. R. R. Salunkhe, Y. Kamachi, N. L. Torad, S. M. Hwang, Z. Sun, S. X. Dou, J. H. Kim and Y. Yamauchi, *J. Mater. Chem. A*, 2014, **2**, 19848-19854.
524. X. Liu, C. Guan, Y. Hu, L. Zhang, A. M. Elshahawy and J. Wang, *Small*, 2018, **14**, 1702641.
525. Y. Qian, T. An, E. Sarnello, Z. Liu, T. Li and D. Zhao, *ACS Appl. Energy Mater.*, 2019, **2**, 1784-1792.
526. M. Zhang, Q. Dai, H. Zheng, M. Chen and L. Dai, *Adv. Mater.*, 2018, **30**, 1705431.
527. Y. Fu, Q. Wei, G. Zhang, X. Wang, J. Zhang, Y. Hu, D. Wang, L. Zuin, T. Zhou and Y. Wu, *Adv. Energy Mater.*, 2018, **8**, 1801445.
528. S. Bai, X. Liu, K. Zhu, S. Wu and H. Zhou, *Nat. Energy*, 2016, **1**, 16094.
529. S. Bai, K. Zhu, S. Wu, Y. Wang, J. Yi, M. Ishida and H. Zhou, *J. Mater. Chem. A*, 2016, **4**, 16812-16817.
530. Y. Qian, Q. Liu, E. Sarnello, C. Tang, M. Chng, J. Shui, T. Li, S. J. Pennycook, M. Han and D. Zhao, *ACS Mater. Lett.*, 2019, **1**, 37-43.

531. W. Chen, J. Pei, C.-T. He, J. Wan, H. Ren, Y. Wang, J. Dong, K. Wu, W.-C. Cheong, J. Mao, X. Zheng, W. Yan, Z. Zhuang, C. Chen, Q. Peng, D. Wang and Y. Li, *Adv. Mater.*, 2018, **30**, 1800396.
532. L. M. Roen, C. H. Paik and T. D. Jarvi, *Electrochem. Solid-State Lett.*, 2004, **7**, A19-A22.
533. U. I. Kramm, M. Lefèvre, N. Larouche, D. Schmeisser and J.-P. Dodelet, *J. Am. Chem. Soc.*, 2014, **136**, 978-985.
534. I. A. Khan, Y. Qian, A. Badshah, M. A. Nadeem and D. Zhao, *ACS Appl. Mater. Interfaces*, 2016, **8**, 17268-17275.
535. Y. Deng, B. Chi, J. Li, G. Wang, L. Zheng, X. Shi, Z. Cui, L. Du, S. Liao, K. Zang, J. Luo, Y. Hu and X. Sun, *Adv. Energy Mater.*, 2019, **9**, 1802856.
536. K. Meyer, M. Ranocchiari and J. A. van Bokhoven, *Energy Environ. Sci.*, 2015, **8**, 1923-1937.
537. J. Sun, B. V. K. J. Schmidt, X. Wang and M. Shalom, *ACS Appl. Mater. Interfaces*, 2017, **9**, 2029-2034.
538. W. Wang, X. Xu, W. Zhou and Z. Shao, *Adv. Sci.*, 2017, **4**, 1600371.
539. F. Ming, H. Liang, H. Shi, X. Xu, G. Mei and Z. Wang, *J. Mater. Chem. A*, 2016, **4**, 15148-15155.
540. K. Murugesan, T. Senthamarai, M. Sohail, A. S. Alshammari, M.-M. Pohl, M. Beller and R. V. Jagadeesh, *Chem. Sci.*, 2018, **9**, 8553-8560.
541. S. Dong, L. Peng, W. Wei and T. Huang, *ACS Appl. Mater. Interfaces*, 2018, **10**, 14665-14672.
542. J. Lee, O. K. Farha, J. Roberts, K. A. Scheidt, S. T. Nguyen and J. T. Hupp, *Chem. Soc. Rev.*, 2009, **38**, 1450-1459.
543. F. X. Llabrés i Xamena, A. Abad, A. Corma and H. Garcia, *J. Catal.*, 2007, **250**, 294-298.
544. H.-C. Lee, T. Heil, J.-K. Sun and B. V. K. J. Schmidt, *Mater. Horiz.*, 2019, **6**, 802-809.
545. L. Jin, X. Zhao, J. Ye, X. Qian and M. Dong, *Catal. Commun.*, 2018, **107**, 43-47.
546. Y. Gong, X. Zhao, H. Zhang, B. Yang, K. Xiao, T. Guo, J. Zhang, H. Shao, Y. Wang and G. Yu, *Appl. Catal. B: Environ.*, 2018, **233**, 35-45.
547. J. Lei, R. Qian, P. Ling, L. Cui and H. Ju, *TrAC, Trends Anal. Chem.*, 2014, **58**, 71-78.
548. X. Zhu, H. Zheng, X. Wei, Z. Lin, L. Guo, B. Qiu and G. Chen, *Chem. Commun.*, 2013, **49**, 1276-1278.
549. L. Xiao, R. Xu, Q. Yuan and F. Wang, *Talanta*, 2017, **167**, 39-43.
550. H. Tan, C. Ma, L. Gao, Q. Li, Y. Song, F. Xu, T. Wang and L. Wang, *Chem. – Eur. J.*, 2014, **20**, 16377-16383.
551. H. Xu, S. Zhou, L. Xiao, H. Wang, S. Li and Q. Yuan, *J. Mater. Chem. C*, 2015, **3**, 291-297.
552. X. Zhang, J. Luo, P. Tang, J. R. Morante, J. Arbiol, C. Xu, Q. Li and J. Fransaer, *Sens. Actuators, B*, 2018, **254**, 272-281.
553. D. Duan, H. Yang, Y. Ding, L. Li and G. Ma, *Electrochim. Acta*, 2019, **302**, 137-144.
554. S. Wuttke, A. Zimpel, T. Bein, S. Braig, K. Stoiber, A. Vollmar, D. Müller, K. Haastert-Talini, J. Schaeske, M. Stiesch, G. Zahn, A. Mohmeyer, P. Behrens, O. Eickelberg, D. A. Bölükbas and S. Meiners, *Adv. Healthcare Mater.*, 2017, **6**, 1600818.
555. M.-X. Wu and Y.-W. Yang, *Adv. Mater.*, 2017, **29**, 1606134.
556. M. Peller, K. Böll, A. Zimpel and S. Wuttke, *Inorg. Chem. Front.*, 2018, **5**, 1760-1779.
557. X. Pan, L. Bai, H. Wang, Q. Wu, H. Wang, S. Liu, B. Xu, X. Shi and H. Liu, *Adv. Mater.*, 2018, **30**, 1800180.
558. N. L. Torad, Y. Li, S. Ishihara, K. Ariga, Y. Kamachi, H.-Y. Lian, H. Hamoudi, Y. Sakka, W. Chaikittisilp and K. C.-W. Wu, *Chem. Lett.*, 2014, **43**, 717-719.
559. X. Fan, F. Yang, J. Huang, Y. Yang, C. Nie, W. Zhao, L. Ma, C. Cheng, C. Zhao and R. Haag, *Nano Lett.*, 2019.
560. S. Li, Y. Chen, X. Pei, S. Zhang, X. Feng, J. Zhou and B. Wang, *Chin. J. Chem.*, 2016, **34**, 175-185.
561. A. Banerjee, R. Gokhale, S. Bhatnagar, J. Jog, M. Bhardwaj, B. Lefez, B. Hannoyer and S. Ogale, *J. Mater. Chem.*, 2012, **22**, 19694-19699.

562. N. L. Torad, M. Hu, S. Ishihara, H. Sukegawa, A. A. Belik, M. Imura, K. Ariga, Y. Sakka and Y. Yamauchi, *Small*, 2014, **10**, 2096-2107.
563. X. Ma, L. Li, R. Chen, C. Wang, H. Li and S. Wang, *Appl. Surf. Sci.*, 2018, **435**, 494-502.
564. M. Oschatz and R. Walczak, *C*, 2018, **4**, 56.

Table of contents

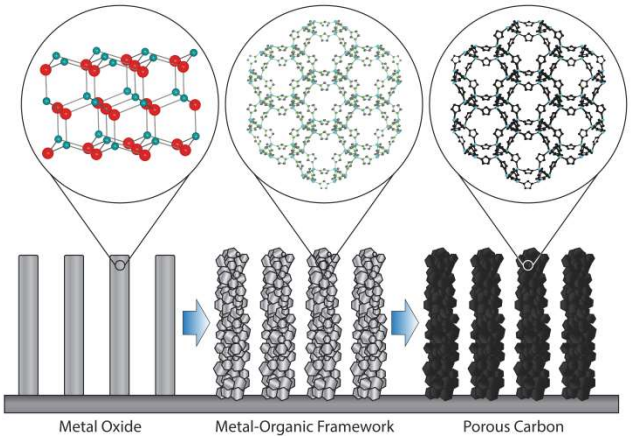

Author Biographies

Jongkook Hwang received his Ph.D. from Pohang University of Science and Technology (POSTECH) under the supervision of Prof. Jinwoo Lee in 2016. After his first post-doctoral training at Max Planck Institute of Colloids and Interfaces, he moved to Utrecht University where he worked on development of heterogeneous catalysts for preferential CO oxidation in H_2. His research interest is synthesis of nanoporous materials with well-defined structures and morphologies for energy- and catalytic applications.

Aleksander Ejsmont received his BS (2016) and MSc (2018) at collaborated universities: Adam Mickiewicz University in Poznań (AMU), Military University of Technology in Warsaw and Lodz University of Technology, followed by a one-year postgraduate research at University of Central Lancashire. In 2019 he started his PhD studies at AMU under supervision of Dr. Joanna Goscianska. His research focuses on the carbon materials, their synthesis, modification and applicability in fields such as adsorption, drug delivery and environmental sciences.

Ralph Freund is currently a PhD student at University of Augsburg (Germany) under the supervision of Prof. Dirk Volkmer. He obtained his MSc degree in chemistry at the University of Munich (LMU, Germany) with Stefan Wuttke in 2018, investigating the chemistry of metal oxide to metal-organic framework conversion reactions. His currently research focuses on electric-field responsive porous-coordination frameworks constructed from pyrazolate linkers.

Joanna Goscianska is an adjunct at the Faculty of Chemistry of Adam Mickiewicz University in Poznań (AMU). She obtained the Master's degree in 2005 and doctoral degree in 2009 in the field of chemistry. During her PhD studies, she participated in three research internships at Laboratoire Catalyse & Spectrochimie in Caen (France). In 2018 she became a laureate of the habilitation fellowship „L'ORÉAL-UNESCO FOR WOMEN IN SCIENCE". Her principal interest is focused on synthesis, modification, characterization of porous materials (*e.g.* metal oxides, ordered mesoporous silica and carbons) and their application in adsorption processes, catalysis, drug delivery systems.

Bernhard V. K. J. Schmidt completed his PhD in 2013 with Prof. Barner-Kowollik at the Karlsruhe Institute of Technology and a Post Doc with Prof. Hawker at the University of California, Santa Barbara. Afterwards he joined the department of Prof. Antonietti at the Max Planck Institute of Colloids and Interfaces as a Group Leader. Recently, he was appointed as Lecturer in Synthetic Polymer Chemistry at the University of Glasgow. His research focusses on block copolymer self-assembly, metal-organic framework/polymer hybrids and carbon nitride/polymer hybrid materials.

Stefan Wuttke created the research group “Wuttkegroup for Science”, initially hosted at the Institute of Physical Chemistry at the University of Munich (LMU, Germany). Currently, he is an Ikerbasque Professor at the Basque Center for Materials, Applications and Nanostructures (BCMaterials, Spain). His research is focused on developing methodologies to write and read chemical information onto and from the backbone of hybrid framework materials. In addition, his research interests also include the acquisition of a fundamental understanding of the chemical and physical processes involved in their synthesis and functionalization.

19